Nanotechnology for the Oil and Gas Industry

Collection Editor:
Andrew R. Barron

Nanotechnology for the Oil and Gas Industry

Collection Editor:

Andrew R. Barron

Authors:

Andrew R. Barron
Ariana Bratt
Melissa Dominguez
Martha Farnsworth
Maclovio Fernandez
Ezekial Fisher
Varun Shenoy Gangoli
Christopher E. Hamilton
Lauren Harrison
Jason Holden
Kevin Kelly
Inna Kurganskaya
Andreas Luttge
Samuel Maguire-Boyle
Sean McCudden
Mary McHale
Alvin Orbaek
Luca Sabbatini
Richa Sethi
McKenzie Smith
Nikolaos Soultanidis
Zhengzong Sun
Liling Zeng
Caoimhe de Fréin

Online:

< http://cnx.org/content/col10700/1.11/ >

C O N N E X I O N S

Rice University, Houston, Texas

Collection structure revised: September 7, 2010
PDF generated: February 14, 2011
For copyright and attribution information for the modules contained in this collection, see p. 211.

Table of Contents

Preface to Nanotechnology for the Oil and Gas Industry[1]

As the population of the world is expected to rise from 6.5 billion in 2004 to nearer 10 billion in 2050, the need for energy is going to increase as a function of population, and this assumes that the present population has enough energy to meet its needs. However, we have over 2 billion people on the planet with no electricity and only biomass for heating fuel. If we cannot provide for our present global community, how can we expect to provide sufficient energy needs for the future population changes? Oil, coal, and natural gas make-up the vast majority of currently available energy—in other words, the majority of our energy demand is met by the combustion of hydrocarbon or carbon-based fuels. While there are arguments as to the limitations of these reserves globally, there is general agreement that obtaining the fuels from the earth is an ever-increasing challenge.

Clearly, if we are to meet the energy needs of the world, new methods must be developed to access heretofore-uneconomic energy sources. A long-term solution will involve the generation of energy from renewable sources, without either the production or the distribution of that energy involving significant pollution or gross consumption of raw materials. In this regard, nanotechnology has a place in the solution for the problem of energy generation, transport, storage, efficiency, and conservation. However, until such a time that all energy and chemical needs are obtained from renewable sources, the efficient recovery of oil and gas is going to be a major challenge of the 21st century.

Given the nature of Connexions, this course is fluid in structure and content. In addition, it contains modules by other authors where appropriate. The content will be updated and expanded with time. If any authors have suitable content, please contact me and I will be glad to assist in transforming the content to a suitable module structure.

Andrew R. Barron

Rice University, Houston, TX 77005. E-mail: arb@rice.edu[2]

[1] This content is available online at <http://cnx.org/content/m25743/1.2/>.

[2] arb@rice.edu

Chapter 1

History of Nanotechnology

1.1 The Early History of Nanotechnology[1]

NOTE: This module was derived from the module *The Early History of Nanotechnology* by Devon Fanfair, Salil Desai, and Christopher Kelty, which was developed as part of a Rice University Class called Nanotechnology: Content and Context.

1.1.1 Introduction

Nanotechnology is an essentially modern scientific field that is constantly evolving as commercial and academic interest continues to increase and as new research is presented to the scientific community. The field's simplest roots can be traced, albeit arguably, to 1959 but its primary development occurred in both the eighties and the early nineties. In addition to specific scientific achievements such as the invention of the STM, this early history is most importantly reflected in the initial vision of molecular manufacturing as it is outlined in three important works. Overall, an understanding of development and the criticism of this vision is integral for comprehending the realities and potential of nanotechnology today.

1.1.2 Richard Feynman: there's plenty of room at the bottom

"But I am not afraid to consider the final question as to whether, ultimately—in the great future—we can arrange the atoms the way we want; the very atoms, all the way down!" -Richard Feynman, *There's Plenty of Room at the Bottom*

The first time the idea of nanotechnology was introduced was in 1959, when Richard Feynman (Figure 1.1), a physicist at Caltech, gave a talk entitled *There's Plenty of Room at the Bottom*. Though he never explicitly mentioned "nanotechnology," Feynman suggested that it will eventually be possible to precisely manipulate atoms and molecules. Moreover, in an even more radical proposition, he thought that, in principle, it was possible to create "nano-scale" machines, through a cascade of billions of factories. According to the physicist, these factories would be progressively smaller scaled versions of machine hands and tools. He proposed that these tiny "machine shops" would then eventually be able to create billions of tinier factories. In these speculations, he also suggested that there are various factors, which uniquely affect the nano-scale level. Specifically, he suggested that as the scale got smaller and smaller, gravity would become more negligible, while both van der Waals attraction and surface tension would become very important. In the end, Feynman's talk has been viewed as the first academic talk that dealt with a main tenet of nanotechnology, the direct manipulation of individual atoms (molecular manufacturing).

[1] This content is available online at <http://cnx.org/content/m35280/1.1/>.

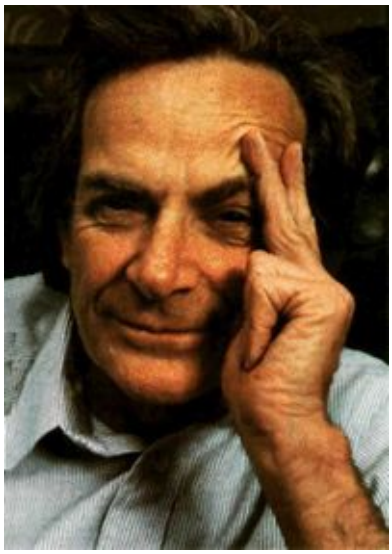

Figure 1.1: American physicist Richard Feynman (1918 - 1988).

Hence, long before STMs and atomic force microscopes were invented Feynman proposed these revolutionary ideas to his peers. As demonstrated in his quote (above), he chose to deal with a "final question" that wasn't fully realized till the eighties and nineties. Ultimately then, it was during these two decades, when the term "nanotechnology" was coined and researchers, starting with Eric Drexler, built up this field from the foundation that Feynman constructed in 1959. However, some such as Chris Toumey minimize the importance of Feynman in the establishment of the intellectual groundwork for nanotechnology. Instead, using evidence from its citation history, Toumey sees *There's Plenty of Room at the Bottom* as a "founding myth" that served only to directly influence Drexler rather than the other important scientists, who affected the future development of nanotechnology. Nevertheless, though the ultimate effect of Feynman's talk is debatable, it is certain that this work directly influenced Drexler's own research, which thus indirectly influenced nanotechnology as a whole.

1.1.3 Eric Drexler: molecular manufacturing

"The revolutionary Feynman vision launched the global nanotechnology race."-Eric Drexler

In 1979, Eric Drexler (Figure 1.2) encountered Feynman's talk on atomic manipulation and "nanofactories." The Caltech physicist's ideas inspired Drexler to put these concepts into motion by expanding Feynman's vision of molecular manufacturing with contemporary developments in understanding protein function. From this moment, Drexler's primary goal was to build upon the physicist's revolutionary foundation. As a result, though the term was yet to be coined, the field of nanotechnology was created.

Figure 1.2: American engineer Kim Eric Drexler (1955-).

In 1981, Drexler published his first article on the subject in the prestigious scientific journal, *Proceedings of the National Academy of Sciences*. Titled "Molecular engineering: An approach to the development of general capabilities for molecular manipulation," Drexler's publication essentially expanded the idea of molecular manufacturing by integrating modern scientific ideas with Feynman's concepts. Hence, he established his own vision of molecular manufacturing in this paper. Specifically, in his abstract, he discusses the possibility of molecular manufacturing as a process of fabricating objects with specific atomic specifications using designed protein molecules. He suggests that this would inevitably lead to the design of molecular machinery that would be able to position reactive groups with atomic precision. Thus, Drexler states that molecular manufacturing and the construction of "nano-machines" is a product of an analogous relationship "between features of natural macromolecules and components of existing machines." In addition, Drexler includes a table that outlines by function the molecular equivalents to macroscopic technologies. For example, he believed that bearings, which provide support for moving parts, are analogous to Sigma bonds. Overall, generating some interest in the scientific community, this publication presented Drexler's initial vision of molecular manufacturing, which was ultimately influenced by Feynman's talk. As a result, the field of nanotechnology continued to evolve, for Drexler took these concepts and expanded their potential in an accessible format through his now infamous book, *Engines of Creation: The Coming Era of Nanotechnology* (Figure 1.3).

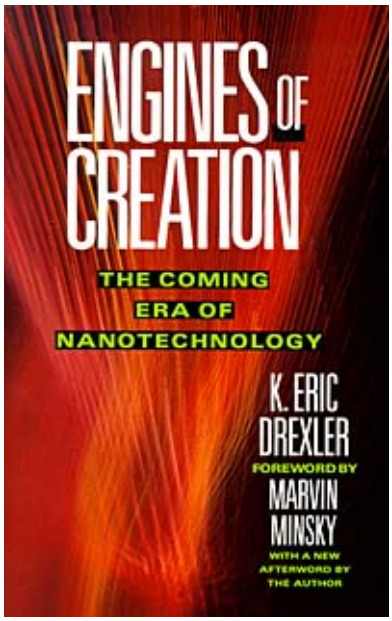

Figure 1.3: The cover of Eric Drexler's book *Engines of Creation: The Coming Era of Nanotechnology*.

1.1.4 Eric Drexler: engines of creation

"Molecular Assemblers will bring a revolution without parallel since the development of ribosomes, the primitive assemblers in the cell. The resulting nanotechnology can help life spread beyond Earth - a step without parallel since life spread beyond the seas; it can let our minds renew and remake our bodies - a step without any parallel at all." - Eric Drexler in *Engines of Creation*.

In this book, Drexler is credited as being the first person to use the word nanotechnology to describe engineering on the billionth of a meter scale. Though the term was used by Norio Taniguchi in 1974, Taniguchi's use of the word referred to nanotechnology in a different context. Published in 1986, *Engines of Creation* served to present Drexler's vision of molecular manufacturing that he outlined in his 1981 paper. Essentially, Drexler presented, albeit simplistically, that if atoms are viewed as small marbles, then molecules are a tight collection of these marbles that "snap" together, depending on their chemical properties. When snapped together in the right way, these molecules could represent normal-scaled tools such as motors and gears. Drexler suggested that these "atomic" tools and machines would operate just as their larger counterparts do. The moving parts of the nano-machine (e.g., Figure 1.4) would be formed by many atoms that are held together by their own atomic bonds. Ultimately, in Engines of Creation, Drexler envisioned that these would then be used as "assemblers" that could put together atoms into a desired shape. Applying this simplistic vision of molecular manufacturing, Drexler, in theory, presented that coal can be turned into diamond and computer chips can be created from sand. These processes would occur by using these fabricated atomic tools to reorganize the atoms that make up these materials. Most importantly, from these principles, he sensationally proclaimed in his book that nanotechnology, through the molecular manufacturing of "universal assemblers," would revolutionize everything from biological science to space travel (see quote above). Thus, with both his 1981 publication and his 1986 book, Drexler presented nanotechnology as a scientific field that solely revolved around his own expanded vision of Feynman's molecular manufacturing.

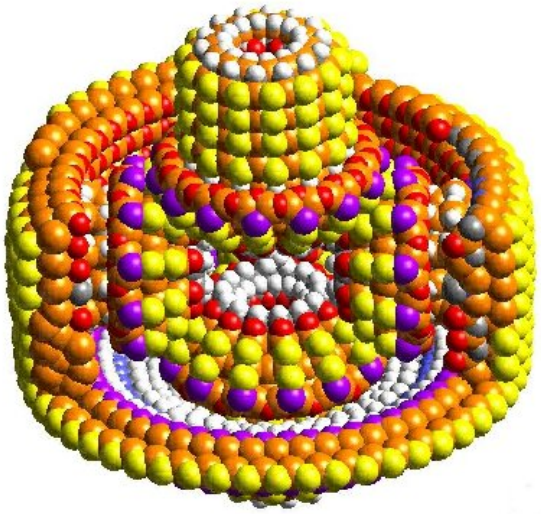

Figure 1.4: Drexler's "differential gear".

In addition, *Engines of Creation* also cautions about the possible dangers that accompany this kind of technology. Primarily, Drexler warns of the "gray goo," an amalgamation of self-replicating nanobots that would consume everything in the universe in order to survive (see Figure 1.5).

Figure 1.5: From Howard Lovy's Nanobot blog: http://nanobot.blogspot.com/

This book was highly influential as it brought nanotechnology to the mainstream scientific community for the first time. Though his theories of "gray goo" and molecular manufacturing were later criticized,

there is no question that Drexler's work had a profound impact on the establishment of nanotechnology as a scientific field.

1.1.5 The Aftermath of Engines of Creation: Impact and Criticism

Directly after the publication of this book, Drexler founded the Foresight Institute, whose stated goal is to "ensure the beneficial implementation of nanotechnology." Drexler used this "institute" as a way to present his vision of molecular manufacturing that he vividly illustrated in Engines of Creation. Thus, this "institute" was used to further propagate research, through his influential yet highly controversial depiction of nanotechnology and its future.

As a result, due to the publicity generated by both Drexler's work and institute, scientists from all over the world began to have a vested interest in the field of nanotechnology. Rice University chemist, Richard Smalley (Figure 1.6), for example, specifically said that he was a "fan of Eric" and that *Engines of Creation* influenced him to pursue nanotechnology. Moreover, he even gave Drexler's book to the top decision-makers at Rice University. Though criticizing Drexler and his work in future years, Smalley, like other scientists, were intrigued by this book and proceeded to do research in this new and evolving field.

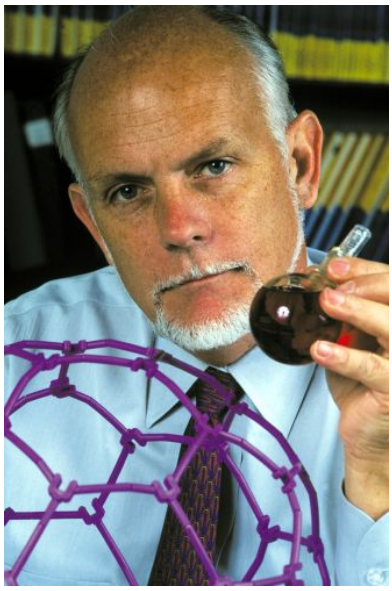

Figure 1.6: American chemist Richard E. Smalley (1943-2005), was awarded the Nobel Prize in Chemistry in 1996 for the discovery of a new form of carbon, buckminsterfullerene ("Buckyball").

Drexler's vision of molecular manufacturing and assemblers has become, on one hand, a scientific goal, through the Foresight Institute, and, on the other, a controversial issue. Some scientists have criticized Drexler's visions as impossible and harmful. Richard Smalley has led this movement against Drexler's almost sensationalist vision of molecular manufacturing. In their open debate in 2003, Smalley writes almost scathingly, "you cannot make precise chemistry occur as desired between two molecular objects with simple mechanical motion along a few degrees of freedom in the assembler-fixed frame of reference." Furthermore, he also chastises Drexler for his "gray goo scenario" saying, "you and the people around you have scared our children—while our future in the real world will be challenging and there are real risks, there will be no such

monster as the self-replicating mechanical nanobot of your dreams." In contrast to Drexler's radical vision, Smalley realistically argued that nanotechnology could be used on a much more practical and attainable level. As a result, due to the onset of academic criticism from scientists such as Richard Smalley, nanotechnology evolved from Drexler's vision of molecular manufacturing to a broad field that encompassed both practical manufacturing and non-manufacturing activities. Chemistry, materials science, and molecular engineering were now all included in this science.

1.1.6 Important successes in nanotechnology

In addition to the criticism of Drexler's vision of molecular manufacturing, three important developments that were independent of Drexler's paper helped turn nanotechnology into this broad field, today. First, the scanning tunneling microscope (STM) was invented by Binnig and Rohrer in 1981 (Figure 1.7). With this technology, individual atoms could be clearly identified for the first time. Despite its limitations (only conducting materials), this breakthrough was essential for the development of the field of nanotechnology because what had been previously concepts were now within view and testable. Some of these limitations in microscopy were eliminated through the 1986 invention of the atomic force microscope (AFM) (Figure 1.8). Using contact to create an image, this microscope could image non-conducting materials such as organic molecules. This invention was integral for the study of carbon Buckyball (Figure 1.9), discovered at Rice University. Ultimately, with these two achievements, nanotechnology could develop through the scientific method rather than through the conceptual and thus untestable visions of Drexler.

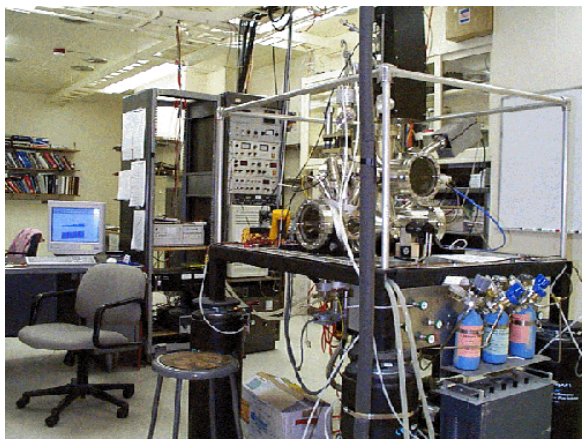

Figure 1.7: 1981-Invention of STM, Image From Steven Sibener, <http://sibener-group.uchicago.edu/facilities.html>.

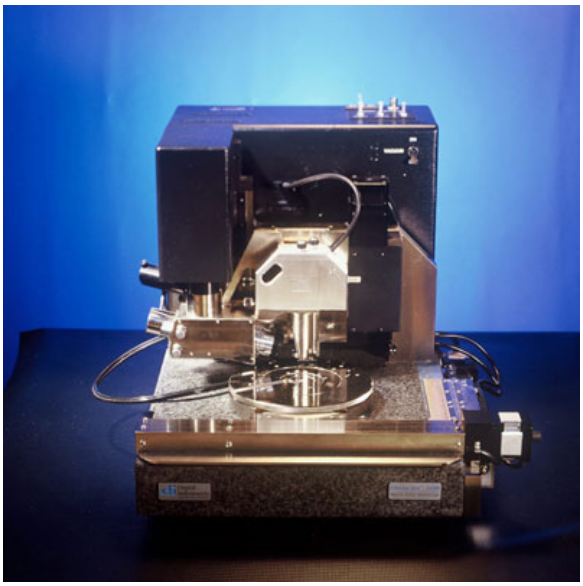

Figure 1.8: 1986-Invention of AFM, image from Mike Tiner, <http://www.cnm.utexas.edu/AFM.HTM>.

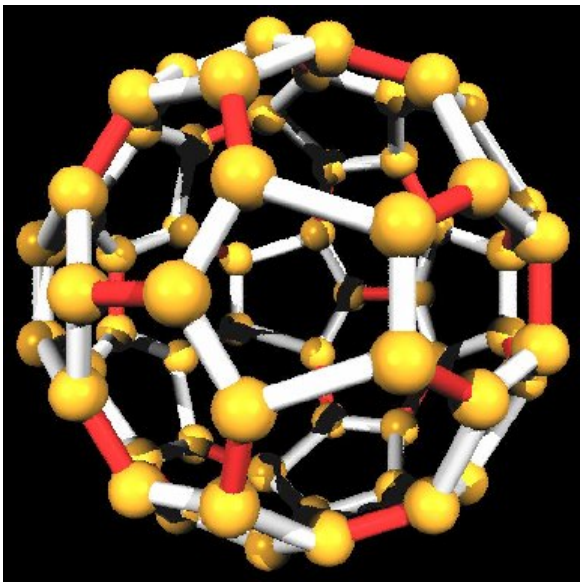

Figure 1.9: 1985-Buckyball discovered at Rice University. Image from Stephen Bond, <http://femto.cs.uiuc.edu/~sbond/reports/c60c60qm1/buckyball.jpg>.

This overall trend created by advancements in microscopy is illustrated through Don Eigler's revolutionary "stunt" at IBM. Here, he manipulated individual Xenon atoms on a Nickel surface to form the letters "IBM" (Figure 1.10). With the microscopy technology that was invented in the early to mid eighties, Eigler and his research team advanced the field of nanotechnology by seeking to simply manipulate atoms. Thus, while Drexler was conceiving sensationalized possibilities of "universal assemblers," Eigler focused his nanotech research on the realistic and attainable level that Smalley presented in his argument with Drexler. From this "stunt," nanotech research followed Eigler's path and therefore strayed away from Drexler's original vision. Because nanotechnology was viewed at this level, the field soon encompassed both practical manufacturing and non-manufacturing activities as Drexler's ideas were put aside.

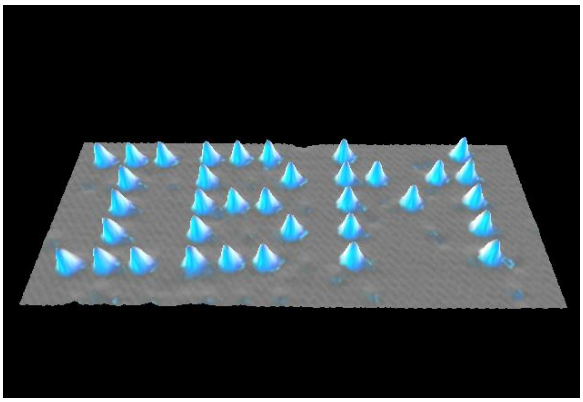

Figure 1.10: 1989-First atomic manipulation at IBM by Don Eigler. <http://www.almaden.ibm.com/vis/stm/atomo.html>.

1.1.7 Conclusion

While nanotechnology came into existence through Feynman's and then Drexler's vision of molecular manufacturing, the field has evolved in the 21st century to largely include research in chemistry and materials science as well as molecular engineering. As evidenced by Smalley's debate, this evolution is partly a response to the criticism of Drexler's views in both *Engines of Creation* and the Foresight Institute. Thus, in regards to the development of nanotechnology in the present, Drexler's vision can be viewed as an indirect influence through the sheer interest and subsequent criticism that he created in the field. As Toumey argues, Drexler and therefore Feynman did not have a direct role in the three most important breakthroughs in nanotechnology, the invention of the STM, the invention of the AFM, and the first manipulation of atoms. Instead, Drexler, through Molecular Manufacturing and Engines of Creation, brought scientists from all over the world to the brand new field. Consequently, criticism for Drexler's vision was established by researchers such as Dr. Smalley. Through this reevaluation and the parallel breakthroughs in microscope technology, nanotechnology as a scientific field was established in a way that diverged from Drexler's original vision of molecular manufacturing. This divergence is illustrated through the contrasting goals of the government's National Nanotechnology Initiative and Drexler's Foresight Institute. As a result, a thorough grasp of this early history is integral to understanding the development and definition of both the realities and potential of nanotechnology, today. Whereas Drexler created interest in the field but also sensationally outlined a nanotech revolution, researchers around the world have brought the nanotechnology that Drexler first envisioned to a more realistic and attainable level. All in all, today, the goal for nanotech research is not to immediately create billions of assemblers that will revolutionize our world but rather to explore the manufacturing and non-manufacturing aspects of nanotechnology, through a combination of chemistry, materials science, and molecular engineering.17Though places such as Drexler's Foresight Institute remain, academic institutions such as Rice University stay away from Drexler's sensationalized vision of nanotechnology as molecular manufacturing. This divergence is epitomized by the contrasting goals of the U.S government's National Nanotechnology Initiative and the Foresight Institute.

1.1.8 Bibliography

- H. Aldersey-Williams , *The Most Beautiful Molecule: The Discovery of the Buckyball*, Wiley, NJ (1997).
- L. E. Foster, *Nanotechnology: Science, Innovation, and Opportunity*, Prentice Hall, NJ (2006).
- J. C. Miller, R. Serrato, J. M. Represas-Cardenas, and G. Kundahl, *The Handbook of Nanotechnology: Business, Policy, and Interllectual Property Law*, Wiley, NJ (2005).

1.2 Buckyballs: Their history and discovery[2]

NOTE: This module was developed as part of a Rice University Class called "Nanotechnology: Content and Context[3] " initially funded by the National Science Foundation under Grant No. EEC-0407237. It was conceived, researched, written and edited by students in the Fall 2005 version of the class, and reviewed by participating professors.

"This year's Nobel Prize in Chemistry has implications for all the natural sciences. The seeds of the discovery were sowed by a desire to understand the behavior of carbon in red giant stars and interstellar gas clouds. The discovery of fullerenes has expanded our knowledge and changed our thinking in chemistry and physics. It has given us new hypotheses on the occurrence of carbon in the universe. It has also led us to discover small quantities of fullerenes in geological formations. Fullerenes are probably present in much larger amounts on earth than previously believed. It has been shown that most sooty flames contain small quantities of fullerenes. Think of this the next time you light a candle!"

-From the presentation speech for the Nobel Prize in Chemistry, 1996

1.2.1 Introduction

In 1996, the Royal Swedish Academy of Sciences awarded the Nobel Prize in Chemistry, the most prestigious award in the world for chemists, to Richard Smalley, Robert Curl, and Harold Kroto for their discovery of fullerenes. They discovered fullerenes (also called buckyballs) in 1985, but the special properties of the buckyballs took a few years to prove and categorize. Although by 1996 no practical applications of buckyballs had been produced, scientists appreciated the direction this discovery based in organic chemistry had led scientific research, as well as its specific contributions to various other fields. The accidental discovery of fullerenes also emphasizes the benefits and unexpected results which can arise when scientists with different backgrounds and research aims collaborate in the laboratory.

1.2.2 What are Buckyballs?

Before going into detail about the actual buckyball, we should discuss the element that makes its structure possible, carbon. Carbon is the sixth element on the periodic table, and has been found to be at least a partial constituent in over 90 per cent of all chemicals known to man. Indeed, its electron-bonding properties grant it a versatility specific to carbon, allowing it to be so widely functionalized, and more importantly, the reason for life on Earth. Anything that is living is necessarily chemically based on Carbon atoms, and for this reason, substances containing carbon are called organic compounds, and the study of them is called organic chemistry.

Though carbon is involved in chemistry with all sorts of other elements and compounds, it can also exist in pure carbon states such as graphite and diamond. Graphite and diamond are two different allotropes of carbon. An allotrope is a specific physical arrangement of atoms of an element. So although diamond and graphite are both pure carbon, because the crystalline structure of each is significantly different, their chemical and physical properties (as well as value) are very different.

[2]This content is available online at <http://cnx.org/content/m14355/1.1/>.
[3]http://frazer.rice.edu/nanotech

Above: diamond Below: carbon. Notice how the structure of the two allotropes vary, even though they are both made of the same carbon atoms (black)

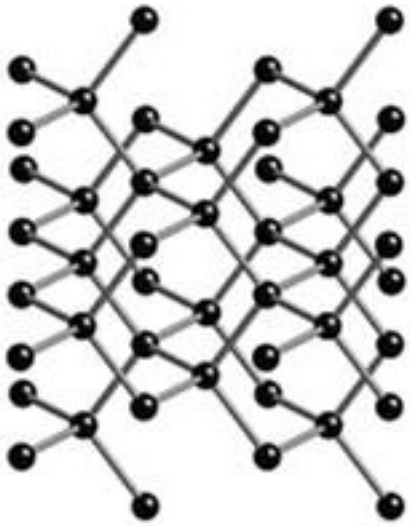

Figure 1.11: Images from The Austrailian Academy of Science[4]

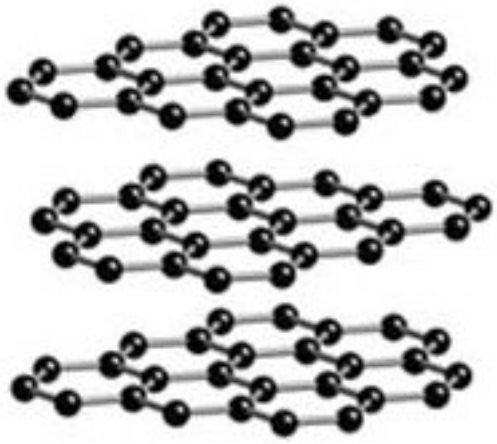

Figure 1.12

Diamond and graphite are not the only known allotropes pf carbon, chaoit and carbon(VI), discovered in 1968 and 1972, respectively, have also been found. Even more recently, the Buckminsterfullerenes, the subject of this module, were discovered at Rice by Smalley, Kroto,and Curl. Buckminsterfullerenes is actually a class of allotropes

[4]http://www.science.org.au/nova/024/024print.htm

Above: C540 Below: C60 Both of these are different allotropes of carbon. C60 is the most common and the most popularized of the Buckminsterfullerenes. Not shown is the second most common Buckyball, C70[5]
.

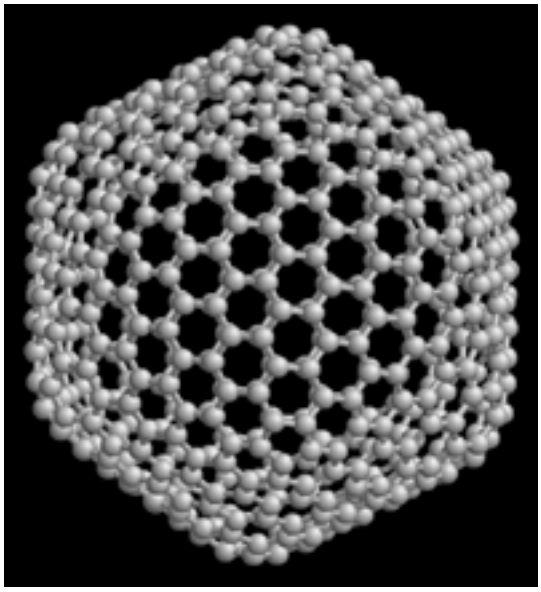

Figure 1.13: The Icosahedral Fullerene C540

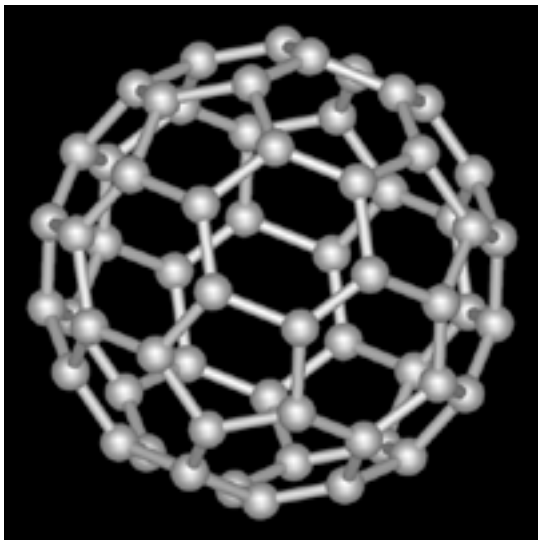

Figure 1.14

[5]http://en.wikipedia.org/wiki/Buckyball

In fact, scientists have now discovered hundreds of buckyballs of different sizes, all with the trademark spherical-like shape. To differentiate them, each allotrope is denoted as C (for carbon) with the number of carbon atoms in the subscript (i.e. C80). Technically, the geometrical shapes that these buckyballs share are actually known as geodesics, or rather, polyhedrons that approximate spheres. Specifically, the commonly depicted C60 buckyball is a truncated icosahedron. A more satisfactory representation of it can be had in a soccer ball, with which it shares the exact same shape. It is made up of 12 pentagons, each surrounded by 5 hexagons (20 in all).

1.2.3 The Discovery

British chemist Harold W. Kroto at the University of Sussex was studying strange chains of carbon atoms found in space through microwave spectroscopy, a science that studies the absorption spectra of stellar particles billions of kilometers away to identify what compounds are found in space. This is possible because every element radiates a specific frequency of light that is unique to that element, which can observed using radiotelescopes. The elements can then be identified because a fundamental rule of matter stating that the intrinsic properties of elements apply throughout the universe, which means that the elements will emit the same frequency regardless of where they are found in the universe. Kroto took spectroscopic readings near carbon-rich red giants, or old stars with very large radii and relatively low surface temperatures, and compared them to spectrum lines of well-characterized substances. He identified the dust to be made of long alternating chains of carbon and nitrogen atoms known as cynopolyynes, which are also found in interstellar clouds. However Kroto believed that the chains were formed in the stellar atmospheres of red giants and not in interstellar clouds, but he had to study the particles more closely.

At the same time, Richard Smalley was doing research on cluster chemistry, at Rice University in Houston, Texas. "Clusters" are aggregates of atoms or molecules, between microscopic and macroscopic sizes, that exist briefly. Smalley had been studying clusters of metal atoms with the help of Robert Curl, using an apparatus Smalley had in his laboratory. This laser-supersonic cluster beam apparatus had the ability to vaporize nearly any known material into plasma using a laser, which is a highly concentrated beam of light with extremely high energy.

Through an acquaintance with Curl, Kroto contacted Smalley and discussed the possibility of using his apparatus to recreate the high-heat conditions of a red giant's atmosphere in order to study the clusters of carbon produced, which might give Kroto insight as to the formation of the carbon chains. Smalley conceded and Kroto arrived in Smalley's laboratory in Rice University on September 1, 1985 whom began working on the experiment along with graduate students J.R. Heath and S.C. O'Brien.

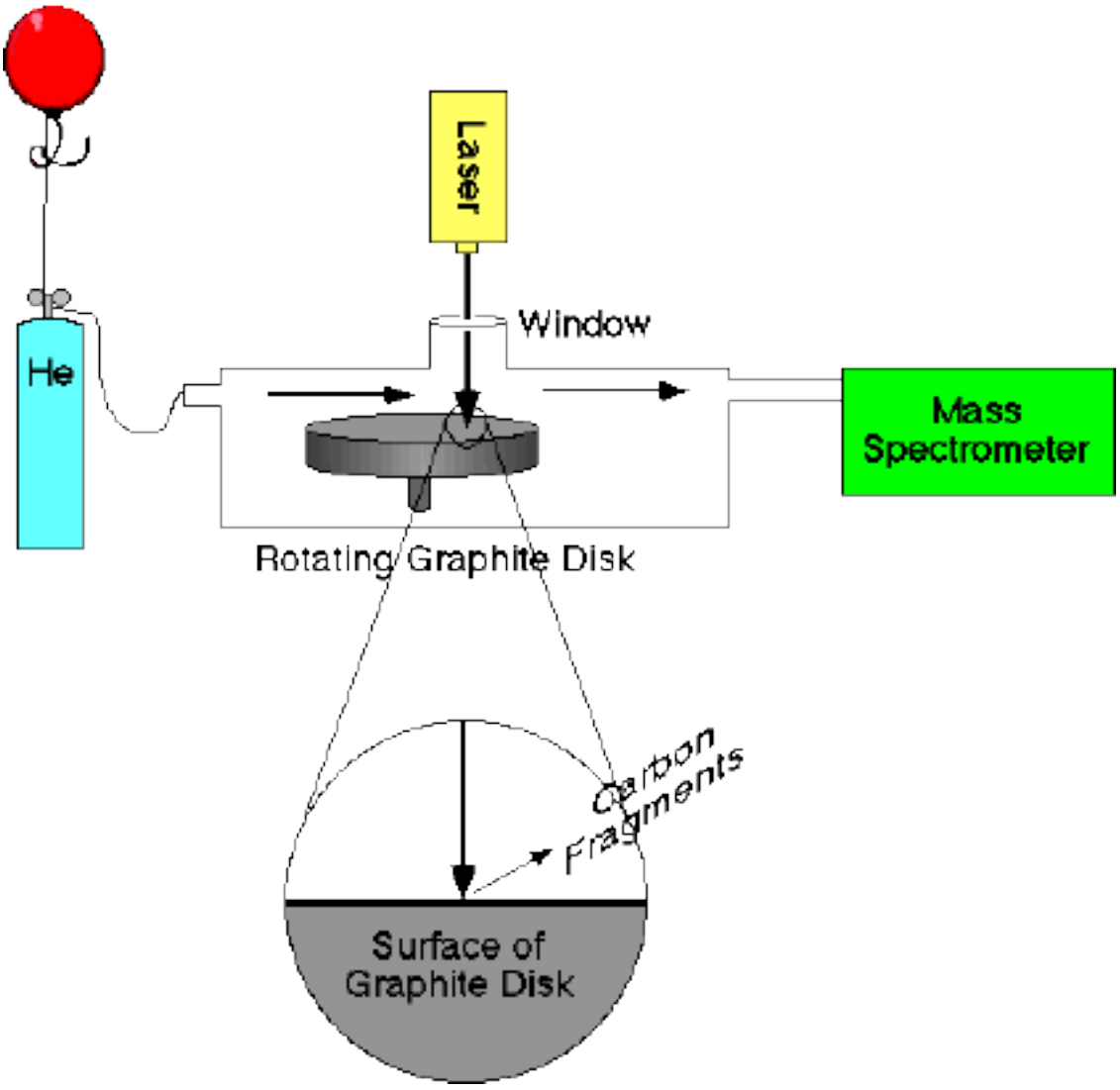

Figure 1.15: Smalley's apparatus[6]

Smalley's apparatus, shown above, fires a high energy laser beam at a rotating disk of graphite in a helium-filled vacuum chamber. Helium is used because it is an inert gas and therefore does not react with the gaseous carbon. The intense heating of the surface of the graphite breaks the C—C bonds because of the intense energy. Once vaporized, the carbon atoms cool and condense in the high-pressure helium gas, colliding and forming new bond arrangements. Immediately upon cooling several degrees above absolute zero in a chamber, the carbon leads to a mass spectrometer for further analysis.

A mass spectrometer uses an atom or molecule's weight and electric charge to separate it from other molecules. This is done by ionizing the molecules, which is done by bombarding the molecules with high energy electrons which then knocks off electrons. If an electron is removed from an otherwise neutral molecule,

[6] http://www.chem.wisc.edu/~newtrad/CurrRef/BDGTopic/BDGFigs/2_1SmalApp.gif

then the molecule becomes a positively charged ion or cation. The charged particles are then accelerated by passing through electric plates and then filtered through a slit. A stream of charged particles exits the slit and is then deflected by a magnetic field into a curved path. Because all the particles have a charge of +1, the magnetic field exerts the same amount of force on them, however, the more massive ions are deflected less, and thus a separation occurs. By adjusting the strength of the accelerating electric plates or the deflecting magnetic field, a specific mass can be selected to enter the receptor on the end. After adjusting the experiment, it became greatly evident that the most dominant molecule measured was 720 amu (atomic mass units). By dividing this number by the mass of a single carbon atom (12 amu), it was deduced that the molecule was comprised of 60 carbon atoms (720 / 12 = 60).

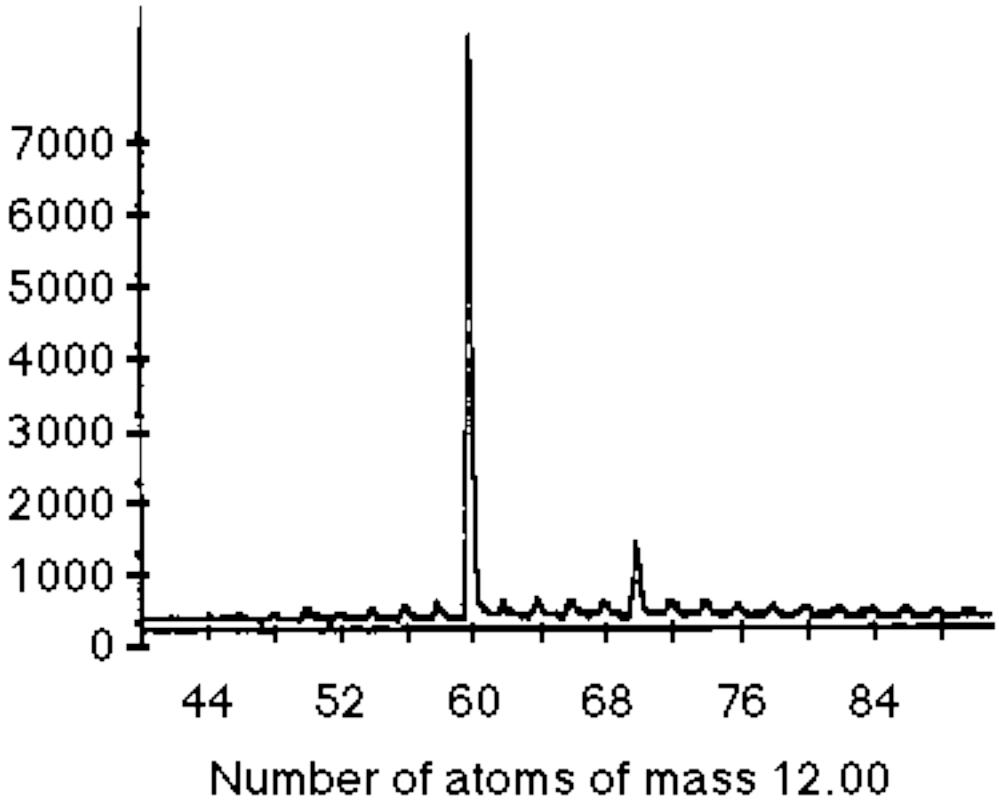

Figure 1.16: University of Wisconsin[7]

The next task was to develop a model for the structure of C60, this new allotrope of carbon. Because it was overwhelmingly dominant, Smalley reasoned the molecule had to be the very stable. The preferred geometry for stable molecule would reasonably be spherical, because this would mean that all bonding capabilities for carbon would be satisfied. If it were a chain or sheet like graphite, the carbon atoms could still bond at the ends, but if it were circular all ends would meet. Another hint as to the arrangement of the molecule was that there must be a high degree of symmetry for a molecule as stable as C60. Constructing a model that satisfied these requirements was fairly difficult and the group of scientists experimented with several models before coming to a conclusion. As a last resort, Smalley made a paper model by cutting out

[7] http://www.chem.wisc.edu/~newtrad/CurrRef/BDGTopic/BDGFigs/2_1SmalApp.gif

paper pentagons and hexagons in which he tried to stick them together so that the figure had 60 vertices. Smalley found that he create a sphere made out of 12 pentagons interlocking 20 hexagons to make a ball. The ball even bounced. To ensure that the shape fulfilled the bonding capabilities of carbon, Kroto and Curl added sticky labels to represent double bonds. The resulting shape is that of a truncated icosahedron, the same as that of a soccer ball. Smalley, Curl, and Kroto named the molecule buckminsterfullerene after the American architect and engineer Richard Buckminster Fuller who used hexagons and pentagons for the basic design of his geodesic domes.

Eleven days after they had begun, the scientist submitted their discovery to the prestigious journal Nature in a manuscript titled "C60 Buckminsterfullerene." The journal received it on the 13th of September and published it on the 14th of November 1985. The controversial discovery sparked approval and criticism for a molecule that was remarkably symmetrical and stable.

1.2.4 How Buckyballs are made?

Experimentally, Smalley, Kroto, and Curl, first created the buckyballs using Smalley's laser-supersonic cluster beam apparatus to knock carbons off of a plate and into a high pressure stream of helium atoms. They would be carried off and immediately be cooled to only a few degrees above absolute zero, where they would aggregate and form these buckyballs. This method however, resulted in low yields of buckyballs, and it took nearly five years until in 1990 newer methods developed by American and German scientists could manufacture buckyballs in large quantities.

The common method today involves transmitting a large current between two graphite electrodes in an inert atmosphere, such as Helium. This gives rise to a carbon plasma arc bridging the two electors, which cools instantaneously and leaves behind a sooty residue from which the buckyballs can be extracted.

These methods of producing buckyballs do deserve a great deal of applaud. However, humans cannot take all, or even most of, the credit for the production of fullerenes. As a matter of fact, buckyballs occur in nature, naturally, and in greater amounts than expected. Buckyballs are known to exist in interstellar dust and in geological formations on Earth. Even closer to home are the buckyballs that naturally form in the wax and soot from a burning candle, as the flame on the wick provides the sufficient conditions for such processes to occur. Buckyballs are the new sensation for us, but to Nature, they are old news.

1.2.5 Chemical and Physical Properties

Since buckyballs are still relatively new, there properties are still being heavily studied. Buckyballs' unique shape and electron bonding give them interesting properties on the physical level, and on the chemical level.

Since spheres in nature are known to be the most stable configurations, one could expect the same from fullerenes. Indeed this is one of the reasons why Smalley, Curl, and Kroto initially considered its shape. Their tests showed that it was extremely stable, and thus, they reasoned, it could be a spherical-like geodesic. Also, fullerenes are resilient to impact and deformation. This means, that squeezing a buckyball and then releasing it would result in its popping back in shape. Or perhaps, if it was thrown against an object it would bounce back; ironically just like the very soccer ball it resembles.

Buckyballs are also extremely stable in the chemical sense. Since all the carbon-carbon bonds are optimized in their configuration, they become very inert, and are not as prone to reactions as other carbon molecules. What makes these bonds special is a property called aromaticity. Normally, electrons are fixed in whatever bond they constitute. Whereas in aromatic molecules, of which hexagonal carbon rings are a prime example, electrons are free to move ("delocalize") among other bonds. Since all the fullerenes have the cyclo-hexanes in abundance, they are very aromatic, and thus have very stable, inert, carbon bonds. Buckyballs, though sparingly soluble in many solvents, are in fact the only known carbon allotropes to be soluble.

An interesting feature of Fullerenes is that their hollow structure allows them to hold other atoms inside them. The applications of this are abound, and are being studied to great extent.

Important to note about any new material is its health concerns. Although believed to be relatively inert, experiments by Eva Oberdörster at Southern Methodist University, presented some possible dangers

of fullerenes. She introduced buckyballs into water at concentrations of 0.5 parts per million, and found that largemouth bass suffered a 17-fold increase in cellular damage in the brain tissue after 48 hours. The damage was of the type lipid peroxidation, which is known to impair the functioning of cell membranes. Their livers were also inflamed and genes responsible for producing repair enzymes were activated. As of 10/20/05, the SMU work had not been peer reviewed.

1.2.6 What have buckyballs contributed to science?

After the astrophysicists D.R. Huffmann and W. Kratschmer managed to produce larger quantities of fullerenes in 1990, scientists further investigated the structure and characteristics of buckyballs. Research on buckyballs has led to the synthesis of over 1000 new compounds with exciting properties, and over 100 patents related to buckyballs have been filed in the US. In addition, an important new material, nanotubes, has exploded onto the scientific scene in recent years. The discovery and manufacture of nanotubes resulted directly from research on buckyballs. Finally, although buckyballs have not yet been used in any practical applications, partly due to the high cost of material, researchers are using buckyballs to learn more about the history of our world, and companies are devising some interesting uses for buckyballs even today.

1.2.7 Nanotubes

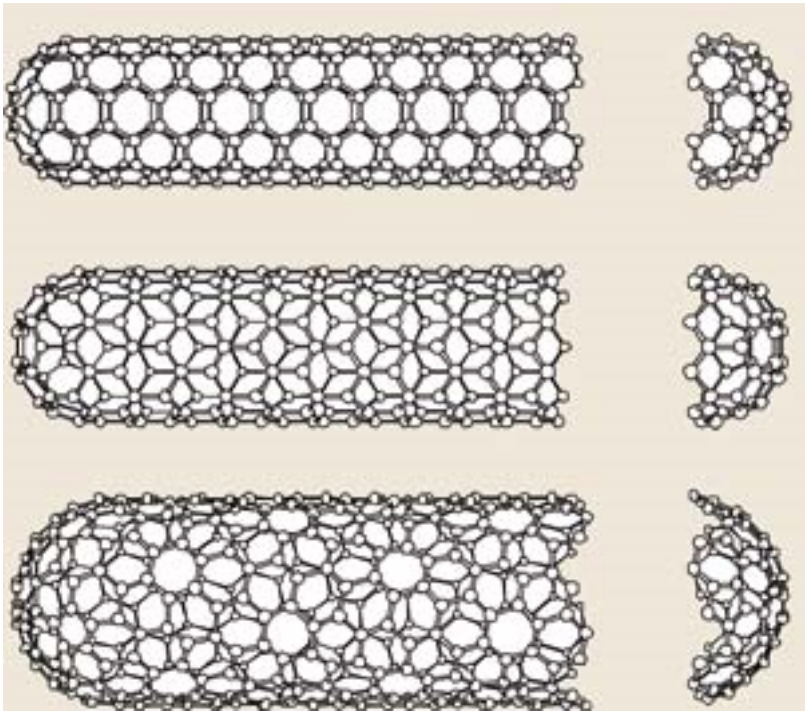

Figure 1.17

The discovery of nanotubes in 1991 by S. Iijima has been by far the buckyball's most significant contribution to current research. Nanotubes, both single- and multi-walled, can be thought of as sheets of graphite rolled into cylinders and sometimes capped with half-fullerenes. Nanotubes, like fullerenes, possess some

very unique properties, such as high electrical and thermal conductivity, high mechanical strength, and high surface area. In fact, carbon nanotubes provide a clear example of the special properties inherent at the quantum level because they can act as either semi-conductors or metals, unlike macroscopic quantities of carbon molecules. These properties make nanotubes extremely interesting to researchers and companies, who are already developing many potentially revolutionary uses for them.

1.2.8 What are buckyballs teaching us about our world?

A paper published on March 28, 2000 in the Proceedings of the National Academy of Sciences (PNAS) by Becker, Poreda, and Bunch uses buckyballs to provide new evidence for early periods in earth's geological and biological history. By exploiting the unique properties of buckyballs, these three scientists were able to study geology in a new way. First of all, the unique ability to extract fullerenes (unlike graphite and diamond) from organic solvents allowed them to isolate carbon material in the meteorites, then the unique cage-like structure of fullerenes allowed them to investigate the noble gases enclosed within the ancient fullerenes. In their study, the researches found helium of extraterrestrial origin trapped inside buckyballs extracted from two meteorites and sedimentary clay layers from 2 billion and 65 million years ago respectively. The helium inside these buckyballs bears unusual ratios of 3He/4He coupled with non-atmospheric ratios of 40Ar/36Ar, which according to their research indicates extraterrestrial origin. In addition, they have shown that these fullerenes could not have been formed upon impact of the meteorite or during subsequent forest fires.iBecker, Poreda, and Bunch. 2982.

The discovery of the extraterrestrial origin of the enclosed helium has far-reaching implications for the history of the earth. For example, the existence of the carrier phase of fullerenes suggests that "fullerenes, volatiles, and perhaps other organic compounds were being exogenously delivered to the early Earth and other planets throughout time."iiBecker, Poreda, and Bunch, 2982. With more research, it might even be possible to determine whether meteorite impacts on earth could have triggered global changes or even brought carbon and gases to earth that allowed for the development of life!

1.2.9 Uses

Why does it matter? Why should anyone care? These buckyballs are giving scientists information about allotropes of carbon never before conceived. More importantly, these buckyballs might allow engineers and doctors do what was never before possible. These are some of the applications for buckyballs currently in research.

Medical uses for buckyballs

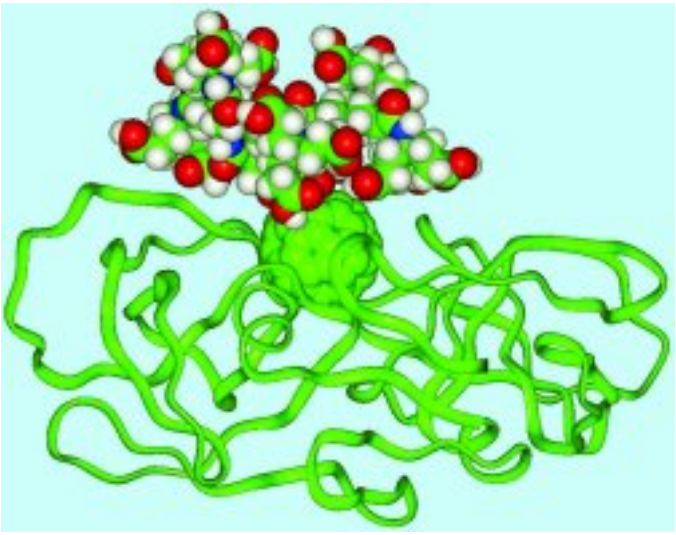

Figure 1.18

Drug Treatments

Buckyballs are now being considered for uses in the field of medicine, both as diagnostic tools and drug candidates. Simon Friedman, a researcher at the University of Kansas, began experimenting with buckyballs as possible drug treatments in 1991. Because buckyballs have a rigid structure (unlike benzene rings, often used for similar purposes), researchers are able to attach other molecules to it in specific configurations to create precise interactions with a target molecule. For example, Friedman has created a protease inhibitor that attaches to the active site of HIV 50 times better than other molecules. C Sixty, a Toronto based company that specializes in medical uses of fullerenes, plans to test on humans two new fullerene-based drugs for Lou Gehrig's disease and HIV in the near future.

Gadolinium Carriers

Another medical use for buckyballs is taking place in the field of diagnostics. Buckyballs unique cage-like structure might allow it to take the place of other molecules in shuttling toxic metal substances through the human body during MRI scans. Usually, the metal gadolinium is attached to another molecule and sent into the body to provide contrast on the MRI scans, but unfortunately these molecules are excreted from the system quickly to reduce the chance of toxic poisoning in the subject. Lon Wilson of Rice University and researchers at TDA Research have encased gadolinium inside buckyballs, where they cannot do harm to the patient, allowing them to remain inside the body longer, but still appear in MRI's. So far this application has been successfully tested in one rat. Wilson and others have begun to develop even more applications for the tiny little cages that could one day help revolutionize medicine.

Engineering Uses

Nano STM

The Scanning Tunneling Microscope (STM) is one of the foremost tools in microscopy today; boasting the ability to to map out the topology of material surfaces at atomic resolution (i.e. on the order of 0.2 nanometers). The STM achieves this feat by bringing a needle point, functioning as a probe, within just several nanometers of a sample's surface. At these minute scales, even small disturbances can cause the tip to crach into the sample and deform itself. A possible solution to this problem would be the replacement of the standard needle point with a buckyball. As discussed previously, fullerenes bear amazing resilience due to their spherical geometry, and would resist distortions from such collisions.

Buckyballs in circuits
European scientists are aiming to use buckyballs in circuit. So far, they have been able to attach a single fullerene to a copper surface, and then, through a process called shrink wrapping, fitted its center with a metal ion and made it smaller to increases electric conductivity by a hundred times.
Lubricants
Because of their shapes, they could be used equivalently to ball bearings, and thus allow surfaces to roll over each other, making the fullerenes equivalently lubricants
Superconductors
It has been shown that fitting a potassium ion in the buckyball causes it to become superconductive. Ways to exploit this are in the research stages.
Catalysts
Attaching metals onto the surface of fullerenes offers the possibility for buckyballs to become catalysts.

1.2.10 Conclusion

As we can see, we have come along way since that fateful year of 1985. Strides have been made. We have seen the rise of nanotubes and the new science of Nanotechnology. We are still studying the chemical and physical properties of buckyballs and continue to be amazed. They have already proved to us why they are important; their possible uses in medicine and in engineering are broad and profound, while the health risks they posed have yet to be fully analyzed. Only time will tell whether they will meet, or exceed our expectations as we unfold this brave new world.

1.2.11 Bibliography

Nobelprize.org: http://nobelprize.org/chemistry/laureates/1996/press.html
http://www.science.org.au/nova/024/024print.htm
http://blogcritics.org/archives/2004/04/10/084049.php
http://www.science.org.au/nova/024/024key.htm
http://www.sciencedaily.com//releases/2003/04/030418081522.htm
http://www.sciencenews.org/articles/20020713/bob10.asp
Gorman, Jessica. Buckymedicine: Coming soon to a pharmacy near you?. Science News Online: July 13, 2002, vol. 162, no. 2. http://www.sciencenews.org/articles/20020713/bob10.asp
Becker, Poreda, and Bunch. Extraterrestrial Helium Trapped in Fullerenes in the Sudbury Impact Structure. Science, Vol 272, Issue 5259, 249-252 , 12 April 1996.
Personal author: Aldersey-Williams, Hugh. Title: The most beautiful molecule : an adventure in chemistry / Hugh Aldersey-Williams. Publication info: London : Aurum Press, 1995. Personal author: Baggott, J. E. Title: Perfect symmetry : the accidental discovery of Buckminsterfullerene / Jim Baggott. Publication info: Oxford [England] ; New York : Oxford University Press, 1994.

Chapter 2

Synthesis of Nanomaterials

2.1 Introduction to Nanoparticle Synthesis[1]

The fabrication of nanomaterials with strict control over size, shape, and crystalline structure has inspired the application of nanochemistry to numerous fields including catalysis, medicine, and electronics. The use of nanomaterials in such applications also requires the development of methods for nanoparticle assembly or dispersion in various media. A majority of studies have been aimed at dispersion in aqueous media aimed at their use in medical applications and studies of environmental effects, however, the principles of nanoparticle fabrication and functionalization of nanoparticles transcends their eventual application. Herein, we review the most general routes to nanoparticles of the key types that may have particular application within the oil and gas industry for sensor, composite, or device applications.

Synthesis methods for nanoparticles are typically grouped into two categories: "top-down" and "bottom-up". The first involves division of a massive solid into smaller portions. This approach may involve milling or attrition, chemical methods, and volatilization of a solid followed by condensation of the volatilized components. The second, "bottom-up", method of nanoparticle fabrication involves condensation of atoms or molecular entities in a gas phase or in solution. The latter approach is far more popular in the synthesis of nanoparticles.

Dispersions of nanoparticles are intrinsically thermodynamically metastable, primarily due to their very high surface area, which represents a positive contribution to the free enthalpy of the system. If the activation energies are not sufficiently high, evolution of the nanoparticle dispersion occurs causing an increase in nanoparticle size as typified by an Ostwald ripening process. Thus, highly dispersed nanoparticles are only kinetically stabilized and cannot be prepared under conditions that exceed some threshold, meaning that so-called "soft-chemical" or "*chemie duce*" methods are preferred. In addition, the use of surface stabilization is employed in many nanomaterials to hinder sintering, recrystallization and aggregation.

2.1.1 Bibliography

- J. Gopalakrishnan, *Chem. Mater.*, 1995, **7**, 1265.

2.2 Carbon Nanomaterials[2]

2.2.1 Introduction

Although nanomaterials had been known for many years prior to the report of C_{60} the field of nanoscale science was undoubtedly founded upon this seminal discovery. Part of the reason for this explosion in

[1] This content is available online at <http://cnx.org/content/m22372/1.2/>.
[2] This content is available online at <http://cnx.org/content/m22580/1.4/>.

nanochemistry is that while carbon materials range from well-defined nano sized molecules (i.e., C_{60}) to tubes with lengths of hundreds of microns, they do not exhibit the instabilities of other nanomaterials as a result of the very high activation barriers to their structural rearrangement. As a consequence they are highly stable even in their unfunctionalized forms. Despite this range of carbon nanomaterials possible they exhibit common reaction chemistry: that of organic chemistry.

The previously unknown allotrope of carbon: C_{60}, was discovered in 1985, and in 1996, Curl, Kroto, and Smalley were awarded the Nobel Prize in Chemistry for the discovery. The other allotropes of carbon are graphite (sp^2) and diamond (sp^3). C_{60}, commonly known as the "buckyball" or "Buckminsterfullerene", has a spherical shape comprising of highly pyramidalized sp^2 carbon atoms. The C_{60} variant is often compared to the typical soccer football, hence buckyball. However, confusingly, this term is commonly used for higher derivatives. Fullerenes are similar in sheet structure to graphite but they contain pentagonal (or sometimes heptagonal) rings that prevent the sheet from being planar. The unusual structure of C_{60} led to the introduction of a new class of molecules known as fullerenes, which now constitute the third allotrope of carbon. Fullerenes are commonly defined as "any of a class of closed hollow aromatic carbon compounds that are made up of twelve pentagonal and differing numbers of hexagonal faces."

The number of carbon atoms in a fullerene range from C_{60} to C_{70}, C_{76}, and higher. Higher order fullerenes include carbon nanotubes that can be described as fullerenes that have been stretched along a rotational axis to form a tube. As a consequence of differences in the chemistry of fullerenes such as C_{60} and C_{70} as compared to nanotubes, these will be dealt with separately herein. In addition there have also been reports of nanohorns and nanofibers, however, these may be considered as variations on the general theme. It should be noted that fullerenes and nanotubes have been shown to be in flames produced by hydrocarbon combustion. Unfortunately, these naturally occurring varieties can be highly irregular in size and quality, as well as being formed in mixtures, making them unsuitable for both research and industrial applications.

2.2.2 Fullerenes

Carbon-60 (C_{60}) is probably the most studied individual type of nanomaterial. The spherical shape of C_{60} is constructed from twelve pentagons and twenty hexagons and resembles a soccer ball (Figure 2.1a). The next stable higher fullerene is C_{70} (Figure 2.1b) that is shaped like a rugby or American football. The progression of higher fullerenes continues in the sequence C_{74}, C_{76}, C_{78}, etc. The structural relationship between each involves the addition of six membered rings. Mathematically (and chemically) two principles define the existence of a stable fullerene, i.e., Euler's theorem and isolated pentagon rule (IPR). Euler's theorem states that for the closure of each spherical network, n ($n \geq 2$) hexagons and 12 pentagons are required while the IPR says no two pentagons may be connected directly with each other as destabilization is caused by two adjacent pentagons.

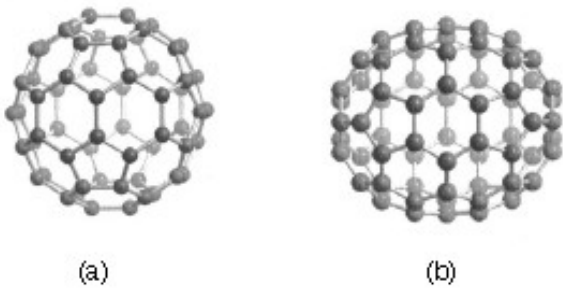

Figure 2.1: Molecular structures of (a) C_{60} and (b) C_{70}.

Although fullerenes are composed of sp^2 carbons in a similar manner to graphite, fullerenes are soluble in various common organic solvents. Due to their hydrophobic nature, fullerenes are most soluble in CS_2 (C_{60} = 7.9 mg/mL) and toluene (C_{60} = 2.8 mg/mL). Although fullerenes have a conjugated system, their aromaticity is distinctive from benzene that has all C-C bonds of equal lengths, in fullerenes two distinct classes of bonds exist. The shorter bonds are at the junctions of two hexagons ([6, 6] bonds) and the longer bonds at the junctions of a hexagon and a pentagon ([5,6] bonds). This difference in bonding is responsible for some of the observed reactivity of fullerenes.

2.2.2.1 Synthesis of fullerenes

The first observation of fullerenes was in molecular beam experiments at Rice University. Subsequent studies demonstrated that C_{60} it was relatively easy to produce grams of fullerenes. Although the synthesis is relatively straightforward fullerene purification remains a challenge and determines fullerene's commercial price. The first method of production of measurable quantities of fullerenes used laser vaporization of carbon in an inert atmosphere, but this produced microscopic amounts of fullerenes. Laboratory scales of fullerene are prepared by the vaporization of carbon rods in a helium atmosphere. Commercial production ordinarily employs a simple ac or dc arc. The fullerenes in the black soot collected are extracted in toluene and purified by liquid chromatography. The magenta C_{60} comes off the column first, followed by the red C_{70}, and other higher fullerenes. Even though the mechanism of a carbon arc differs from that of a resistively heated carbon rod (because it involves a plasma) the He pressure for optimum C_{60} formation is very similar.

A ratio between the mass of fullerenes and the total mass of carbon soot defines fullerene yield. The yields determined by UV-Vis absorption are approximately 40%, 10-15%, and 15% in laser, electric arc, and solar processes. Interestingly, the laser ablation technique has both the highest yield and the lowest productivity and, therefore, a scale-up to a higher power is costly. Thus, fullerene commercial production is a challenging task. The world's first computer controlled fullerene production plant is now operational at the MER Corporation, who pioneered the first commercial production of fullerene and fullerene products.

2.2.2.2 Endohedral fullerenes

Endohedral fullerenes are fullerenes that have incorporated in their inner sphere atoms, ions or clusters. Endohedral fullerenes are generally divided into two groups: endohedral metallofullerenes and non-metal doped fullerenes. The first endohedral metallofullerenes was called $La@C_{60}$. The @ sign in the name reflects the notion of a small molecule trapped inside a shell.

Doping fullerenes with metals takes place *in-situ* during the fullerene synthesis in an arc reactor or via laser evaporation. A wide range of metals have been encased inside a fullerene, i.e., Sc, Y, La, Ce, Ba, Sr, K, U, Zr, and Hf. Unfortunately, the synthesis of endohedral metallofullerenes is unspecific because in addition a high yield of unfilled fullerenes, compounds with different cage sizes are prepared (e.g., $La@C_{60}$ or $La@C_{82}$). A characteristic of endohedral metallofullerenes is that electrons will transfer from the metal atom to the fullerene cage and that the metal atom takes a position off-center in the cage. The size of the charge transfer is not always simple to determine, but it is usually between 2 and 3 units (e.g., $La_2@C_{80}$) but can be as high as 6 electrons (e.g., $Sc_3N@C_{80}$). These anionic fullerene cages are very stable molecules and do not have the reactivity associated with ordinary empty fullerenes (see below). This lack of reactivity is utilized in a method to purify endohedral metallofullerenes from empty fullerenes.

The endohedral $He@C_{60}$ and $Ne@C_{60}$ form when C_{60} is exposed to a pressure of around 3 bar of the appropriate noble gases. Under these conditions it was possible to dope 1 in every 650,000 C_{60} cages with a helium atom. Endohedral complexes with He, Ne, Ar, Kr and Xe as well as numerous adducts of the $He@C_{60}$ compound have also been proven with operating pressures of 3000 bars and incorporation of up to 0.1 % of the noble gases. The isolation of $N@C_{60}$, $N@C_{70}$ and $P@C_{60}$ is very unusual and unlike the metal derivatives no charge transfer of the pnictide atom in the center to the carbon atoms of the cage takes place.

2.2.2.3 Chemically functionalized fullerenes

Although fullerenes have a conjugated aromatic system all the carbons are quaternary (i.e., containing no hydrogen), which results in making many of the characteristic substitution reactions of planar aromatics impossible. Thus, only two types of chemical transformations exist: redox reactions and addition reactions. Of these, addition reactions have the largest synthetic value. Another remarkable feature of fullerene addition chemistry is the thermodymics of the process. Since the sp^2 carbon atoms in a fullerene are paramidalized there is significant strain energy. For example, the strain energy in C_{60} is *ca* 8 kcal/mol, which is 80% of its heat of formation. So the relief of this strain energy leading to sp^3 hybridized C atoms is the major driving force for addition reactions (Figure 2.2). As a consequence, most additions to fullerenes are exothermic reactions.

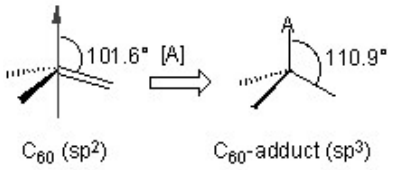

Figure 2.2: Strain release after addition of reagent A to a pyramidalize carbon of C_{60}.

Cyclic voltammetry (CV) studies show that C_{60} can be reduced and oxidized reversibly up to 6 electrons with one-electron transfer processes. Fulleride anions can be generated by electrochemical method and then be used to synthesize covalent organofullerene derivatives. Alkali metals can chemically reduce fullerene in solution and solid state to form M_xC_{60} (x = 3 - 6). C_{60} can also be reduced by less electropositive metals like mercury to form C_{60}^- and C_{60}^{2-}. In addition, salts can also be synthesized with organic molecules, for example $[TDAE^+][C_{60}^-]$ possesses interesting electronic and magnetic behavior.

Geometric and electronic analysis predicted that fullerene behaves live an electro-poor conjugated poly-olefin. Indeed C_{60} and C_{70} undergo a range of nucleophilic reactions with carbon, nitrogen, phosphorous and oxygen nucleophiles. C60 reacts readily with organolithium and Grignard compounds to form alkyl, phenyl or alkanyl fullerenes. Possibly the most widely used additions to fullerene is the Bingel reaction (Figure 2.3), where a carbon nucleophile, generated by deprotonation of α-halo malonate esters or ketones, is added to form a cyclopropanation product. The α-halo esters and ketones can also be generated in situ with I_2 or CBr_4 and a weak base as 1,8-diazabicyclo[5.4.0]unde-7ene (DBU). The Bingel reaction is considered one of the most versatile and efficient methods to functionalize C_{60}.

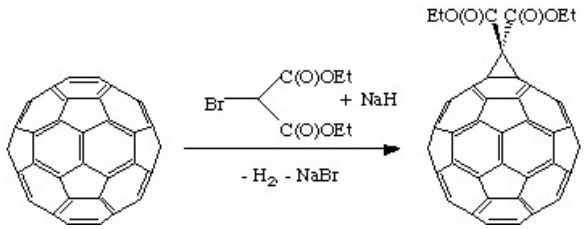

Figure 2.3: Bingel reaction of C_{60} with 2-bromoethylmalonate.

Cycloaddition is another powerful tool to functionalize fullerenes, in particular because of its selectivity with the 6,6 bonds, limiting the possible isomers (Figure 2.4). The dienophilic feature of the [6,6] double bonds of C_{60} enables the molecule to undergo various cycloaddition reactions in which the monoadducts can be generated in high yields. The best studies cycloadditon reactions of fullerene are [3+2] additions with diazoderivatives and azomethine ylides (Prato reactions). In this reaction, azomethine ylides can be generated *in situ* from condensation of α-amino acids with aldehydes or ketones, which produce 1,3 dipoles to further react with C_{60} in good yields (Figure 2.5). Hundreds of useful building blocks have been generated by those two methods. The Prato reactions have also been successfully applied to carbon nanotubes.

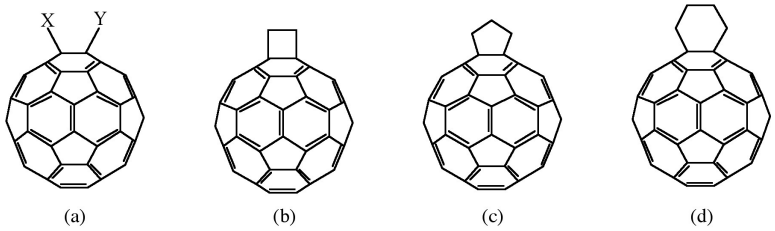

Figure 2.4: Geometrical shapes built onto a [6,6] ring junction: a) open, b) four-membered ring, c) five-membered ring, and d) six-membered ring.

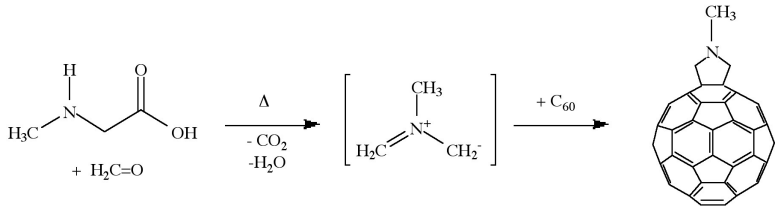

Figure 2.5: Prato reaction of C_{60} with N-methyglycine and paraformaldehyde.

The oxidation of fullerenes, such as C_{60}, has been of increasing interest with regard to applications in photoelectric devices, biological systems, and possible remediation of fullerenes. The oxidation of C_{60} to $C_{60}O_n$ (n = 1, 2) may be accomplished by photooxidation, ozonolysis, and epoxidation. With each of these methods, there is a limit to the isolable oxygenated product, $C_{60}O_n$ with $n < 3$. Highly oxygenated fullerenes, $C_{60}O_n$ with $3 \leq n \leq 9$, have been prepared by the catalytic oxidation of C_{60} with $ReMeO_3/H_2O_2$.

2.2.3 Carbon nanotubes

A key breakthrough in carbon nanochemistry came in 1993 with the report of needle-like tubes made exclusively of carbon. This material became known as carbon nanotubes (CNTs). There are several types of nanotubes. The first discovery was of multi walled tubes (MWNTs) resembling many pipes nested within each other. Shortly after MWNTs were discovered single walled nanotubes (SWNTs) were observed. Single walled tubes resemble a single pipe that is potentially capped at each end. The properties of single walled

and multi walled tubes are generally the same, although single walled tubes are believed to have superior mechanical strength and thermal and electrical conductivity; it is also more difficult to manufacture them.

Single walled carbon nanotubes (SWNTs) are by definition fullerene materials. Their structure consists of a graphene sheet rolled into a tube and capped by half a fullerene (Figure 2.6). The carbon atoms in a SWNT, like those in a fullerene, are sp2 hybridized. The structure of a nanotube is analogous to taking this graphene sheet and rolling it into a seamless cylinder. The different types of SWNTs are defined by their diameter and chirality. Most of the presently used single-wall carbon nanotubes have been synthesized by the pulsed laser vaporization method, however, increasingly SWNTs are prepared by vapor liquid solid catalyzed growth.

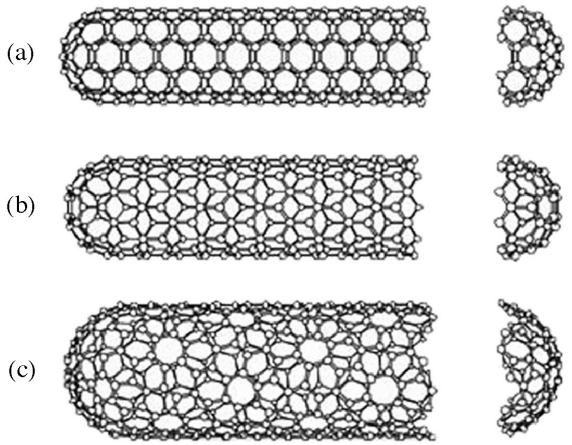

Figure 2.6: Structure of single walled carbon nanotubes (SWNTs) with (a) armchair, (b) zig-zag, and (c) chiral chirality.

The physical properties of SWNTs have made them an extremely attractive material for the manufacturing of nano devices. SWNTs have been shown to be stronger than steel as estimates for the Young's modulus approaches 1 Tpa. Their electrical conductance is comparable to copper with anticipate current densities of up to 10^{13} A/cm^2 and a resistivity as low as 0.34 x 10^{-4} Ω.cm at room temperatures. Finally, they have a high thermal conductivity (3000 - 6000 W.m/K).

The electronic properties of a particular SWNT structure are based on its chirality or twist in the structure of the tube which is defined by its *n,m* value. The values of *n* and *m* determine the chirality, or "twist" of the nanotube. The chirality in turn affects the conductance of the nanotube, its density, its lattice structure, and other properties. A SWNT is considered metallic if the value *n-m* is divisible by three. Otherwise, the nanotube is semi-conducting. The external environment also has an effect on the conductance of a tube, thus molecules such as O_2 and NH_3 can change the overall conductance of a tube, while the presence of metals have been shown to significantly effect the opto-electronic properties of SWNTs.

Multi walled carbon nanotubes (MWNTs) range from double walled NTs, through many-walled NTs (Figure 2.7) to carbon nanofibers. Carbon nanofibers are the extreme of multi walled tubes (Figure 2.8) and they are thicker and longer than either SWNTs or MWNTs, having a cross-sectional of ca. 500 Å^2 and are between 10 to 100 μm in length. They have been used extensively in the construction of high strength composites.

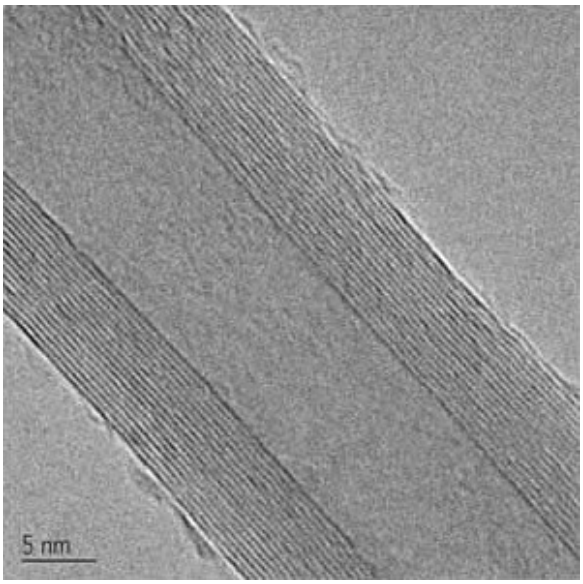

Figure 2.7: TEM image of an individual multi walled carbon nanotube (MWNTs). Copyright of Nanotech Innovations.

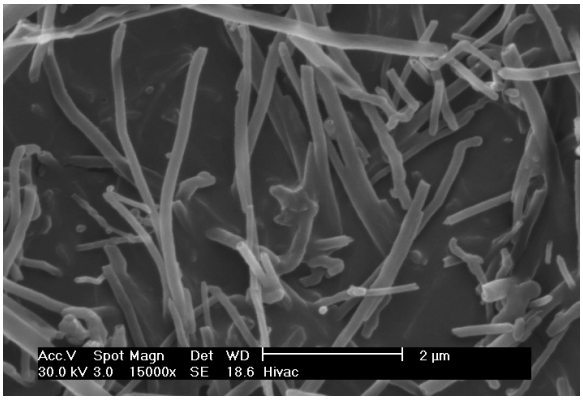

Figure 2.8: SEM image of vapor grown carbon nanofibers.

2.2.3.1 Synthesis of carbon nanotubes

A range of methodologies have been developed to produce nanotubes in sizeable quantities, including arc discharge, laser ablation, high pressure carbon monoxide (HiPco), and vapor liquid solid (VLS) growth. All

these processes take place in vacuum or at low pressure with a process gases, although VLS growth can take place at atmospheric pressure. Large quantities of nanotubes can be synthesized by these methods; advances in catalysis and continuous growth processes are making SWNTs more commercially viable.

The first observation of nanotubes was in the carbon soot formed during the arc discharge production of fullerenes. The high temperatures caused by the discharge caused the carbon contained in the negative electrode to sublime and the CNTs are deposited on the opposing electrode. Tubes produced by this method were initially multi walled tubes (MWNTs). However, with the addition of cobalt to the vaporized carbon, it is possible to grow single walled nanotubes. This method it produces a mixture of components, and requires further purification to separate the CNTs from the soot and the residual catalytic metals. Producing CNTs in high yield depends on the uniformity of the plasma arc, and the temperature of the deposit forming on the carbon electrode.

Higher yield and purity of SWNTs may be prepared by the use of a dual-pulsed laser. SWNTs can be grown in a 50% yield through direct vaporization of a Co/Ni doped graphite rod with a high-powered laser in a tube furnace operating at 1200 °C. The material produced by this method appears as a mat of "ropes", 10 - 20 nm in diameter and up to 100 μm or more in length. Each rope consists of a bundle of SWNTs, aligned along a common axis. By varying the process parameters such as catalyst composition and the growth temperature, the average nanotube diameter and size distribution can be varied. Although arc-discharge and laser vaporization are currently the principal methods for obtaining small quantities of high quality SWNTs, both methods suffer from drawbacks. The first is that they involve evaporating the carbon source, making scale-up on an industrial level difficult and energetically expensive. The second issue relates to the fact that vaporization methods grow SWNTs in highly tangled forms, mixed with unwanted forms of carbon and/or metal species. The SWNTs thus produced are difficult to purify, manipulate, and assemble for building nanotube-device architectures for practical applications.

In order to overcome some of the difficulties of these high-energy processes, the chemical catalysis method was developed in which a hydrocarbon feedstock is used in combination with a metal catalyst. The catalyst is typically, but not limited to iron, colbalt, or iron/molybdenum, it is heated under reducing conditions in the presence of a suitable carbon feedstock, e.g., ethylene. This method can be used for both SWNTs and MWNTs; the formation of each is controlled by the identity of the catalyst and the reaction conditions. A convenient laboratory scale apparatus is available from Nanotech Innovations, Inc., for the synthesis of highly uniform, consistent, research sample that uses pre-weighed catalyst/carbon source ampoules. This system, allows for 200 mg samples of MWNTs to be prepared for research and testing. The use of CO as a feedstock, in place of a hydrocarbon, led to the development of the high-pressure carbon monoxide (HiPco) procedure for SWNT synthesis. By this method, it is possible to produce gram quantities of SWNTs, unfortunately, efforts to scale beyond that have not met with complete success.

Initially developed for small-scale investigations of catalyst activity, vapor liquid solid (VLS) growth of nanotubes has been highly studied, and now shows promise for large-scale production of nanotubes. Recent approaches have involved the use of well-defined nanoparticle or molecular precursors and many different transition metals have been employed, but iron, nickel, and cobalt remain to be the focus of most research. The nanotubes grow at the sites of the metal catalyst; the carbon-containing gas is broken apart at the surface of the catalyst particle, and the carbon is transported to the edges of the particle, where it forms the nanotube. The length of the tube grown in surface supported catalyst VLS systems appears to be dependent on the orientation of the growing tube with the surface. By properly adjusting the surface concentration and aggregation of the catalyst particles it is possible to synthesize vertically aligned carbon nanotubes, i.e., as a carpet perpendicular to the substrate.

Of the various means for nanotube synthesis, the chemical processes show the greatest promise for industrial scale deposition in terms of its price/unit ratio. There are additional advantages to the VLS growth, which unlike the other methods is capable of growing nanotubes directly on a desired substrate. The growth sites are controllable by careful deposition of the catalyst. Additionally, no other growth methods have been developed to produce vertically aligned SWNTs.

2.2.3.2 Chemical functionalization of carbon nanotubes

The limitation of using carbon nanotubes in any practical applications has been its solubility; for example SWNTs have little to no solubility in most solvent due to the aggregation of the tubes. Aggregation/roping of nanotubes occurs as a result of the high van der Waals binding energy of *ca.* 500 eV per mm of tube contact. The van der Waals force between the tubes is so great, that it take tremendous energy to pry them apart, making it very to make combination of nanotubes with other materials such as in composite applications. The functionalization of nanotubes, i.e., the attachment of "chemical functional groups" provides the path to overcome these barriers. Functionalization can improve solubility as well as processibility, and has been used to align the properties of nanotubes to those of other materials. The clearest example of this is the ability to solubilize nanotubes in a variety of solvents, including water. It is important when discussing functionalization that a distinction is made between covalent and non-covalent functionalization.

Current methods for solubilizing nanotubes without covalent functionalization include highly aromatic solvents, super acids, polymers, or surfactants. Non-covalent "functionalization" is generally on the concept of supramolecular interactions between the SWNT and some macromolecule as a result of various adsorption forces, such as van der Waals' and π-stacking interactions. The chemical speciation of the nanotube itself is not altered as a result of the interaction. In contrast, covalent functionalization relies on the chemical reaction at either the sidewall or end of the SWNT. As may be expected the high aspect ratio of nanotubes means that sidewall functionalization is much more important than the functionalization of the cap. Direct covalent sidewall functionalization is associated with a change of hybridization from sp^2 to sp^2 and a simultaneous loss of conjugation. An alternative approach to covalent functionalization involves the reaction of defects present (or generated) in the structure of the nanotube. Defect sites can be the open ends and holes in the sidewalls, and pentagon and heptagon irregularities in the hexagon graphene framework (often associated with bends in the tubes). All these functionalizations are exohedral derivatizations. Taking the hollow structure of nanotubes into consideration, endohedral functionalization of SWNTs is possible, i.e., the filling of the tubes with atoms or small molecules. It is important to note that covalent functionalization methods have one problem in common: extensive covalent functionalization modifies SWNT properties by disrupting the continuous π–system of SWNTs.

Various applications of nanotubes require different, specific modification to achieve desirable physical and chemical properties of nanotubes. In this regard, covalent functionalization provides a higher degree of fine-tuning the chemistry and physics of SWNTs than non-covalent functionalization. Until now, a variety of methods have been used to achieve the functionalization of nanotubes (Figure 2.9).

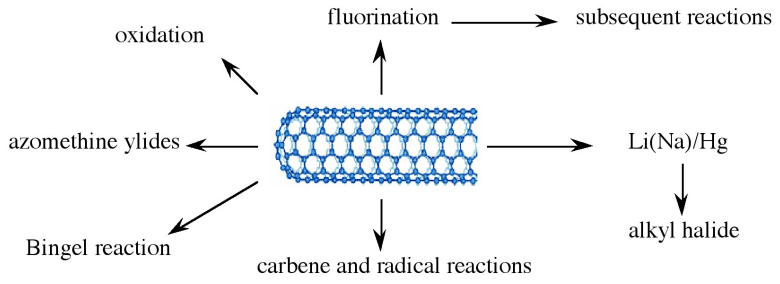

Figure 2.9: Schematic description of various covalent functionalization strategies for SWNTs.

Taking chemistry developed for C_{60}, SWNTs may be functionalized using 1,3 dipolar addition of azomethine ylides. The functionalized SWNTs are soluble in most common organic solvents. The azomethine ylide functionalization method was also used for the purification of SWNTs. Under electrochemical conditions, aryl

diazonium salts react with SWNTs to achieve functionalized SWNTs, alternatively the diazonium ions may be generated *in-situ* from the corresponding aniline, while a solvent free reaction provides the best chance for large-scale functionalization this way. In each of these methods it is possible to control the amount of functionalization on the tube by varying reaction times and the reagents used; functionalization as high as 1 group per every 10 - 25 carbon atoms is possible.

Organic functionalization through the use of alkyl halides, a radical pathway, on tubes treated with lithium in liquid ammonia offers a simple and flexible route to a range of functional groups. In this reaction, functionalization occurs on every 17 carbons. Most success has been found when the tubes are dodecylated. These tubes are soluble in chloroform, DMF, and THF.

The addition of oxygen moieties to SWNT sidewalls can be achieved by treatment with acid or wet air oxidation, and ozonolysis. The direct epoxidation of SWNTs may be accomplished by the direct reaction with a peroxide reagent, or catalytically. Catalytic de-epoxidation (Figure 2.10) allows for the quantitative analysis of sidewall epoxide and led to the surprising result that previously assumed "pure" SWNTs actually contain *ca.* 1 oxygen per 250 carbon atoms.

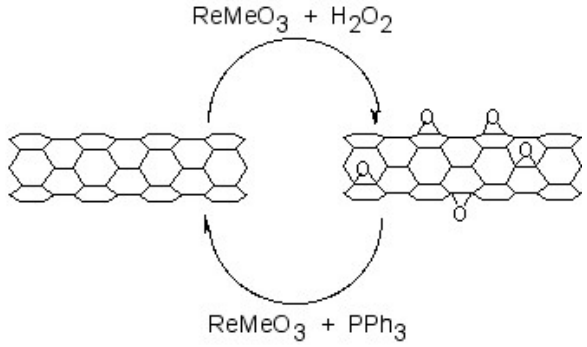

Figure 2.10: Catalytic oxidation and de-epoxidation of SWNTs.

One of the easiest functionalization routes, and a useful synthon for subsequent conversions, is the fluorination of SWNTs, using elemental fluorine. Importantly, a C:F ratios of up to 2:1 can be achieved without disruption of the tubular structure. The fluorinated SWNTs (F-SWNTs) proved to be much more soluble than pristine SWNTs in alcohols (1 mg/mL in *iso*-propanol), DMF and other selected organic solvents. Scanning tunneling microscopy (STM) revealed that the fluorine formed bands of approximately 20 nm, while calculations using DFT revealed 1,2 addition is more energetically preferable than 1,4 addition, which has been confirmed by solid state ^{13}C NMR. F-SWNTs make highly flexible synthons and subsequent elaboration has been performed with organo lithium, Grignard reagents, and amines.

Functionalized nanotubes can be characterized by a variety of techniques, such as atomic force microscopy (AFM), transmission electron microscopy (TEM), UV-vis spectroscopy, and Raman spectroscopy. Changes in the Raman spectrum of a nanotube sample can indicate if functionalization has occurred. Pristine tubes exhibit two distinct bands. They are the radial breathing mode (230 cm^{-1}) and the tangential mode (1590 cm^{-1}). When functionalized, a new band, called the disorder band, appears at *ca.*1350 cm^{-1}. This band is attributed to sp^3-hybridized carbons in the tube. Unfortunately, while the presence of a significant D mode is consistent with sidewall functionalization and the relative intensity of D (disorder) mode versus the tangential G mode (1550 – 1600 cm^{-1}) is often used as a measure of the level of substitution. However, it has been shown that Raman is an unreliable method for determination of the extent of functionalization since the relative intensity of the D band is also a function of the substituents distribution as well as concentration.

Recent studies suggest that solid state ^{13}C NMR are possibly the only definitive method of demonstrating covalent attachment of particular functional groups.

2.2.3.3 Coating carbon nanotubes: creating inorganic nanostructures

Fullerenes, nanotubes and nanofibers represent suitable substrates for the seeding other materials such as oxides and other minerals, as well as semiconductors. In this regard, the carbon nanomaterial acts as a seed point for the growth as well as a method of defining unusual aspect ratios. For example, silica fibers can be prepared by a number of methods, but it is only through coating SWNTs that silica nano-fibers with of micron lengths with tens of nanometers in diameter may be prepared.

While C_{60} itself does not readily seed the growth of inorganic materials, liquid phase deposition of oxides, such as silica, in the presence of fullerenol, $C_{60}(OH)_n$, results in the formation of uniform oxide spheres. It appears the fullerenol acts as both a reagent and a physical point for subsequent oxide growth, and it is C_{60}, or an aggregate of C_{60}, that is present within the spherical particle. The addition of fullerenol alters the morphology and crystal phase of $CaCO_3$ precipitates from aqueous solution, resulting in the formation of spherical features, 5-pointed flower shaped clusters, and triangular crystals as opposed to the usual rhombic crystals. In addition, the meta-stable vaterite phase is observed with the addition of $C_{60}(OH)_n$.

As noted above individual SWNTs may be obtained in solution when encased in a cylindrical micelle of a suitable surfactant. These individualized nanotubes can be coated with a range of inorganic materials. Liquid phase deposition (LPD) appears to have significant advantages over other methods such as incorporating surfacted SWNTs into a preceramic matrix, *in situ* growth of the SWNT in an oxide matrix, and sol-gel methods. The primary advantage of LPD growth is that individual SWNTs may be coated rather than bundles or ropes. For example, SWNTs have been coated with silica by liquid phase deposition (LPD) using a silica/H_2SiF_6 solution and a surfactant-stabilized solution of SWNTs. The thickness of the coating is dependent on the reaction mixture concentration and the reaction time. The SWNT core can be removed by thermolysis under oxidizing conditions to leave a silica nano fiber. It is interesting to note that the use of a surfactant is counter productive when using MWNTs and VGFs, in this case surface activation of the nanotube offers the suitable growth initiation. Pre-oxidation of the MWNT or VGF allows for uniform coatings to be deposited. The coated SWNTs, MWNTs, and VGFs can be subsequently reacted with suitable surface reagents to impart miscibility in aqueous solutions, guar gels, and organic matrixes. In addition to simple oxides, coated nanotubes have been prepared with minerals such as carbonates and semiconductors.

2.2.4 Bibliography

- S. M. Bachilo, M. S. Strano, C. Kittrell, R. H. Hauge, R. E. Smalley, and R. B. Weisman, *Science*, 2002, **298**, 2361.
- D. S. Bethune, C. H. Klang, M. S. deVries, G. Gorman, R. Savoy, J. Vazquez, and R. Beyers, *Nature*, 1993, **363**, 605.
- J, J. Brege, C. Gallaway, and A. R. Barron, *J. Phys. Chem., C*, 2007, **111**, 17812.
- C. A. Dyke and J. M. Tour, *J. Am. Chem. Soc.*, 2003, **125**, 1156.
- Z. Ge, J. C. Duchamp, T. Cai, H. W. Gibson, and H. C. Dorn, *J. Am. Chem. Soc.*, 2005, **127**, 16292.
- L. A. Girifalco, M. Hodak, and R. S. Lee, *Phys. Rev. B*, 2000, **62**, 13104.
- T. Guo, P. Nikolaev, A. G. Rinzler, D. Tománek, D. T. Colbert, and R. E. Smalley, *J. Phys. Chem.*, 1995, **99**, 10694.
- J. H. Hafner, M. J. Bronikowski, B. R. Azamian, P. Nikolaev, A. G. Rinzler, D. T. Colbert, K. A. Smith, and R. E. Smalley, *Chem. Phys. Lett.*, 1998, **296**, 195.
- A. Hirsch, *Angew. Chem. Int. Ed.*, 2002, **40**, 4002.
- S. Iijima and T. Ichihashi, *Nature*, 1993, **363**, 603.
- H. R. Jafry, E. A. Whitsitt, and A. R. Barron, *J. Mater. Sci.*, 2007, **42**, 7381.
- H. W. Kroto, J. R. Heath, S. C. O'Brien, R. F. Curl, and R. E. Smalley, *Nature*, 1985, **318**, 162.
- F. Liang, A. K. Sadana, A. Peera, J. Chattopadhyay, Z. Gu, R. H. Hauge, and W. E. Billups, *Nano Lett.*, 2004, **4**, 1257.

- D. Ogrin and A. R. Barron, *J. Mol. Cat. A: Chem.*, 2006, **244**, 267.
- D. Ogrin, J. Chattopadhyay, A. K. Sadana, E. Billups, and A. R. Barron, *J. Am. Chem. Soc.*, 2006, **128**, 11322.
- R. E. Smalley, *Acc. Chem. Res.*, 1992, **25**, 98.
- M. M. J. Treacy, T. W. Ebbesen, and J. M. Gibson, *Nature*, 1996, **381**, 678.
- E. A. Whitsitt and A. R. Barron, *Nano Lett.*, 2003, **3**, 775.
- J. Yang and A. R. Barron, *Chem. Commun.*, 2004, 2884.
- L. Zeng, L. B. Alemany, C. L. Edwards, and A. R. Barron, *Nano Res.*, 2008, **1**, 72.

2.3 Graphene[3]

2.3.1 Introduction

Graphene is a one-atom-thick planar sheet of sp^2-bonded carbon atoms that are densely packed in a honeycomb crystal lattice (Figure 2.11). The name comes from "graphite" and "alkene"; graphite itself consists of many graphene sheets stacked together.

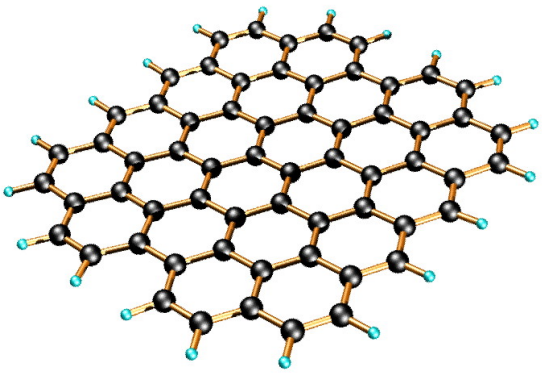

Figure 2.11: Idealized structure of a single graphene sheet.

Single-layer graphene nanosheets were first characterized in 2004, prepared by mechanical exfoliation (the "scotch-tape" method) of bulk graphite. Later graphene was produced by epitaxial chemical vapor deposition on silicon carbide and nickel substrates. Most recently, graphene nanoribbons (GNRs) have been prepared by the oxidative treatment of carbon nanotubes and by plasma etching of nanotubes embedded in polymer films.

2.3.2 Physical properties of graphene

Graphene has been reported to have a Young's modulus of 1 TPa and intrinsic strength of 130 GP; similar to single walled carbon nanotubes (SWNTs). The electronic properties of graphene also have some similarity with carbon nanotubes. Graphene is a zero-bandgap semiconductor. Electron mobility in graphene is extraordinarily high (15,000 cm^2/V.s at room temperature) and ballistic electron transport is reported to

[3]This content is available online at <http://cnx.org/content/m29187/1.3/>.

be on length scales comparable to that of SWNTs. One of the most promising aspects of graphene involves the use of GNRs. Cutting an individual graphene layer into a long strip can yield semiconducting materials where the bandgap is tuned by the width of the ribbon.

While graphene's novel electronic and physical properties guarantee this material will be studied for years to come, there are some fundamental obstacles yet to overcome before graphene based materials can be fully utilized. The aforementioned methods of graphene preparation are effective; however, they are impractical for large-scale manufacturing. The most plentiful and inexpensive source of graphene is bulk graphite. Chemical methods for exfoliation of graphene from graphite provide the most realistic and scalable approach to graphene materials.

Graphene layers are held together in graphite by enormous van der Waals forces. Overcoming these forces is the major obstacle to graphite exfoliation. To date, chemical efforts at graphite exfoliation have been focused primarily on intercalation, chemical derivatization, thermal expansion, oxidation-reduction, the use of surfactants, or some combination of these.

2.3.3 Graphite oxide

Probably the most common route to graphene involves the production of graphite oxide (GO) by extremely harsh oxidation chemistry. The methods of Staudenmeier or Hummers are most commonly used to produce GO, a highly exfoliated material that is dispersible in water. The structure of GO has been the subject of numerous studies; it is known to contain epoxide functional groups along the basal plane of sheets as well as hydroxyl and carboxyl moieties along the edges (Figure 2.12). In contrast to other methods for the synthesis of GO, the the *m*-peroxybenzoic acid (*m*-CPBA) oxidation of microcrystalline synthetic graphite at room temperature yields graphite epoxide in high yield, without significant additional defects.

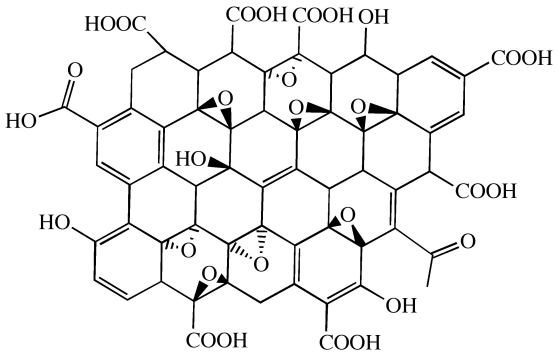

Figure 2.12: Idealized structure proposed for graphene oxide (GO). Adapted from C. E. Hamilton, PhD Thesis, Rice University (2009).

As graphite oxide is electrically insulating, it must be converted by chemical reduction to restore the electronic properties of graphene. Chemically converted graphene (CCG) is typically reduced by hydrazine or borohydride. The properties of CCG can never fully match those of graphene for two reasons:

1. Oxidation to GO introduces defects.
2. Chemical reduction does not fully restore the graphitic structure.

As would be expected, CCG is prone to aggregation unless stabilized. Graphene materials produced from pristine graphite avoid harsh oxidation to GO and subsequent (incomplete) reduction; thus, materials produced are potentially much better suited to electronics applications.

A catalytic approach to the removal of epoxides from fullerenes and SWNTs has been applied to graphene epoxide and GO. Treatment of oxidized graphenes with methyltrioxorhenium ($MeReO_3$, MTO) in the presence of PPh_3 results in the oxygen transfer, to form $O{=}PPh_3$ and allow for quantification of the C:O ratio.

2.3.4 Homogeneous graphene dispersions

An alternate approach to producing graphene materials involves the use of pristine graphite as starting material. The fundamental value of such an approach lies in its avoidance of oxidation to GO and subsequent (incomplete) reduction, thereby preserving the desirable electronic properties of graphene. There is precedent for exfoliation of pristine graphite in neat organic solvents without oxidation or surfactants. It has been reported that *N*,*N*-dimethylformamide (DMF) dispersions of graphene are possible, but no detailed characterization of the dispersions were reported. In contrast, Coleman and coworkers reported similar dispersions using *N*-methylpyrrolidone (NMP), resulting in individual sheets of graphene at a concentration of $\leq$0.01 mg/mL. NMP and DMF are highly polar solvents, and not ideal in cases where reaction chemistry requires a nonpolar medium. Further, they are hygroscopic, making their use problematic when water must be excluded from reaction mixtures. Finally, DMF is prone to thermal and chemical decomposition.

Recently, dispersions of graphene has been reported in *ortho*-dichlorobenzene (ODCB) using a wide range of graphite sources. The choice of ODCB for graphite exfoliation was based on several criteria:

1. ODCB is a common reaction solvent for fullerenes and is known to form stable SWNT dispersions.
2. ODCB is a convenient high-boiling aromatic, and is compatible with a variety of reaction chemistries.
3. ODCB, being aromatic, is able to interact with graphene *via* π-π stacking.
4. It has been suggested that good solvents for graphite exfoliation should have surface tension values of $40 - 50$ mJ/m^2. ODCB has a surface tension of 36.6 mJ/m^2, close to the proposed range.

Graphite is readily exfoliated in ODCB with homogenization and sonication. Three starting materials were successfully dispersed: microcrystalline synthetic, thermally expanded, and highly ordered pyrolytic graphite (HOPG). Dispersions of microcrystalline synthetic graphite have a concentration of 0.03 mg/mL, determined gravimetrically. Dispersions from expanded graphite and HOPG are less concentrated (0.02 mg/mL).

High resolution transmission electron microscopy (HRTEM) shows mostly few-layer graphene ($n < 5$) with single layers and small flakes stacked on top (Figure 2.13). Large graphitic domains are visible; this is further supported by selected area electron diffraction (SAED) and fast Fourier transform (FFT) in selected areas. Atomic force microscope (AFM) images of dispersions sprayed onto silicon substrates shows extremely thin flakes with nearly all below 10 nm. Average height is 7 - 10 nm. The thinnest are less than 1 nm, graphene monolayers. Lateral dimensions of nanosheets range from $100 - 500$ nm.

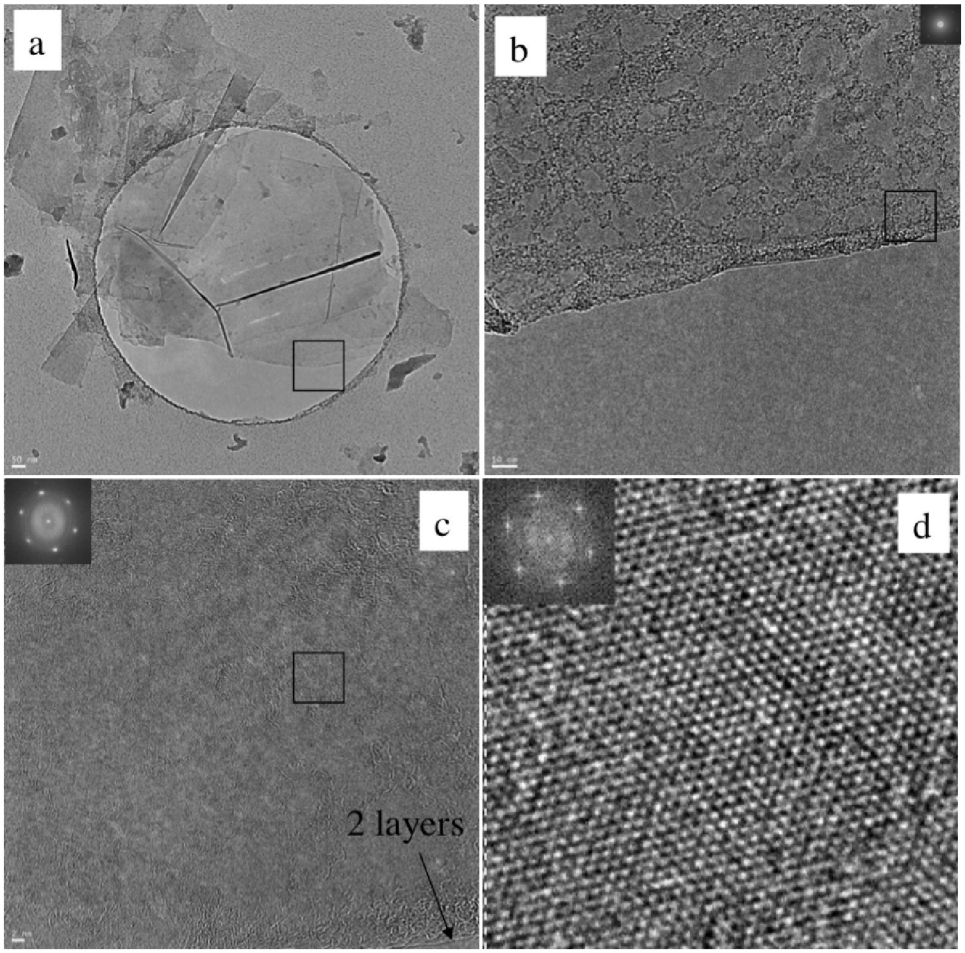

Figure 2.13: TEM images of single layer graphene from HOPG dispersion. (a) monolayer and few layer of graphene stacked with smaller flakes; (b) selected edge region from (a), (c) selected area from (b) with FFT inset, (d) HRTEM of boxed region in (c) showing lattice fringes with FFT inset. Adapted from C. E. Hamilton, PhD Thesis, Rice University (2009).

As-deposited films cast from ODCB graphene show poor electrical conductivity, however, after vacuum annealing at 400 °C for 12 hours the films improve vastly, having sheet resistances on the order of 60 Ω/sq. By comparison, graphene epitaxially grown on Ni has a reported sheet resistance of 280 Ω/sq.

2.3.5 Covalent functionalization of graphene and graphite oxide

The covalent functionalization of SWNTs is well established. Some routes to covalently functionalized SWNTs include esterification/ amidation, reductive alkylation (Billups reaction), and treatment with azomethine ylides (Prato reaction), diazonium salts, or nitrenes. Conversely, the chemical derivatization of graphene and GO is still relatively unexplored.

Some methods previously demonstrated for SWNTs have been adapted to GO or graphene. GO carboxylic acid groups have been converted into acyl chlorides followed by amidation with long-chain amines.

Additionally, the coupling of primary amines and amino acids via nucleophilic attack of GO epoxide groups has been reported. Yet another route coupled isocyanates to carboxylic acid groups of GO. Functionalization of partially reduced GO by aryldiazonium salts has also been demonstrated. The Billups reaction has been performed on the intercalation compound potassium graphite (C_8K), as well as graphite fluoride, and most recently GO. Graphene alkylation has been accomplished by treating graphite fluoride with alkyllithium reagents.

ODCB dispersions of graphene may be readily converted to covalently functionalize graphene. Thermal decomposition of benzoyl peroxide is used to initiate radical addition of alkyl iodides to graphene in ODCB dispersions.

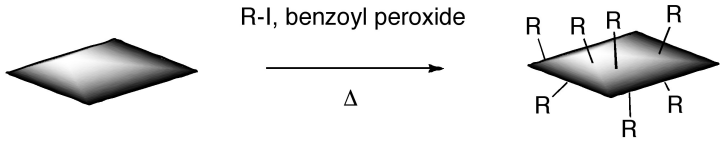

(2.1)

Additionally, functionalized graphene with nitrenes generated by thermal decomposition of aryl azides

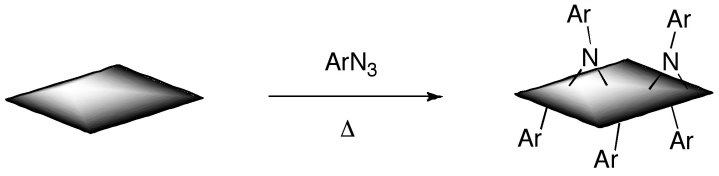

(2.2)

2.3.6 Bibliography

- P. Blake, P. D. Brimicombe, R. R. Nair, T. J. Booth, D. Jiang, F. Schedin, L. A. Ponomarenko, S. V. Morozov, H. F. Gleeson, E. W. Hill, A. K. Geim, and K. S. Novoselov, *Nano Lett.*, 2008, **8**, 1704.
- J. Chattopadhyay, A. Mukherjee, C. E. Hamilton, J.-H. Kang, S. Chakraborty, W. Guo, K. F. Kelly, A. R. Barron, and W. E. Billups, *J. Am. Chem. Soc.*, 2008, **130**, 5414.
- G. Eda, G. Fanchini, and M. Chhowalla, *Nat. Nanotechnol.*, 2008, **3**, 270.
- M. Y. Han, B. Ozyilmaz, Y. Zhang, and P. Kim, *Phys. Rev. Lett.*, 2008, **98**, 206805.
- Y. Hernandez, V. Nicolosi, M. Lotya, F. M. Blighe, Z. Sun, S. De, I. T. McGovern, B. Holland, M. Byrne, Y. K. Gun'Ko, J. J. Boland, P. Niraj, G. Duesberg, S. Krishnamurthy, R. Goodhue, J. Hutchinson, V. Scardaci, A. C. Ferrari, and J. N. Coleman, *Nat. Nanotechnol.*, 2008, **3**, 563.
- W. S. Hummers and R. E. Offeman, *J. Am. Chem. Soc.*, 1958, **80**, 1339.
- L. Jiao, L. Zhang, X. Wang, G. Diankov, and H. Dai, *Nature*, 2009, **458**, 877.
- D. V. Kosynkin, A. L. Higginbotham, A. Sinitskii, J. R. Lomeda, A. Dimiev, B. K. Price, and J. M. Tour, *Nature*, 2009, **458**, 872.
- D. Li, M. B. Mueller, S. Gilje, R. B. Kaner, and G. G. Wallace, *Nat. Nanotechnol.*, 2008, **3**, 101.
- S. Niyogi, E. Bekyarova, M. E. Itkis, J. L. McWilliams, M. A. Hamon, and R. C. Haddon, *J. Am. Chem. Soc.*, 2006, **128**, 7720.
- Y. Si and E. T. Samulski, *Nano Lett.*, 2008, **8**, 1679.
- L. Staudenmaier, *Ber. Dtsch. Chem. Ges.*, 1898, **31**, 1481.

2.4 Oxide Nanoparticles[4]

2.4.1 Introduction to oxide nanoparticles

The most widespread route to fabrication of metal oxide nanoparticles involves the "bottom-up" approach involving the precipitation from aqueous solution from metal salts. Organometallic species can also be used, but due to their cost and the difficulty in manipulating these compounds, they are used less frequently. An alternative "top-down" approach has been demonstrated for aluminum and iron oxide nanoparticles; however, it is possible that this methodology could be extended to other oxides.

2.4.2 From molecular species to nanoparticles

Hydroxide, oxyhydroxide or hydrated oxide solid phases obtained via precipitation are made of particles whose average size may range from a few nanometers to a few microns. Particle morphology may vary depending on synthesis conditions. Moreover, aging in aqueous solution may bring about significant dimensional, morphological and structural changes.

2.4.2.1 Use of metal salts

The dissolution of metal salts in water results in the formation of solvated coordination compounds in which the chemistry of such complexes, and especially their acid behavior, provides a framework for understanding how the solid (oxide) forms *via* polycondensation. The binding of water molecules to the metal cation results in the increase in the acidity such that they tend to be deprotonate spontaneously according to the hydrolysis equilibrium

$[M(H_2O)_n]^{z+} + h\ H_2O \rightarrow [M(OH)_h(H_2O)_{n-h}]^{(z-h)+} + h\ H_3O^+$

or by the neutralisation with a base,

$[M(H_2O)_n]^{z+} + h\ HO\text{-} \rightarrow [M(OH)_h(H_2O)_{n-h}]^{(z-h)+} + h\ H_2O$

in which h is the hydroxylation ratio of the cation. The resulting hydroxylated complexes condense *via* two basic mechanisms of nucleophilic substitution, depending on the nature of the coordination sphere of the cations. Condensation of aquohydroxo complexes proceeds by elimination of water and formation of hydroxo bridges (olation), while for oxohydroxo complexes, condensation proceedes *via* the formation of oxo bridges (oxolation).

In order to understand how small particles form and what role the experimental parameters play on their characteristics and on evolution, it is useful to review the kinetic aspects of condensation reactions. The precipitation of a solid involves four kinetic steps.

i. Formation of the zero-charge precursor. $[M(OH)_z(H_2O)_{n-z}]^0$, which is able to condense and form a solid phase.
ii. Creation of nuclei, through condensation of zero-charge precursors.
iii. Growth of the nuclei through addition of matter, until the primary particle stage is reached.
iv. Nucleation and growth steps form particles under kinetic control following a reaction path of minimum activation energy under conditions imposed to the system (acidity, concentration, temperature), but the products are not necessarily thermodynamically stable.

Aging of the suspensions, which may take place over a long time scale (hours, days or months), allows the system to tend toward, or reach stability, and it is often associated with modifications of some physical or chemical characteristics of the particles.

2.4.2.2 Use of metallo-oragnic compounds

Metallo-organic compounds, and especially metal alkoxides, are used in so-called sol-gel chemistry of oxide nanomaterials. Metal alkoxides are also precursors of hybrid organic-inorganic materials, because such

[4]This content is available online at <http://cnx.org/content/m22969/1.2/>.

compounds can be used to introduce an organic part inside the mineral component. Sol-gel chemistry mainly involves hydrolysis and condensation reactions of alkoxides $M(OR)_n$ in solution in an alcohol ROH, schematically represented as follows.

$M(OR)_n + n\ H_2O \rightarrow M(OH)_n + n\ ROH \rightarrow MO_{n/2} + {}^{n}/_{2}\ H_2O$

These reactions, hydroxylation and condensation, proceed by nucleophilic substitution of alkoxy or hydroxy ligands by hydroxylated species according to.

$M(OR)_n + x\ HOX \rightarrow [M(OR)_{n-x}(OX)_x] + n\ ROH$

If X = H, the reaction is a hydroxylation. For X = M, it is a condensation and if X represents an organic or inorganic ligand, the reaction is a complexation. The reactivity of metal alkoxides towards hydrolysis and condensation is governed by three main parameters: the electrophilic character of the metal (its polarizing power), the steric effect of the alkoxy ligands and the molecular structure of the metal alkoxide. Generally, the reactivity of alkoxides towards substitutions increases when the electronegativity of the metal is low and its size is high. The reactivity of metal alkoxides is also very sensitive to the steric hindrance of the alkoxy groups. It strongly decreases when the size of the OR group increases. The acidity of the medium also influences the rate of hydrolysis and condensation reaction to a great extent as well as the morphology of the products.

2.4.2.3 Non-hydrolytic routes

Non hydrolytic sol-gel chemistry has proved to be a promising route to metal oxides, and it has become a widely explored approach to synthesize metal oxide nanoparticles under various conditions. These methods involve either the self-condensation of various metal compounds or the thermolysis of metal coordination compounds. However, since water may be produced by the thermolysis of the organic derivatives, a hydrolytic pathway cannot be excluded. One of the most studied approaches involves the thermolytic decomposition of an inorganic complex at high temperatures. Two approaches include: the decomposition of $Fe(acac)_3$ or $FeCl_3$ and $M(acac)_2$ salts, and the decomposition of $Fe(CO)_5$ and $M(acac)_2$ salts. For simple oxides (e.g., Fe_3O_4) the precursor, e.g., $Fe(acac)_3$, is added to a suitable solvent heated to a temperature that allows for the rapid decomposition of the precursor. The choice of temperature and the temperature control (i.e., variation of the temperature during the reaction) are important in defining the resulting nanoparticle size and size distribution. By this method highly uniform nanoparticles can be obtained (Figure 2.14).

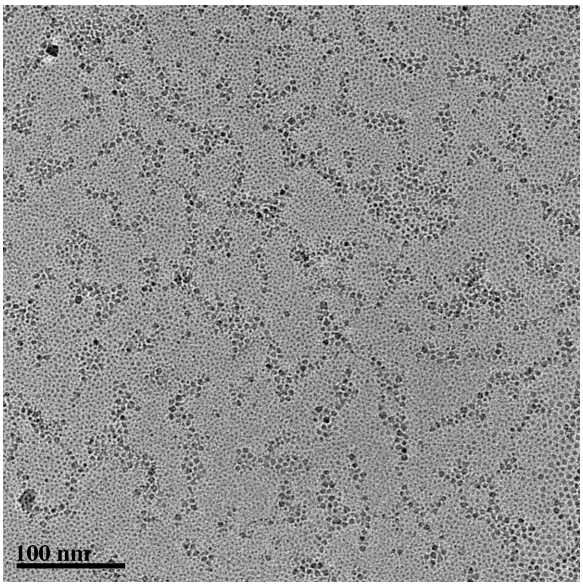

Figure 2.14: TEM image of 4 nm Fe_3O_4 nanoparticles prepared from the thermal decomposition of $Fe(acac)_3$.

In addition to simple metal oxides (M_xO_y) a range of mixed metal oxides can also be prepared. For example, nanospheres and nanocubes of cobalt ferrite can be obtained from cobalt and iron acetylacetonates, $Co(acac)_2$ and $Fe(acac)_3$ in solution in phenyl ether and hexadecanediol in the presence of oleic acid and oleylamine. Heating at 260 °C forms $CoFe_2O_4$ spherical nanocrystals with a diameter of 5 nm. These nanocrystals serve as seeds for a new growth as the second step of the synthesis, giving perfect nanocubes from 8 to 12 nm, depending on the conditions. Nanocubes in the 8 nm range can also be used as seeds to obtain spheres. The tuning of the shape of ferrite nanocrystals is managed by the parameters of growth such as heating rate, temperature, reaction time, ratio of seed to precursors, and ratio of oleic acid, acting as surfactant stabilizing the nanocrystal, to oleylamine providing basic conditions needed for the formation of spinel oxide.

Various morphologies of numerous oxide nanocrystals including Fe, Co, Mn ferrites, Co_3O_4, Cr_2O_3, MnO, NiO, ZnO, and others have been obtained by pyrolysis of metal carboxylates in the presence of different fatty acids (oleic, myristic). Control over the chemical composition of the nanoparticle is readily attained through the relative concentration of reagents used for nanoparticle growth. In many systems there is a direct linear relationship between the relative composition in the nano particles and the reagent solutions used.

2.4.3 From minerals to materials

As described above the "bottom-up" approach of reacting small inorganic molecules to form oligomeric and polymeric materials and subsequently nano particles is a common approach for a wide range of metal and non-metal oxides. However, in the case of aluminum oxide nanoparticles, the relative rate of the hydrolysis and condensation reactions often makes particle size control difficult. Once the structure of alumina sol-gels (known as alumoxanes) had been determined to comprise of a boehmite-like nanoparticle core, it was proposed that alumina nanoparticles could be prepared directly from the mineral. Such a "top-down" approach represented a departure from the traditional synthetic methodologies. Thus, it has been shown that

carboxylic acids (RCO_2H) react with boehmite, $[Al(O)(OH)]_n$, to yield the appropriate carboxy-alumoxane.

$[Al(O)(OH)]_n + HO_2CR \rightarrow [Al(O)_x(OH)_y(O_2CR)_z]_n$

Initial syntheses were carried out using the acid as the solvent or xylene, however, subsequent research demonstrated the use of water as a solvent and acetic acid as the most convenient capping agent. A solventless synthesis has also been developed. Thus, the synthesis of alumoxane nanoparticles may be summarized as involving the reaction between dirt (boehmite), vinegar (acetic acid), and water. The function of the acid is two-fold. First, to cleave the mineral lattice and "carve out" nanoscale fragment, and second to provide a chemical cap to the fragment (Figure 2.15).

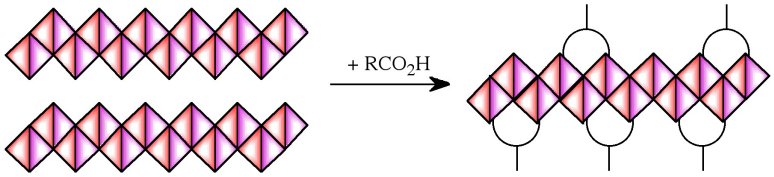

Figure 2.15: Pictorial representation of the reaction of boehmite with carboxylic acids.

The carboxylate-alumoxane nanoparticles prepared from the reaction of boehmite and carboxylic acids are air and water stable. The soluble carboxylate-alumoxanes can be dip-coated, spin coated, and spray-coated onto various substrates. The size of the alumoxane nanoparticles is dependant on the substituents, the reaction conditions (concentration, temperature, time, etc.), and the pH of the reaction solution. Unlike other forms of oxide nanoparticle, the alumoxanes are not mono-dispersed but have a range of particle sizes. Also unlike other metal oxide nanoparticles, the core of the alumoxane can undergo a low temperature reaction that allows for the incorporation of other metals (e.g., Ti, La, Mo, V, Ca). This occurs by reaction of metal acetylacetenoates $[M(acac)_n]$ with the carboxylate alumoxane (Figure 2.16).

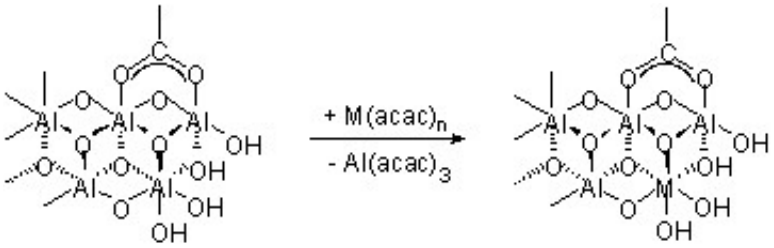

Figure 2.16: Schematic representation of the exchange reaction that occurs between a metal complex and the core of the alumoxane nanoparticle.

Given the analogous structure of Fe(O)(OH) (lepidocrocite) to boehmite, it is not surprising that the iron analog of alumoxane nanoparticles (i.e., ferroxanes) is readily prepared. Ferroxanes have been extensively characterized, and have shown to have identical structural features to alumoxanes and undergo similar exchange reactions.

2.4.4 Bibliography

- A. W. Apblett, A. C. Warren, and A. R. Barron, *Chem. Mater.* , 1992, **4**, 167.
- R. L. Callender and A. R. Barron, *J. Am. Ceram. Soc.* , 2000, **83**, 1777.
- R. L. Callender, C. J. Harlan, N. M. Shapiro, C. D. Jones, D. L. Callahan, M. R. Wiesner, R. Cook, and A. R. Barron, *Chem. Mater.* , 1997, **9**, 2418.
- C. Crouse and A. R. Barron, *J. Mater. Chem.* , 2008, **18**, 4146.
- S. Han, T. Yu, J. Park, B. Koo, J. Joo, T. Hyeon, S. Hong, and J. Im, *J. Phys. Chem. B* , 2004, **108**, 8091.
- J. Rose, M. M. Cortalezzi-Fidalgo, S. Moustier, C. Magnetto, C. D. Jones, A. R. Barron, M. R. Wiesner, and J. Y. Bottero, *Chem. Mater.* , 2002, **14**, 621.
- N. Shahid and A. R. Barron, *J. Mater. Chem.* , 2004, **14**, 1235. Y. W. Jun, J. S. Choi, and J. Cheon, *Angew. Chem. Int. Ed.* , 2006, **45**, 2.
- A. Vioux, *Chem. Mater.*, 1997, **9**, 2292.

2.5 Synthesis of Magnetite Nanoparticles[5]

Numerous schemes have been devised to synthesize magnetite nanoparticles (nMag). The different methods of nMag synthesis can be generally grouped as aqueous or non-aqueous according to the solvents used. Two of the most widely used and explored methods for nMag synthesis are the aqueous co-precipitation method and the non-aqueous thermal decomposition method.

The co-precipitation method of nMag synthesis consists of precipitation of Fe_3O_4 (nMag) by addition of a strong base to a solution of Fe^{2+} and Fe^{3+} salts in water. This method is very simple, inexpensive and produces highly crystalline nMag. The general size of nMag produced by co-precipitation is in the 15 to 50 nm range and can be controlled by reaction conditions, however a large size distribution of nanoparticles is produced by this method. Aggregation of particles is also observed with aqueous methods.

The thermal decomposition method consists of the high temperature thermal decomposition of an iron-oleate complex derived from an iron precursor in the presence of surfactant in a high boiling point organic solvent under an inert atmosphere. For the many variations of this synthetic method many different solvents and surfactants are used. However, in most every method nMag is formed through the thermal decomposition of an iron-oleate complex to form highly crystalline nMag in the 5 to 40 nm range with a very small size distribution. The size of nMag produced is a function of reaction temperature, the iron to surfactant ratio, and the reaction time, and various methods are used that achieve good size control by manipulation of these parameters. The nMag synthesized by organic methods is soluble in organic solvents because the nMag is stabilized by a surfactant surface coating with the polar head group of the surfactant attached to and the hydrophobic tail extending away from the nMag (Figure 2.17). An example of a thermal decomposition method is shown in Figure 2.17.

[5]This content is available online at <http://cnx.org/content/m22167/1.6/>.

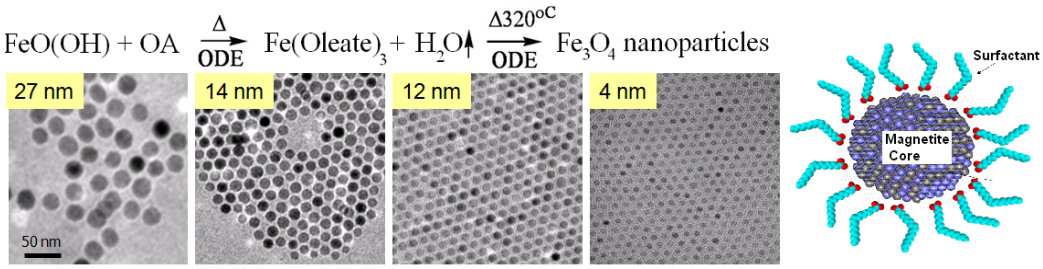

Figure 2.17: Top - The reaction equation for this method shows the iron precursor = iron oxo-hydrate, surfactant = oleic acid (OA), and solvent = 1-octadecene. The intermediate iron-oleate complex which thermally decomposes to nMag is formed upon heating the reaction mixture to the 320 °C reaction temperature. Bottom - TEM images showing size control by reaction time (time decreases left to right, constant molar ratio Fe:OA = 1:4 mol, and constant reaction temp T = 320 °C) and small size distribution of nMag. Right - Cartoon of surfactant coated nMag.

2.5.1 Bibliography

- A. Vioux, *Chem. Mater.* , 1997, **9** , 2292.

2.6 Kitchen Synthesis of Nanorust[6]

Kitchen Synthesis of Nanorust

J.T. Mayo, Courtney Payne, Lauren Harrison, Cafer Yavuz, Dr. Mary McHale, Professor Vicki Colvin

Objectives

- To perform a kitchen synthesis
- To obtain functional iron oxide nanocrystals that can be used for water purification of arsenic in Third World countries by using everyday items found in any kitchen.
- To appreciate the many forms of iron and the many uses of iron oxide nanocrystals.
- To appreciate the advanced analytical instruments that are used in the continuing research of nanotechnology.
- Remember: Thinking simple saves money and lives.

Grading

Your grade will be determined according to the following:

- Pre-lab (10%)
- Lab Report Form (80%)
- TA points (10%)

Background

[6] This content is available online at <http://cnx.org/content/m20813/1.3/>.

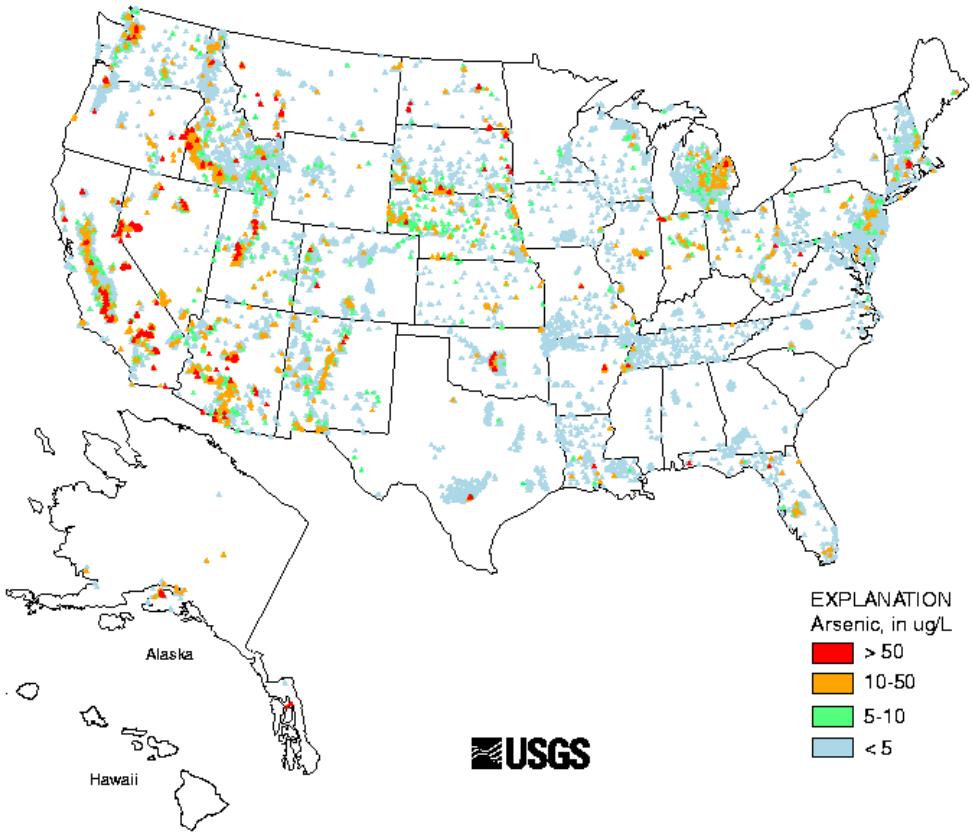

Figure 2.18

Having clean drinking water is one of the most fundamental necessities of life. There are many different forms of possible contamination, but among the most well-studied and problematic inorganic contaminants is arsenic. Arsenic is one of the oldest known carcinogens. In 1999, the US National Academy of Sciences reported that arsenic can cause bladder, lung and skin cancer, and possibly cause liver and kidney cancer. The physical symptoms of arsenic poisoning include: extreme fatigue, nausea, vomiting, partial paralysis, and reproductive damage.[7] Arsenic is naturally occurring in water due to its abundance in certain types of rocks, but it can have anthropogenic origins as well.

Arsenic can be found all over the world, but is currently a particular problem in Third World countries due to the costly nature of water purification. It is especially abundant in Bangladesh, but arsenic has also been found in the ground water of Argentina, Chile, India, Mexico, Taiwan and Thailand. Additionally, closer to home, most states in the western US have levels of arsenic concentrations of greater than 10 parts per billion (10 ppb). This was not a cause for concern until the Environmental Protection Agency (EPA) in 2006 lowered the maximum allowable level of arsenic from 50 ppb to 10 ppb. In 2001, approximately 13 million Americans were drinking water that had elevated levels of arsenic in the water.[8]

Previous methods for arsenic removal have included: manganese greensand columns that have been pretreated with dilute acid, coagulation/microfiltration, iron oxide based filtration, and activated alumina. The "Arsenic Removal Using Bottom Ash" or "ARUBA" method, invented by Ashok Gadgil of the Lawrence Berkeley National Laboratory, involves coating the surface of the contaminants with bottom ash and ferric

[7] **National Research Council.** *Arsenic in drinking water.* Washington, DC, National Academy Press, 1999.
[8] http://www.epa.gov/safewater/arsenic/index.html

hydroxide. Bottom ash is sterile waste material from coal-fired power plants which would make the cost of remediation about 0.5 cents per kg ARUBA of which generally 4-5 grams of ARUBA is needed for 1 liter of water, initially containing 400 ppb arsenic.

Nanomagnetite synthesis for arsenic removal has been hailed as Forbes: 'Top 5 Nanotech Breakthroughs of 2006' and Esquire listed it as 'Six Ideas That Will Change the World' in 2007. Basically, the technique entails forming iron oxide nanocrystals that possess very unique and size-dependent characteristics for environmental remediation of arsenic contaminated water.

Introduction

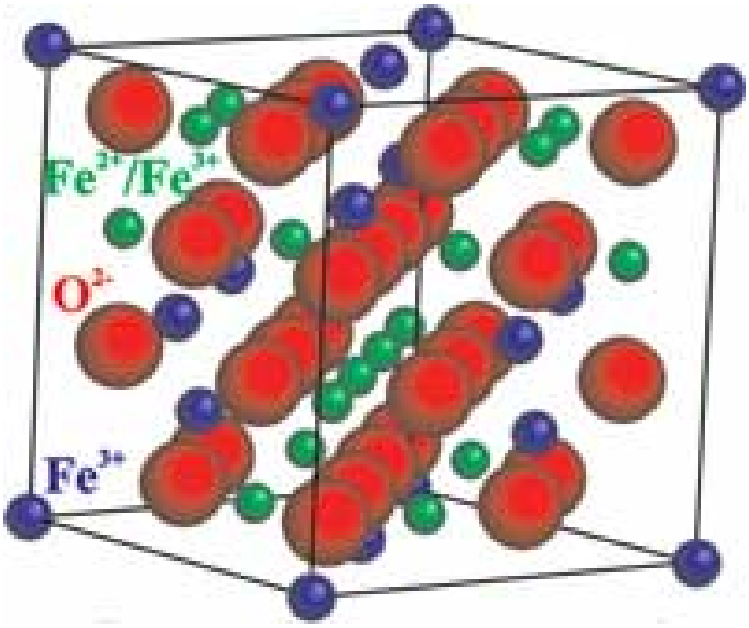

Figure 2.19

Both iron oxide nanocrystals: Fe_3O_4 (magnetite) and Fe_2O_3 (maghemite, as it is a cross between MAGnetite and HEMatite) are ferrimagnetic materials which means they can behave as permanent magnets. Additionally, those oxides below 10 nanometers in diameter, exhibit superparamagnetic properties and are used as MRI contrast agents.

Remember that last semester, you prepared a solution of magnetite ferrofluid by mixing iron(II) chloride and iron(III) chloride in the presence of tetramethylammonium hydroxide.

Magnetite is the most magnetic of all the naturally occurring minerals on Earth and has shown a lot of promise in environmental remediation as it efficiently removes As(III) and As(V) from water, this efficiency of the removal increases ~200 times when the magnetite particle size decreases from 300 to 12 nm. Since arsenic contaminated drinking water is a major problem around the world, using magnetite as a sorbent shows a great deal of promise.

Additionally, Fe(II) compounds have been used to oxidize organic contaminants such as trichloroethylene (TCE), while inorganic contaminants such as arsenic, lead and uranium are separated out of solution. Between 10 and 20 nanometers, the contaminants can be removed from water via handheld magnets, which is an important consideration in purifying water in the Third World, where power is not a standard commodity.

We will produce nanocrystalline and functional iron oxides following a green approach by using everyday

items and equipment found in kitchens worldwide. The nanocrystalline and functional oxides are produced by thermal decomposition of the iron-precursors in order to form highly uniform, isolatable nanocrystals of tunable size. The iron precursors will decompose into iron oxides in organic solvents (thermally stable non-polar solvents, aka fatty acids such as oleic acid) at temperatures in excess of 200^{o}C; the presence of amphiphilic stabilizers, in this case fatty acids derived from soap, limits the growth of crystalline products which are either magnetite, maghemite, or mixtures of both phases.

The beauty of this method lies in the ability to use inexpensive iron sources, such as rust, to form iron carboxylate intermediates, that when scaled to the gram level effectively produces a relatively low cost method for removal of arsenic from contaminated water (see Table 1).

Rust is a mixture of iron hydroxides, oxides, and in some cases even zero-valent iron, but is as effective as FeOOH used in any laboratory method. The fatty acid used in conventional methods is oleic acid, an unsaturated 18 carbon fatty acid. It can be replaced by many cooking oils that can be processed to create a homemade soap through saponification, by the addition of a base such as lye. The soap is allowed to cure for a few days and then dissolved in a weak acid, such as vinegar. The organic layer of the liquid can be collected and used without further processing. The "fatty acid mixture" or FAM is an impure fatty acid whose exact composition depends on the starting edible oil. Olive oil contains the most oleic acid; coconut oils contain more lineolic acid. For this lab, the FAM is derived from vegetable oil, a standard starting reactant.

Pure lab chemicals		Everyday chemicals	
Chemical	Price per kg	Chemical	Price per kg
FeOOH	$ 778.00	Rust	$ 0.20*
Oleic acid	$ 20.60	Edible oil (coconut oil)	$ 0.25
1-octadecene	$ 24.75	Crystal drain opener (NaOH)	$ 1.24
		Vinegar	$ 0.65
Magnetite Nanocrystals	**$ 2,624.00**	Magnetite Nanocrystals	**$ 21.7**

Table 2.1

Table 1. Cost comparison of the materials needed for a FAM/rust synthesis of magnetite nanocrystals with a conventional laboratory synthesis. Most of the savings results from the reduction in cost of the iron source. *Cost of the rust is an estimate.

In the kitchen synthesis, the black product that forms can be separated from the solution by simply using a handheld magnet rather than the expensive and large centrifuges used in a conventional laboratory setting.

Experimental Procedure

Caution!! While all of the following chemicals and utensils can be found in a kitchen, this procedure is potentially dangerous (even the soap is caustic). Gloves and goggles must be worn at all times!!

Materials

- vegetable oil
- lye or 100% NaOH drain opener
- wooden spoon
- glass bowl
- 5% vinegar
- cooking pot
- hot plate
- turkey baster or plastic pipette
- rust

Part 1: Soap making process

This step requires a week of advanced preparation and has been done for you

1. In a crystallization dish or a similar container, weigh 100 g. of the liquid oil (if not liquid gently melt it and keep as melted).
2. In a 50 mL vial (or a cup) weigh 15 g. of crystal drain opener (or caustic soda, or sodium hydroxide, or potash).
3. Add 30 mL of tap water and shake (or stir) until all solid is dissolved (CAUTION: solution gets hot!). While still warm pour it into the liquid oil.
4. Stir with a spoon (or a magnetic stir bar) for about **15 minutes** (or until tracing occurs – tracing is the visible tracks of stirring).
5. Let it sit open to air in a hood (or ventilated area) to dry and cure for a few weeks. If a shorter time span is allotted, the soap can be dried in an oven. To help the drying process, the excess oil can be decanted after 48 hours. Use caution when decanting the soap as there may be excess unreacted NaOH present.

Part 2: Oleic acid from soap with commercial vinegar

1. Grate the soap given to you and weigh it. You should have approximately 30 grams. If you have extra soap, do not discard it; give it back to your TA.
2. Check the vinegar's acidity (i.e. 5%).
3. Use 1 mL of acid for every gram of soap (i.e. 30 mL of acid, 600 mL of commercial vinegar with 5% acidity).
4. Combine the vinegar and soap in a cooking pot.
5. Heat on med-high and stir with a wooden spoon until all of the chunks are dissolved (light boiling is preferred). – This takes 15 to 30 minutes.

Caution!! This must be done a hood or other well-ventilated area!!

1. Turn off the heating and cool the solution down.
2. Pour your solution into the 1L beaker provided. You should see two layers separating from each other.
3. Separate the top yellowish layer using a turkey baster or plastic pipette into a 50 mL beaker. Make sure you get as much of the organic layer that as you can out of the vinegar/acid mixture.
4. Separate the organic layer off again into another 50 mL beaker so that you are left with only the organic layer. This is your fatty acid mixture (FAM)
5. Thoroughly clean your cooking pot in the sink with soap and water.

Part 3: Magnetite nanocrystals from rust and fatty acids

1. Carefully measure 0.5 grams of rust. Do not discard excess rust; put it back in the stock container.
2. Mix the rust with the fatty acid mixture in the cooking pot.
3. Cover the top of the container with a loose cap for proper ventilation. The reaction smokes and steams. This method produces 50-90 nm nanocrystals.
4. Start heating and timing. The rust should be heated for roughly 1 hour**,** until the solution is dark black with little or no smoking. Remember to continue stirring at regular intervals. Do not heat the oil to the point of popping and spattering. Adjust the heat as necessary so that the solution only steams and smokes.

Caution!! This must be done a hood or other well-ventilated area!!

1. If your rust solution looks like it might dry out, notify your TA immediately and they will provide you with extra oleic acid to complete your reaction. DO NOT LET YOUR RUST DRY ONTO THE FRYING PAN!!!!!!!

2. Once the rust solution appears dark black and little to no smoke is being produced, pour the nanorust solution into a 50 mL beaker.
3. Hold a magnet to the side of the beaker and observe what happens. Hold the magnet to the beaker for several minutes.
4. Clean the cooking pot thoroughly again with soap and water. If there is any black or burnt crusting, this needs to be scrubbed away.

2.7 Semiconductor Nanoparticles[9]

The most studied non-oxide semiconductors are cadmium chalcogenides (CdE, with E = sulfide, selenide and telluride). CdE nanocrystals were probably the first material used to demonstrate quantum size effects corresponding to a change in the electronic structure with size, i.e., the increase of the band gap energy with the decrease in size of particles (Figure 2.20). These semiconductors nanocrystals are commonly synthesized by thermal decomposition of an organometallic precursor dissolved in an anhydrous solvent containing the source of chalcogenide and a stabilizing material (polymer or capping ligand). Stabilizing molecules bound to the surface of particles control their growth and prevent particle aggregation.

Figure 2.20: Picture of cadmium selenide (CdSe) quantum dots, dissolved in toluene, fluorescing brightly, as they are exposed to an ultraviolet lamp, in three noticeable different colors (blue ~481 nm, green ~520 nm, and orange ~612 nm) due to the quantum dots' bandgap (and thus the wavelength of emitted light) depends strongly on the particle size; the smaller the dot, the shorter the emitted wavelength of light. The "blue" quantum dots have the smallest particle size, the "green" dots are slightly larger, and the "orange" dots are the largest.

Although cadmium chalcogenides are the most studies semiconducting nanoparticles, the methodology for the formation of semiconducting nanoparticles was first demonstrated independently for InP and GaAs, e.g., (2.3). This method has been adapted for a range of semiconductor nanoparticles.

$$InCl_3 + P(SiMe_3)_3 \rightarrow InP + 3\,Me_3SiCl \tag{2.3}$$

In the case of CdE, dimethylcadmium $Cd(CH_3)_2$ is used as a cadmium source and bis(trimethylsilyl)sulfide, $(Me_3Si)_2S$, trioctylphosphine selenide or telluride (TOPSe, TOPTe) serve as sources of selenide in trioctylphosphine oxide (TOPO) used as solvent and capping molecule. The mixture is heated at 230-260

[9] This content is available online at <http://cnx.org/content/m22374/1.4/>.

°C over a few hours while modulating the temperature in response to changes in the size distribution as estimated from the absorption spectra of aliquots removed at regular intervals. These particles, capped with TOP/TOPO molecules, are non-aggregated (Figure 2.21) and easily dispersible in organic solvents forming optically clear dispersions. When similar syntheses are performed in the presence of surfactant, strongly anisotropic nanoparticles are obtained, e.g., rod-shaped CdSe nanoparticles can be obtained.

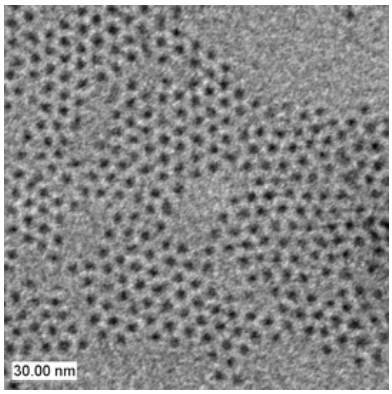

Figure 2.21: TEM image of CdSe nanoparticles.

Because $Cd(CH_3)_2$ is extremely toxic, pyrophoric and explosive at elevated temperature, other Cd sources have been used. CdO appears to be an interesting precursor. CdO powder dissolves in TOPO and HPA or TDPA (tetradecylphosphonic acid) at about 300 °C giving a colorless homogeneous solution. By introducing selenium or tellurium dissolved in TOP, nanocrystals grow to the desired size.

Nanorods of CdSe or CdTe can also be produced by using a greater initial concentration of cadmium as compared to reactions for nanoparticles. This approach has been successfully applied for synthesis of numerous other metal chalcogenides including ZnS, ZnSe, and $Zn_{1-x}Cd_xS$. Similar procedures enable the formation of MnS, PdS, NiS, Cu_2S nanoparticles, nano rods, and nano disks.

2.7.1 Bibliography

- C. R. Berry, *Phys. Rev.*, 1967, **161**, 848.
- M. D. Healy, P. E. Laibinis, P. D. Stupik, and A. R. Barron, *J. Chem. Soc., Chem. Commun.*, 1989, 359.
- L. Manna, E. C. Scher, and A. P. Alivisatos, *J. Am. Chem. Soc.*, 2000, **122**, 12700.
- C. B. Murray, D. J. Norris, and M. G. Bawendi, *J. Am. Chem. Soc.*, 1993, **115**, 8706.
- Z. A. Peng and X. Peng, *J. Am. Chem. Soc.*, 2002, **12**, 3343.
- R. L. Wells, C. G. Pitt, A. T. McPhail, A. P. Purdy, S. R. B. Shafieezad, and Hallock *Chem. Mater.*, 1989, **1**, 4.
- X. Zong, Y. Feng, W. Knoll, and H. Man, *J. Am. Chem. Soc.*, 2003, **125**, 13559.

2.8 Silver Nanoparticles: A Case Study in Cutting Edge Research[10]

Alvin Orbaek, Mallam Phillips, Dr. Mary McHale, Prof. Andrew Barron,

[10] This content is available online at <http://cnx.org/content/m19597/1.11/>.

2.8.1 Objective

To gain an insight into nanotechnology, what it is and how it can be useful, using silver nanoparticles as an example. We will look at what exactly nanoparticles are, see how they are made, and how they can be characterized.

The characterization technique involves Ultra-Violet and Visible spectroscopy, so we will look briefly into the interaction of the nanoparticles and light, which will hopefully help you gain an appreciation for one of the special aspects of nanotechnology.

When making the nanoparticles we will do a time study allowing us to graph the spectroscopic response - which will show the nature of the particle as it grows, i.e., ripens. We can use some data to calculate the size of the nanoparticle at the beginning and at the end of our experiment.

2.8.2 Background

2.8.2.1 What is nanotechnology?

Nano is the ancient Greek word for dwarf. In scientific terms it has been used to identify length scales that are one billionth of a unit. This is typically a meter and so you often here things that are nanometers in size. In terms of nanotechnology it has been defined as anything that has a unique property or function resulting from the size of the artifact being in the nano regime, and that the size regime is between 0.1 and 100 nm. This size range is rather broad; encompassing simple molecules to more complicated molecules like enzymes. However, these items can be looked at from many points of view, from a chemist that considers molecules, to that of an engineer that would look at how each of the molecules interacts in the bigger system and creates new materials from these building blocks. For this reason there are many disciplines that are interested in the study of nanotechnology such as Chemistry, Physics, Engineering, Biological sciences, Material Sciences, Computer Science and many more besides. For this reason nanotechnology is not a strict discipline and many people use their skills and backgrounds from other areas to contribute to research in this particular field.

2.8.2.2 Why care about nanotechnology?

There are many effects that occur at the nanoscale that we do not notice on a larger macro scale. Most of nature actually works at the nanoscale, and by understanding the forces that are at work using knowledge from chemistry, physics and engineering one can better understand the working of organic life. Enzymes are very large molecules that are too large to consider in terms of chemistry alone, other effects come into play In order to understand the full picture we need to borrow from physics and computer modeling to gain a better understand of what is happening.

There are many effects that occur at the nanoscale that we do not notice on a larger macro scale. Most of nature actually works at the nanoscale, and by understanding the forces that are at work using knowledge from chemistry, physics and engineering one can better understand the working of organic life. Enzymes are very large molecules that are too large to consider in terms of chemistry alone, other effects come into play In order to understand the full picture we need to borrow from physics and computer modeling to gain a better understand of what is happening.

When we cross from the small scale as in molecules and atoms, to the large scale that we see with our own eyes, we travel through the nanoscale. In that scale we go from quantum physics to classical physics and a lot of very interesting effects can be used to our benefit, and actually nanoparticles are an excellent example of this. Just by virtue of their size they are able to absorb four times more light than is even shone on them! This is very different from the bulk material, it is difficult to understand in one sitting, but let's just say that there is a coupling between the light energy and the matter of the nanoparticles that is best explained through quantum mechanics, but we won't go into that now.

When you make something very large, there is lots of room for error, the more parts you have in a system the more chances there are that some of those parts can be faulty. However when you make something in the nanoscale you have far less parts in the system and each part has to be virtually perfect. Material

scientists are concerned with the defects that are created in materials, because these are the parts that cause a material to break down often and stop functioning correctly. As you get into the nanoscale there are less defects and you get enhanced effects from the purer material, that don't occur on the larger scale. One example of this is carbon nanotubes, by virtue of there shape and size they are 6 times lighter than steel, but almost 100 times stronger. There is great potential for using these in new materials in the future that are ultra lightweight and extremely strong.

When we make things with modern technology we have for centuries been using a top down approach, and this brings us down to a fine limit but not as fine as that on which nature works. Nanotechnology is more about understanding the fundamental forces in nature by physics, and seeing their interaction through chemistry, and then making something larger from our engineering skills. And we can always take examples from biology that has been doing this for far longer than we have. So really what we do is take a bottom up approach, so that we can create large materials that we can use, that has every part of the interaction tailored all the way from how the atoms interact and how the molecules are formed and bonded together to make building blocks for new materials and applications. This bottom up approach is a change in the way things have been done and for this reason nanotechnology is a very potent discipline, with an immense capacity for expansion.

In all we have only really begun to scratch the surface of what could be possible when we create things using nanotechnology, and we should be aware of this because nanotechnology is finding its way into every corner of life, from health studies, medicine, robotics, materials and maybe even food and many many more.

2.8.2.3 What are nanoparticles and how are they made?

A simple way of seeing this is by imagining tennis balls that are squeezed down to a few billionths of a meter. The particles are rounded because they try to minimize the surface energy as much as possible; any edges will make things more energetic since typically nature follows the path of least resistance the particles tend to form colloids, or spheres with as few edges as possible. It is possible though, to direct the growth of nanoparticles into various shapes such as cubes, and tetrahedrons. We will concern ourselves with only colloidal nanoparticles for the moment.

The nanoparticles have a large surface area compared with the total volume. The surface area to volume ratio is interesting because chemical reactions typically occur on surfaces, so nanoparticles that have a high surface to energy ratio can be used in many interesting ways, such as in catalysis. One teaspoon of nanoparticles might weigh only 200 mg, but because of their shape and the large amount of surface area the tea spoon could have the same surface area as a whole football field! This gives them huge potential and potency compared to the bulk material. Imagine laying out a football field with a thin layer of silver, think how much silver that would need, and then compare that with the amount that is in the spoon! This high surface area to volume ratio is one of the most important properties about nanoparticles.

With all that surface area and the energy that exists, the nanoparticles need to be held together 'somehow'. That is where the furry parts of the tennis ball come into play. Imagine them as small molecules that hold on to the surface of the particle and stop it from breaking up under its own energy. It is like a tree whose roots can prevent soil erosion because the soil is bonded to the root in the ground. The chemical we use in this lab is mercaptosuccinic acid, and this helps to hold the nanoparticles in shape by bonding to the surface of the particles.

There are a few basic points to remember about making nanoparticles:

1) You need a nucleation point, a place for the metal (silver in this case) to start bonding to one another and start growing into a larger particle. For this you often need some ingredient that can break down a metal salt, in this case silver nitrate, which is accomplished by using sodium borohydride. This reduces the silver nitrate into silver ions that are free then to bond with each other.

2) You need some mechanism to keep the particles at the nanoscale and stop them from ripping and growing into something much larger, this is accomplished using the capping agent mentioned earlier (mercaptosuccinic acid). A great deal of cutting edge research revolves around varying the capping agent in order to control the size of your nanoparticles and tailor them for specific tasks. But not only can you change the size of particles in this way, you can also change the shapes.

2.8.2.4 Why silver nanoparticles?

Silver is a very easily oxidized material; it has been used already commercially for its anti-microbial properties from athletic wear to sterilizing water. It has a very interesting interaction with light due to a dielectric constant that makes the light response occur in the visible regime. Notably silver is one of the only metals that can be tailored to respond across the full visible spectrum.

Their light interaction can then be used in various fields such as photonics where new materials can be made to transport light in a similar fashion to the optical cables that we use now, but with a higher yield. These waveguides act like wires and could be made smaller and lighter than present day wires, but carry more light.

Another use of this light interaction can be used for imaging in biological systems, where the nanoparticles can be used as vectors to carry drugs to specific sights because of specific capping agents being used, and the internal core can be used to image the delivery and ensure the cargo is delivered correctly to the correct location in the body. One group at Rice that is working on this exciting research is the Barron lab (http://python.rice.edu/∼arb/Barron.html[11]).

2.8.3 TA Demonstration on the Hydrophobicity of Silver

Adapted from George Lisensky's procedure that demonstrates the hydrophobicity of silver based on the Tollen's test and the ability of self-assembly of thiol monolayers (SAM) on gold surfaces:

Essentially your TA will coat silver with a monolayer of octadecanethiol, effectively producing a non-polar surface and causing water that is dropped onto this surface to bead up.

Once your TA has placed a clean microscope slide in a Petri dish. Your TA will place 8 small drops (or 4 large drops) of a 0.5 M solution on the microscope slide (Figure 2.22).

[11] http://python.rice.edu/∼arb/Barron.html

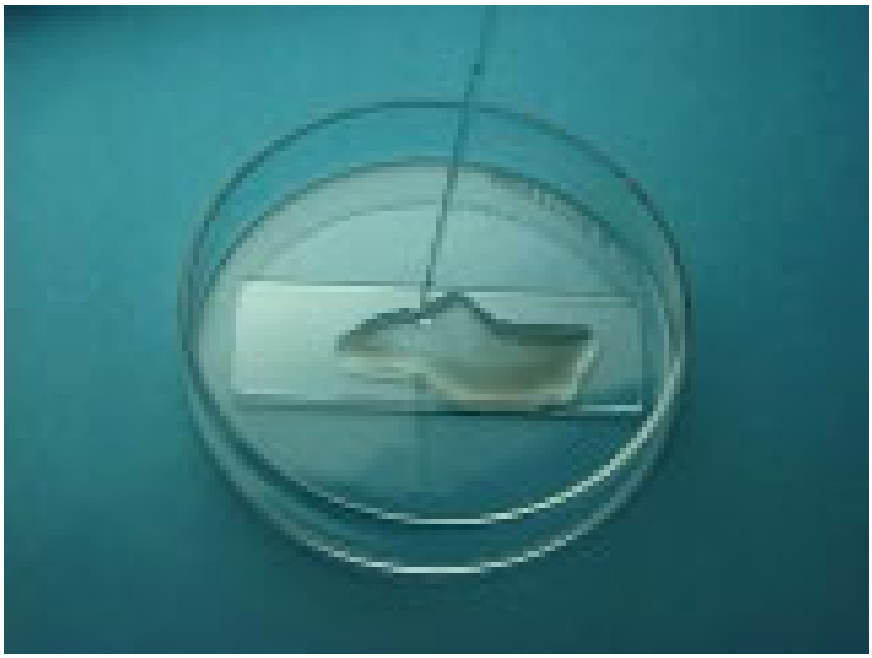

Figure 2.22: Image of a glucose solution beading on a glass slide.

Then your TA will add 25 small drops (or 12 large drops) of an active silver ion[12] solution (made by adding concentrated ammonia drop wise to 10 mL of 0.1 M silver nitrate solution until the initial precipitate just dissolves., followed by adding 5 mL of 0.8 M KOH solution; a dark precipitate will form (Figure 2.23). Add more ammonia drop wise until the precipitate just redissolves. This "active silver" solution has to be used within an hour of preparation. CAUTION: To avoid the formation of explosive silver nitride, discard any remaining active solution by washing down the drain with plenty of water) to the glucose solution and gently agitate to mix the solution.

[12] http://mrsec.wisc.edu/Edetc/nanolab/Agthiol/#materials2#materials2

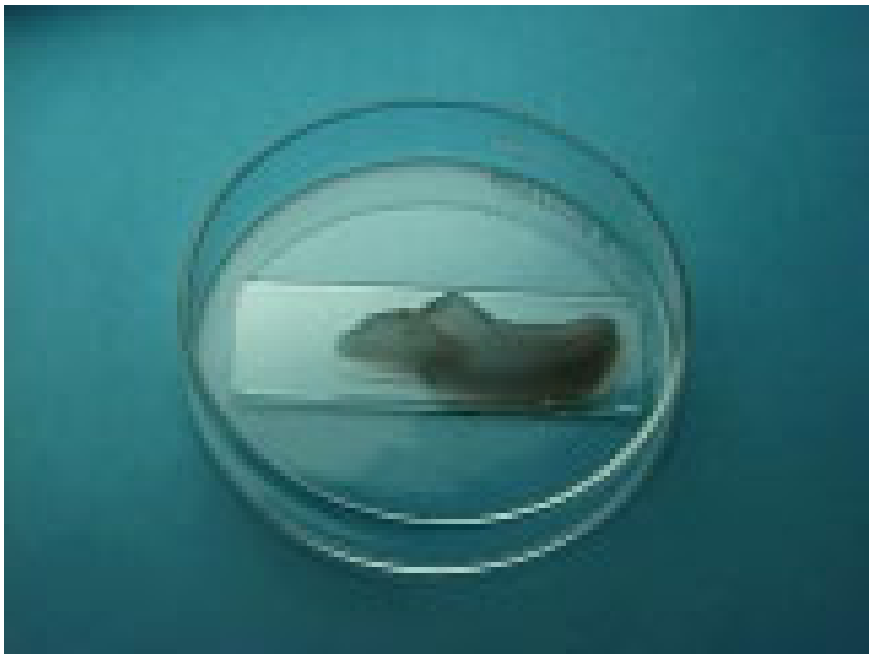

Figure 2.23: Image of the preparation of the silver layer seen as a dark precipitate.

After waiting several minutes while the solution darkens and a grayish precipitate forms, a silver mirror is also forming on the slide, though it may be obscured by the precipitate c.f., Tollen's reagent. Your TA will use water from a wash bottle to wash off the precipitate and reveal the silver mirror (Figure 2.24) being careful to avoid contact with the solution since it will stain their hands.

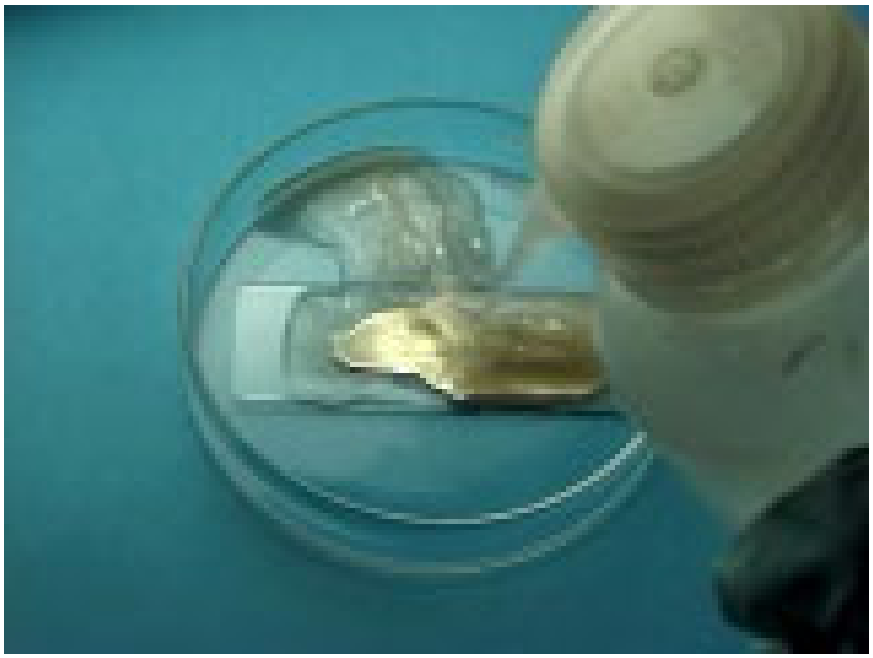

Figure 2.24: Image showing the silver mirror formed on the glass slide.

Your TA will remove the slide from the Petri dish ensuring that he/she does not touch the silver solution, and rinse the silver mirror with water. How attracted are the water drops to the surface? (Like attracts like.) Do water drops on silver spread out or bead up?

The contact angle is between the side of a drop and the slide. Is the contact angle wide (small attraction to the slide) or narrow (large attraction to the slide)?

Your TA will wait for the surface to appear dry. (For faster drying we will use a hair dryer.) Cover the silver with a few drops of a long chain alkanethiol solution[13] , octadecanethiol, in ethanol (add a small amount of octadecanethiol, to 20 mL of ethanol. When finished, dispose of this solution by adding about 5 mL of household bleach. Let stand for several minutes then wash solution down the sink).

After the ethanol has evaporated, your TA will now have an alkanethiol monolayer with the sulfur atoms bound to the silver and the hydrocarbon tails pointing away. Your TA has effectively coated the surface with hydrocarbons.

How attracted are the water drops to the surface? (Like attracts like.)

Do water drops on the monolayer coated surface spread out or bead up?

Is the contact angle greater or less than before the alkanethiol was added?

Is the water attracted more to the plain glass, to the silver, or to the alkanethiol monolayer-coated silver?

2.8.4 Experimental Procedure no1 - ripening of silver nanoparticle

Solutions of silver nitrate (250 mg to 500 mL) and mercaptosuccinic acid (405 mg to 500 mL) have ALL been previously prepared for you. This can be gathered from the glass bottles situated in the lab.

[13] http://mrsec.wisc.edu/Edetc/nanolab/Agthiol/#materials3#materials3

1. Find and open the microlab program. Ensure that the accompanying box has power and is turned on, and that it is connected to the laptop via the USB plug. Once everything is connected and you double clock the microlab.exe file, a box will open in front of you.
2. In the tab labeled "New" you will find the icon for the "Spectrophotometer", please double click this.
3. This brings up the program that we will use, at which point you should take a reading of a blank sample, this is done by filling a vial with DI water and placing in the appropriate slot, and covering with the film case. When the blank sample is in place, click the button "Read Blank". This will a generate a series of data points that you can see.
4. Please take note to read from the Absorbance tab, this is the third option on the top right.
5. In a beaker gather 50 mL of silver nitrate solution; use the photo spectrometer to take an absorbance measurement of the silver solution on its own. To do this place twenty drops (approx 1 mL) into the glass vial provided, and dilute to the top with DI water. Shake the vial twice to ensure the solution is homogenous. Record the UV-Vis spectrum.
6. Place the 50 mL silver solution into the Erlenmeyer flask and start stirring, your TA will have the stir bars.
7. Complete the same process as above but this time uses 50 mL of the solution of mercaptosuccinic acid. Please make sure to rinse out the glass vial thoroughly. Take a spectrum using the photo spectrometer of the MSA solution.
8. Now place the 50 mL of MSA solution into the Erlenmeyer with the silver that you are already stirring vigorously – this means stirring at such a rate that you can see a vortex created.
9. Take a spectrum of the solution that is currently stirring, this should include the MSA and silver. You should notice, similar to DI water, and the MSA and silver on their own, that there is no response in absorbance of either of the chemicals when analyzed combined that would indicate that the nanoparticles have not been formed yet, but all the final ingredients are already there. This is why we need to add the sodium borohydride, as this will break the silver nitrate up so the silver can bind with the sulfur atom in the MSA molecule and the silver ions can start bunching up and the nanoparticles can begin to form.
10. Make the sodium borohydride solution by diluting 300 mg with DI water to 100 mL using a volumetric flask. From the equation of the chemical, $NaBH_4$, and upon the addition of water did you notice anything occurring, what happened in the reactions? (Did it change color, consistency, did gas evolve) what could have caused this? Sodium borohydride is highly hygroscopic, that means it reacts very readily with water, and the water in the atmosphere (especially in Houston) could have caused the salt to harden – this means you may have to coax the salt a little with some prodding using the spatula – without breaking the spatula!
11. To the solution of silver nitrate and mercaptosuccinic acid that is stirring place a few drops of the sodium borohydride solution, note the color change, then place some more sodium borohydride and note the color change again. What do you think is happening here, and why is the colors changing? What were the colors of the solution? Stop adding sodium borohydride when the color has reached a steady state and is not changing anymore. If you add too much sodium borohydride the products could come out of solution.
12. When you have a steady dark, black coffee color, you have added sufficient sodium borohydride Immediately take 20 drops of your Ag nanoparticle solution and place into the glass vial; make sure it is diluted down to a slightly sandy color by the addition of DI water. Place the filled vial into the slot and acquire spectroscopic data in the same manner as before, this will be your "time = 0" run – now what is different this time, compared with the last spectra you aquired? And how has this occurred?
13. Continue to repeat this process of taking 20 drops of your Ag nanoparticle solution and dilute in a vial and take spectroscopic data every 5 minutes for a total of 50 minutes,
14. When you are finished completing the experimental runs, then you can export the data so that it can be graphed in Excel.
15. Go to File, then scroll down to 'Export Data as.' and then select "Comma separated values'. This generates a file ending in .csv that can be later opened and used in Microsoft Excel; please take note

where the file was saved.

16. Use excel to graph each of the data sets on the same graph. Complete an Area graph, with 3D visualization to graph the ripening process. You should notice some of the intensity changing from the first data set until the last – why do you think this is happening?
17. Using Excel again take the data from the first profile and data from the profile with the tallest peak. Graph each one separately. This is to demonstrate how the nanoparticles ripen over time. So you can see there is some movement in the system and it can take several hours before the entire system reaches some equilibrium. Note: You will not see the trough that we showed you in the PowerPoint as MicroLab does not go down to 310 nm, which is why we are posting data so that you can calculate the full width half maximum..
18. You have now successfully made some silver nanoparticles! Congratulations.
19. Finally plot a graph from the data posted online in order to calculate the diameter of the nanoparticels once you have extrapolated the full width half maximum (FWHM), using the equation:

D = 230/(FWHM-50). For help on getting the FWHM use Figure 2.25.

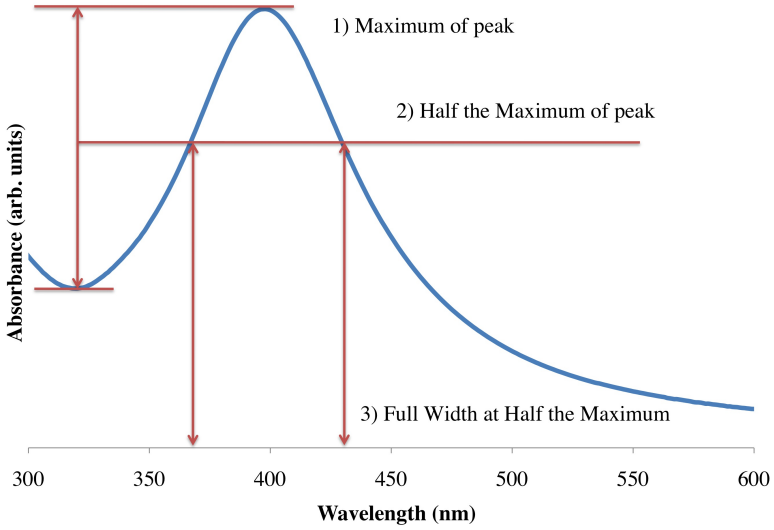

Figure 2.25: A plot demonstrating the three steps to obtain the FWHM from a graph of the UV-vis spectrum for the silver nanoparticles.

2.8.5 Experimental procedure no2 - lasers and colloids

When the nanoparticles form they are able to scatter huge amounts of light. As atoms the silver will not scatter any light, but when it is made into the form of nanoparticles the light scattering is possible to see using a simple laser light. Large chunks of silver cannot be soluble in water but it in the nanoparticle form it can be. We can use the laser pointers to see when the nanoparticles are forming.

During the first reaction you can see how sodium citrate takes a long time to create nanoparticles, at the beginning the laser does not shine through the solution. But over a period of about 20 minutes you will be able to see the nanoparticle form by using the laser light. When the nanoparticles have formed you will be able to see the laser run through the solution.

When you make the nanoparticles with sodium borohydride now, it is so strong it will make nanoparticles much faster. This reaction only takes about 2 minutes to occur.

Aim

1. To synthesize silver nanoparticles using two different reducing agents
2. To see the difference in the rates of reaction between the two reducing agents
3. To use laser pointers to determine when the nanoparticles form and hence, to see which reducing agent works faster

Sodium Citrate

1. In a glass vessel gather 75 mL of silver nitrate solution. Put this on a hot plate and place a stir bar inside it. Start heating the solution with a medium setting, start the stir bar so that a small vortex occurs in the solution.
2. After a period of five minutes when the solution is getting warmer, place 2 mL of tri sodium citrate into the solution that is warming on the heat place. Make sure to add the sodium citrate drop wise. This will take about two minutes to do.
3. Now use a laser pointer to see if any nanoparticles have formed.
4. Over a period of 20 minutes you should notice a change in color that occurs because of the formation of the silver nanoparticles. Continuously use the laser pointer to look for the formation of nanoparticles.
5. Turn off the hot plates and take the glass away from the heat.
6. When the solution has cooled to room temperature place the waste in the waste container.

Sodium Borohydride

1. In a glass vessel gather 75 mL of silver nitrate solution. Place a stir bar inside the reaction vessel and start stirring with a speed that creates a small vortex.
2. Gather 50 mL of mercaptosucininc acid (MSA) and place this inside the same vessel as the silver nitrate that you have recently got.
3. Use the laser to light to see if there are any nanoparticles present.
4. Now get your TA to help distribute some sodium borohydride for you. This is a very reactive chemical and will loose strength over time. Your TA will place sodium borohydride in the reaction vessel.
5. While your TA is adding the sodium borohydride, check to see if any nanoparticles are forming by using the laser light.
6. When the reaction is completed place the materials in the waste container.
7. Clean all your glassware.

Conclusion

Nanoparticles are an exciting and emerging technology. There is much to learn about how to use these new structures. It is a delicate and complex process to learn how to make thing so small, but as you have discovered today, it is not impossible to do. The detection of nanoparticles can be easily achieved with the use of a hand held laser pointer. This is due to the extremely large scattering cross section that nanoparticles have.

2.8.6 Additional Information

We use light to see things around us, that light has a certain size, or wavelength. And if something is smaller than light, we cannot use the light to see it directly, so we have to use things with smaller wavelengths. Let's use an example, consider a hand of a certain size, and some hieroglyphics on a wall(er?). With very large

hands the details in the wall are difficult to make out, but still you can note that they are there. But when you use smaller and smaller hands the details become easier to make out. It's the same kind of idea when using the light. For us as human beings it is not usually a problem in our everyday lives, the size of the light is much smaller than the artifacts we deal with as we move around. But when looking at smaller and smaller things as in the nanoscale, we can't use visible light because the light passes right over the objects normally, and it's as if they don't exist.

One trick around this is to use shorter wavelengths of light, like using X-rays at the hospital to image brakes and fractures of the skeletal system. And in nanotechnology what we often use are electrons, Because the wavelength of the electrons are far smaller than the object we are looking at, we can get a good picture of what is going on at the nanoscale. There are two main instruments to do this: the TEM (transmission electron microscope), and the SEM (scanning electron microscope). In the same way that the X-rays at the hospital pass through the skin but not the bones, the TEM accelerates electrons through materials, and depending on the type and size of the material the electrons either pass through or not. And we get a black and white image of our system at the nanoscale. In Figure 2.26 you see a picture of the type of silver nanoparticles that you made in the lab, this was taken with a TEM in Dell Butcher Hall here at Rice. The dense silver particles don't allow the transmission of the electrons, and we get a black and white picture of the nanoparticles. This has been calibrated and can be used to tell us the size of the particles; they are around 10 nm on average.

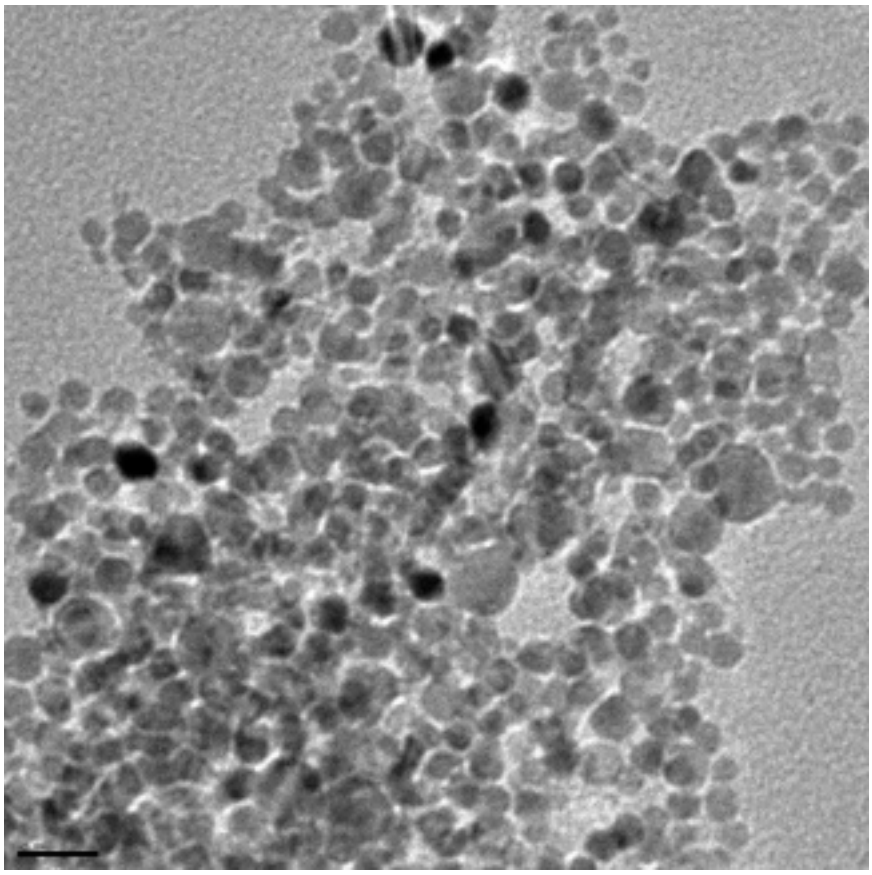

Figure 2.26: TEM image of silver nanoparticles, scale bar is 20 nm.

But when electrons pass through the material it is not always a clean break, some of the energy can be imparted on the materials and so it won't pass all the way through. This can cause a secondary effect that depends on the material that is being imaged, and this is essentially how the SEM works. Instead of electrons passing through like in the X-rays in the hospital, the materials you image have a reaction to the bombardment of electrons in the electron beam. In Figure 2.27 you see a bunch of larger silver nanoparticles that have been imaged using an SEM here in Dell Butcher Hall at Rice University.

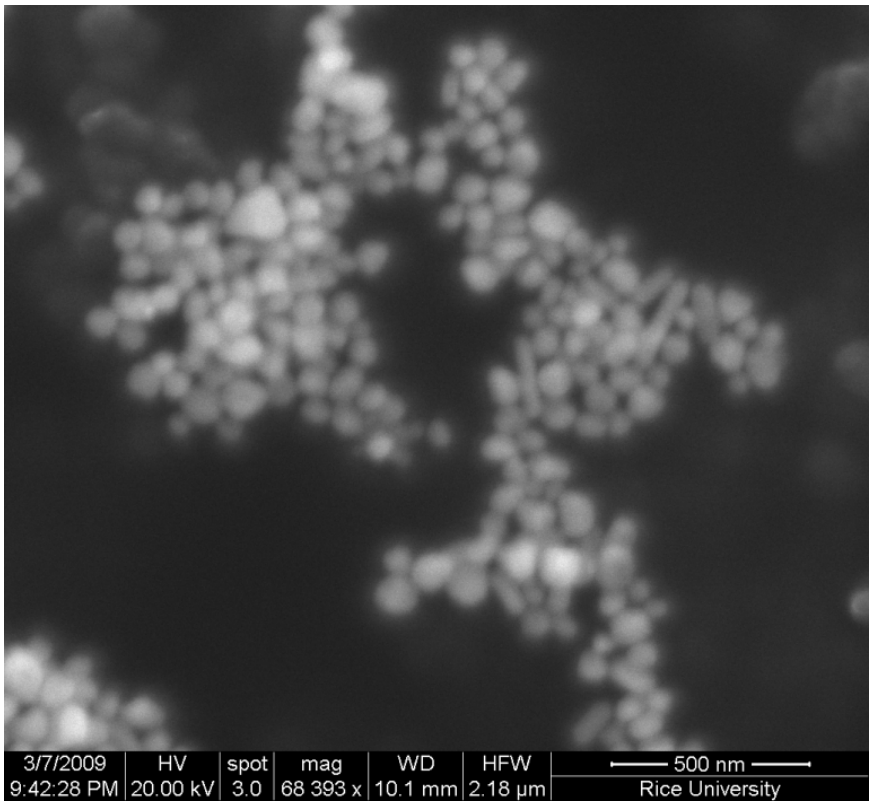

Figure 2.27: SEM image of larger silver nanoparticles, scale bar is 500 nm.

Chapter 3

Characterization of Nanomaterials

3.1 The Application of VSI (Vertical Scanning Interferometry) to the Study of Crystal Surface Processes[1]

3.1.1 Introduction

The processes which occur at the surfaces of crystals depend on many external and internal factors such as crystal structure and composition, conditions of a medium where the crystal surface exists and others. The appearance of a crystal surface is the result of complexity of interactions between the crystal surface and the environment. The mechanisms of surface processes such as dissolution or growth are studied by the physical chemistry of surfaces. There are a lot of computational techniques which allows us to predict the changing of surface morphology of different minerals which are influenced by different conditions such as temperature, pressure, pH and chemical composition of solution reacting with the surface. For example, Monte Carlo method is widely used to simulate the dissolution or growth of crystals. However, the theoretical models of surface processes need to be verified by natural observations. We can extract a lot of useful information about the surface processes through studying the changing of crystal surface structure under influence of environmental conditions. The changes in surface structure can be studied through the observation of crystal surface topography. The topography can be directly observed macroscopically or by using microscopic techniques. Microscopic observation allows us to study even very small changes and estimate the rate of processes by observing changing the crystal surface topography in time.

Much laboratory worked under the reconstruction of surface changes and interpretation of dissolution and precipitation kinetics of crystals. Invention of AFM made possible to monitor changes of surface structure during dissolution or growth. However, to detect and quantify the results of dissolution processes or growth it is necessary to determine surface area changes over a significantly larger field of view than AFM can provide. More recently, vertical scanning interferometry (VSI) has been developed as new tool to distinguish and trace the reactive parts of crystal surfaces. VSI and AFM are complementary techniques and practically well suited to detect surface changes.

VSI technique provides a method for quantification of surface topography at the angstrom to nanometer level. Time-dependent VSI measurements can be used to study the surface-normal retreat across crystal and other solid surfaces during dissolution process. Therefore, VSI can be used to directly and nondirectly measure mineral dissolution rates with high precision. Analogically, VSI can be used to study kinetics of crystal growth.

[1] This content is available online at <http://cnx.org/content/m22326/1.4/>.

3.1.2 Physical principles of optical interferometry

Optical interferometry allows us to make extremely accurate measurements and has been used as a laboratory technique for almost a hundred years. Thomas Young observed interference of light and measured the wavelength of light in an experiment, performed around 1801. This experiment gave an evidence of Young's arguments for the wave model for light. The discovery of interference gave a basis to development of interferomertry techniques widely successfully used as in microscopic investigations, as in astronomic investigations.

The physical principles of optical interferometry exploit the wave properties of light. Light can be thought as electromagnetic wave propagating through space. If we assume that we are dealing with a linearly polarized wave propagating in a vacuum in z direction, electric field E can be represented by a sinusoidal function of distance and time.

$$E\left(x,y,z,t\right)=a\cos\left[2\pi\left(\mathrm{vt}-z/\lambda\right)\right] \tag{3.1}$$

Where a is the amplitude of the light wave, v is the frequency, and λ is its wavelength. The term within the square brackets is called the phase of the wave. Let's rewrite this equation in more compact form,

$$E\left(x,y,z,t\right)=a\cos\lceil\omega\mathrm{t}-\mathrm{kz}\rceil \tag{3.2}$$

where $\omega=2\pi v$ is the circular frequency, and $k=2\pi/\lambda$ is the propagation constant. Let's also transform this second equation into a complex exponential form,

$$E\left(x,y,z,t\right)=\mathrm{Re}\{a\exp\left(\mathrm{i}\varphi\right)\exp\left(\mathrm{i}\omega\mathrm{t}\right)\}=\mathrm{Re}\{A\exp\left(\mathrm{i}\omega\mathrm{t}\right)\} \tag{3.3}$$

where $\varphi=2\pi z/\lambda$ and $A=\exp\left(-\mathrm{i}\varphi\right)$ is known as the complex amplitude. If n is a refractive index of a medium where the light propagates, the light wave traverses a distance d in such a medium. The equivalent optical path in this case is

$$p=n\cdot d \tag{3.4}$$

When two light waves are superposed, the result intensity at any point depends on whether reinforce or cancel each other (Figure 3.1). This is well known phenomenon of interference. We will assume that two waves are propagating in the same direction and are polarized with their field vectors in the same plane. We will also assume that they have the same frequency. The complex amplitude at any point in the interference pattern is then the sum of the complex amplitudes of the two waves, so that we can write,

$$A=A_1+A_2 \tag{3.5}$$

where $A_1=a_1\exp\left(-\mathrm{i}\varphi_1\right)$ and $A_2=a_2\exp\left(-\mathrm{i}\varphi_2\right)$ are the complex amplitudes of two waves. The resultant intensity is, therefore,

$$I=\mid A\mid^2=I_1+I_2+2\left(I_1I_2\right)^{1/2}\cos\Delta\varphi \tag{3.6}$$

where I_1 and I_2 are the intensities of two waves acting separately, and $\Delta\varphi=\varphi_1-\varphi_2$ is the phase difference between them. If the two waves are derived from a common source, the phase difference corresponds to an optical path difference,

$$\Delta\mathrm{p}=\left(\lambda/2\pi\right)\Delta\varphi \tag{3.7}$$

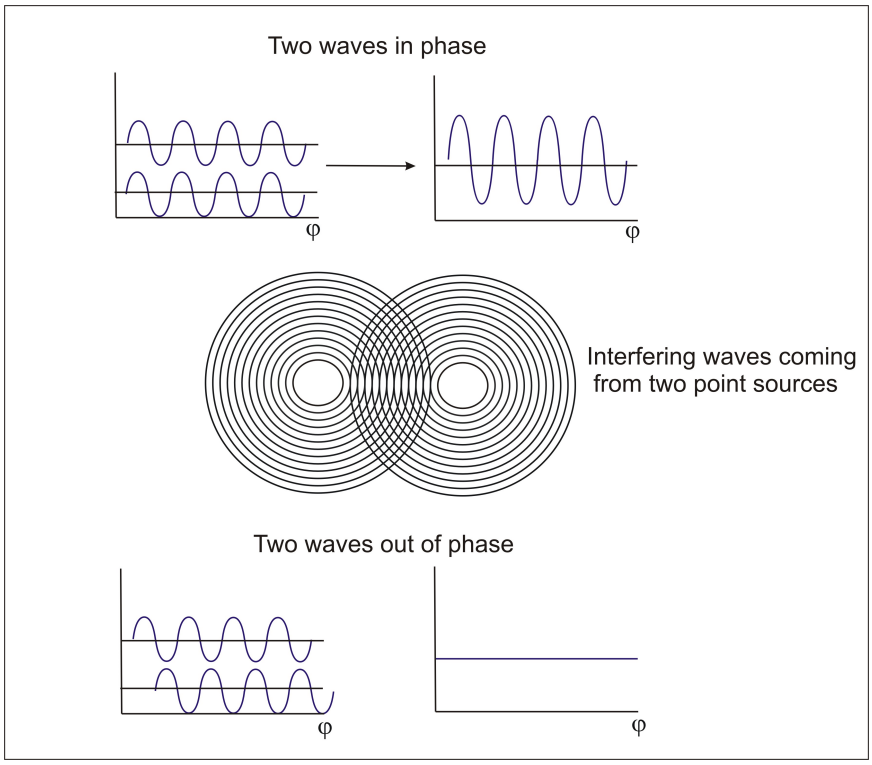

Figure 3.1: The scheme of interferometric wave interaction when two waves interact with each other, the amplitude of resulting wave will increase or decrease. The value of this amplitude depends on phase difference between two original waves.

If $\Delta\varphi$, the phase difference between the beams, varies linearly across the field of view, the intensity varies cosinusoidally, giving rise to alternating light and dark bands or fringes (Figure 3.1). The intensity in an interference pattern has its maximum value

$$I_{\max} = I_1 + I_2 + 2\left(I_1 I_2\right)^{1/2} \tag{3.8}$$

when $\Delta\varphi = 2m\pi$, where m is an integer and its minimum value

$$I_{\min} = I_1 + I_2 - 2\left(I_1 I_2\right)^{1/2} \tag{3.9}$$

when $\Delta\varphi = (2m+1)\,\pi$.

The principle of interferometry is widely used to develop many types of interferometric set ups. One of the earliest set ups is Michelson interferometry. The idea of this interferometry is quite simple: interference fringes are produced by splitting a beam of monochromatic light so that one beam strikes a fixed mirror and the other a movable mirror. An interference pattern results when the reflected beams are brought back together. The Michelson interferometric scheme is shown in Figure 3.2.

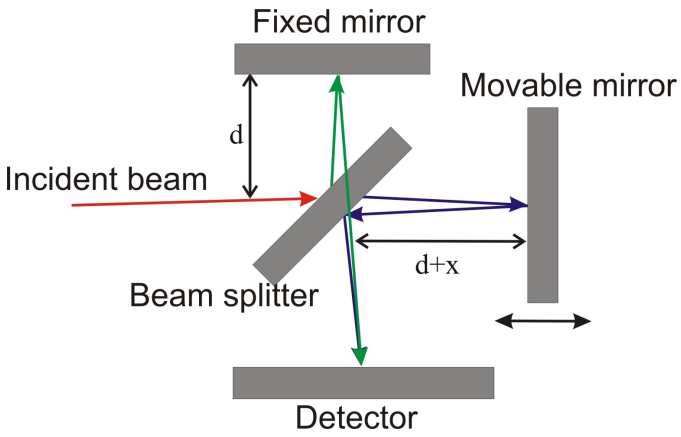

Figure 3.2: Schematic representation of a Michelson interferometry set-up.

The difference of path lengths between two beams is 2x because beams traverse the designated distances twice. The interference occurs when the path difference is equal to integer numbers of wavelengths,

$$\Delta \mathrm{p} = 2x = \mathrm{m}\lambda, m = 0, \pm 1, \pm 2... \tag{3.10}$$

Modern interferometric systems are more complicated. Using special phase-measurement techniques they capable to perform much more accurate height measurements than can be obtained just by directly looking at the interference fringes and measuring how they depart from being straight and equally spaced. Typically interferometric system consist of lights source, beamsplitter, objective system, system of registration of signals and transformation into digital format and computer which process data. Vertical scanning interferometry is contains all these parts. Figure 3.3 shows a configuration of VSI interferometric system.

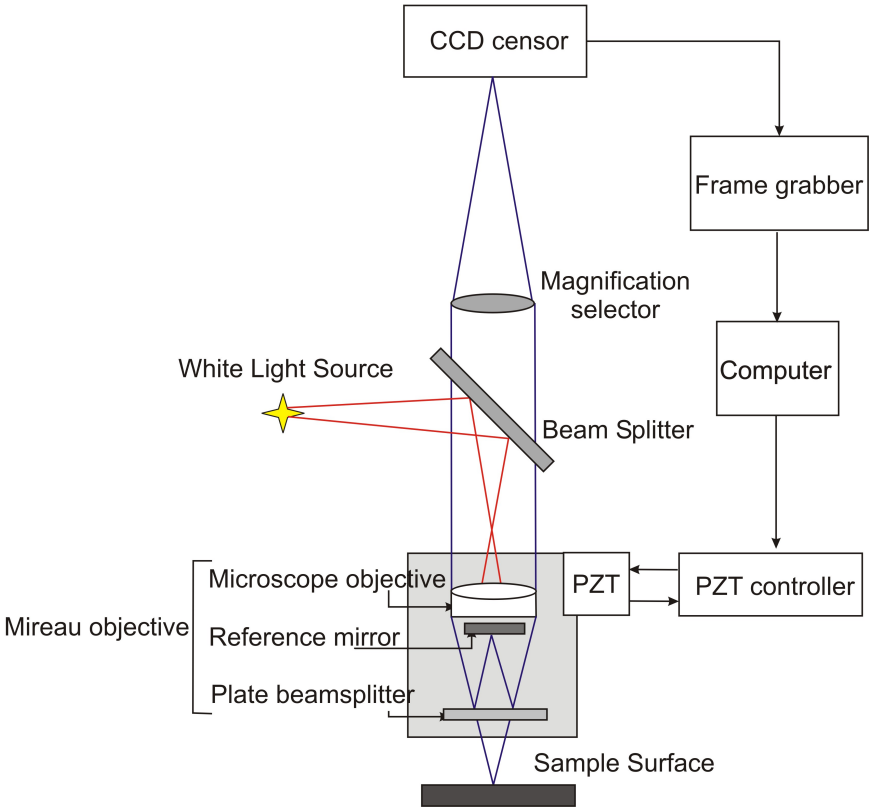

Figure 3.3: Schematic representation of the Vertical scanning interferometry (VSI) system.

Many of modern interferometric systems use Mirau objective in their constructions. Mireau objective is based on a Michelson interferometer. This objective consists of a lens, a reference mirror and a beamsplitter. The idea of getting interfering beams is simple: two beams (red lines) travel along the optical axis. Then they are reflected from the reference surface and the sample surface respectively (blue lines). After this these beams are recombined to interfere with each other. An illumination or light source system is used to direct light onto a sample surface through a cube beam splitter and the Mireau objective. The sample surface within the field of view of the objective is uniformly illuminated by those beams with different incidence angles. Any point on the sample surface can reflect those incident beams in the form of divergent cone. Similarly, the point on the reference symmetrical with that on the sample surface also reflects those illuminated beams in the same form.

The Mireau objective directs the beams reflected of the reference and the sample surface onto a CCD (charge-coupled device) sensor through a tube lens. The CCD sensor is an analog shift register that enables the transportation of analog signals (electric charges) through successive stages (capacitors), controlled by a clock signal. The resulting interference fringe pattern is detected by CCD sensor and the corresponding signal is digitized by a frame grabber for further processing with a computer.

The distance between a minimum and a maximum of the interferogram produced by two beams reflected from the reference and sample surface is known. That is, exactly half the wavelength of the light source. Therefore, with a simple interferogram the vertical resolution of the technique would be also limited to $\lambda/2$. If we will use a laser light as a light source with a wavelength of 300 nm the resolution would be only 150

nm. This resolution is not good enough for a detailed near-atomic scale investigation of crystal surfaces. Fortunately, the vertical resolution of the technique can be improved significantly by moving either the reference or the sample by a fraction of the wavelength of the light. In this way, several interferograms are produced. Then they are all overlayed, and their phase shifts compared by the computer software Figure 3.4. This method is widely known as phase shift interferometry (PSI).

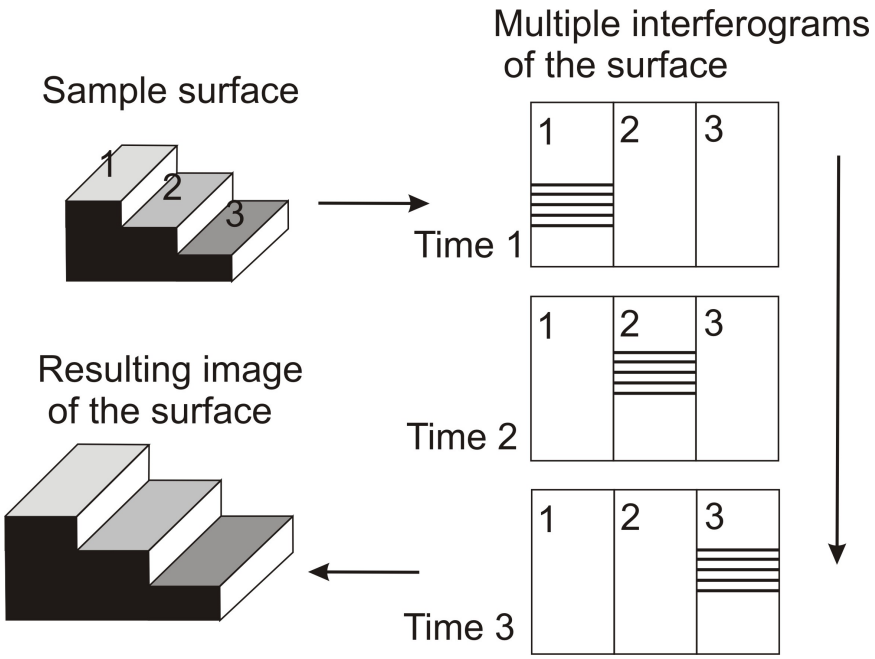

Figure 3.4: Sketch illustrating phase-shift technology. The sample is continuously moved along the vertical axes in order to scan surface topography. All interferograms are automatically overlayed using computer software.

Most optical testing interferometers now use phase-shifting techniques not only because of high resolution but also because phase-shifting is a high accuracy rapid way of getting the interferogram information into the computer. Also usage of this technique makes the inherent noise in the data taking process very low. As the result in a good environment angstrom or sub-angstrom surface height measurements can be performed. As it was said above, in phase-shifting interferometry the phase difference between the interfering beams is changed at a constant rate as the detector is read out. Once the phase is determined across the interference field, the corresponding height distribution on the sample surface can be determined. The phase distribution $\phi(x, y)$ is recorded by using the CCD camera.

Let's assign $A(x, y)$, $B(x, y)$, $C(x, y)$ and $D(x, y)$ to the resulting interference light intensities which are corresponded to phase-shifting steps of 0, $\pi/2$, π and $3\pi/2$. These intensities can be obtained by moving the reference mirror through displacements of $\lambda/8$, $\lambda/4$ and $3\lambda/8$, respectively. The equations for the resulting intensities would be:

$$A(x,y) = I_1(x,y) + I_2(x,y)\cos\alpha(x,y) \tag{3.11}$$

$$B(x,y) = I_1(x,y) - I_2(x,y)\sin\alpha(x,y) \tag{3.12}$$

$$C(x,y) = I_1(x,y) - I_2(x,y)\cos\alpha(x,y) \tag{3.13}$$

$$D(x,y) = I_1(x,y) + I_2(x,y)\sin\alpha(x,y) \tag{3.14}$$

where $I_1(x,y)$and $I_2(x,y)$ are two overlapping beams from two symmetric points on the test surface and the reference respectively. Solving equations (3.11)–(3.14), the phase map $\phi(x, y)$ of a sample surface will be given by the relation:

$$\varphi(x,y) = \frac{B(x,y) - D(x,y)}{A(x,y) - C(x,y)} \tag{3.15}$$

Once the phaseis determined across the interference field pixel by pixel on a two-dimensional CCD array, the local height distribution/contour, $h(x, y)$, on the test surface is given by

$$h(x,y) = \frac{\lambda}{4\pi}\varphi(x,y) \tag{3.16}$$

Normally the resulted fringe can be in the form of a linear fringe pattern by adjusting the relative position between the reference mirror and sample surfaces. Hence any distorted interference fringe would indicate a local profile/contour of the test surface.

It is important to note that the Mireau objective is mounted on a capacitive closed-loop controlled PZT (piezoelectric actuator) as to enable phase shifting to be accurately implemented. The PZT is based on piezoelectric effect referred to the electric potential generated by applying pressure to piezoelectric material. This type of materials is used to convert electrical energy to mechanical energy and vice-versa. The precise motion that results when an electric potential is applied to a piezoelectric material has an importance for nanopositioning. Actuators using the piezo effect have been commercially available for 35 years and in that time have transformed the world of precision positioning and motion control.

Vertical scanning interferometer also has another name; white-light interferometry (WLI) because of using the white light as a source of light. With this type of source a separate fringe system is produced for each wavelength, and the resultant intensity at any point of examined surface is obtained by summing these individual patterns. Due to the broad bandwidth of the source the coherent length L of the source is short:

$$L = \frac{\lambda^2}{\mathrm{n}\Delta\lambda} \tag{3.17}$$

where λ is the center wavelength, n is the refractive index of the medium, $\Delta\lambda$ is the spectral width of the source. In this way good contrast fringes can be obtained only when the lengths of interfering beams pathways are closed to each other. If we will vary the length of a pathway of a beam reflected from sample, the height of a sample can be determined by looking at the position for which a fringe contrast is a maximum. In this case interference pattern exist only over a very shallow depth of the surface. When we vary a pathway of sample-reflected beam we also move the sample in a vertical direction in order to get the phase at which maximum intensity of fringes will be achieved. This phase will be converted in height of a point at the sample surface.

The combination of phase shift technology with white-light source provides a very powerful tool to measure the topography of quite rough surfaces with the amplitude in heights about and the precision up to 1-2 nm. Through a developed software package for quantitatively evaluating the resulting interferogram, the proposed system can retrieve the surface profile and topography of the sample objects Figure 3.5.

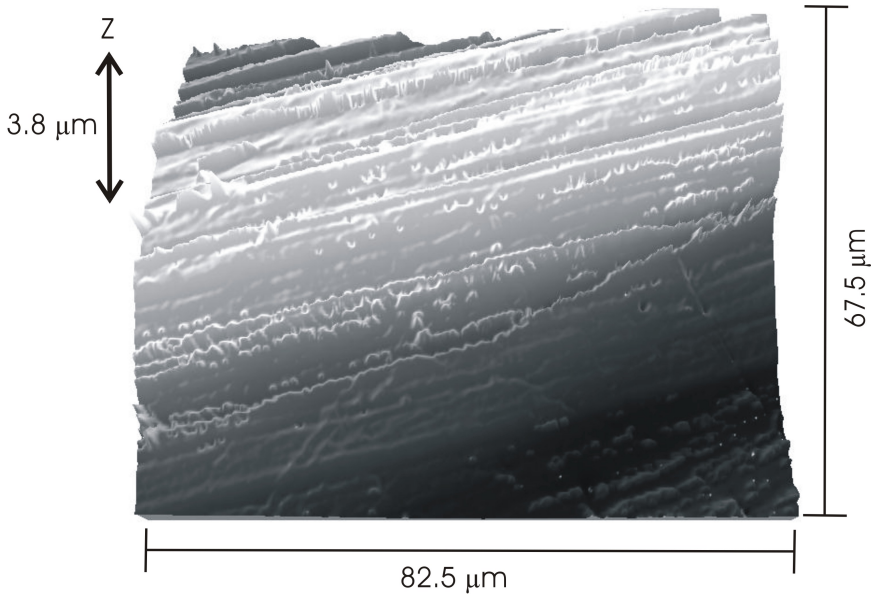

Figure 3.5: Example of muscovite surface topography, obtained by using VSI- 50x objective.

3.1.3 A comparison of common methods to determine surface topography: SEM, AFM and VSI

Except the interferometric methods described above, there are a several other microscopic techniques for studying crystal surface topography. The most common are scanning electron microscopy (SEM) and atomic force microscopy (AFM). All these techniques are used to obtain information about the surface structure. However they differ from each other by the physical principles on which they based.

3.1.3.1 Scanning electron microscopy

SEM allows us to obtain images of surface topography with the resolution much higher than the conventional light microscopes do. Also it is able to provide information about other surface characteristics such as chemical composition, electrical conductivity etc, see Figure 3.6. All types of data are generated by the reflecting of accelerated electron beams from the sample surface. When electrons strike the sample surface, they lose their energy by repeated random scattering and adsorption within an outer layer into the depth varying from 100 nm to 5 microns.

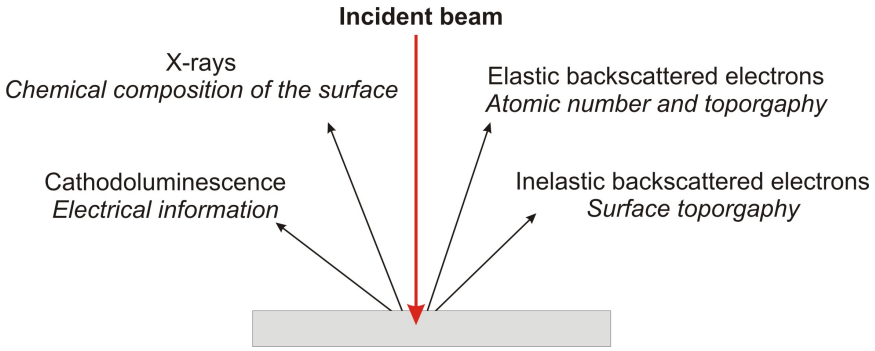

Figure 3.6: Scheme of electron beam-sample interaction at SEM analysis

The thickness of this outer layer also knows as interactive layer depends on energy of electrons in the beam, composition and density of a sample. Result of the interaction between electron beam and the surface provides several types of signals. The main type is secondary or inelastic scattered electrons. They are produced as a result of interaction between the beam of electrons and weakly bound electrons in the conduction band of the sample. Secondary electrons are ejected from the k-orbitals of atoms within the surface layer of thickness about a few nanometers. This is because secondary electrons are low energy electrons (<50 eV), so only those formed within the first few nanometers of the sample surface have enough energy to escape and be detected. Secondary backscattered electrons provide the most common signal to investigate surface topography with lateral resolution up to 0.4 - 0.7 nm.

High energy beam electrons are elastic scattered back from the surface. This type of signal gives information about chemical composition of the surface because the energy of backscattered electrons depends on the weight of atoms within the interaction layer. Also this type of electrons can form secondary electrons and escape from the surface or travel father into the sample than the secondary. The SEM image formed is the result of the intensity of the secondary electron emission from the sample at each x,y data point during the scanning of the surface.

3.1.3.2 Atomic force microscopy

AFM is a very popular tool to study surface dissolution. AFM set up consists of scanning a sharp tip on the end of a flexible cantilever which moves across a sample surface. The tips typically have an end radius of 2 to 20 nm, depending on tip type. When the tip touch the surface the forces of these interactions leads to deflection of a cantilever. The interaction between tip and sample surface involve mechanical contact forces, van der Waals forces, capillary forces, chemical bonding, electrostatic forces, magnetic forces etc. The deflection of a cantilever is usually measured by reflecting a laser beam off the back of the cantilever into a split photodiode detector. A schematic drawing of AFM can be seen in Figure 3.7. The two most commonly used modes of operation are contact mode AFM and tapping mode AFM, which are conducted in air or liquid environments.

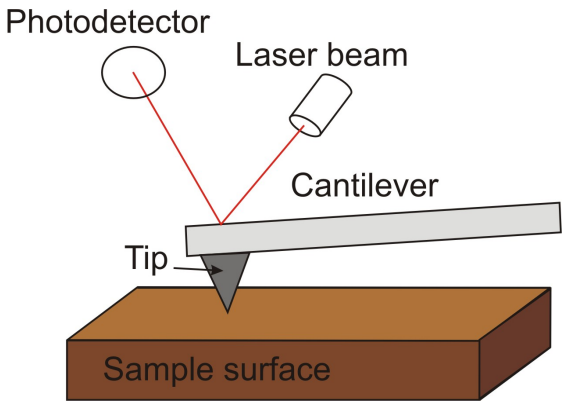

Figure 3.7: Schematic drawing of an AFM apparatus.

Working under the contact mode AFM scans the sample while monitoring the change in cantilever deflection with the split photodiode detector. Loop maintains a constant cantilever reflection by vertically moving the scanner to get a constant signal. The distance which the scanner goes by moving vertically at each x,y data point is stored by the computer to form the topographic image of the sample surface. Working under the tapping mode AFM oscillates the cantilever at its resonance frequency (typically∼300 kHz) and lightly "taps" the tip on the surface during scanning. The electrostatic forces increase when tip gets close to the sample surface, therefore the amplitude of the oscillation decreases. The laser deflection method is used to detect the amplitude of cantilever oscillation. Similar to the contact mode, feedback loop maintains a constant oscillation amplitude by moving the scanner vertically at every x,y data point. Recording this movement forms the topographical image. The advantage of tapping mode over contact mode is that it eliminates the lateral, shear forces present in contact mode. This enables tapping mode to image soft, fragile, and adhesive surfaces without damaging them while work under contact mode allows the damage to occur.

3.1.3.3 Comparison of techniques

All techniques described above are widely used in studying of surface nano- and micromorphology. However, each method has its own limitations and the proper choice of analytical technique depends on features of analyzed surface and primary goals of research.

All these techniques are capable to obtain an image of a sample surface with quite good resolution. The lateral resolution of VSI is much less, then for other techniques: 150 nm for VSI and 0.5 nm for AFM and SEM. Vertical resolution of AFM (0.5 Å) is better then for VSI (1 - 2 nm), however VSI is capable to measure a high vertical range of heights (1 mm) which makes possible to study even very rough surfaces. On the contrary, AFM allows us to measure only quite smooth surfaces because of its relatively small vertical scan range (7 μm). SEM has less resolution, than AFM because it requires coating of a conductive material with the thickness within several nm.

The significant advantage of VSI is that it can provide a large field of view (845 $\times$ 630 μm for 10x objective) of tested surfaces. Recent studies of surface roughness characteristics showed that the surface roughness parameters increase with the increasing field of view until a critical size of 250,000 μm is reached. This value is larger then the maximum field of view produced by AFM (100 $\times$ 100 μm) but can be easily obtained by VSI. SEM is also capable to produce images with large field of view. However, SEM is able to provide only 2D images from one scan while AFM and VSI let us to obtain 3D images. It makes quantitative

analysis of surface topography more complicated, for example, topography of membranes is studied by cross section and top view images.

	VSI	**AFM**	**SEM**
Lateral resolution	0.5-1.2 μm	0.5 nm	0.5-1 nm
Vertical resolution	2 nm	0.5 Å	Only 2D images
Field of view	845 $\times$ 630 μm (10x objective)	100 $\times$ 100 μm	1-2 mm
Vertical range of scan	1 mm	10 μm	-
Preparation of a sample	-	-	Required coating of a conducted material
Required environment	Air	Air, liquid	Vacuum

Table 3.1: A comparison of VSI sample and resolution with AFM and SEM.

3.1.4 The experimental studying of surface processes using microscopic techniques

The limitations of each technique described above are critically important to choose appropriate technique for studying surface processes. Let's explore application of these techniques to study dissolution of crystals.

When crystalline matter dissolves the changes of the crystal surface topography can be observed by using microscopic techniques. If we will apply an unreactive mask (silicon for example) on crystal surface and place a crystalline sample into the experiment reactor then we get two types of surfaces: dissolving and remaining the same or unreacted. After some period of time the crystal surface starts to dissolve and change its z-level. In order to study these changes *ex situ* we can pull out a sample from the reaction cell then remove a mask and measure the average height difference $\Delta \overset{\Psi}{h}$between the unreacted and dissolved areas. The average heights of dissolved and unreacted areas are obtained through digital processing of data obtained by microscopes. The velocity of normal surface retreat v_{SNR} during the time interval Δt is defined as

$v_{\mathrm{SNR}} = \frac{\Delta \overline{h}}{\Delta \mathrm{t}}$

Dividing this velocity by the molar volume $\overline{V}(\mathrm{cm}^3/\mathrm{mol})$ gives a global dissolution rate in the familiar units of moles per unit area per unit time:

$$R = \frac{v_{\mathrm{SNR}}}{\overline{V}} \tag{3.18}$$

This method allows us to obtain experimental values of dissolution rates just by precise measuring of average surface heights. Moreover, using this method we can measure local dissolution rates at etch pits by monitoring changes in the volume and density of etch pits across the surface over time. VSI technique is capable to perform these measurements because of large vertical range of scanning. In order to get precise values of rates which are not depend on observing place of crystal surface we need to measure enough large areas. VSI technique provides data from areas which are large enough to study surfaces with heterogeneous dissolution dynamics and obtain average dissolution rates. Therefore, VSI makes possible to measure rates of normal surface retreat during the dissolution and observe formation, growth and distribution of etch pits on the surface.

However, if the mechanism of dissolution is controlled by dynamics of atomic steps and kink sites within a smooth atomic surface area, the observation of the dissolution process need to use a more precise technique. AFM is capable to provide information about changes in step morphology *in situ* when the dissolution

occurs. For example, immediate response of the dissolved surface to the changing of environmental conditions (concentrations of ions in the solution, pH etc.) can be studied by using AFM.

SEM is also used to examine micro and nanotexture of solid surfaces and study dissolution processes. This method allows us to observe large areas of crystal surface with high resolution which makes possible to measure a high variety of surfaces. The significant disadvantage of this method is the requirement to cover examine sample by conductive substance which limits the resolution of SEM. The other disadvantage of SEM is that the analysis is conducted in vacuum. Recent technique, environmental SEM or ESEM overcomes these requirements and makes possible even examine liquids and biological materials. The third disadvantage of this technique is that it produces only 2D images. This creates some difficulties to measure $\Delta\overline{h}$ within the dissolving area. One of advantages of this technique is that it is able to measure not only surface topography but also chemical composition and other surface characteristics of the surface. This fact is used to monitor changing in chemical composition during the dissolution.

3.1.5 Bibliography

- A. C. Lasaga, *Kinetic Theory in the Earth Sciences*. Princeton Univ. Press, Princeton, NJ (1998).
- A. Luttge, E. V. Bolton, and A. C. Lasaga A.C., *Am. J. Sci.*, 1999, **299**, 652.
- D. Kaczmarek, *Vacuum*, 2001, **62**, 303.
- P. Hariharan. *Optical interferometry*, Second edition, Academic press (2003) ISBN 0-12-311630-9.
- A. Luttge and P. G. Conrad, *Appl. Environ. Microbiol.*, 2004, **70**, 1627.
- A. C. Lasaga and A. Luttge, *American Mineralogist*, 2004, **89**, 527.
- K. J. Davis and A. Luttge, *Am. J. Sci.*, 2005, **305**, 727.
- S. H. Wang and Tay, *Meas. Sci. Technol.*, 2006, **17**, 617.
- A. Luttge and R. S. Arvidson, in *Kinetics of water-rock interaction*, Ed. S. Brantley, J. Kubicki, and A. White, Springer (2007).
- L. Zhang and A. Luttge, *American Mineralogist*, 2007, **92**, 1316.
- C. Fischer A. and Luttge, *Am. J. Sci.*, 2007, **307**, 955.
- Y. Wyart, G. Georges, C. Deumie, C. Amra, and P. Moulina, *J. Membrane Sci.*, 2008, **315**, 82.
- T. C. Vaimakis, E. D. Economou, and C. C. Trapalis, *J. Therm. Anal. Cal.*, 2008, **92**, 783.

3.2 Beyond Optical Microscopy[2]

NOTE: "This module was developed as part of a Rice University Class called "Nanotechnology: Content and Context[3] " initially funded by the National Science Foundation under Grant No. EEC-0407237. It was conceived, researched, written and edited by students in the Fall 2005 version of the class, and reviewed by participating professors."

[2]This content is available online at <http://cnx.org/content/m14353/1.2/>.
[3]http://frazer.rice.edu/nanotech

Figure 3.8: Dell Butcher Hall, home of the SEA fish tank, where the SEM, AFM, and STM reside.

3.2.1 Introduction

Light microscopes are used in a number of areas such as medicine, science, and engineering. However, light microscopes cannot give us the high magnifications needed to see the tiniest objects like atoms. As the study of both microstructures and macrostructures of materials have come to the forefront of materials research and development new methods and equipment have been developed. Both the usage of electrons and atomic force rather than light permits advanced degrees of observations than would allow an optical microscope. As the interest in new materials in general and nanomaterials in particular is growing alternatives to optical microscopy are proving fundamental to the advancement of nanoscale science and technology.

3.2.2 Scanning Electron Microscope

SEM: A Brief History

The scanning electron microscope is an incredible tool for seeing the unseen worlds of microspace. The scanning electron microscope reveals new levels of detail and complexity in the world of micro-organisms and miniature structures. While conventional light microscopes use a series of glass lenses to bend light waves

and create a magnified image, the scanning electron microscope creates magnified images by using electrons instead of light waves.

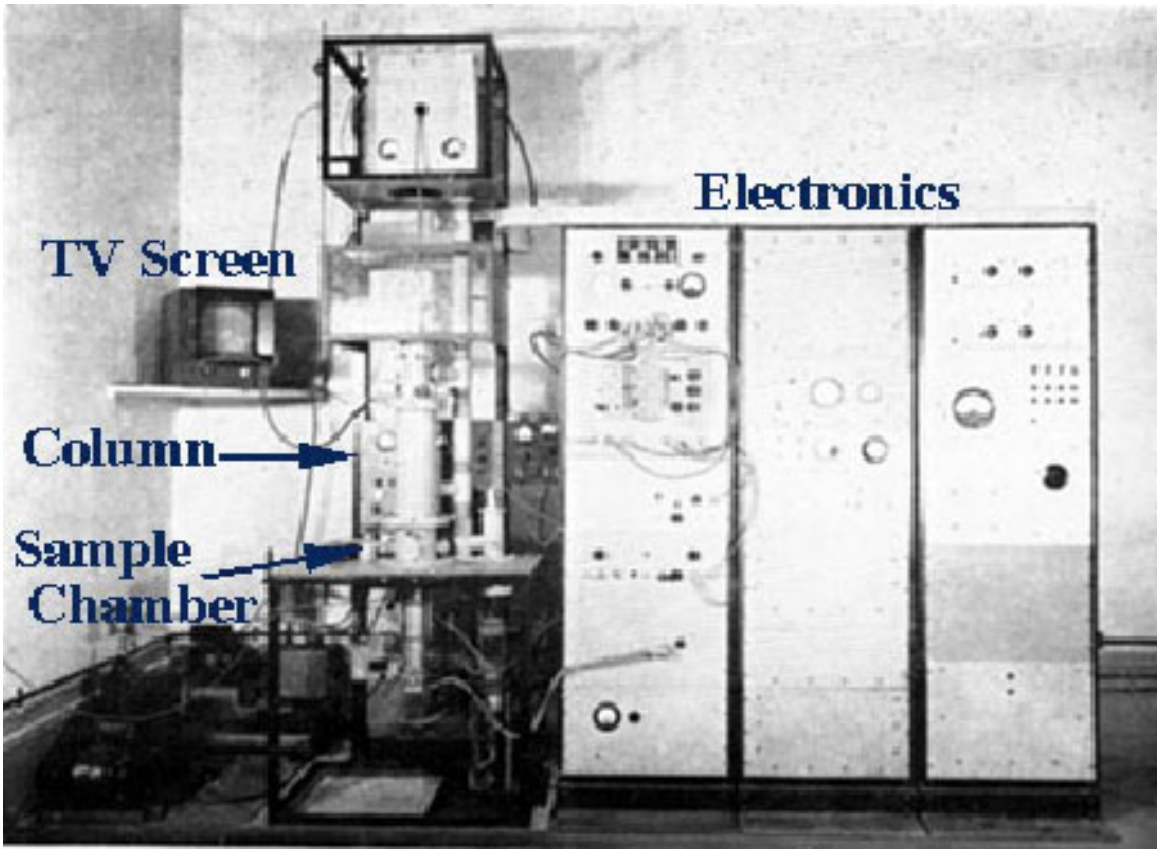

Figure 3.9: One of the first SEMs

The earliest known work describing the conceptualization of the scanning electron microscope was in 1935 by M. Knoll who, along with other pioneers in the field of electron optics, was working in Germany. Although it was Manfred von Ardenne who laid the foundations of both transmission and surface scanning electron microscopy just before World War II, it is Charles Oatley who is recognized as the great innovator of scanning electron microscopy. Oatley's involvement with the SEM began immediately after World War II when, his recent wartime experience in the development of radar, allowed him to develop new techniques that could be brought to overcome some of the fundamental problems encountered by von Ardenne in his pre-war research.

Von Ardenne (1938) constructed a scanning transmission electron microscope (STEM) by adding scan coils to a transmission electron microscope. [1][4] In the late 1940s Oatley, then a lecturer in the Engineering Department of Cambridge University, England, showed interest in conducting research in the field of electron optics and decided to re-investigate the SEM as an accompaniment to the work being done on the TEM (by V. E. Cosslett, also being developed in Cambridge at the Physics Department). One of Oatley's students, Ken Sander, began working on a column for a transmission electron microscope using electrostatic lenses,

[4] http://www2.eng.cam.ac.uk/~bcb/history.htm

but after a long period of illness was forced to suspend his research. His work then was taken up by Dennis McMullan in 1948, when he and Oatley built their first SEM by 1951. By 1952 this instrument had achieved a resolution of 50 nm.

How the SEM works

In the SEM, electromagnets are used to bend an electron beam which is then utilized to produce the image on a screen. The beam of electrons is produced at the top of the microscope by heating a metallic filament. The electron beam follows a vertical path through the column of the microscope. It makes its way through electromagnetic lenses which focus and direct the beam down towards the sample. Once it hits the sample, other electrons are ejected from the sample. Detectors collect the secondary or backscattered electrons, and convert them to a signal that is sent to a viewing screen similar to the one in an ordinary television, producing an image.

Figure 3.10: JEOL 5300 Scanning Electron Microscope, Rice University Mechanical Engineering Building

By using electromagnets an observer can have more control over how much magnification he/she obtains. The SEM has a large depth of field, which allows a large amount of the sample to be in focus at one time. The electron beam also provides greater clarity in the image produced. The SEM allows a greater depth of focus than the optical microscope. For this reason the SEM can produce an image that is a good representation of the three-dimensional sample.

The SEM also produces images of high resolution, which means that closely spaced features can be

examined at a high magnification. Preparation of the samples is relatively easy since most SEMs only require the sample to be conductive. The combination of higher magnification, larger depth of focus, greater resolution, and ease of sample observation makes the SEM one of the most heavily used instruments in research areas today.

SEM Usage

The SEM is designed for direct studying of:

- Topography: study of the surfaces of solid objects
- Morphology: study of shape and size
- Brief history of each microscope
- Composition: analysis of elements and compounds
- Crystallographic information: how atoms are arranged in a sample

SEM has become one of the most widely utilized instruments for material characterization. Given the overwhelming importance and widespread use of the SEM, it has become a fundamental instrument in universities and colleges with materials-oriented programs. [2][5] Institutions of higher learning and research have been forced to take extremely precautious measures with their equipment as it is expensive and maintenance is also costly.

Rice University, for example, has created what is called the Rice Shared Equipment Authority (SEA) to organize schedules, conduct training sessions, collect usage fees and maintain the usage of its high tech microscopic equipment. The following chart indicates prices, location, and necessary training for three of the most popular instruments under SEA jurisdiction:

[5] http://www.tms.org/pubs/journals/JOM/9509/Chumbley-9509.html

SEM 6500	SEM 5300	AFM
The JEOL 6500F is a high resolution (1.5 nm) thermal field emission electron microscope capable of imaging at voltages from 200 V to 30 kV. It is also equipped with a back-scattered electron detector for compositional and topographical imaging. The 6500F has a high speed electrostatic beam blanker and is configured for electron beam lithography via the Nabity NPGS system. Lithography resolution is approximately 20 nm.	The JEOL 5300 is a simple medium resolution (5 nm) tungsten filament electron microscope. It is useful for general secondary electron imaging on properly prepared samples.	Atomic force microscopy measures the topographic features of a surface under ambient conditions, or in some cases the features of materials immersed in liquids; typical resolution with these instruments is 10's of nanometers lateral (x y) and .3 nanometers in z.
$25/hr for academic use $125/hr for external users Dell Butcher Hall, 160A Training consists of 2-3, 2 hour sessions spread out over 3 weeks.	$10/hour academic use $125/hour external use Sputter coating available Mechanical Engineering Building, 204 To begin training, contact a super-user or faculty in charge.	$7.50/hour academic use, $50/hour + tip cost external use. Dell Butcher Hall, 160A Training for this instrument usually consists of 2 or 3 two-hour sessions at $15.00/hour.

Figure 3.11: Chart comparing costs, location, and training for three instruments

Advantages and Disadvantages

Among the advantages is the most obvious, better resolution and depth of field than light microscopes. The SEM also provides compositional information for small areas, is relatively easy to use (after training), and the coatings make it semi non-destructive to beam damage. Its disadvantages, however, are all related to the specimen being examined. There are occasions when vacuum compatibility does not allow clear visibility. Specimen preparation can also cause contamination by introducing unwanted artifacts. Lastly, specimen must also be conductive for maximum visibility.

Questions for Review

- What makes the SEM such a useful instrument? What can it do that a normal optical microscope cannot?
- Explain the usage of the electron beam in the SEM.
- What is meant by “images of high resolution"?

3.2.3 Scanning Tunneling Microscopes

A Brief Historical Note

The scanning tunneling microscope (STM) had its birth in 1981, invented by Gerd Binnig and Heinrich Rohrer of IBM, in Zurich, Germany. They won the 1986 Nobel Prize in physics for this accomplishment, but use of the microscope itself was somewhat slow to spread into the academic world. STM is used to scan surfaces at the atomic level, producing a map of electron densities; the surface science community was somewhat skeptical and resistant of such a pertinent tool coming from an outside, industrial source. There were questions as to the interpretations of the early images (how are we really sure those are the individual silicon atoms?), as well as the difficulty of interpreting them in the first place – the original STMs did not include computers to integrate the data. The older electron microscopes were generally easier to use, and more reliable; hence they retained preference over STMs for several years after the STM development. STM gained publicity slowly, through accomplishments such as IBM's famous xenon atom arrangement feat (see fig. 3) in 1990, and the determination of the structure of "crystalline" silicon.

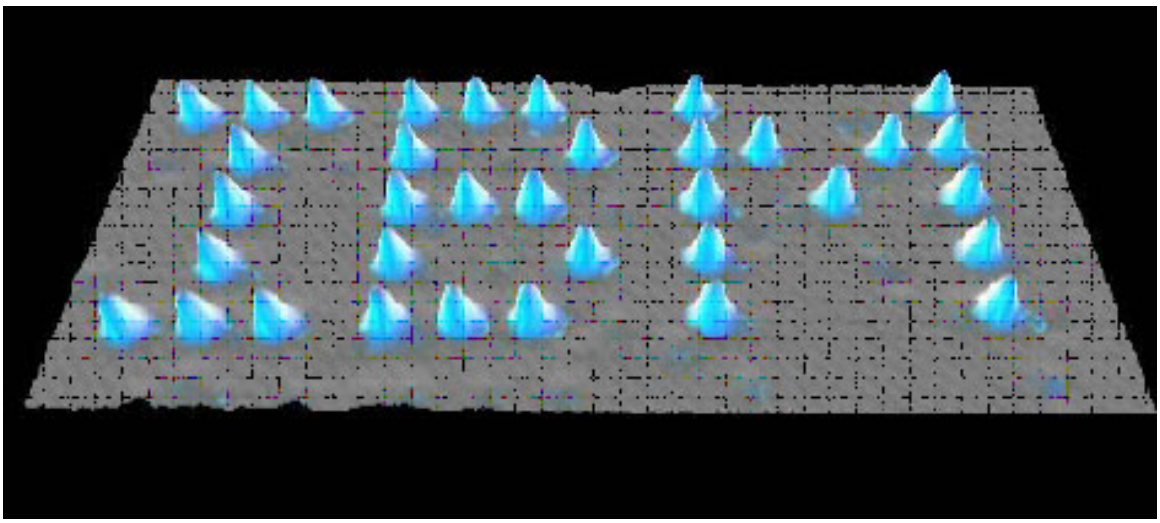

Figure 3.12: false-color STM image of xenon atoms arranged on a nickel background. From: D.M. Eigler, E.K. Schweizer. Positioning single atoms with a scanning tunneling microscope. Nature 344, 524-526 (1990).

How STMs Work: The Basic Ideas

I. The Probe - Scanning Tunneling Microscopy relies on a tiny probe of tungsten, platinum-iridium, or another conductive material to collect the data. The probe slowly "scans" across a surface, yielding an electron-density map of the nanoscale features of the surface. To achieve this resolution, the probe must be a wire with a protruding peak of a single atom; the sharper the peak, the better the resolution. A voltage difference between the tip and the sample results in an electron "tunneling" current when the tip comes close enough (within around 10 Å). This "tunneling" is a phenomenon explained by the quantum mechanical properties of particles; the current is either held constant and probe height recorded, or the probe's height is maintained and the change in current is measured to produce the scanning data. In constant current microscopy, the probe height must be constantly adjusted, which makes for relatively slow scanning, but allows fairly irregular surfaces to be examined. By contrast, constant height mode allows for faster scanning, but will only be effective for relatively smooth sample surfaces.

II. Piezoelectric Scanner - In order to make the sub-nanometer vertical adjustments required for STM, piezoelectric ceramics are used in the scanning platform on which the sample is held.

Piezoelectric materials undergo infinitesimally small mechanical changes under an applied voltage; therefore in the positioning device of a STM, they provide the motion to change the tip height at small enough increments that collision with the sample surface can be avoided. A data feedback loop is maintained between probe and piezoelectric positioner, so that the tip's height can be adjusted as necessary in constant-current mode, and can be brought close enough to the sample to begin scanning in the first place.

III. The Computer - Though the earliest STMs did not include a computer with the scanning apparatus, current models have one attached to filter and integrate the data as it is received, as well as to monitor and control the actual scanning process. Grayscale primary images can be colored to give contrast to different types of atoms in the sample; most published STM images have been enhanced in this way.

The very high degree of focus of a STM allows it to be used as a spectroscopic tool as well as a larger scale image producer. Properties of a single point on a sample surface can be analyzed through focused examination of the electronic structure.

Complications and Caveats

The integral use of the tunneling current in STM requires that both the probe and the sample be conductive, so the electrons can move between them. Non-conductive samples, therefore, must be coated in a metal, which obscures details as well as masks the actual properties of the sample. Furthermore, like with the SEM, oxidation and other contamination of the sample surface can be a problem, depending on the material(s) being studied. To avoid this, STM work is often carried out in an ultra-high vacuum (UHV) environment rather than in air. Some samples, however, are fairly well-suited to study in ambient conditions; one can strip away successive levels of a layered sample material in order to "clean" the surface as the study is being conducted.

Another seemingly simple problem involved in STM is control of vibration. Since the distances between probe and sample are so minute, the tiniest shake can result in data errors or cause the tip to collide with the surface, damaging the sample and possibly ruining the tip of the probe. A variety of systems have been implemented to control vibration, often involving frames with springs, or a sling in which the microscope is hung.

STM is plagued by artifacts, systematic errors in the observed data due to the mechanistic details of the microscope. For example, repetition of a particular shape in the same orientation throughout the image may be a case of tip artifacts, where a feature on the sample was sharper than the tip itself, resulting in the tip's shape being recorded rather than that of the sample feature. Lack of optimization of the microscope's feedback loop can produce large amounts of noise in the data, or, alternatively, cause a surface to be much smoother than it is. Finally, while sophisticated image processing software lends much-needed clarity to STM data, it can be misused such that meaning is created where there is none. Image filters used must be carefully evaluated against more "raw" image data to affirm their utility.

Counterbalancing the technique's obvious usefulness is the general difficulty of STM as a process. Whereas a scanning electron microscope can be operated successfully by a researcher with minimum skills as a technician, STMs are notoriously finicky and require expertise, time, and patience to produce a decent image. They are therefore not particularly popular research tools, though improvements in design and artifact control have been and are being made, making STM increasingly more practical.

Questions for Review

- In what types of situations would constant current microscopy be preferred over constant height? And vice-versa?
- What are potential problems of the large amount of data filtering and processing involved in STM?
- What errors are likely to be present in data from a particularly jagged, sharp-featured sample, and why?

3.2.4 Atomic Force Microscope

Another New Microscope

The requirement to have a conducting sample limited the usefulness of the STM. Gerd Binnig, Christoph Gerber, and Calvin Quate solved this problem with the invention of the Atomic Force Microscope (AFM) in 1986. [3][6] As suggested by its name, the AFM uses atomic forces—not the flow of electrons—to scan a sample, so it can be inductive as well as conductive. Still, the set up of the two microscopes is similar (see Figure 6). The AFM has a sharp tip a few micrometers long and usually a diameter less than 100 Å. It is attached to the end of a flexible tube 100-200 μm in length called a cantilever. The tip is brought close enough to the sample to feel forces that contribute to atomic bonds, called van der Waals forces. These are due to the attraction and repulsion of positively-charged protons and negatively-charged electrons. As electrons zip around an atom, they create temporary regions of positive and negative charges, which attract oppositely-charged regions on other atoms. If the atoms get too close, though, the repulsive force of the electrons overshadows this weaker attraction. In terms of the AFM, the temporary positive and negative charges attract the atoms in the tip and sample when they are far apart (several angstroms), but if they come too close (1-2 Å, less than the length of an atomic bond), the electrons on the tip and sample repel each other. This feature led to the development of two types of AFM: contact and non-contact.

[6] http://www.ieee-virtual-museum.org/

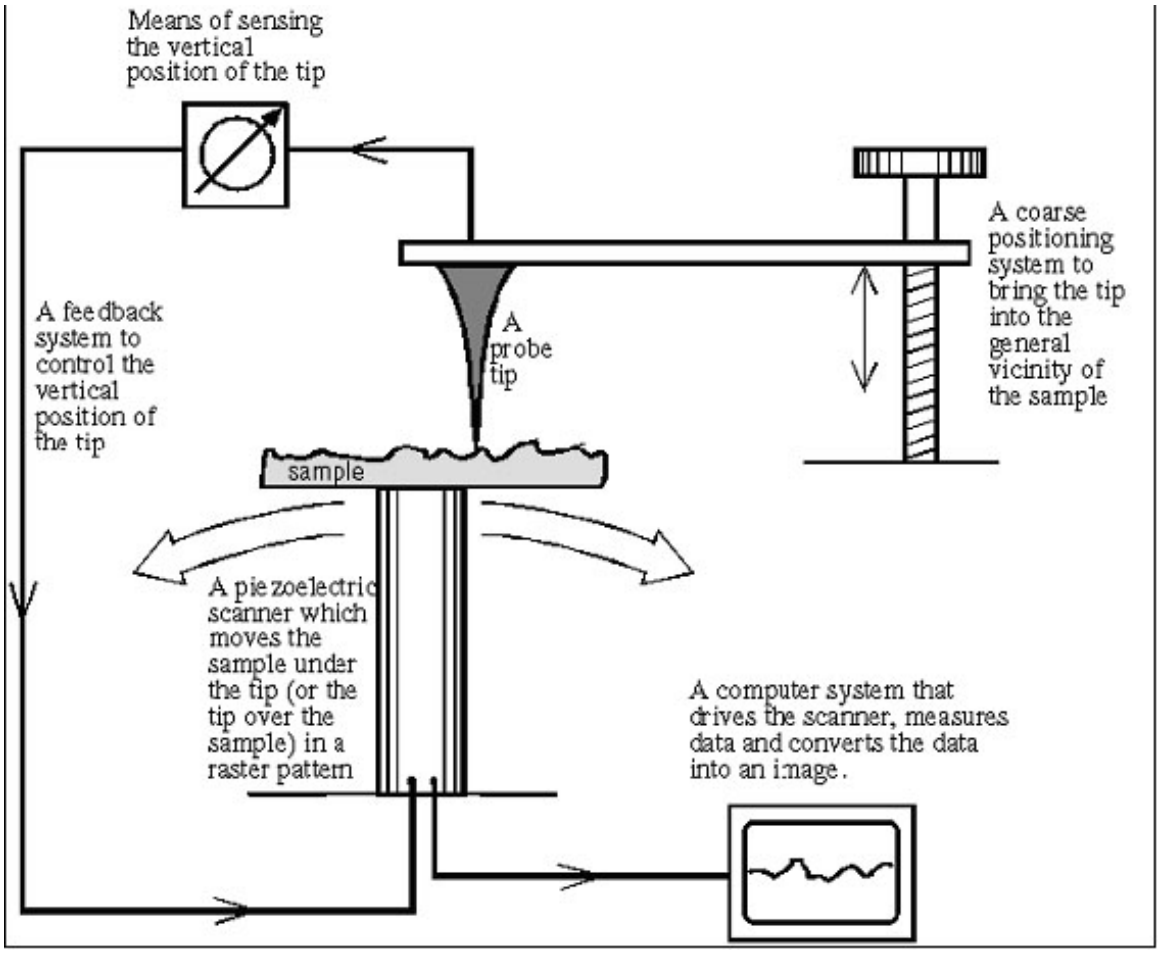

Figure 3.13: General schematic of AFM or STM, http://web.mit.edu/cortiz/www/AFMGallery/PracticalGuide.pdf[7]

[7] http://web.mit.edu/cortiz/www/AFMGallery/PracticalGuide.pdf

Figure 3.14: Digital Instrument Nanoscope, Rice University Dell Butcher Hall (Fish Tank)

The Contact AFM

A contact AFM is so called because the tip and the sample are closer to each other than atoms of the same molecule are. (It is difficult to define "contact" at the molecular level; bonds form when electrons from different atoms overlap. There is no rubbing together of atoms as we think of it at the macrolevel.) Since the cantilever is flexible, it is sensitive to the mutually repulsive force exerted between the tip and sample. This force varies with the topography of the latter–bumps bring the sample closer to the tip, increasing the force between them, while dips decrease the force. The variance in force is measured in two ways. In "constant-height" mode, the cantilever moves across the sample at a constant height, subjecting the tip to stronger and weaker forces, which cause the cantilever end to bend. This movement is measured by a laser beam that bounces off the reflective cantilever and onto a detector. In "constant-force" mode, the height of the cantilever is adjusted to keep the force between the tip and sample constant. Thus, the bend in the tip stays the same and the height adjustment is measured instead.

The Non-Contact AFM

As suggested by its name, the tip and sample are farther apart in a non-contact AFM. The cantilever vibrates so that the tip is tens to hundreds of angstroms from the sample, greater than the distance of a typical atomic bond, meaning that the force between them is attractive (compare to the 1-2 Å distance of the contact AFM). As the tip vibrates, it is pulled by this force, affecting its vibration frequency. A bump in the sample will cause a greater attractive force than a dip, so the topography is analyzed by recording

the vibration frequency.

Comparing the Two

Contact and non-contact AFMs generate similar pictures of a sample, which can be roughly interpreted as a topographical map (though other factors affect the force readings, such as local deviations in the electron density of the sample). However, each has its advantages and disadvantages that better suit it for certain sample types. In non-contact, the sample and tip remain far enough apart that the force between them is low and does not significantly affect the sample itself. This makes changes in topography more difficult to detect, but it also preserves the sample, which is especially important if it is soft and elastic, as well as the tip. In addition, the cantilever must be stiffer than for a contact AFM, otherwise it may bend too much, causing the tip to "contact" the sample. A contact AFM is more useful for sample surfaces that may be covered with a thin layer of water. Even in a high vacuum, this can occur when gaseous water condenses upon it. A non-contact AFM will not penetrate the water layer and will record its topography instead of the sample, but a contact AFM gets close enough to break through this problem.

Questions for Review

- What was significant about the invention of the AFM (what could be done that was not possible before)?
- Why is are the names "contact" and "non-contact" associated with these types of AFM?
- AFM tips are commonly composed of silicon or silicon nitride. Given that the latter is a tougher, more durable material, which would be more appropriate for a contact AFM?

3.3 TEM Imaging of Carbon Nanomaterials[8]

3.3.1 Introduction to TEM

Transmission electron microscopy (TEM) is a form of microscopy that uses an high energy electron beam (rather than optical light). A beam of electrons is transmitted through an ultra thin specimen, interacting with the specimen as it passes through. The image (formed from the interaction of the electrons with the sample) is magnified and focused onto an imaging device, such as a photographic film, a fluorescent screen,or detected by a CCD camera. In order to let the electrons pass through the specimen, the specimen has to be ultra thin, usually thinner than 10 nm.

The resolution of TEM is significantly higher than light microscopes. This is because the electron has a much smaller de Broglie wavelength than visible light (wavelength of 400∼700 nm). Theoretically, the maximum resolution, d, has been limited by λ, the wavelength of the detecting source (light or electrons) and NA, the numerical aperture of the system.

$$d = \frac{\lambda}{2n\sin\alpha} \approx \frac{\lambda}{2NA} \tag{3.19}$$

For high speed electrons (in TEM, electron velocity is close to the speed of light, c, so that the special theory of relativity has to be considered), the λ_e:

$$\lambda_e = \frac{h}{\sqrt{(2m_0E(1+E/2m_0c^2))}} \tag{3.20}$$

According to this formula, if we increase the energy of the detecting source, its wavelength will decrease, and we can get higher resolution. Today, the energy of electrons used can easily get to 200 keV, sometimes as high as 1 MeV, which means the resolution is good enough to investigate structure in sub-nanometer scale. Because the electrons is focused by several electrostatic and electromagnetic lenses, like the problems optical camera usually have, the image resolution is also limited by aberration, especially the spherical aberration called

[8] This content is available online at <http://cnx.org/content/m22963/1.5/>.

C_s. Equipped with a new generation of aberration correctors, transmission electron aberration-corrected microscope (TEAM) can overcome spherical aberration and get to half angstrom resolution.

Although TEAM can easily get to atomic resolution, the first TEM invented by Ruska in April 1932 could hardly compete with optical microscope, with only $3.6 \times 4.8 = 14.4$ magnification. The primary problem was the electron irradiation damage to sample in poor vacuum system. After World War II, Ruska resumed his work in developing high resolution TEM. Finally, this work brought him the Nobel Prize in physics 1986. Since then, the general structure of TEM hasn't changed too much as shown in Figure 3.15. The basic components in TEM are: electron gun, condenser system, objective lens (most important len in TEM which determines the final resolution), diffraction lens, projective lenses (all lens are inside the equipment column, between apertures), image recording system (used to be negative films, now is CCD cameras) and vacuum system.

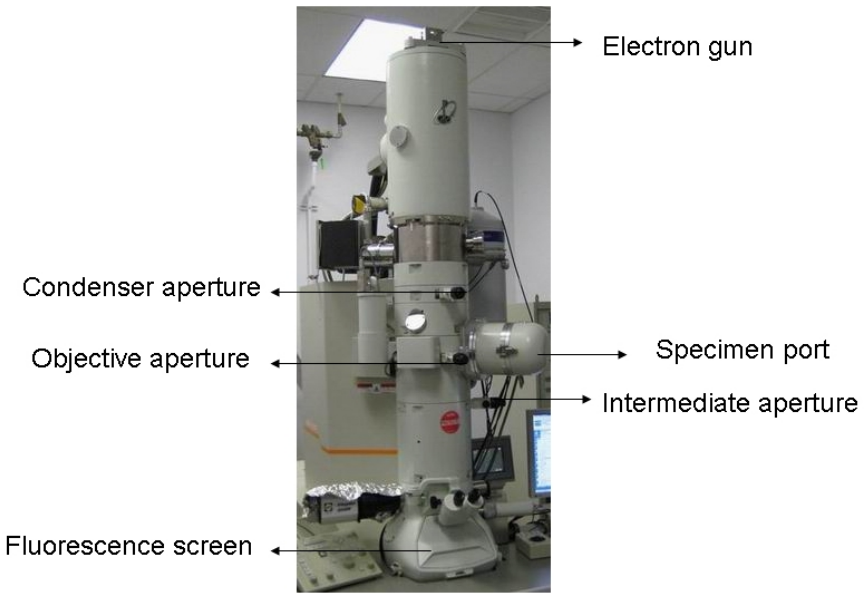

Figure 3.15: Position of the basic components in a TEM.

3.3.2 The family of carbon allotropes and carbon nanomaterials

Common carbon allotropes include diamond, graphite, amorphrous C (a-C), fullerene (also known as buckyball), carbon nanotube (CNT, including single wall CNT and multi wall CNT), graphene. Most of them are chemically inert and have been found in nature. We can also define carbon as sp^2 carbon (which is graphite), sp^3 carbon (which is diamond) or hybrids of sp^2 and sp^3 carbon. As shown in Figure 3.16, (a) is the structure of diamond, (b) is the structure of graphite, (c) graphene is a single sheet of graphite, (d) is amorphous carbon, (e) is C_{60}, and (f) is single wall nanotube. As for carbon nanomaterials, fullerene, CNT and graphene are the three most well investigated, due to their unique properties in both mechanics and electronics. Under TEM, these carbon nanomaterials will display three different projected images.

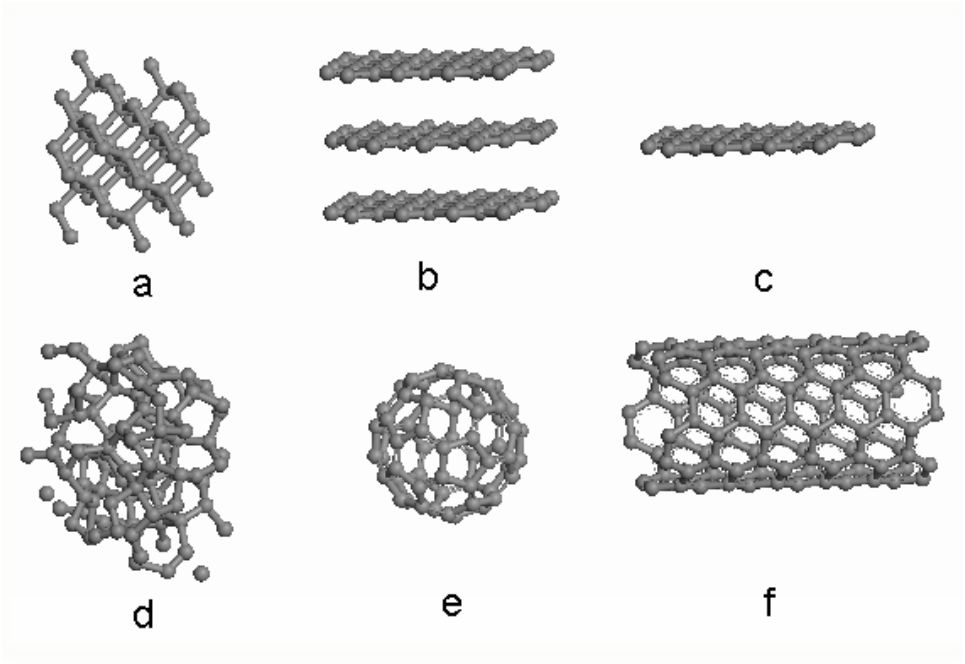

Figure 3.16: Six allotropes of carbon: a) diamond, b) graphite, c) graphene, d) amorphous carbon, e) C_{60} (Buckminsterfullerene or buckyball), f) single-wall carbon nanotube or buckytube.

3.3.3 Atomic structure of carbon nanomaterials under TEM

All carbon naomaterials can be investigated under TEM. Howerver, because of their difference in structure and shape, specific parts should be focused in order to obtain their atomic structure.

For C_{60}, which has a diameter of only 1 nm, it is relatively difficult to suspend a sample over a lacey carbon grid (a common kind of TEM grid usually used for nanoparticles). Even if the C_{60} sits on a thin a-C film, it also has some focus problems since the surface profile variation might be larger than 1 nm. One way to solve this problem is to encapsulate the C_{60} into single wall CNTs, which is known as nano peapods. This method has two benefits:

1. CNT helps focus on C_{60}. Single wall is aligned in a long distance (relative to C_{60}). Once it is suspended on lacey carbon film, it is much easier to focus on it. Therefore, the C_{60} inside can also be caught by minor focus changes.
2. The CNT can protect C_{60} from electron irradiation. Intense high energy electrons can permanently change the structure of the CNT. For C_{60}, which is more reactive than CNTs, it can not survive after exposing to high dose fast electrons.

In studying CNT cages, C_{92} is observed as a small circle inside the walls of the CNT. While a majority of electron energy is absorbed by the CNT, the sample is still not irradiation-proof. Thus, as is seen in Figure 3.17, after a 123 s exposure, defects can be generated and two C_{92} fused into one new larger fullerene.

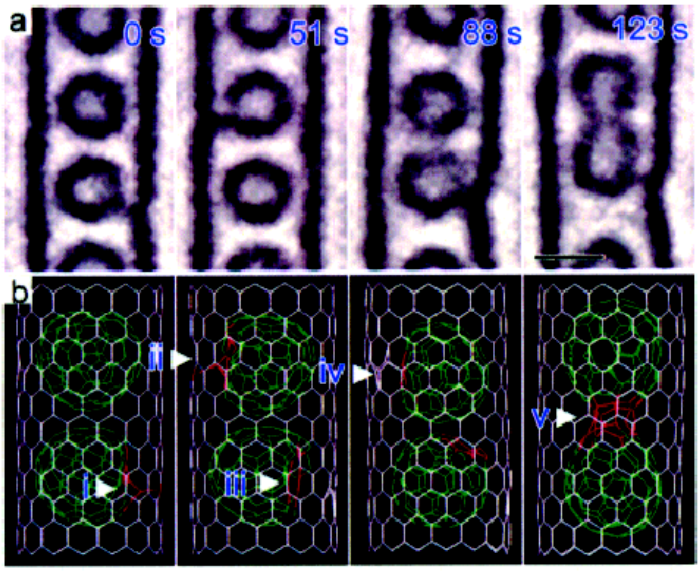

Figure 3.17: C_{92} encapsulated in SWNTs under different electron irradiation time. Courtesy of Dr. Kazutomo SUENAGA, adapted from K. Urita, Y. Sato, K. Suenaga, A. Gloter, A. Hasimoto, M. Ishida, T. Shimada, T. Shinohara, S. Iijima, *Nano Lett.*, 2004, **4**, 2451. Copyright American Chemical Society (2004).

Although, the discovery of C_{60} was first confirmed by mass spectra rather than TEM. When it came to the discovery of CNTs, mass spectra was no longer useful because CNTs shows no individual peak in mass spectra since any sample contains a range of CNTs with different lengths and diameters. On the other hand, HRTEM can provide a clear image evidence of their existence. An example is shown in Figure 3.18.

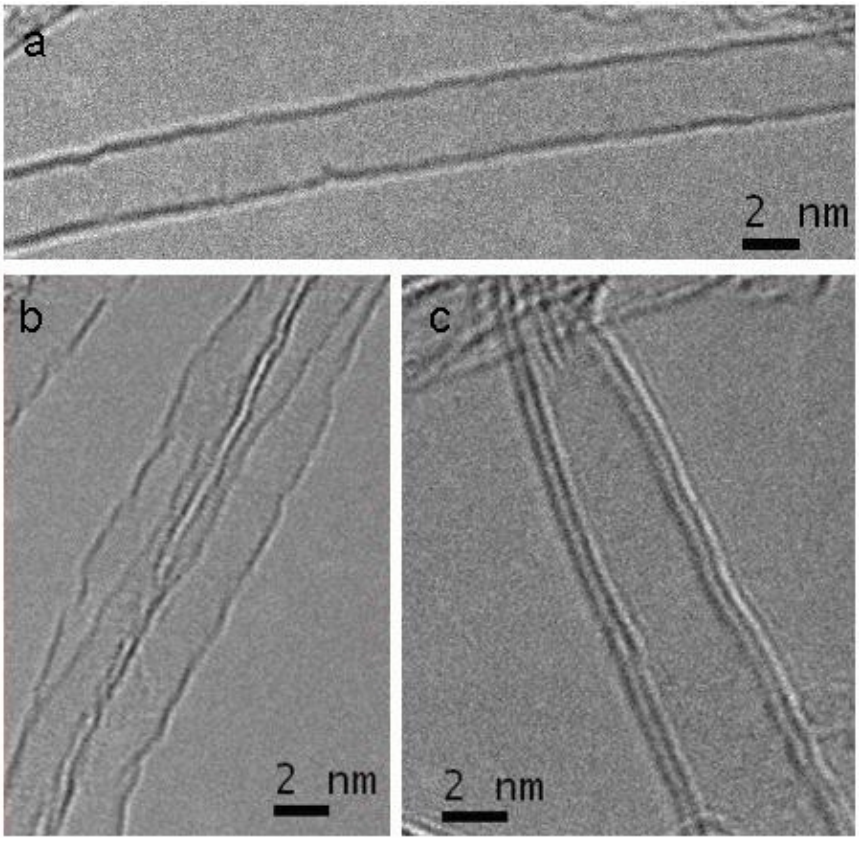

Figure 3.18: TEM images of SWNT and DWCNTs. Parallel dark lines corresponds to (002) lattice image of graphite. (a) and (b) SWNTs have 1 layer graphene sheet, diameter 3.2 nm. (c) DWCNT, diameter 4.0 nm.

Graphene is a planar fullerene sheet. Until recently, Raman, AFM and optical microscopy (graphene on 300 nm SiO_2 wafer) were the most convenient methods to characterize samples. However, in order to confirm graphene's atomic structure and determine the difference between mono-layer and bi-layer, TEM is still a good option. In Figure 3.19, a monolayer suspended graphene is observed with its atomic structure clearly shown. Inset is the FFT of the TEM image, which can be used as a filter to get an optimized structure image. High angle annular dark field (HAADF) image usually gives better contrast for different particles on it. It is also sensitive with changes of thickness, which allows a determination of the number of graphene layers.

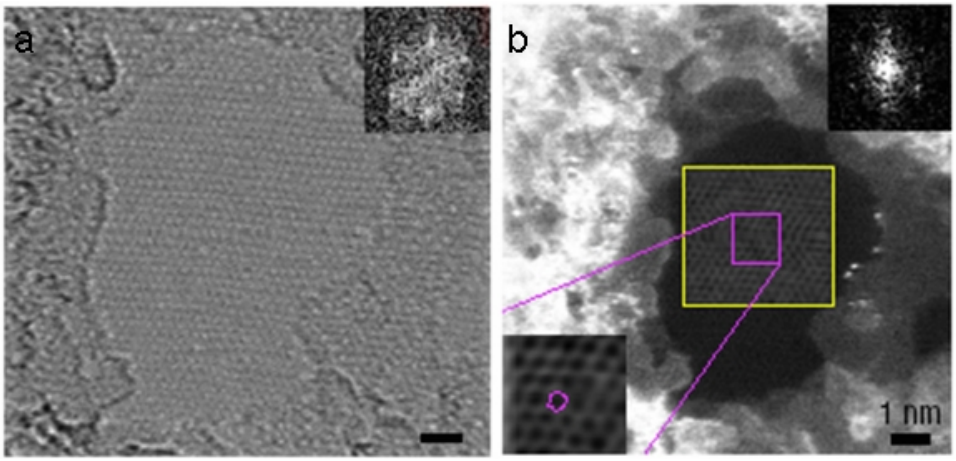

Figure 3.19: HRTEM of monolayer graphene. (a) Bright filed. (b) High Angle Annular Dark Field. Courtesy of Dr M. H. Gass, adapted from M. H. Gass, U. Bangert, A. L. Bleloch, P. Wang, R. R. Nair, and A. K. Geim, *Nature Nanotechnol.*, 2008, **3**, 676.

3.3.4 Graphene stacking and edges direction

Like the situation in CNT, TEM image is a projected image. Therefore, even with exact count of edge lines, it is not possible to conclude that a sample is a single layer graphene or multi-layer. If folding graphene has AA stacking (one layer is superposed on the other), with a projected direction of [001], one image could not tell the thickness of graphene. In order to distinguish such a bilayer of graphene from a single layer of graphene, a series of tilting experiment must be done. Different stacking structures of graphene are shown in Figure 3.20a.

Theoretically, graphene has the potential for interesting edge effects. Based upon its sp^2 structure, its edge can be either that of a zigzag or armchair configuration. Each of these possess different electronic properties similar to that observed for CNTs. For both research and potential application, it is important to control the growth or cutting of graphene with one specific edge. But before testing its electronic properties, all the edges have to be identified, either by directly imaging with STM or by TEM. Detailed information of graphene edges can be obtained with HRTEM, simulated with fast fourier transform (FFT). In Figure 3.20b, armchair directions are marked with red arrow respectively. A clear model in Figure 3.20c shows a 30 degree angle between zigzag edge and armchair edge.

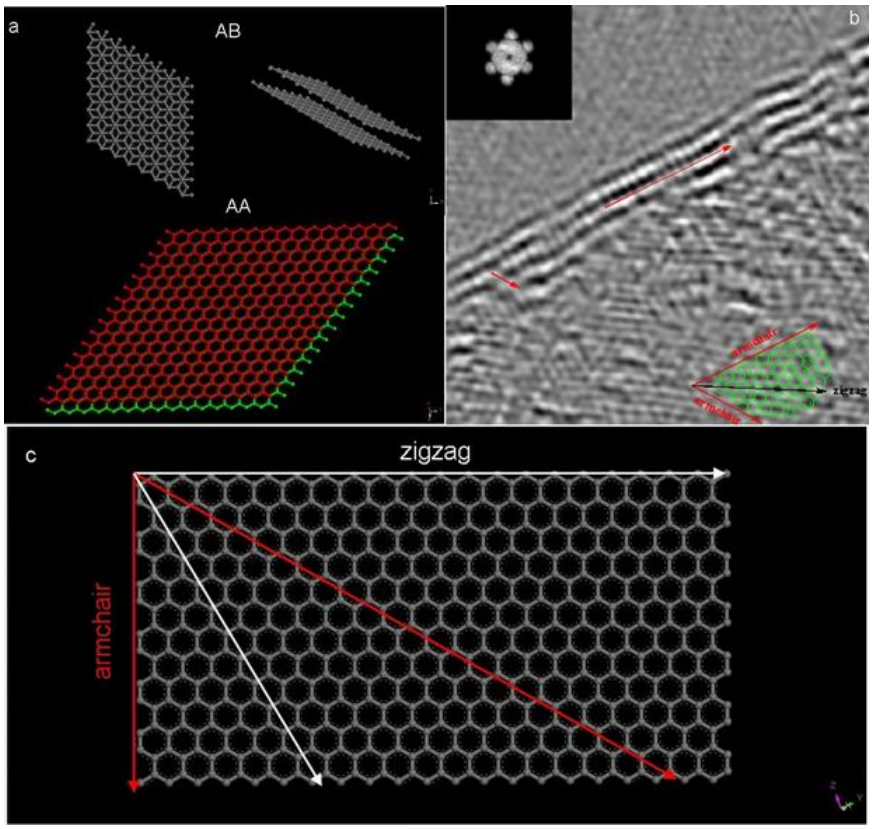

Figure 3.20: (a) Graphene stacking structure; (b) HRTEM image of graphene edges: zigzag and armchain (inset is FFT); (c) graphene edge model, a 30 ° angle between zigzag and armchair direction.

3.3.5 Bibliography

- K. Urita, Y. Sato, K. Suenaga, A. Gloter, A. Hasimoto, M. Ishida, T. Shimada, T. Shinohara, and S. Iijima, *Nano Lett.*, 2004, **4**, 2451.
- H. W. Kroto, J. R. Heath, S. C. O'Brien, R. F. Curl, and R. E. Smalley, *Nature*, 1985, **318**, 162.
- S. Iijima, *Nature*, 1991, **354**, 56.
- M. H. Gass, U. Bangert, A. L. Bleloch, P. Wang, R. R. Nair, and A. K. Geim, *Nature Nanotechnol.*, 2008, **3**, 676.
- L. Zheng and S. Iijima, *Phys. Rev. Lett.*, 2009, **102**, 015501.
- J. Campos-Delgado, J. M. Romo-Herrera, X. Jia, D. A. Cullen, H. Muramatsu, Y. A. Kim, T. Hayashi, Z. Ren, D. J. Smith, Y. Okuno, T. Ohba, H. Kanoh, K. Kaneko, M. Endo, H. Terrones, M. S. Dresselhaus, and M. Terrones, *Nano Lett.*, 2008, **8**, 2773.

3.4 Characterization of Covalently Functionalized Single-Walled Carbon Nanotubes[9]

3.4.1 Introduction

Characterization of nanoparticles in general, and carbon nanotubes in particular, remains a technical challenge even though the chemistry of covalent functionalization has been studied for more than a decade. It has been noted by several researchers that the characterization of products represents a constant problem in nanotube chemistry. A systematic tool or suites of tools are needed for adequate characterization of chemically functionalized single-walled carbon nanotubes (SWNTs), and is necessary for declaration of success or failure in functionalization trials.

So far, a wide range of techniques have been applied to characterize functionalized SWNTs: infra red (IR), Raman, and UV/visible spectroscopies, thermogravimetric analysis (TGA), atomic force microscopy (AFM), transmission electron microscopy (TEM), X-ray photoelectron spectroscopy (XPS), etc. A summary of the attribute of each of the characterization method is given in Table 3.2.

Method	Sample	Information	Limitations
TGA	solid	functionalization ratio	no evidence for covalent functionalization, not specific
XPS	solid	elements, functionalization ratio	no evidence of covalent functionalization, not specific, quantification complicated
Raman	solid	sp^3 indicated by D mode	not specific, quantification not reliable
Infra red (IR)	solid for (ATR-IR) or solution	substituent groups	no direct evidence for covalent functionalization, quantification not possible
UV/visible	solution	sidewall functionalization	not specific or quantitative, need highly dispersed sample
Solution NMR	solution	substituents	no evidence of covalent functionalization, high solubility of sample
Solid state NMR	solid	substituents, sp^3 molecular motions, quantification at high level of funcitionalization	high functionalization needed, long time for signal acquisition, quantification not available for samples with protons on side chains

continued on next page

[9]This content is available online at <http://cnx.org/content/m22299/1.4/>.

AFM	solid on substrate	topography	only a small portion of sample characterized, no evidence of covalent functionalization, no chemical identity
TEM	solid on substrate	image of sample distribution dispersion	only a small portion of sample characterized, no evidence of covalent functionalization, no chemical identity dispersion information complicated
STM	solid on substrate	distribution	no chemical identity of functional groups small portion of sample conductive sample only

Table 3.2: Common characterization methodology for functionalized SWNTs.

3.4.2 Elemental and Physical Analysis

3.4.2.1 Thermogravimetric analysis (TGA)

Thermogravimetric analysis (TGA) is the mostly widely used method to determine the level of sidewall functionalization. Since most functional groups are labile or decompose upon heating, while the SWNTs are stable up to 1200 °C under Ar atmosphere. The weight loss at 800 °C under Ar is often used to determine functionalization ratio using this indirect method. Unfortunately, quantification can be complicated with presence of multiple functional groups. Also, TGA does not provide direct evidence for covalent functionalization since it cannot differentiate between covalent attachment and physical adsorption.

3.4.2.2 X-ray photoelectron spectroscopy (XPS)

XPS confirms the presence of different elements in functionalized SWNTs. This is useful for identification of heteroatom elements such as F and N, and then XPS can be used for quantification with simple substituent groups and used indirectly. Deconvolution of XPS is useful to study fine structures on SWNTs. However, the overlapping of binding energies in the spectrum complicates quantification.

3.4.3 Spectroscopy

3.4.3.1 Raman spectroscopy

Raman spectroscopy is very informative and important for characterizing functionalized SWNTs. The tangential G mode (*ca.* $1550 - 1600$ cm^{-1}) is characteristic of sp^2 carbons on the hexagonal graphene network. The D-band, so-called disorder mode (found at *ca.* 1295 cm^{-1}) appears due to disruption of the hexagonal sp^2 network of SWNTs. The D-band was largely used to characterize functionalized SWNTs and ensure functionalization is covalent and occurred at the sidewalls. However, the observation of D band in Raman can also be related to presence of defects such as vacancies, 5-7 pairs, or dopants. Thus, using Raman to provide evidence of covalent functionalization needs to be done with caution. In particular, the use of Raman spectroscopy for a determination of the degree of functionalization is not reliable.

It has been shown that quantification with Raman is complicated by the distribution of functional groups on the sidewall of SWNTs. For example, if fluorinated-SWNTs (F-SWNTs) are functionalized with thiol or

thiophene terminated moieties, TGA shows that they have similar level of functionalization. However, their relative intensities of D:G in Raman spectrum are quite different. The use of sulfur substituents allow for gold nanoparticles with 5 nm in diameter to be attached as a "chemical marker" for direct imaging of the distribution of functional groups. AFM and STM suggest that the functional groups of thio-SWNTs are group together while the thiophene groups are widely distributed on the sidewall of SWNTs. Thus the difference is not due to significant difference in substituent concentration but on substituent distribution, while Raman shows different D:G ratio.

3.4.3.2 Infra red spectroscopy

IR spectroscopy is useful in characterizing functional groups bound to SWNTs. A variety of organic functional groups on sidewall of SWNTs have been identified by IR, such as COOH(R), -CH_2, -CH_3, -NH_2, -OH, etc. However, it is difficult to get direct functionalization information from IR spectroscopy. The C-F group has been identified by IR in F-SWNTs. However, C-C, C-N, C-O groups associated with the side-wall functionalization have not been observed in the appropriately functionalized SWNTs.

3.4.3.3 UV/visible spectroscopy

UV/visible spectroscopy is maybe the most accessible technique that provides information about the electronic states of SWNTs, and hence functionalization. The absorption spectrum shows bands at *ca.* 1400 nm and 1800 nm for pristine SWNTs. A complete loss of such structure is observed after chemical alteration of SWNTs sidewalls. However, such information is not quantitative and also does not show what type of functional moiety is on the sidewall of SWNTs.

3.4.3.4 Nuclear magnetic resonance

NMR can be considered as a "new" characterization technique as far as SWNTs are concerned. Solution state NMR is limited for SWNT characterization because low solubility and slow tumbling of the SWNTs results in broad spectra. Despite this issue, there are still solution ^{1}H NMR reported of SWNTs functionalized by carbenes, nitrenes and azomethine ylides because of the high solubility of derivatized SWNTs. However, proof of covalent functionalization cannot be obtained from the ^{1}H NMR. As an alternative, solid state ^{13}C NMR has been employed to characterize several functionalized SWNTs and show successful observation of sidewall organic functional groups, such as carboxylic and alkyl groups. But there has been a lack of direct evidence of sp^3 carbons on the sidewall of SWNTs that provides information of covalent functionalization.

Solid state ^{13}C NMR has been successfully employed in the characterization of F-SWNTs through the direct observation of the sp^3C-F carbons on sidewall of SWNTs. This methodology has been transferred to more complicated systems; however, it has been found that longer side chain length increases the ease to observe sp^3C-X sidewall carbons.

Solid state NMR is a potentially powerful technique for characterizing functionalized SWNTs because molecular dynamic information can also be obtained. Observation that higher side chain mobility can be achieved by using a longer side chain length offers a method of exploring functional group conformation. In fact, there have been reports using solid state NMR to study molecular mobility of functionalized multi-walled carbon nanotubes.

3.4.4 Microscopy

AFM, TEM and STM are useful imaging techniques to characterize functionalized SWNTs. As techniques, they are routinely used to provide an "image" of an individual nanoparticle, as opposed to an average of all the particles.

3.4.4.1 Atomic force microscopy

AFM shows morphology on the surface of SWNTs. The height profile on AFM is often used to show presence of functional groups on sidewall of SWNTs. Individual SWNTs can be probed by AFM and sometimes provide information of dispersion and exfoliation of bundles. Measurement of heights along an individual SWNT can be correlated with the substituent group, i.e., the larger an alkyl chain of a sidewall substituent the greater the height measured. AFM does not distinguish whether those functional groups are covalently attached or physically adsorbed on the surface of SWNTs.

3.4.4.2 Transmission electron microscopy

TEM can be used to directly image SWNTs and at high resolution clearly shows the sidewall of individual SWNT. However, the resolution of TEM is not sufficient to directly observe covalent attachment of chemical modification moieties, i.e., to differentiate between sp^2 and sp^3 carbon atoms. TEM can be used to provide information of functionalization effect on dispersion and exfoliation of ropes.

Samples are usually prepared from very dilute concentration of SWNTs. Sample needs to be very homogeneous to get reliable data. As with AFM, TEM only shows a very small portion of sample, using them to characterize functionalized SWNTs and evaluate dispersion of samples in solvents needs to be done with caution.

3.4.4.3 Scanning tunneling microscopy

STM offers a lot of insight on structure and surface of functionalized SWNTs. STM measures electronic structure, while sometimes the topographical information can be indirectly inferred by STM images. STM has been used to characterize F-SWNTs gold-marked SWNTs, and organic functionalized SWNTs. Distribution of functional groups can be inferred from STM images since the location of a substituent alters the localized electronic structure of the tube. STM images the position/location of chemical changes to the SWNT structure. The band-like structure of F-SWNTs was first disclosed by STM.

STM has the same problem that is inherent with AFM and TEM, that when using small sample size, the result may not be statistically relevant. Also, chemical identity of the features on SWNTs cannot be determined by STM; rather, they have to be identified by spectroscopic methods such as IR or NMR. A difficulty with STM imaging is that the sample has to be conductive, thus deposition of the SWNT onto a gold (or similar) surface is necessary.

3.4.5 Bibliography

- L. B. Alemany, L. Zhang, L. Zeng, C. L. Edwards, and A. R. Barron, *Chem. Mater.*, 2007, **19**, 735.
- J. L. Bahr and J. M. Tour, *J. Mater. Chem.*, 2002, **12**, 1952.
- M. S. Dresselhaus, G. Dresselhaus, and A. Jorio, *J. Phys. Chem. C*, 2007, **111**, 17887.
- A. Hirsch, *Angew. Chem. Int. Ed.*, 2002, **41**, 1853.
- M. Holzinger, J. Abraham, P. Whelan, R. Graupner, L. Ley, F. Hennrich, M. Kappes, and A. Hirsch, *J. Am. Chem. Soc.*, 2003, **125**, 8566.
- K. F. Kelly, I. W. Chiang, E. T. Mickelson, R. H. Hauge, J. L. Margrave, X. Wang, G. E. Scuseria, C. Radloff, and N. J. Halas, *Chem. Phys. Lett.*, 1999, **313**, 455.
- V. N. Khabashesku, W. E. Billups, and J. L. Margrave, *Acc. Chem. Res.*, 2002, **35**, 1087.
- F. Liang, L. B. Alemany, J. M. Beach, and W. E. Billups, *J. Am. Chem. Soc.*, 2005, **127**, 13941.
- D. Tasis, N. Tagmatarchis, A. Bianco, and M. Prato, *Chem. Rev.*, 2006, **106**, 1105.
- H-L. Wu, Y-T. Yang, C-C. M. Ma, and H-C. Kuan, *J. Polym. Sci. A. Polym. Chem.*, 2005, 6084.
- L. Zeng, L. Zhang, and A. R. Barron, *Nano Lett.*, 2005, **5**, 2001.
- L. Zhang, J. Zhang, N. Schmandt, J. Cratty, V. N. Khabashesku, K. F. Kelly, and A. R. Barron, *Chem. Commun.*, 2005, 5429.

3.5 Characterization of Single-Walled Carbon Nanotubes by Raman Spectroscopy[10]

3.5.1 Introduction

Carbon nanotubes (CNTs) have proven to be a unique system for the application of Raman spectroscopy, and at the same time Raman spectroscopy has provided an exceedingly powerful tool useful in the study of the vibrational properties and electronic structures of CNTs. Raman spectroscopy has been successfully applied for studying CNTs at single nanotube level.

The large van der Waals interactions between the CNTs lead to an agglomeration of the tubes in the form of bundles or ropes. This problem can be solved by wrapping the tubes in a surfactant or functionalizing the SWNTs by attaching appropriate chemical moieties to the sidewalls of the tube. Functionalization causes a local change in the hybridization from sp^2 to sp^3 of the side-wall carbon atoms, and Raman spectroscopy can be used to determine this change. In addition information on length, diameter, electronic type (metallic or semiconducting), and whether nanotubes are separated or in bundle can be obtained by the use of Raman spectroscopy. Recent progress in understanding the Raman spectra of single walled carbon nanotubes (SWNT) have stimulated Raman studies of more complicated multi-wall carbon nanotubes (MWNT), but unfortunately quantitative determination of the latter is not possible at the present state of art.

3.5.2 Characterizing SWNTs

Raman spectroscopy is a single resonance process, i.e., the signals are greatly enhanced if either the incoming laser energy (E_{laser}) or the scattered radiation matches an allowed electronic transition in the sample. For this process to occur, the phonon modes are assumed to occur at the center of the Brillouin zone (q = 0). Owing to their one dimensional nature, the Π-electronic density of states of a perfect, infinite, SWNTs form sharp singularities which are known as van Hove singularities (vHs), which are energetically symmetrical with respect to Fermi level (E_f) of the individual SWNTs. The allowed optical transitions occur between matching vHs of the valence and conduction band of the SWNTs, i.e., from first valence band vHs to the first conduction band vHs (E_{11}) or from the second vHs of the valence band to the second vHs of the conduction band (E_{22}). Since the quantum state of an electron (k) remains the same during the transition, it is referred to as k-selection rule.

The electronic properties, and therefore the individual transition energies in SWNTs are given by their structure, i.e., by their chiral vector that determines the way SWNT is rolled up to form a cylinder. Figure 3.21 shows a SWNT having vector R making an angle θ, known as the chiral angle, with the so-called zigzag or r_1 direction.

[10] This content is available online at <http://cnx.org/content/m22925/1.2/>.

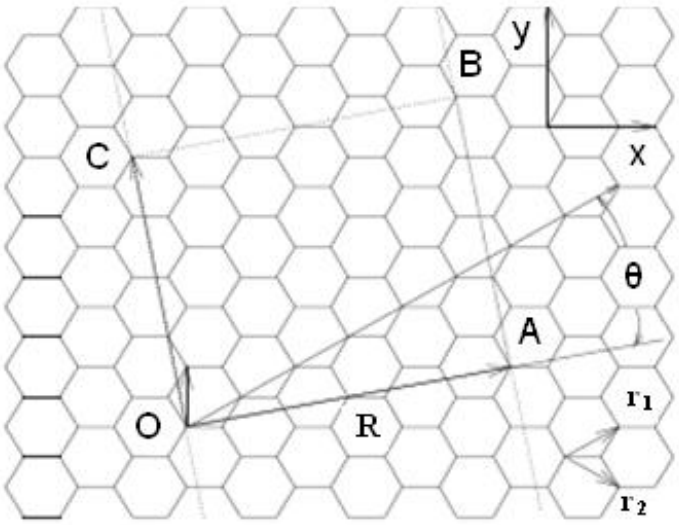

Figure 3.21: The unrolled honeycomb lattice of a nanotube. When the sites O and A, and the sites B and C are connected, a portion of a graphene sheet can be rolled seamlessly to form a SWNT. The vectors OA and OB define the chiral vector R of the nanotube, respectively. The rectangle OABC defines the unit cell if the nanotube. The figure is constructed for (n,m) = (4,2) nanotube. Adapted from M. S. Dresselhaus, G. Dresselhaus, R. Saito, and A. Jorio, *Physics Reports*, 2004, **2**, 47.

Raman spectroscopy of an ensemble of many SWNTs having different chiral vectors is sensitive to the subset of tubes where the condition of allowed transition is fulfilled. A 'Kataura-Plot' gives the allowed electronic transition energies of individual SWNTs as a function of diameter d, hence information on which tubes are resonant for a given excitation wavelength can be inferred. Since electronic transition energies vary roughly as $1/d$, the question whether a given laser energy probes predominantly semiconducting or metallic tubes depends on the mean diameter and diameter distribution in the SWNT ensemble. However, the transition energies that apply to an isolated SWNT do not necessarily hold for an ensemble of interacting SWNTs owing to the mutual van der Waals interactions.

Figure 3.22 shows a typical Raman spectrum from 100 to 3000 cm^{-1} taken of SWNTs produced by catalytic decomposition of carbon monoxide (HiPco-process). The two dominant Raman features are the radial breathing mode (RBM) at low frequencies and tangential (G-band) multifeature at higher frequencies. Other weak features, such as the disorder induced D-band and the G' band (an overtone mode) are also shown.

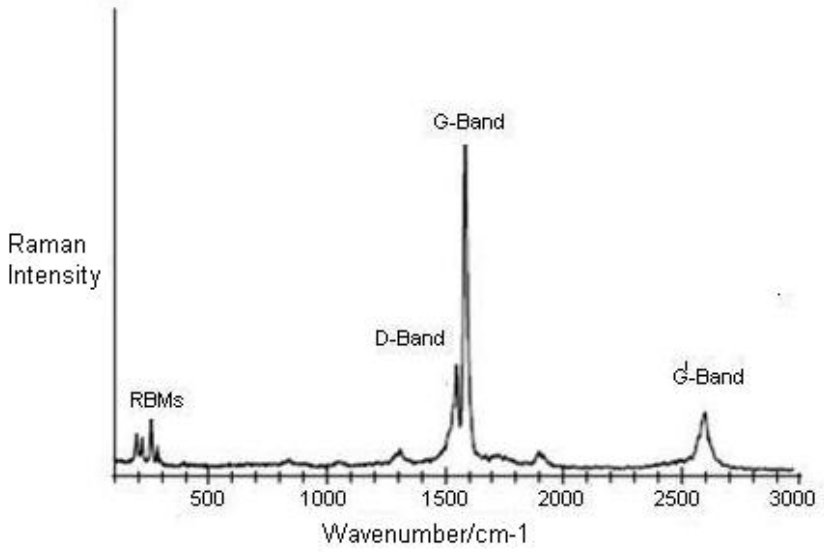

Figure 3.22: Raman spectrum of HiPco SWNTs using a laser of wavelength of $\lambda_{exc} = 633$ nm. Adapted from R. Graupner, *J. Raman Spectrosc.*, 2007, **38**, 673.

3.5.3 Modes in the Raman spectra of SWNTs

3.5.3.1 Radial breathing modes (RBMs)

Out of all Raman modes observed in the spectra of SWNTs, the radial breathing modes are unique to SWNTs. They appear between 150 $cm^{-1} < \omega_{RBM} < 300$ cm^{-1} from the elastically scattered laser line. It corresponds to the vibration of the C atoms in the radial direction, as if the tube is breathing (Figure 3.23). An important point about these modes is the fact that the energy (or wavenumber) of these vibrational modes depends on the diameter (d) of the SWNTs, and not on the way the SWNT is rolled up to form a cylinder, i.e., they do not depend on the θ of the tube.

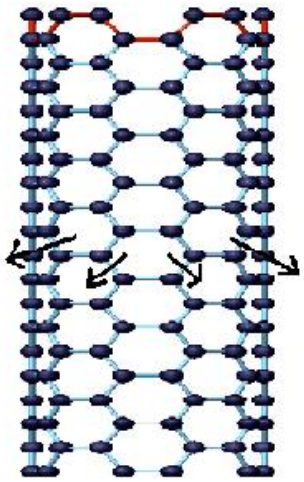

Figure 3.23: Schematic picture showing vibration for RBM. Adapted from A. Jorio, M. A. Pimenta, A. G. S. Filho, R. Saito, G. Dresselhaus, and M. S. Dresselhaus, *New J. Phys.*, 2003, **5**, 139.

These features are very useful for characterizing nanotube diameters through the relation $\omega_{\mathrm{RBM}} = \mathrm{A}/d + \mathrm{B}$, where A and B are constants and their variations are often attributed to environmental effects, i.e., whether the SWNTs are present as individual tubes wrapped in a surfactant, isolated on a substrate surface, or in the form of bundles. However, for typical SWNT bundles in the diameter range, $d = 1.5 \pm 0.2$ nm, A = 234 cm^{-1} nm and B = 10 cm^{-1} (where B is an upshift coming from tube-tube interactions). For isolated SWNTs on an oxidized Si substrate, A= 248 cm^{-1} nm and B = 0. As can be seen from Figure 3.24, the relation $\omega_{\mathrm{RBM}} = \mathrm{A/d} + \mathrm{B}$ holds true for the usual diameter range i.e., when d lies between 1 and 2 nm. However, for d less than 1 nm, nanotube lattice distortions lead to chirality dependence of ω_{RBM} and for large diameters tubes when, d is more than 2 nm the intensity of RBM feature is weak and is hardly observable.

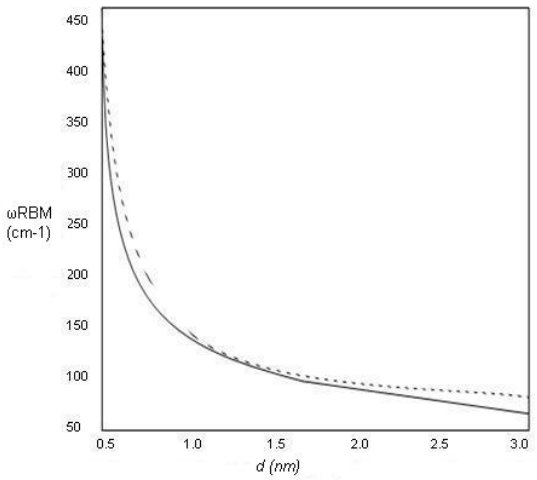

Figure 3.24: RBM frequencies $\omega_{\mathrm{RBM}} = \mathrm{A}/d + \mathrm{B}$ versus nanotube diameter for (i) A = 234 cm^{-1} nm and B = 10 cm^{-1}, for SWNT bundles (dashed curve); (ii) A = 248 cm^{-1} nm and B = 0, for isolated SWNTs (solid curve). Adapted from A. Jorio, M. A. Pimenta, A. G. S. Filho, R. Saito, G. Dresselhaus, and M. S. Dresselhaus, *New J. Phys.*, 2003, **5**, 139.

Hence, a single Raman measurement gives an idea of the tubes that are in resonance with the laser line, but does not give a complete characterization of the diameter distribution of the sample. However, by taking Raman spectra using many laser lines, a good characterization of the diameter distributions in the sample can be obtained. Also, natural line widths observed for isolated SWNTs are $\omega_{\mathrm{RBM}} = 3$ cm^{-1}, but as the tube diameter is increased, broadening is observed which is denoted by Γ_{RBM}. It has been observed that for $d > 2$ nm, $\Gamma_{\mathrm{RBM}} > 20$ cm^{-1}. For SWNT bundles, the line width does not reflect Γ_{RMB}, it rather reflects an ensemble of tubes in resonance with the energy of laser.

3.5.3.1.1 Variation of RBM intensities upon functionalization

Functionalization of SWNTs leads to variations of relative intensities of RBM compared to the starting material (unfunctionalized SWNTs). Owing to the diameter dependence of the RBM frequency and the resonant nature of the Raman scattering process, chemical reactions that are sensitive to the diameter as well as the electronic structure, i.e., metallic or semiconducting of the SWNTs can be sorted out. The difference in Raman spectra is usually inferred by thermal defunctionalization, where the functional groups are removed by annealing. The basis of using annealing for defunctionalizing SWNTs is based on the fact that annealing restores the Raman intensities, in contrast to other treatments where a complete disintegration of the SWNTs occurs. Figure 3.25 shows the Raman spectra of the pristine, functionalized and annealed SWNTs. It can be observed that the absolute intensities of the radial breathing modes is drastically reduced after functionalization. This decrease can be attributed to vHs, which themselves are a consequence of translational symmetry of the SWNTs. Since the translational symmetry of the SWNTs is broken as a result of irregular distribution of the sp^3-sites due to the functionalization, these vHs are broadened and strongly reduced in intensity. As a result, the resonant Raman cross section of all modes is strongly reduced as well.

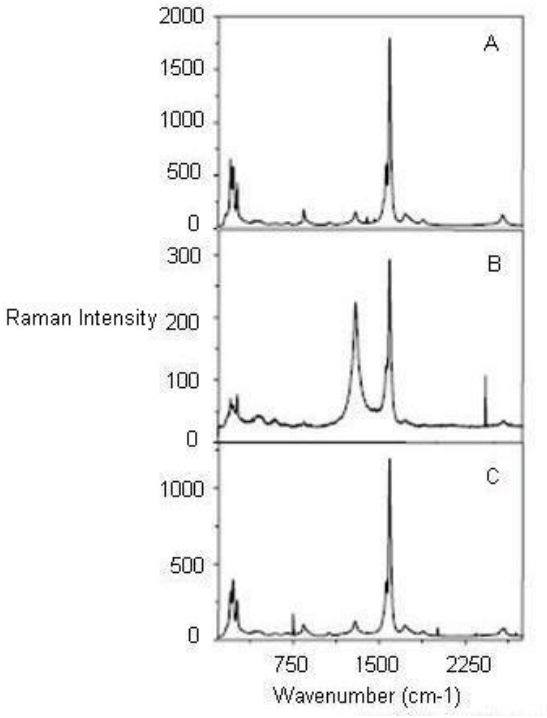

Figure 3.25: Raman spectra of sidewall functionalized SWNTs of (A) pristine material, (B) functionalized SWNTs, and (C) after annealing at 750 °C in Ar. Adapted from R. Graupner, *J. Raman Spectrosc.*, 2007, **38**, 673.

For an ensemble of functionalized SWNTs, a decrease in high wavenumber RBM intensities has been observed which leads to an inference that destruction of small diameter SWNT takes place. Also, after prolonged treatment with nitric acid and subsequent annealing in oxygen or vacuum, diameter enlargement of SWNTs is observed from the disappearance of RBMs from small diameter SWNTs and the appearance of new RBMs characteristic of SWNTs with larger diameters. In addition, laser irradiation seems to damage preferentially small diameter SWNTs. In all cases, the decrease of RBM intensities is either attributed to the complete disintegration of SWNTs or reduction in resonance enhancement of selectively functionalized SWNTs. However, change in RBM intensities can also have other reasons. One reason is doping induced bleaching of electronic transitions in SWNTs. When a dopant is added, a previously occupied electronic state can be filled or emptied, as a result of which E_f in the SWNTs is shifted. If this shift is large enough and the conduction band vHs corresponding to the respective E_{ii} transition that is excited by the laser light gets occupied (n-type doping) or the valence band vHs is emptied (p-type doping), the resonant enhancement is lost as the electronic transitions are quenched.

Sample morphology has also seen to affect the RBMs. The same unfunctionalized sample in different aggregation states gives rise to different spectra. This is because the transition energy, E_{ii} depends on the aggregation state of the SWNTs.

3.5.3.2 Tangential modes (G-band)

The tangential modes are the most intensive high-energy modes of SWNTs and form the so-called G-band, which is typically observed at around 1600 cm^{-1}. For this mode, the atomic displacements occur along the cicumferential direction (Figure 3.26). Spectra in this frequency can be used for SWNT characterization, independent of the RBM observation. This multi-peak feature can, for example, also be used for diameter characterization, although the information provided is less accurate than the RBM feature, and it gives information about the metallic character of the SWNTs in resonance with laser line.

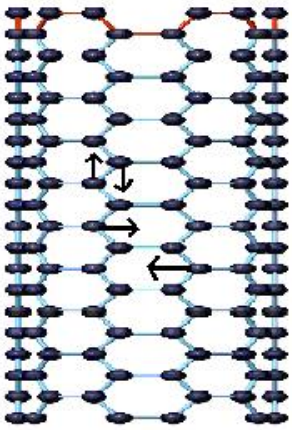

Figure 3.26: Schematic picture showing the atomic vibrations for the G-band. Adapted from A. Jorio, M. A. Pimenta, A. G. S. Filho, R. Saito, G. Dresselhaus, and M. S. Dresselhaus, *New J. Phys.*, 2003, **5**, 139.

The tangential modes are useful in distinguishing semiconducting from metallic SWNTs. The difference is evident in the G- feature (Figure 3.27 and Figure 3.28) which broadens and becomes asymmetric for metallic SWNTs in comparison with the Lorentzian lineshape for semiconducting tubes, and this broadening is related to the presence of free electrons in nanotubes with metallic character. This broadened G-feature is usually fit using a Breit-Wigner-Fano (BWF) line that accounts for the coupling of a discrete phonon with a continuum related to conduction electrons. This BWF line is observed in many graphite-like materials with metallic character, such as n-doped graphite intercalation compounds (GIC), n-doped fullerenes, as well as metallic SWNTs. The intensity of this G- mode depends on the size and number of metallic SWNTs in a bundle (Figure 3.29).

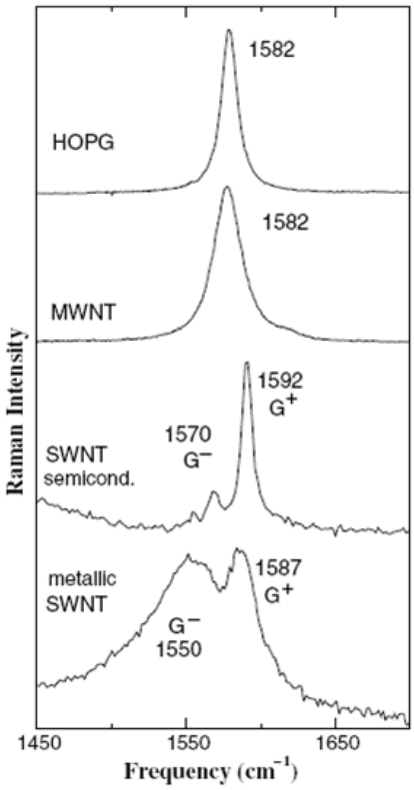

Figure 3.27: G-band for highly ordered pyrolytic graphite (HOPG), MWNT bundles, one isolated semiconducting SWNT and one isolated metallic SWNT. The multi-peak G-band feature is not clear for MWNTs due to the large tube size. A. Jorio, M. A. Pimenta, A. G. S. Filho, R. Saito, G. Dresselhaus, and M. S. Dresselhaus, *New J. Phys.*, 2003, **5**, 139. Copyright Institute of Physics (2005).

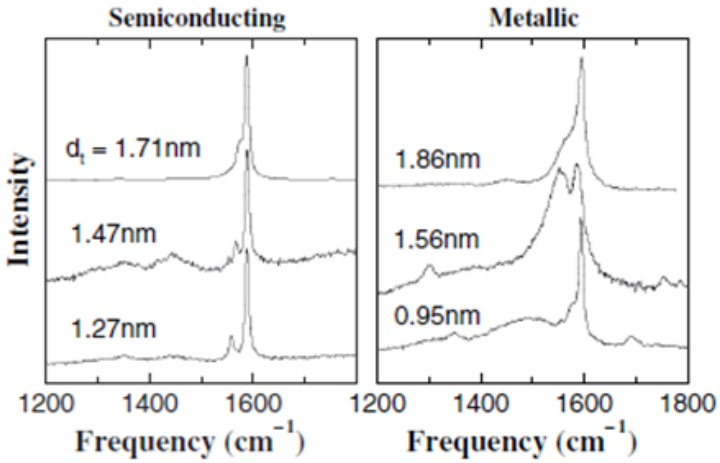

Figure 3.28: Raman signal from three isolated semiconducting and three isolated metallic SWNTs showing the G-and D-band profiles. SWNTs in good resonance (strong signal with low signal to noise ratio) show practically no D-band. A. Jorio, M. A. Pimenta, A. G. S. Filho, R. Saito, G. Dresselhaus, and M. S. Dresselhaus, *New J. Phys.*, 2003, **5**, 139. Copyright Institute of Physics (2005).

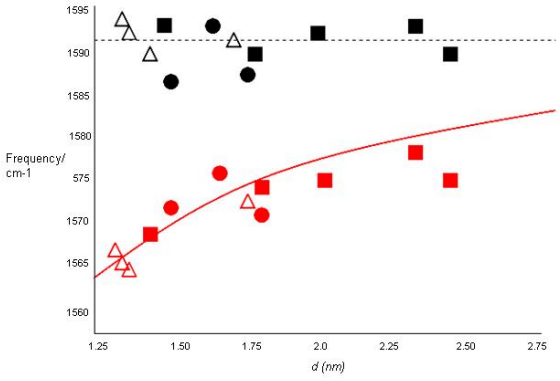

Figure 3.29: Dependence of G+ (black symbols) and G- (red symbols) frequencies as a function of diameter. Adapted from M. Paillet, T. Michel, J. C. Meyer, V. N. Popov, L. Henrad, S. Roth, and J. L. Sauvajol, *Phy. Rev. Lett.*, 2006, **96**, 257401.

3.5.3.2.1 Change of G-band line shape on functionalization

Chemical treatments are found to affect the line shape of the tangential line modes. Selective functionalization of SWNTs or a change in the ratio of metallic to semiconducting SWNTs due to selective etching is responsible for such a change. According to Figure 3.30, it can be seen that an increase or decrease of the BWF line shape is observed depending on the laser wavelength. At λ_{exc} = 633 nm, the preferentially functionalized small diameter SWNTs are semiconducting, therefore the G-band shows a decrease in the BWG asymmetry. However, the situation is reversed at 514 nm, where small metallic tubes are probed. BWF resonance intensity of small bundles increases with bundle thickness, so care should be taken that the effect ascribed directly to functionalization of the SWNTs is not caused by the exfoliation of the previously bundles SWNT.

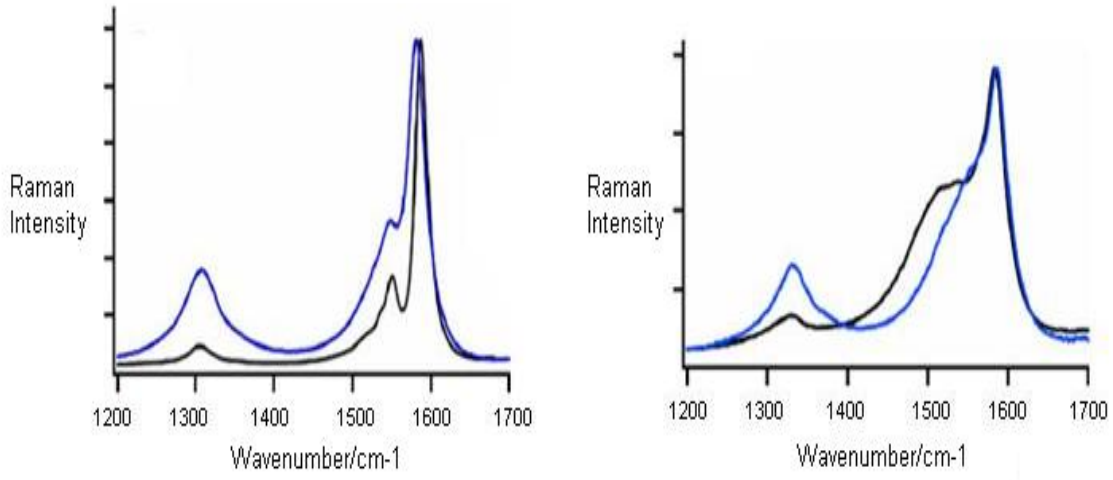

Figure 3.30: G-and D-band spectra of pristine (black) and ozonized (blue) SWNTs at 633 nm (left) and 514 nm (right) excitation. Adapted from R. Graupner, *J. Raman Spectrosc.*, 2007, **38**, 673.

3.5.3.3 Disorder-induced D-band

This is one of the most discussed modes for the characterization of functionalized SWNTs and is observed at 1300-1400 cm^{-1}. Not only for functionalized SWNTs, D-band is also observed for unfunctionalized SWNTs. From a large number of Raman spectra from isolated SWNTs, about 50% exhibit observable D-band signals with weak intensity (Figure 3.28). A large D-peak compared with the G-peak usually means a bad resonance condition, which indicates the presence of amorphous carbon.

The appearance of D-peak can be interpreted due to the breakdown of the k-selection rule. It also depends on the laser energy and diameter of the SWNTs. This behavior is interpreted as a double resonance effect, where not only one of the direct, k-conserving electronic transitions, but also the emission of phonon is a resonant process. In contrast to single resonant Raman scattering, where only phonons around the center of the Brillouin zone (q = 0) are excited, the phonons that provoke the D-band exhibit a non-negligible q vector. This explains the double resonance theory for D-band in Raman spectroscopy. In few cases, the overtone of the D-band known as the G'-band (or D*-band) is observed at 2600-2800 cm^{-1}, and it does not

require defect scattering as the two phonons with q and –q are excited. This mode is therefore observed independent of the defect concentration.

The presence of D-band cannot be correlated to the presence of various defects (such as hetero-atoms, vacancies, heptagon-pentagon pairs, kinks, or even the presence of impurities, etc). Following are the two main characteristics of the D-band found in carbon nanotubes:

1. Small linewidths: Γ_D values for SWNTs range from 40 cm^{-1} down to 7 cm^{-1}.
2. Lower frequencies: D-band frequency is usually lower than the frequency of sp^2-based carbons, and this downshift of frequency shows $1/d$ dependence.

3.5.3.3.1 D-Band intensity as a measure of functionalization versus defect density

Since D-peak appears due to the presence defects, an increase in the intensity of the band is taken as a fingerprint for successful functionalization. But, whether D-band intensity is a measure of degree of functionalization or not is still sure. So, it is not correct to correlate D-peak intensity or D-peak area to the degree of functionalization. From Figure 3.31, it can be observed that for lower degree of functionalization, intensity of the D-band scales linearly with defect density. As the degree of functionalization is further increased, both D and G-band area decrease, which is explained by the loss of resonance enhancement due to functionalization. Also, normalization of the D-peak intensity to the G-band in order to correct for changes in resonance intensities also leads to a decrease for higher densities of functional groups.

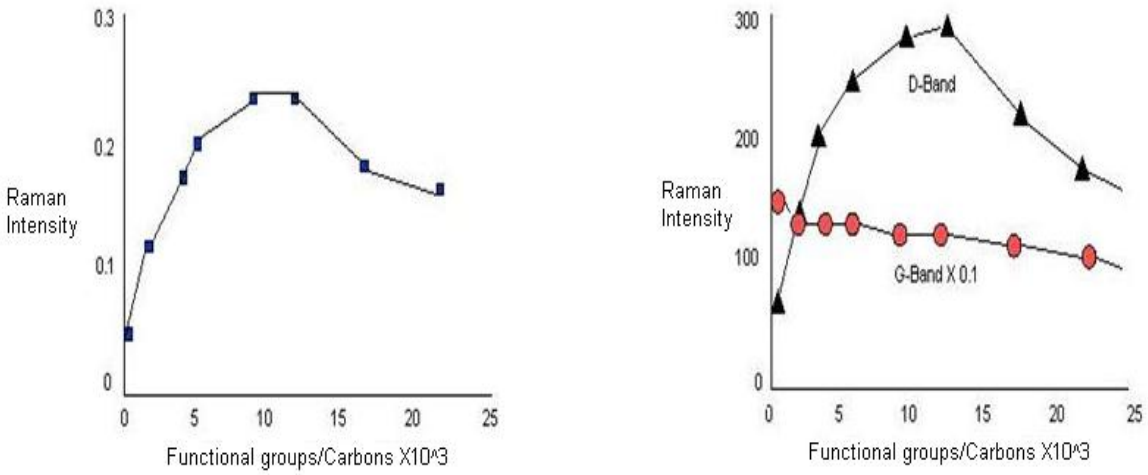

Figure 3.31: The left figure shows the intensity ratio I_D/I_G and the right figure shows D- and G-band intensity at $\lambda_{exc} = 532$ nm with respect to degree of functionalization using diazonium reagents. Adapted from R. Graupner, *J. Raman Spectrosc.*, 2007, **38**, 673.

3.5.3.4 Limitations of Raman spectroscopy

Though Raman spectroscopy has provides an exceedingly important tool for characterization of SWNTs, however, it suffers from few serious limitations. One of the main limitations of Raman spectroscopy is that it does not provide any information about the extent of functionalization in the SWNTs. The presence of

D-band indicates disorder, i.e. side wall distribution, however it cannot differentiate between the number of substituents and their distribution. Following are the two main limitations of Raman Spectroscopy:

3.5.3.4.1 Quantification of substituents

This can be illustrated by the following examples. Purified HiPco tubes may be fluorinated at 150 °C to give F-SWNTs with a C:F ratio of approximately 2.4:1. The Raman spectra (using 780 nm excitation) for F-SWNTs shows in addition to the tangential mode at ~1587 cm^{-1} an intense broad D (disorder) mode at ~ 1295 cm^{-1} consistent with the side wall functionalization. Irrespective of the arrangements of the fluorine substituents, thermolysis of F-SWNTs results in the loss of fluorine and the re-formation of unfunctionalized SWNTs alnog with their cleavage into shorter length tubes. As can be seen from Figure 3.32, the intensity of the D-band decreases as the thermolysis temperature increases. This is consistent with the loss of F-substituents. The G-band shows a concomitant sharpening and increase in intensity.

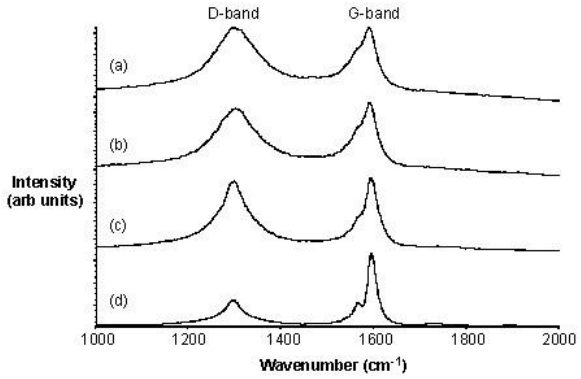

Figure 3.32: Raman spectra of F-SWNTs (a) as prepared at 150 °C and after heating to (b) 400, (c) 450 and (d) 550 °C.

As discussed above, the presence of a significant D mode has been the primary method for determining the presence of sidewall functionalization. It has been commonly accepted that the relative intensity of the D mode *versus* the tangential G mode is a quantitative measure of level of substitution. However, as discussed below, the G:D ratio is also dependent on the distribution of substituents. Using Raman spectroscopy in combination with XPS analysis of F-SWNTs that have been subjected to thermolysis at different temperatures, a measure of the accuracy of Raman as a quantitative tool for determining substituent concentration can be obtained. As can be seen from Figure 3.33, there is essentially no change in the G:D band ratio despite a doubling amount of functional groups.Thus, at low levels of functionalization the use of Raman spectroscopy to quantify the presence of fluorine substituents is a clearly suspect.

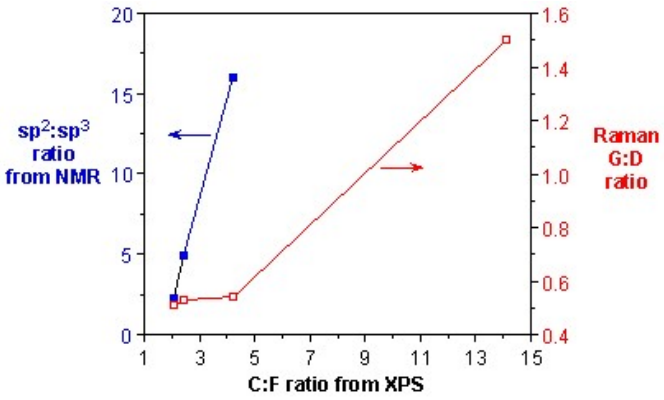

Figure 3.33: C(sp^2):C-F(sp^3) ratio (blue) and Raman G-band:D-band ratio (red) as a function of C:F ratio from XPS.

On the basis of above data it can be concluded that Raman spectroscopy does not provide an accurate quantification of small differences at low levels of functionalization, whereas when a comparison between samples with high levels of functionalization or large differences in degree of functionalization is requires Raman spectroscopy provides a good quantification.

3.5.3.4.2 Number versus distribution

Fluorinated nanotubes may be readily functionalized by reaction with the appropriate amine in the presence of base according to the scheme shown in Figure 3.34.

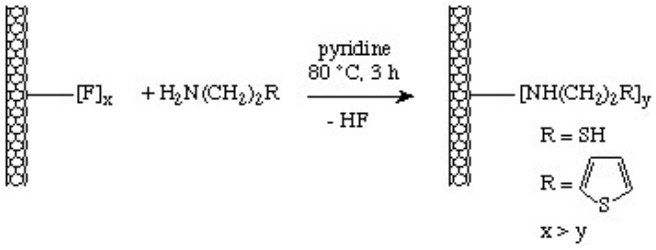

Figure 3.34: Synthesis of functionalized SWNTs.

When the Raman spectra of the functionalized SWNTs is taken (Figure 3.35), it is found out that the relative intensity of the disorder D-band at ~1290 cm^{-1} *versus* the tangential G-band (1500 - 1600 cm^{-1}) is much higher for thiophene-SWNT than thiol-SWNT. If the relative intensity of the D mode is the measure of the level of substitution, it can be concluded that there are more number of thiophene groups present per C than thiol groups. However, from the TGA weight loss data the SWNT-C:substituent ratios are calculated to be 19:1 and 17.5:1. Thus, contrary to the Raman data the TGA suggest that the number of substituents per C (in the SWNT) is actually similar for both substituents.

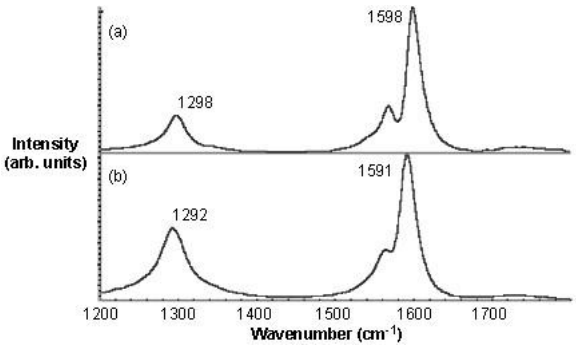

Figure 3.35: Raman spectrum of (a) thiol-SWNT and (b)thiophene-SWNT using 780 nm excitation showing the relative intensity of D-band at ~1300 cm^{-1} versus the G-band at ~1590 cm^{-1}.

This result would suggest that Raman spectroscopy is potentially unsuccessful in correctly providing the information about the number of substituents on the SWNTs. Subsequent imaging of the functionalized SWNTs by STM showed that the distribution of the functional groups was the difference between the thiol and thiphene functionalized SWNTs Figure 3.36. Thus, relative ratio of the D- and G-bands is a measure of concentration and distribution of functional groups on SWNTs.

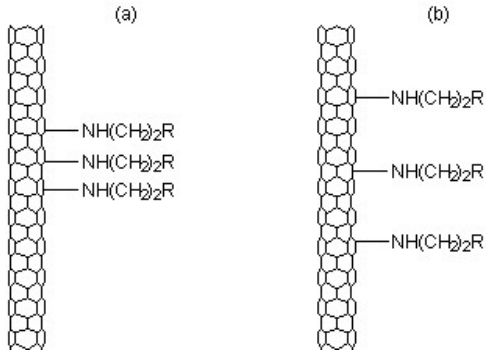

Figure 3.36: Schematic representation of the functional group distribution for (a) thiol-SWNT and (b) thiophene-SWNT.

3.5.4 Multi-walled carbon nanotubes (MWNTs)

Most of the characteristic differences that distinguish the Raman spectra in SWNTs from the spectra of graphite are not so evident for MWNTs. It is because the outer diameter for MWNTs is very large and the ensemble of CNTs in them varies from small to very large. For example, the RBM Raman feature associated with a small diameter inner tube (less than 2 nm) can sometimes be observed when a good resonance condition is established, but since the RBM signal from large diameter tubes is usually too weak

to be observable and the ensemble average of inner tube diameter broadens the signal, a good signal is not observed. However, when hydrogen gas in the arc discharge method is used, a thin innermost nanotube within a MWNT of diameter 1 nm can be obtained which gives strong RBM peaks in the Raman spectra.

Thereas the G+ - G- splitting is large for small diameter SWNT, the corresponding splitting of the G-band in MWNTs is both small in intensity and smeared out due to the effect of the diameter distribution. Therefore the G-band feature predominantly exists a weakly asymmetric characteristic lineshape, and a peak appearing close to the graphite frequency of 1582 cm^{-1}.however for isolated MWNTs prepared in the presence of hydrogen gas using the arc discharge method, it is possible to observe multiple G-band splitting effects even more clearly than for the SWNTs, and this is because environmental effects become relatively small for the innermost nanotube in a MWNT relative to the interactions occurring between SWNTs and different environments. The Raman spectroscopy of MWNTs has not been well investigated up to now. The new directions in this field are yet to be explored.

3.5.5 Bibliography

- R. Graupner, *J. Ramn Spectrosc.*, 2007, **38**, 673.
- S. Costa, B. Palen, M. Kruszynska, A. Bachmatiuk, and R.J. Kalenczuk, *Mat. Sci. Poland*, 2008, **26**, 433.
- M. Paillet, T. Michel , J. C. Meyer, V. N. Popov, L. Henrad, S. Roth, and J. L. Sauvajol, *Phy. Rev. Lett.*, 2006, **96**, 257401.
- L. Zhang, J. Zhang, N. Schmandt, J. Cratty, V. N. Khabashesku, K. F. Kelly, and A. R. Barron, *Chem. Commun.*, 2005, 5429.
- L. B. Alemany, L. Zhang, L. Zeng, C. L. Edwards, and A. R. Barron, *Chem. Mater.*, 2006, **19**, 735.
- M. S. Dresselhaus, G. Dresselhaus, R. Saito, and A. Jorio, *J. Phys. Rep.*, 2005, **2**, 47.
- A. Jorio, M. A. Pimenta, A. G. S. Filho, R. Saito, G. Dresselhaus, and M. S. Dresselhaus, *New J. Phys.*, 2003, **5**, 139.

3.6 Mossbauer Analysis of Iron Oxide Nanoparticles[11]

3.6.1 Spectra and formula calculations

Due to the potential applications of magnetite nanoparticles (Fe_3O_4, nMag) many methods have been devised for its synthesis. However, stoichiometric Fe_3O_4 is not always achieved by different synthetic methods. B-site vacancies introduced into the cubic inverse spinel crystal structure of nMag result in nonstoichiometric iron oxide of the formula $(Fe^{3+})_A(Fe_{(1-3x)}{}^{2+}\ Fe_{(1+2X)}{}^{3+}Ø_x)_BO_4$ where Ø represents B-site vacancy. The magnetic susceptibility which is key to most nMag applications decreases with increased B-site vacancy hence the extent of B-site vacancy is important. The very high sensitivity of the Mossbauer spectrum to the oxidation state and site occupancy of Fe^{3+} in cubic inverse spinel iron oxides makes Mossbauer spectroscopy valuable for addressing the issues of whether or not the product of a synthetic method is actually nMag and the extent of B-site vacancy.

As with most analysis using multiple instrumental methods in conjunction is often helpful. This is exemplified by the use of XRD along with Mossbauer spectroscopy in the following analysis. Figure 3.37 shows the XRD results and Mossbauer spectra "magnetite" samples prepared by a Fe^{2+}/Fe^{3+} co-precipitation (Mt025), hematite reduction by hydrogen (MtH2) and hematite reduction with coal(MtC). The XRD analysis shows MtH2 and MT025 exhibiting only magnetite peaks while MtC shows the presence of magnetite, maghemite, and hematite. This information becomes very useful when fitting peaks to the Mossbauer spectra because it gives a chemical basis for peak fitting parameters and helps to fit the peaks correctly.

[11] This content is available online at <http://cnx.org/content/m22619/1.3/>.

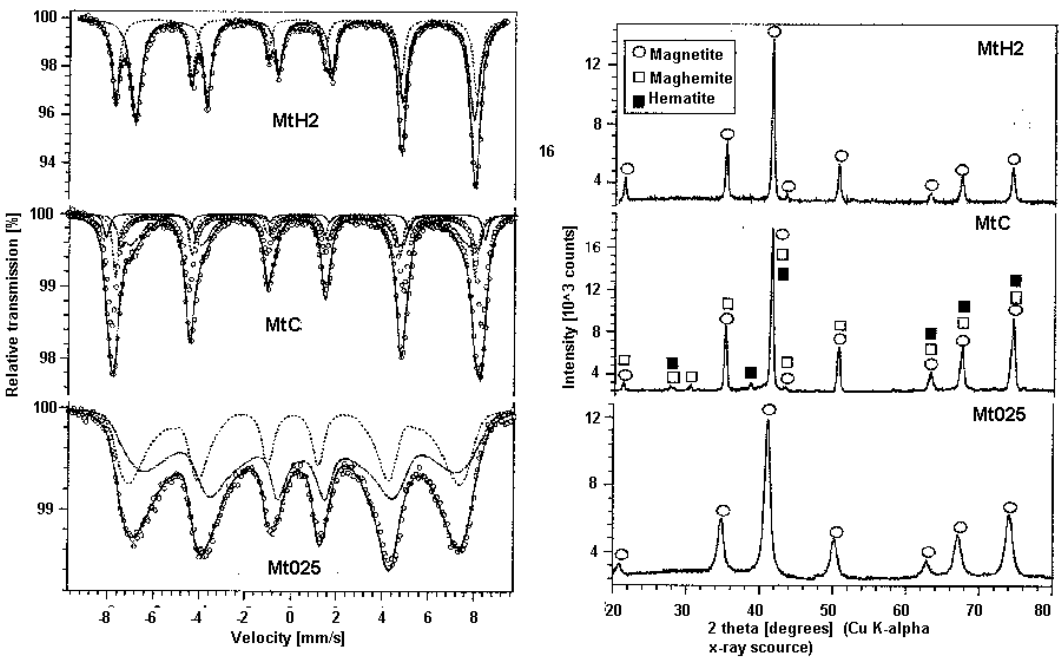

Figure 3.37: Mossbauer spectra (left) and corresponding XRD spectra of iron oxide sample prepared by different methods. Adapted from A. L. Andrade, D. M. Souza, M. C. Pereira, J. D. Fabris, and R. Z. Domingues. *J. Nanosci. Nanotechnol.*, 2009, **9**, 2081.

Being that the iron occupies two local environments, the A-site and B site, and two species (Fe^{2+} and Fe^{3+}) occupy the B-site one might expect the spectrum to be a combination of 3 spectra, however delocalization of electrons or electron hopping between Fe^{2+} and Fe^{3+} in the B site causes the nuclei to sense an average valence in the B site thus the spectrum are fitted with two curves accordingly. This is most easily seen in the Mt025 spectrum. The two fitted curves correspond to Fe^{3+} in the A-site and mixed valance $Fe^{2.5+}$ in the B-site. The isomer shift of the fitted curves can be used to determined which curve corresponds to which valence. The isomer shift relative to the top fitted curve is reported to be 0.661 and the bottom fitted curve is 0.274 relative to αFe thus the top fitted curve corresponds to less s-electron dense $Fe^{2.5+}$. The magnetic splitting is quite apparent. In each of the spectra, six peaks are present due to magnetic splitting of the nuclear energy states as explained previously. Quadrupole splitting is not so apparent, but actually is present in the spectra. The three peaks to the left of the center of a spectrum should be spaced the same as those to the right due to magnetic splitting alone since the energy level spacing between sublevels is equal. This is not the case in the above spectra, because the higher energy I = 3/2 sublevels are split unevenly due to magnetic and quadrupole splitting interactions.

Once the peaks have been fitted appropriately, determination of the extent of B-site vacancy in $(Fe^{3+})_A(Fe_{(1-3x)}{}^{2+}\ Fe_{(1+2X)}{}^{3+}\emptyset_x)_B O_4$ is a relatively simple matter. All one has to due to determine the number of vacancies (x) is solve the equation:

$\frac{RA_B}{RA_A} = \frac{2-6x}{1-5x}$ where $RA_{B\text{ or }A}$ = relative area ($\frac{Area\ A\ or\ B\ site\ curve}{Area\ of\ both\ curves}$) of the curve for the B or A site respectively

The reasoning for this equation is as follows. Taking into account that the mixed valance $Fe^{2.5+}$

curve is a result of paired interaction between Fe^{2+} and Fe^{3+} the nonstochiometric chemical formula is $(Fe^{3+})_A(Fe_{(1-3x)}{}^{2+}\ Fe_{(1+2X)}{}^{3+}\emptyset_x)_BO_4$. The relative intensity (or relative area) of the Fe-A and Fe-B curves is very sensitive to stoichiometry because vacancies in the B-site reduce the Fe-A curve and increase Fe-B curve intensities. This is due to the unpaired $Fe_{5x}{}^{3+}$ adding to the intensity of the Fe-A curve rather than the Fe-B curve. Since the relative area is directly proportional to the number of Fe contributing to the spectrum the ratio of the relative areas is equal to stoichiometric ratio of $Fe^{2.5+}$ to Fe^{3+}, which yields the above formula.

Example Calculation:

For MtH2 $RA_A/RA_B = 1.89$

Plugging x into the nonstoichiometric iron oxide formula yeilds:

$$\frac{RA_B}{RA_A}=\frac{2\text{-}6x}{1\text{-}5x} \quad \text{solving for x yeilds} \quad x=\frac{2-\frac{RA_A}{RA_B}}{5\frac{RA_A}{RA_B}+6}=\frac{2\text{-}1.89}{5(1.89)+6}=0.00712$$

$(Fe^{3+})_A(Fe_{1.9572}{}^{2+}\ Fe_{0.0356}{}^{3+})_BO_4$ (very close to stoichiometric)

Sample	RA_B/RA_A	X	Chemical formula
MtH2	1.89	0.007	$(Fe^{3+})_A(Fe_{0.979}{}^{2+}\ Fe_{1.014}{}^{3+})_BO_4$
MtC	1.66	0.024	$(Fe^{3+})_A(Fe_{0.929}{}^{2+}\ Fe_{1.048}{}^{3+})_BO_4$
Mt025	1.60	0.029	$(Fe^{3+})_A(Fe_{0.914}{}^{2+}\ Fe_{1.057}{}^{3+})_BO_4$

Table 3.3: Parameters and nonstoichiometric formulas for MtC, Mt025, and MtH2

3.6.2 Bibliography

- F. C. Voogt, T. Fujii, P. J. M. Smulders, L. Niesen, M. A. James, and T. Hibma, *Phys. Rev. B*, 1999, **60**, 11193.
- A. L. Andrade, D. M. Souza, M. C. Pereira, J. D. Fabris, and R. Z. Domingues, *J. Nanosci. Nanotechnol.*, 2009, **9**, 2081.
- J. B. Yang, X. D. Zhou, W. B. Yelon, W. fJ. James, Q. Cai, K. V. Gopalakrishnan, S. K. Malik, X. C. Sun, and D. E. Nikles, *J. Appl. Phys.*, 2004, **95**, 7540.
- R.E. Vandenberghe, I. Nedkov, T. Merodiiska, and L. Slavov, *Hyperfine Interact.* 2005, **165**, 267.

3.7 Measuring the Specific Surface Area of Nanoparticle Suspensions using NMR[12]

3.7.1 Introduction

Surface area is a property of immense importance in the nano-world, especially in the area of heterogeneous catalysis. A solid catalyst works with its active sites binding to the reactants, and hence for a given active site reactivity, the higher the number of active sites available, the faster the reaction will occur. In heterogeneous catalysis, if the catalyst is in the form of spherical nanoparticles, most of the active sites are believed to be present on the outer surface. Thus it is very important to know the catalyst surface area in order to get a measure of the reaction time. One expresses this in terms of volume specific surface area, i.e., surface area/volume although in industry it is quite common to express it as surface area per unit mass of catalyst, e.g., m^2/g.

[12] This content is available online at <http://cnx.org/content/m34663/1.1/>.

3.7.2 Overview of NMR

Nuclear magnetic resonance (NMR) is the study of the nuclei of the response of an atom to an external magnetic field. Many nuclei have a net magnetic moment with $I \neq 0$, along with an angular momentum in one direction where I is the spin quantum number of the nucleus. In the presence of an external magnetic field, a nucleus would precess around the field. With all the nuclei precessing around the external magnetic field, a measurable signal is produced.

NMR can be used on any nuclei with an odd number of protons or neutrons or both, like the nuclei of hydrogen (^{1}H), carbon (^{13}C), phosphorous (^{31}P), etc. Hydrogen has a relatively large magnetic moment (μ = 14.1 x 10^{-27} J/T) and hence it is used in NMR logging and NMR rock studies. The hydrogen nucleus composes of a single positively charged proton that can be seen as a loop of current generating a magnetic field. It is may be considered as a tiny bar magnet with the magnetic axis along the spin axis itself as shown in Figure 3.38. In the absence of any external forces, a sample with hydrogen alone will have the individual magnetic moments randomly aligned as shown in Figure 3.39.

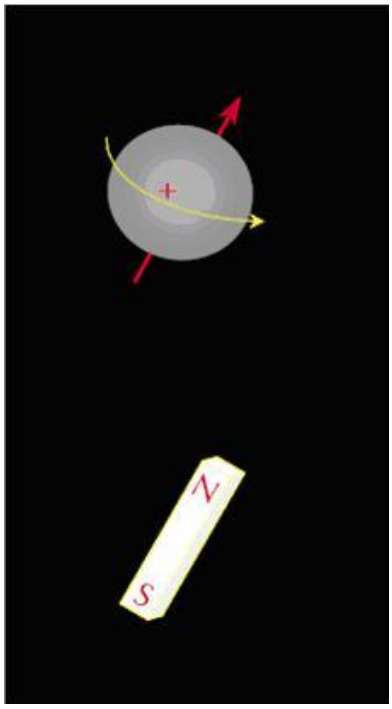

Figure 3.38: A simplistic representation of a spinning nucleus as bar magnet. Copyright: Halliburton Energy Services, Duncan, OK (1999).

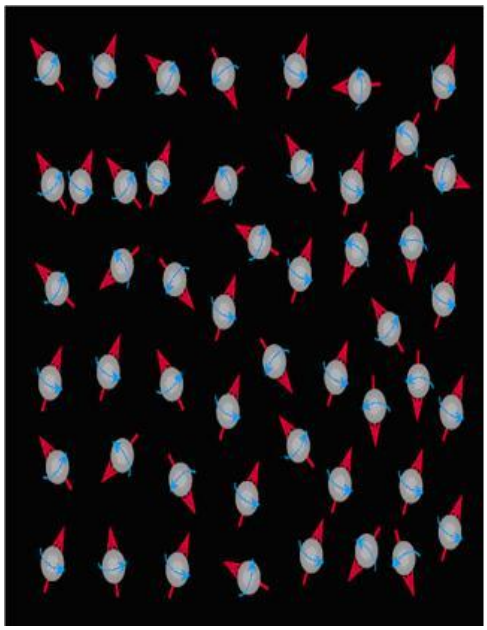

Figure 3.39: Representation of randomly aligned hydrogen nuclei. Copyright: Halliburton Energy Services, Duncan, OK (1999).

3.7.3 Advantages of NMR over BET technique

BET measurements follow the BET (Brunner-Emmet-Teller) adsorption isotherm of a gas on a solid surface. Adsorption experiments of a gas of known composition can help determine the specific surface area of the solid particle. This technique has been the main source of surface area analysis used industrially for a long time. However BET techniques take a lot of time for the gas-adsorption step to be complete while one shall see in the course of this module that NMR can give you results in times averaging around 30 minutes depending on the sample. BET also requires careful sample preparation with the sample being in dry powder form, whereas NMR can accept samples in the liquid state as well.

3.7.4 How does NMR work?

3.7.4.1 Polarization

Polarization involves the alignment of the individual magnetic nuclei in the presence of a static external magnetic field B_o. This external field exerts a torque that forces the spinning nuclei to precess around it by a frequency given by the *Larmor frequency* given by (3.21), where γ is the gyromagnetic ratio which is a characteristic property of the nucleus. For hydrogen, $\gamma/2\pi = 42.58$ MHz/Tesla. This value is different for different elements.

$$f = \frac{\gamma\beta_o}{2\pi} \tag{3.21}$$

Considering the case of a proton under the influence of an external magnetic field, it will be in one of two possible energy states depending on the orientation of the precession axis. If the axis is parallel to B_o, the

proton is in the lower energy state (preferred state) and in the higher energy state if anti-parallel shown by Figure 3.40.

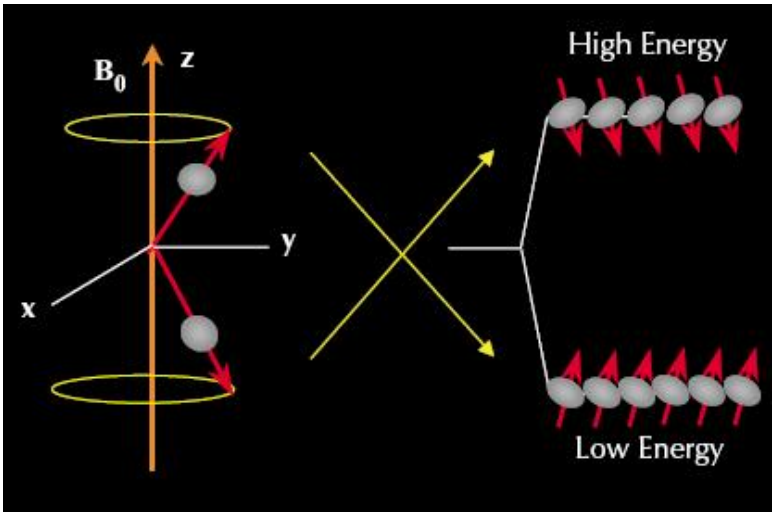

Figure 3.40: Alignment of precession axis. Copyright: Halliburton Energy Services, Duncan, OK (1999).

We define the net magnetization per unit volume of material, M_o, from Curie's law as (3.22), where N = number of protons, h = Planck's constant (6.626 x 10^{-34} Js), I = spin quantum number of the nucleus, k = Boltzmann's constant (1.381 x 10^{-23} m^2 Kg s^{-2} K^{-1}), and T = temperature (K)

$$M_o = \frac{N\gamma^2 h^2 I\left(I+1\right) B_o}{12\Pi^2 kT} \tag{3.22}$$

3.7.4.2 T_1 relaxation

The protons are said to be polarized completely once they are all aligned with the static external field. Polarization grows with a time constant called the *longitudinal relaxation time* (T_1) as shown in (3.23), where t = time of exposure to B_o, $M_z(t)$ = magnitude of magnetization at time t, with B_o along z-axis and T_1 = time at which $M_z(t)$ reaches 90% of its final value, i.e., M_o.

$$M_z\left(t\right) = M_o\left(1 - e^{\frac{-t}{T_1}}\right) \tag{3.23}$$

T_1 is the time at which $M_z(t)$ reaches 63% of its final value, M_o. A typical T_1 relaxation experiment involves application of a 90° RF pulse that rotates the magnetization to the transverse direction. With time, the magnetization returns to its original value in the same fashion described by the above equation.

Click on the video below to see the mechanism of T_1 relaxation

[Media Object][13]

[13]This media object is a video file. Please view or download it at

<T1_Relaxation_Video.wmv>

T_1 relaxation mechanism.

3.7.4.3 T_2 Relaxation

Once the polarization is complete, the magnetization direction is tipped from the longitudinal plane to a transverse plane by applying an oscillating field B_1 perpendicular to B_o. The frequency of B_1 must equal the Larmor frequency of the material from B_o. This oscillating field causes a possible change in energy state, and in-phase precession. The total phenomenon is called *nuclear magnetic resonance* as shown in Figure 3.41.

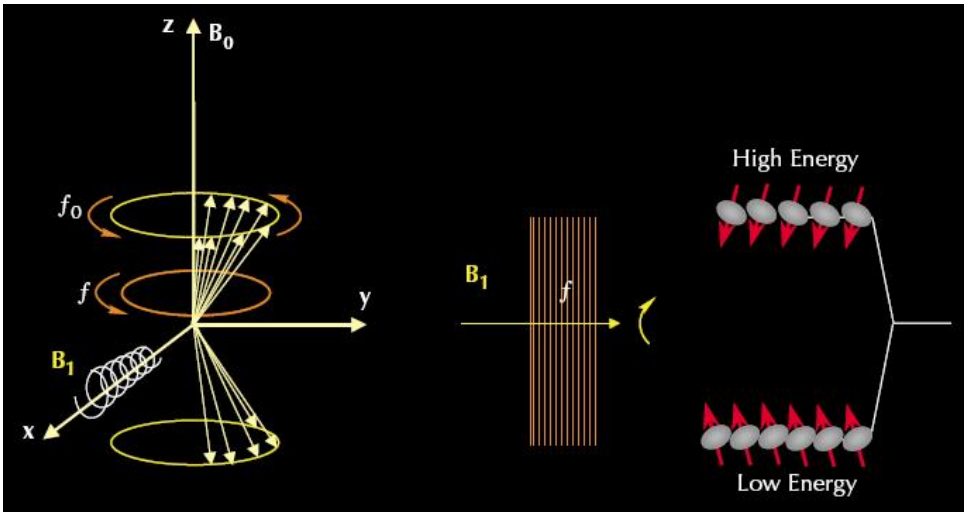

Figure 3.41: A schematic representation of the phenomenon of nuclear magnetic resonance. Copyright: Halliburton Energy Services, Duncan, OK (1999).

The oscillating field is generally pulsed in nature and so terms in books such a 180° pulse or 90° pulse indicates the angle through which the net magnetization gets tipped over. Application of a 90° pulse causes precession in the transverse phase. When the field B_1 is removed, the nuclei begin to de-phase and the net magnetization decreases. Here a receiver coil detects the decaying signal in a process called *free induction decay (FID)*. This exponential decay has an FID time constant (T_2) which is in the order of microseconds.

The time constant of the transverse relaxation is referred as T_2, and the amplitude of the decaying signal is given by (3.24), with symbols as defined earlier.

$$M_x(t) = M_o e^{\frac{-t}{T_2}} \tag{3.24}$$

Click on the video below to see the mechanism of T_2 relaxation

[Media Object][14]
T_2 relaxation mechanism.

[14]This media object is a video file. Please view or download it at

<T2_Relaxation_Video.wmv>

3.7.4.4 CPMG sequence

The de-phasing caused by T_1 relaxation can be reversed by applying a 180° pulse after a time τ has passed after application of the initial 90° pulse. Thus the phase of the transverse magnetization vector is now reversed by 180° so that "slower" vectors are now ahead of the "faster" vectors. These faster vectors eventually over-take the slower vectors and cause rephasing which is detected by a receiver coil as a s*pin echo*. Thus time τ also passes between the application of the 180° pulse and the maximum peak in the spin echo. The entire sequence is illustrated in Figure 3.42. A single echo decays very quickly and hence a series of 180^0 pulses are applied repeatedly in a sequence called the *Carr-Purcell-Meiboom-Gill (CPMG) sequence*.

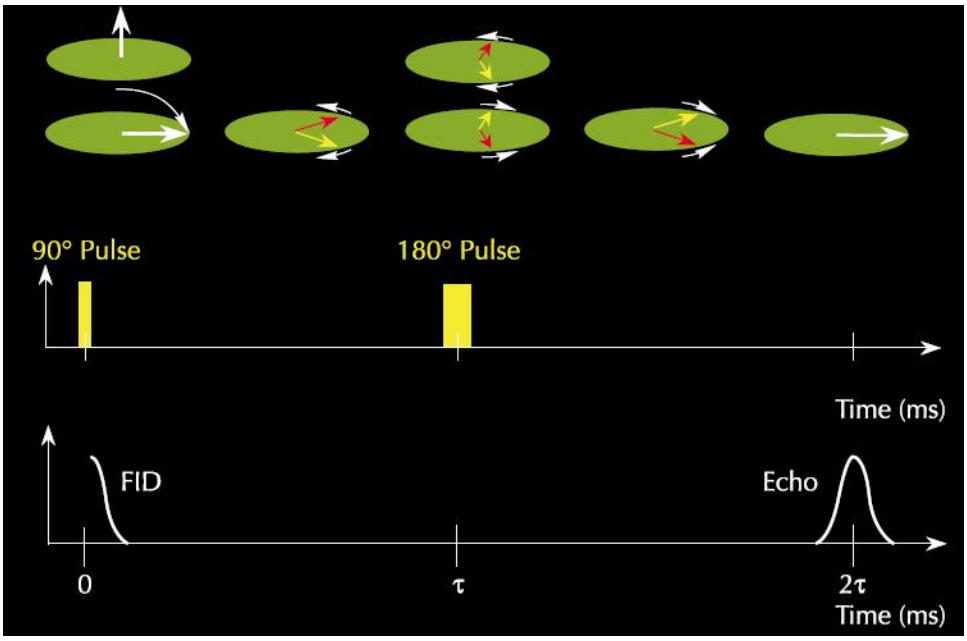

Figure 3.42: A schematic representation of the generation of a spin echo. Copyright: Halliburton Energy Services, Duncan, OK (1999).

3.7.5 NMR relaxation mechanism in solid suspensions

3.7.5.1 Calculations

From an atomic stand point, T_1 relaxation occurs when a precessing proton transfers energy with its surroundings as the proton relaxes back from higher energy state to its lower energy state. With T_2 relaxation, apart from this energy transfer there is also dephasing and hence T_2 is less than T_1 in general. For solid suspensions, there are three independent relaxation mechanisms involved:-

1) Bulk fluid relaxation, which affects both T_1 and T_2 relaxation.
2) Surface relaxation, which affects both T_1 and T_2 relaxation.
3) Diffusion in the presence of the magnetic field gradients, which affects only T_2 relaxation.

These mechanisms act in parallel so that the net effects are given by (3.25) and (3.26)

$$\frac{1}{T_2} = \frac{1}{T_{2,\text{bulk}}} + \frac{1}{T_{2,\text{surface}}} + \frac{1}{T_{2,\text{diffusion}}} \tag{3.25}$$

$$\frac{1}{T_1} = \frac{1}{T_{1,\text{bulk}}} + \frac{1}{T_{1,\text{surface}}} \tag{3.26}$$

The relative importance of each of these terms depend on the specific scenario. For the case of most solid suspensions in liquid, the diffusion term can be ignored by having a relatively uniform external magnetic field that eliminates magnetic gradients. Theoretical analysis has shown that the surface relaxation terms can be written as (3.27) and (3.28), where ρ = surface relaxivity and s/v = specific surface area.

$$\frac{1}{T_{1,\text{surface}}} = \rho_1 \left(\frac{S}{V}\right)_{\text{particle}} \tag{3.27}$$

$$\frac{1}{T_{2,\text{surface}}} = \rho_2 \left(\frac{S}{V}\right)_{\text{particle}} \tag{3.28}$$

Thus one can use T_1 or T_2 relaxation experiment to determine the specific surface area. We shall explain the case of the T_2 technique further as (3.29).

$$\frac{1}{T_2} = \frac{1}{T_{2,\text{bulk}}} + \rho_2 \left(\frac{S}{V}\right)_{\text{particle}} \tag{3.29}$$

One can determine T_2 by spin-echo measurements for a series of samples of known S/V values and prepare a calibration chart as shown in Figure 3.43, with the intercept as $\frac{1}{T_{2,\text{bulk}}}$ and the slope as ρ_2, one can thus find the specific surface area of an unknown sample of the same material.

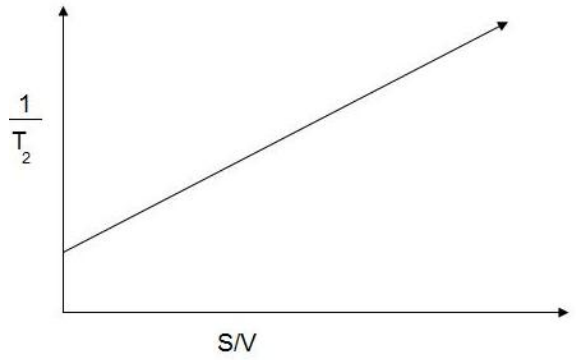

Figure 3.43: Example of a calibration plot of $1/T_2$ versus specific surface area (S/V) of a sample.

3.7.6 Sample preparation and experimental setup

The sample must be soluble in the solvent. For proton NMR, about 0.25-1.00 mg/mL are needed depending on the sensitivity of the instrument.

NOTE: The solvent properties will have an impact of some or all of the spectrum. Solvent viscosity affects obtainable resolution, while other solvents like water or ethanol have exchangeable protons that will prevent the observation of such exchangeable protons present in the solute itself. Solvents must be chosen such that the temperature dependence of solute solubility is low in the operation temperature range. Solvents containing aromatic groups like benzene can cause shifts in the observed spectrum compared to non-aromatic solvents.

NMR tubes are available in a wide range of specifications depending on specific scenarios. The tube specifications need to be extremely narrow while operating with high strength magnetic fields. The tube needs to be kept extremely clean and free from dust and scratches to obtain good results, irrespective of the quality of the tube. Tubes can cleaned without scratching by rinsing out the contents and soaking them in a degreasing solution, and by avoiding regular glassware cleaning brushes. After soaking for a while, rinse with distilled water and acetone and dry the tube by blowing filterened nitrogen gas through a pipette or by using a swob of cotton wool.

Filter the sample solution by using a Pasteur pipette stuffed with a piece of cotton wool at the neck. Any suspended material like dust can cause changes in the spectrum. When working with dilute aqueous solutions, sweat itself can have a major effect and so gloves are recommended at all times.

NOTE: Sweat contains mainly water, minerals (sodium 0.9 g/L, potassium 0.2 g/L, calcium 0.015 g/L, magnesium 0.0013 g/L and other trace elements like iron, nickel, zinc, copper, lead and chromium), as well as lactate and urea. In presence of a dilute solution of the sample, the proton-containing substances in sweat (e.g., lactate and urea) can result in a large signal that can mask the signal of the sample.

The NMR probe is the most critical piece of equipment as it contains the apparatus that must detect the small NMR signals from the sample without adding a lot of noise. The size of the probe is given by the diameter of the NMR tube it can accommodate with common sizes 5, 10 and 15 mm. A larger size probe can be used in the case of less sensitive samples in order to get as much solute into the active zone as possible. When the sample is available in less quantity, use a smaller size tube to get an intrinsically higher sensitivity.

3.7.6.1 NMR analysis

A result sheet of T_2 relaxation has the plot of magnetization versus time, which will be linear in a semi-log plot as shown in Figure 3.44. Fitting it to the equation, we can find T_2 and thus one can prepare a calibration plot of $1/T_2$ versus S/V of known samples.

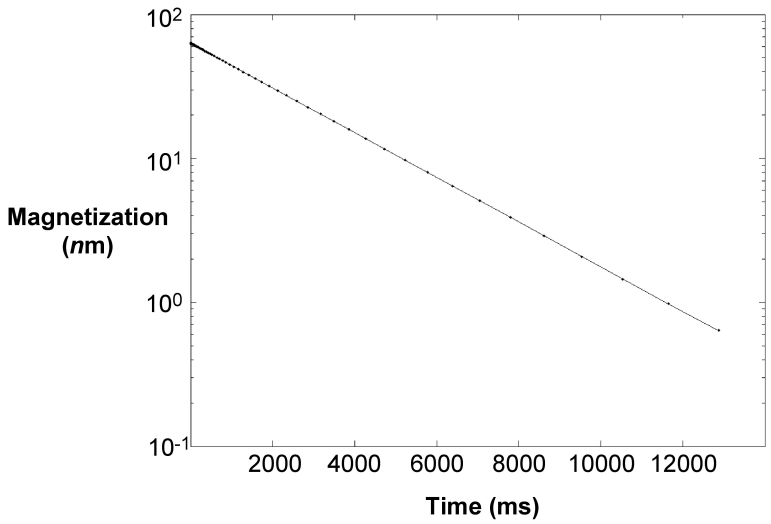

Figure 3.44: Example of T_2 relaxation with magnetization versus time on a semi-log plot.

3.7.6.2 Limitations of the T_2 technique

The following are a few of the limitations of the T_2 technique:

- One can't always guarantee no magnetic field gradients, in which case the T_1 relaxation technique is to be used. However this takes much longer to perform than the T_2 relaxation.
- There is the requirement of the odd number of nucleons in the sample or solvent.
- The solid suspension should not have any para- or ferromagnetic substance (for instance, organics like hexane tend to have dissolved O_2 which is paramagnetic).
- The need to prepare a calibration chart of the material with known specific surface area.

3.7.6.3 Example of usage

A study of colloidal silica dispersed in water provides a useful example. Figure 3.45 shows a representation of an individual silica particle.

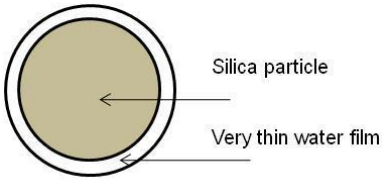

Figure 3.45: A representation of the silica particle with a thin water film surrounding it.

A series of dispersion in DI water at different concentrations was made and surface area calculated. The T_2 relaxation technique was performed on all of them with a typical T_2 plot shown in Figure 3.46 and T_2 was recorded at 2117 milliseconds for this sample.

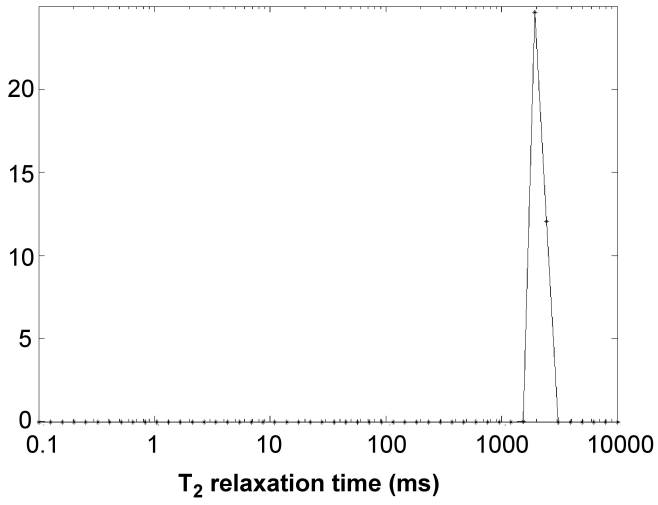

Figure 3.46: T_2 measurement for 2.3 wt% silica in DI water.

A calibration plot was prepared with $1/T_2 - 1/T_{2,bulk}$ as ordinate (the y-axis coordinate) and S/V as abscissa (the x-axis coordinate). This is called the *surface relaxivity plot* and is illustrated in Figure 3.47.

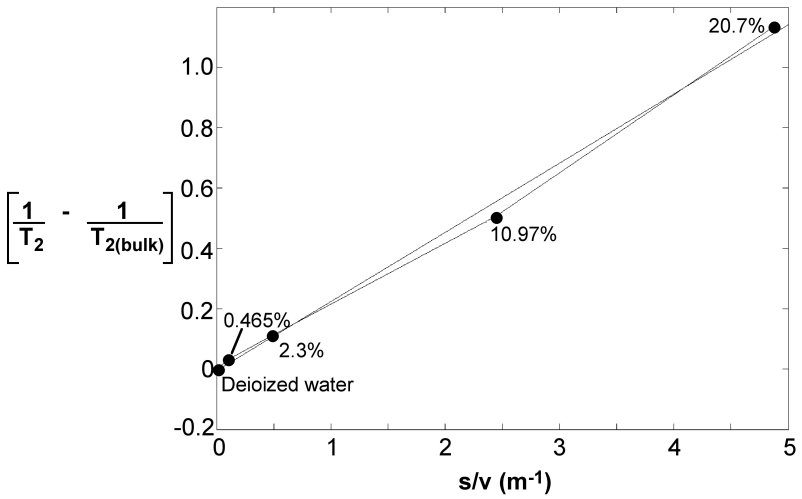

Figure 3.47: Calibration plot of $(1/T_2 - 1/T_{2,Bulk})$ versus specific surface area for silica in DI water.

Accordingly for the colloidal dispersion of silica in DI water, the best fit resulted in (3.30), from which one can see that the value of surface relaxivity, 2.3 x 10^{-8}, is in close accordance with values reported in literature.

$$\frac{1}{T_2} - \frac{1}{T_{2,\text{bulk}}} = 2.3x10^{-8}\left(\frac{S}{V}\right) - 0.0051 \tag{3.30}$$

The T_2 technique has been used to find the pore-size distribution of water-wet rocks. Information of the pore size distribution helps petroleum engineers model the permeability of rocks from the same area and hence determine the extractable content of fluid within the rocks.

Usage of NMR for surface area determination has begun to take shape with a company, Xigo nanotools, having developed an instrument called the Acorn Area^{TM} to get surface area of a suspension of aluminum oxide. The results obtained from the instrument match closely with results reported by other techniques in literature. Thus the T_2 NMR technique has been presented as a strong case to obtain specific surface areas of nanoparticle suspensions.

3.7.7 Bibliography

- G. R Coates, L. Xiao, and M.G. Prammer, *NMR Logging: Principles & Applications*, Halliburton Energy Services, Houston (2001).
- B. Cowan, *Nuclear magnetic resonance and relaxation*, Cambridge University Press, Cambridge UK (2001).
- W. E. Kenyon, *The Log Analyst*, 1997, **6**, 2.
- A. E. Derome, *Modern NMR Techniques for Chemistry Research*, Vol 6, Pergamon Press, Oxford (1988).

3.8 XPS of Carbon Nanomaterials[15]

3.8.1 Introduction

X-ray photoelectron spectroscopy (XPS), also called electron spectroscopy for chemical analysis (ESCA), is a method used to determine the elemental composition of a material's surface. It can be further applied to determine the chemical or electronic state of these elements.

The photoelectric effect is the ejection of electrons from the surface of a material upon exposure to electromagnetic radiation of sufficient energy. Electrons emitted have characteristic kinetic energies proportional to the energy of the radiation, according to (3.31), where KE is the kinetic energy of the electron, h is Planck's constant, ν is the frequency of the incident radiation, E_b is the ionization, or binding, energy, and ϕ is the work function. The work function is a constant which is dependent upon the spectrometer.

$$KE = h\nu - E_b - \varphi \tag{3.31}$$

In photoelectron spectroscopy, high energy radiation is used to expel core electrons from a sample. The kinetic energies of the resulting core electrons are measured. Using the equation with the kinetic energy and known frequency of radiation, the binding energy of the ejected electron may be determined. By Koopman's theorem, which states that ionization energy is equivalent to the negative of the orbital energy, the energy of the orbital from which the electron originated is determined. These orbital energies are characteristic of the element and its state.

3.8.2 Basics of XPS

3.8.2.1 Sample preparation

As a surface technique, samples are particularly susceptible to contamination. Furthermore, XPS samples must be prepared carefully, as any loose or volatile material could contaminate the instrument because of the ultra-high vacuum conditions. A common method of XPS sample preparation is embedding the solid sample into a graphite tape. Samples are usually placed on 1 x 1 cm or 3 x 3 cm sheets.

3.8.2.2 Experimental set-up

Monochromatic aluminum ($h\nu$ = 1486.6 eV) or magnesium ($h\nu$ = 1253.6 eV) K_α X-rays are used to eject core electrons from the sample. The photoelectrons ejected from the material are detected and their energies measured. Ultra-high vacuum conditions are used in order to minimize gas collisions interfering with the electrons before they reach the detector.

3.8.2.3 Measurement specifications

XPS analyzes material between depths of 1 and 10 nm, which is equivalent to several atomic layers, and across a width of about 10 μm. Since XPS is a surface technique, the orientation of the material affects the spectrum collected.

3.8.2.4 Data collection

X-ray photoelectron (XP) spectra provide the relative frequencies of binding energies of electrons detected, measured in electron-volts (eV). Detectors have accuracies on the order of $\pm$0.1 eV. The binding energies are used to identify the elements to which the peaks correspond. XPS data is given in a plot of intensity versus binding energy. Intensity may be measured in counts per unit time (such as counts per second, denoted c/s). Often, intensity is reported as arbitrary units (arb. units), since only relative intensities provide relevant information. Comparing the areas under the peaks gives relative percentages of the elements detected in the

[15] This content is available online at <http://cnx.org/content/m34549/1.2/>.

sample. Initially, a survey XP spectrum is obtained, which shows all of the detectable elements present in the sample. Elements with low detection or with abundances near the detection limit of the spectrometer may be missed with the survey scan. Figure 3.48 shows a sample survey XP scan of fluorinated double-walled carbon nanotubes (DWNTs).

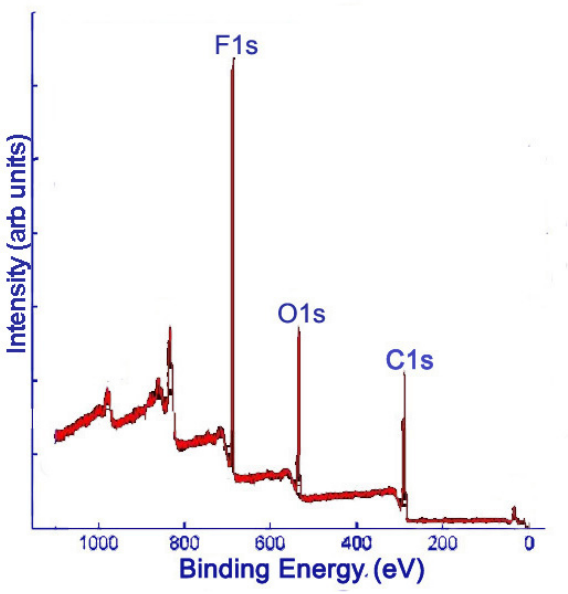

Figure 3.48: Survey XP spectrum of F-DWNTs (O. Kuznetsov, Rice University).

Subsequently, high resolution scans of the peaks can be obtained to give more information. Elements of the same kind in different states and environments have slightly different characteristic binding energies. Computer software is used to fit peaks within the elemental peak which represent different states of the same element, commonly called deconvolution of the elemental peak. Figure 3.49 and Figure 3.50 show high resolutions scans of C1s and F1s peaks, respectively, from Figure 3.48, along with the peak designations.

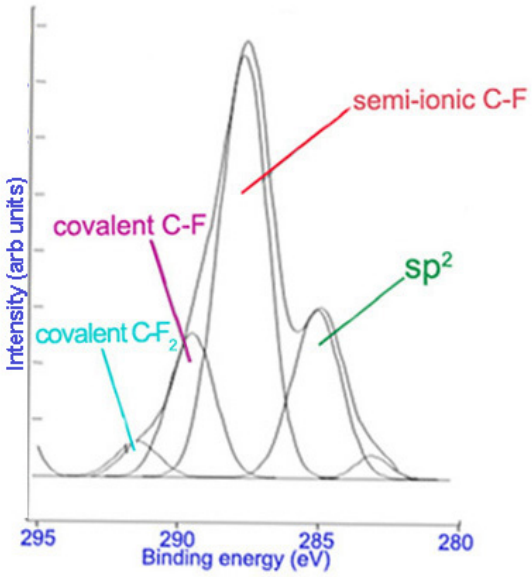

Figure 3.49: Deconvoluted high resolution C1s spectrum of F-DWNTs (O. Kuznetsov, Rice University).

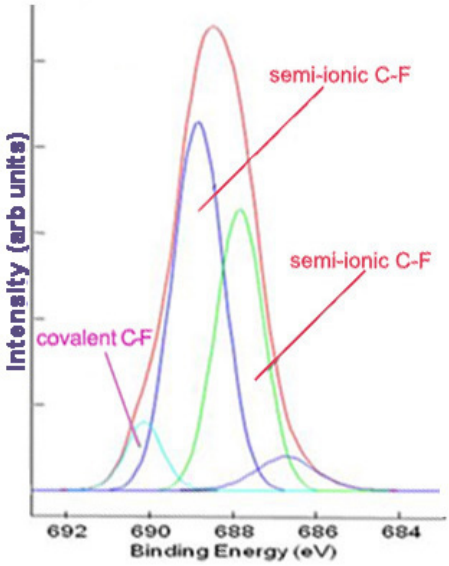

Figure 3.50: Deconvoluted high resolution F1s spectrum of F-DWNTs (O. Kuznetsov, Rice University).

3.8.2.5 Limitations

Both hydrogen and helium cannot be detected using XPS. For this reason, XPS can provide only relative, rather than absolute, ratios of elements in a sample. Also, elements with relatively low atomic percentages close to that of the detection limit or low detection by XPS may not be seen in the spectrum. Furthermore, each peak represents a distribution of observed binding energies of ejected electrons based on the depth of the atom from which they originate, as well as the state of the atom. Electrons from atoms deeper in the sample must travel through the above layers before being liberated and detected, which reduces their kinetic energies and thus increases their apparent binding energies. The width of the peaks in the spectrum consequently depends on the thickness of the sample and the depth to which the XPS can detect; therefore, the values obtained vary slightly depending on the depth of the atom. Additionally, the depth to which XPS can analyze depends on the element being detected.

High resolution scans of a peak can be used to distinguish among species of the same element. However, the identification of different species is discretionary. Computer programs are used to deconvolute the elemental peak. The peaks may then be assigned to particular species, but the peaks may not correspond with species in the sample. As such, the data obtained must be used cautiously, and care should be taken to avoid over-analyzing data.

3.8.3 XPS for carbon nanomaterials

Despite the aforementioned limitations, XPS is a powerful surface technique that can be used to accurately detect the presence and relative quantities of elements in a sample. Further analysis can provide information about the state and environment of atoms in the sample, which can be used to infer information about the surface structure of the material. This is particularly useful for carbon nanomaterials, in which surface structure and composition greatly influence the properties of the material. There is much research interest in modifying carbon nanomaterials to modulate their properties for use in many different applications.

3.8.3.1 Sample preparation

Carbon nanomaterials present certain issues in regard to sample preparation. The use of graphite tape is a poor option for carbon nanomaterials because the spectra will show peaks from the graphite tape, adding to the carbon peak and potentially skewing or overwhelming the data. Instead, a thin indium foil (between 0.1 and 0.5 mm thick) is used as the sample substrate. The sample is simply pressed onto a piece of the foil.

3.8.4 Analysis and applications for carbon nanomaterials

3.8.4.1 Chemical Speciation

The XP survey scan is an effective way to determine the identity of elements present on the surface of a material, as well as the approximate relative ratios of the elements detected. This has important implications for carbon nanomaterials, in which surface composition is of greatest importance in their uses. XPS may be used to determine the purity of a material. For example, nanodiamond powder is a created by detonation, which can leave nitrogenous groups and various oxygen containing groups attached to the surface. Figure 3.51 shows a survey scan of a nanodiamond thin film with the relative atomic percentages of carbon, oxygen, and nitrogen being 91.25%, 6.25%, and 1.7%, respectively. Based on the XPS data, the nanodiamond material is approximately 91.25% pure.

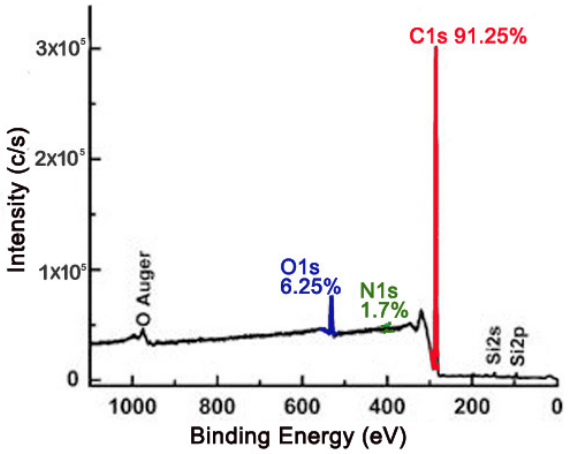

Figure 3.51: Survey XPS of a nanodiamond thin film. Adapted from F. Y. Xie, W. G. Xie, J. Chen, X. Liu, D. Y. Lu, and W. H. Zhang, *J. Vac. Sci. Tech. B*, 2008, **26**, 102.

XPS is a useful method to verify the efficacy of a purification process. For example, high-pressure CO conversion single-walled nanotubes (HiPco SWNTs) are made using iron as a catalyst. Figure 3.52 shows the Fe2p XP spectra for pristine and purified HiPco SWNTs.

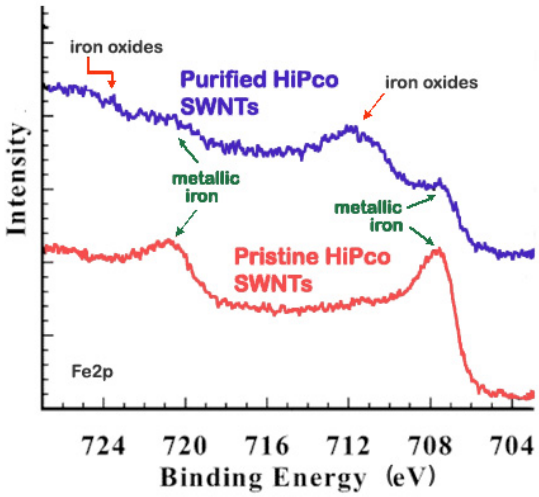

Figure 3.52: High resolution scan of Fe2p peak for pristine and purified HiPco SWNTs. Adapted with permission from C. M. Yang, H. Kanoh, K. Kaneko, M. Yudasaka, and S. Iijima, *J. Phys. Chem. B*, 2002, **106**, 8994. Copyright: American Chemical Society (2002).

For this application, XPS is often done in conjunction with thermogravimetric analysis (TGA), which measures the weight lost from a sample at increasing temperatures. TGA data serves to corroborate the changes observed with the XPS data by comparing the percentage of weight loss around the region of the impurity suspected based on the XP spectra. The TGA data support the reduction in iron content with purification suggested by the XP spectra above, for the weight loss at temperatures consistent with iron loss decreases from 27% in pristine SWNTs to 18% in purified SWNTs. Additionally, XPS can provide information about the nature of the impurity. In Figure 3.52, the Fe2p spectrum for pristine HiPco SWNTs shows two peaks characteristic of metallic iron at 707 and 720 eV. In contrast, the Fe2p spectrum for purified HiPco SWNTs also shows two peaks at 711 and 724 eV, which are characteristic of either Fe_2O_3 or Fe_3O_4. In general, the atomic percentage of carbon obtained from the XPS spectrum is a measure of the purity of the carbon nanomaterials.

3.8.4.2 Bonding and functional groups

XP spectra give evidence of functionalization and can provide insight into the identity of the functional groups. Carbon nanomaterials provide a versatile surface which can be functionalized to modulate their properties. For example, the sodium salt of phenyl sulfonated SWNTs is water soluble. In the XP survey scan of the phenyl sulfonated SWNTs, there is evidence of functionalization owing to the appearance of the S2p peak. Figure 3.53 shows the survey XP spectrum of phenyl sulfonated SWNTs.

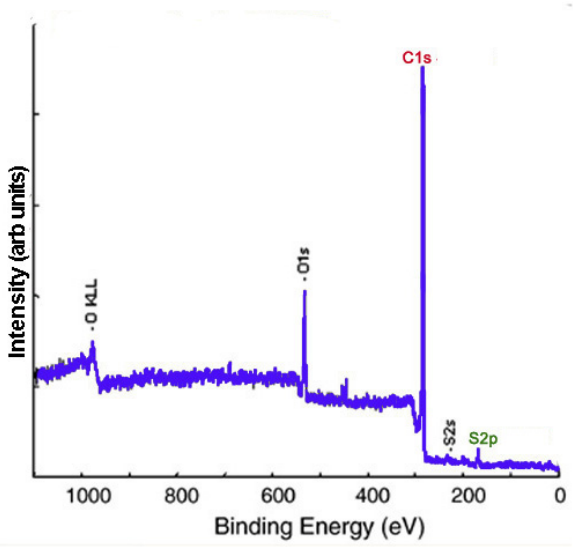

Figure 3.53: Survey XP spectrum of phenyl sulfonated SWNTs. Adapted with permission from F. Liang, J. M. Beach, P. K. Rai, W. H. Guo, R. H. Hauge, M. Pasquali, R. E. Smalley, and W. E. Billups, *Chem. Mater.*, 2006, **18**, 1520. Copyright: American Chemical Society (2006).

The survey XP spectrum of the sodium salt shows a Na1s peak (Figure 3.54) and the high resolution scans of Na1s and S2p show that the relative atomic percentages of Na1s and S2p are nearly equal (Figure 3.55), which supports the formation of the sodium salt.

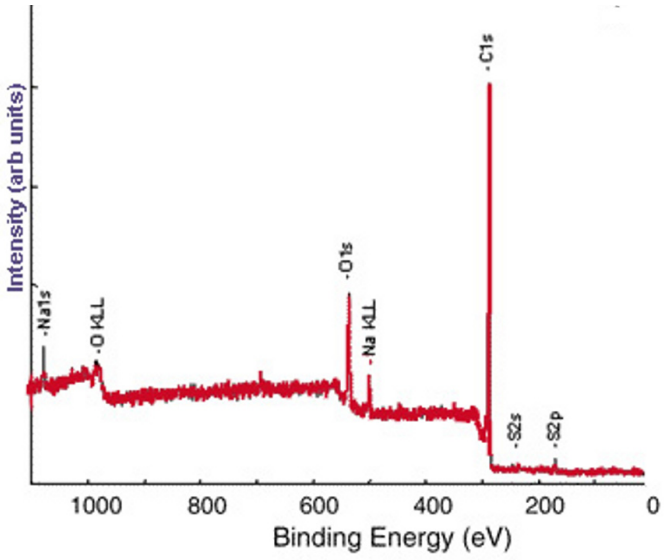

Figure 3.54: Survey XP spectrum of phenyl sulfonated SWNTs. Adapted with permission from F. Liang, J. M. Beach, P. K. Rai, W. H. Guo, R. H. Hauge, M. Pasquali, R. E. Smalley, and W. E. Billups, *Chem. Mater.*, 2006, **18**, 1520. Copyright: American Chemical Society (2006).

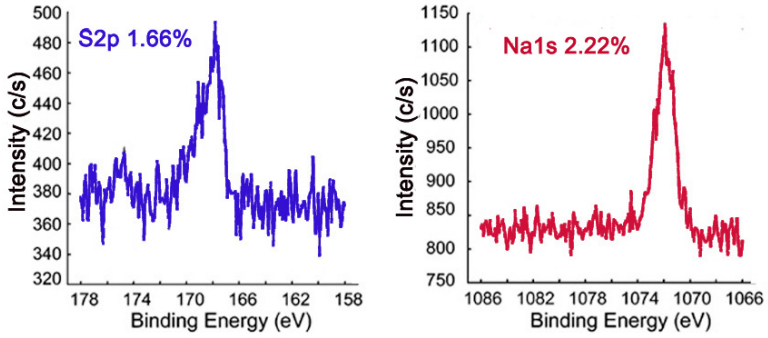

Figure 3.55: High resolution S2p (left) and Na1s (right) XP spectra of phenyl sulfonated SWNTs. Adapted with permission from F. Liang, J. M. Beach, P. K. Rai, W. H. Guo, R. H. Hauge, M. Pasquali, R. E. Smalley, and W. E. Billups, *Chem. Mater.*, 2006, **18**, 1520. Copyright: American Chemical Society (2006).

3.8.4.3 Further characterization

High resolution scans of each of the element peaks of interest can be obtained to give more information about the material. This is a way to determine with high accuracy the presence of elements as well as relative ratios of elements present in the sample. This can be used to distinguish species of the same element in different chemical states and environments, such as through bonding and hybridization, present in the material. The distinct peaks may have binding energies that differ slightly from that of the convoluted elemental peak. Assignment of peaks can be done using XPS databases, such as that produced by NIST[16] . The ratios of the intensities of these peaks can be used to determine the percentage of atoms in a particular state. Discrimination between and identity of elements in different states and environments is a strength of XPS that is of particular interest for carbon nanomaterials.

3.8.4.3.1 Hybridization

The hybridization of carbons influences the properties of a carbon nanomaterial and has implications in its structure. XPS can be used to determine the hybridization of carbons on the surface of a material, such as graphite and nanodiamond. Graphite is a carbon material consisting of sp^2 carbons. Thus, theoretically the XPS of pure graphite would show a single C1s peak, with a binding energy characteristic of sp^2 carbon (around 284.2 eV). On the other hand, nanodiamond consists of sp^3 bonded carbons. The XPS of nanodiamond should show a single C1s peak, with a binding energy characteristic of sp^3 carbon (around 286 eV). The ratio of the sp^2 and sp^3 peaks in the C1s spectrum gives the ratio of sp^2 and sp^3 carbons in the nanomaterial. This ratio can be altered and compared by collecting the C1s spectra. For example, laser treatment of graphite creates diamond-like material, with more sp^3 character when a higher laser power is used. This can be observed in Figure 3.56, in which the C1s peak is broadened and shifted to higher binding energies as increased laser power is applied.

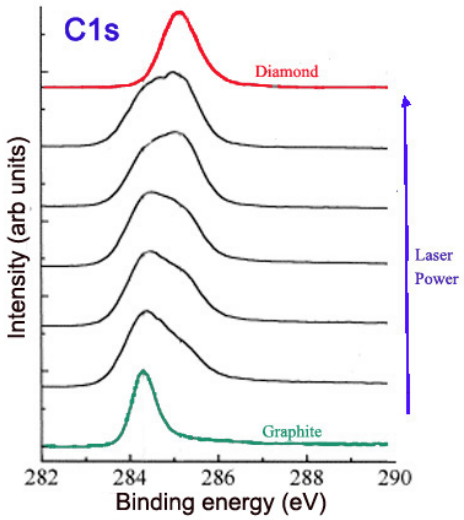

Figure 3.56: C1s high resolution XP spectra of graphite, nanodiamond, and graphite samples with increasing laser power treatment. Adapted from P. Merel, M. Tabbal, M. Chaker, S. Moisa, and J. Margot, *Appl. Surf. Sci.*, 1998, **136**, 105.

[16] http://srdata.nist.gov/xps/Default.aspx

Alternatively, annealing nanodiamond thin films at very high temperatures creates graphitic layers on the nanodiamond surface, increasing sp^2 content. The extent of graphitization increases with the temperature at which the sample is annealed, as shown in Figure 3.57.

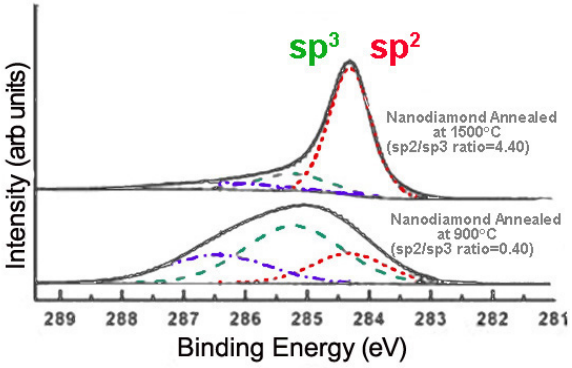

Figure 3.57: Deconvoluted high resolution C1s XP spectra for annealed nanodiamond. Adapted from F. Y. Xie, W. G. Xie, J. Chen, X. Liu, D. Y. Lu, and W. H. Zhang, *J. Vac. Sci. Tech. B*, 2008, **26**, 102.

3.8.4.3.2 Reaction completion

Comparing the relative intensities of various C1s peaks can be powerful in verifying that a reaction has occurred. Fluorinated carbon materials are often used as precursors to a broad range of variously functionalized materials. Reaction of fluorinated SWNTs (F-SWNTs) with polyethyleneimine (PEI) leads to decreases in the covalent carbon-fluoride C1s peak, as well as the evolution of the amine C1s peak. These changes are observed in the C1s spectra of the two samples (Figure 3.58).

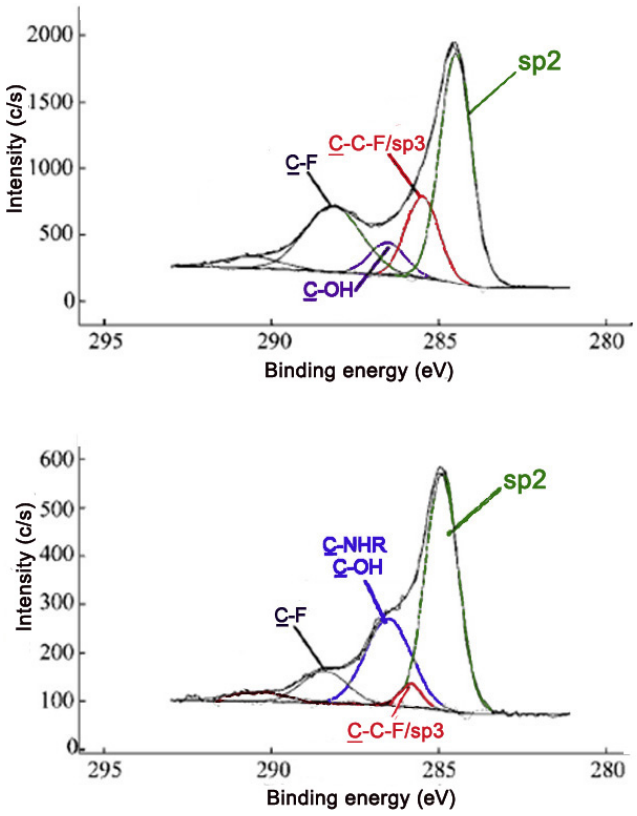

Figure 3.58: High resolution C1s XP spectra of F-SWNTs (top) and PEI-SWNTs (bottom). Adapted with permission from E. P. Dillon, C. A. Crouse, and A. R. Barron, *ACS Nano*, 2008, **2**, 156. Copyright: American Chemical Society (2008).

3.8.4.3.3 Nature and extent of functionalization

XPS can also be applied to determine the nature and extent of functionalization. In general, binding energy increases with decreasing electron density about the atom. Species with more positive oxidation states have higher binding energies, while more reduced species experience a greater degree of shielding, thus increasing the ease of electron removal.

The method of fluorination of carbon materials and such factors as temperature and length of fluorination affect the extent of fluoride addition as well as the types of carbon-fluorine bonds present. A survey scan can be used to determine the amount of fluorine compared to carbon. High resolution scans of the C1s and F1s peaks can also give information about the proportion and types of bonds. A shift in the peaks, as well as changes in peak width and intensity, can be observed in spectra as an indication of fluorination of graphite. Figure 3.59 shows the Cls and F1s spectra of samples containing varying ratios of carbon to fluorine.

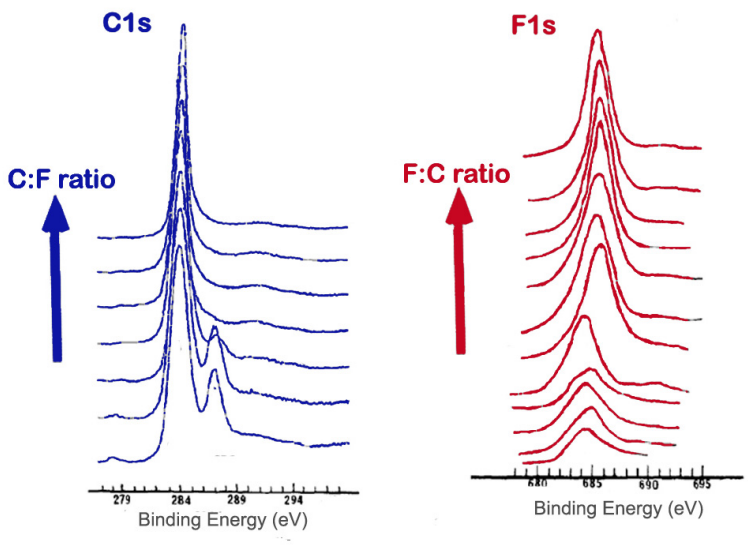

Figure 3.59: C1s and F1s high resolution XP spectra for graphite fluorides. Adapted from I. Palchan, M. Crespin, H. Estrade-Szwarckopf, and B. Rousseau. *Chem. Phys. Lett.*, 1989, **157**, 321.

Furthermore, different carbon-fluorine bonds show characteristic peaks in high resolution C1s and F1s spectra. The carbon-fluorine interactions in a material can range from ionic to covalent. Covalent carbon-fluorine bonds show higher core electron binding energies than bonds more ionic in character. The method of fluorination affects the nature of the fluorine bonds. Graphite intercalation compounds are characterized by ionic carbon-fluorine bonding. Figure 3.60 shows the F1s spectra for two fluorinated exfoliated graphite samples prepared with different methods.

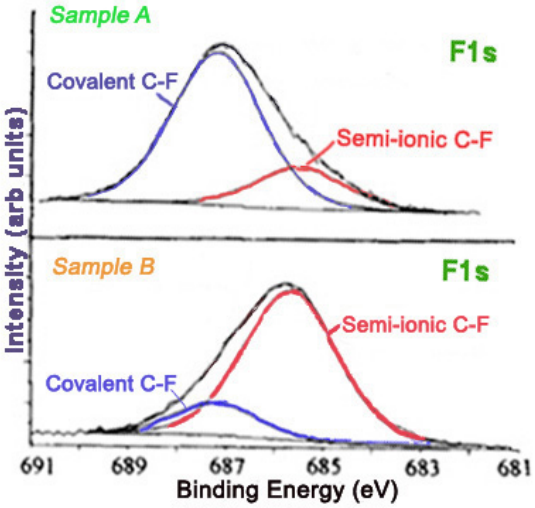

Figure 3.60: High resolution F1s XP spectra of two fluorinated exfoliated graphite samples. Adapted from A. Tressaud, F. Moguet, S. Flandrois, M. Chambon, C. Guimon, G. Nanse, E. Papirer, V. Gupta, and O.P. Bahl. *J. Phys. Chem. Solids*, 1996, **57**, 745.

Also, the peaks for carbons attached to a single fluorine atom, two fluorine atoms, and carbons attached to fluorines have characteristic binding energies. These peaks are seen in that C1s spectra of F- and PEI-SWNTs shown in Figure 3.61.

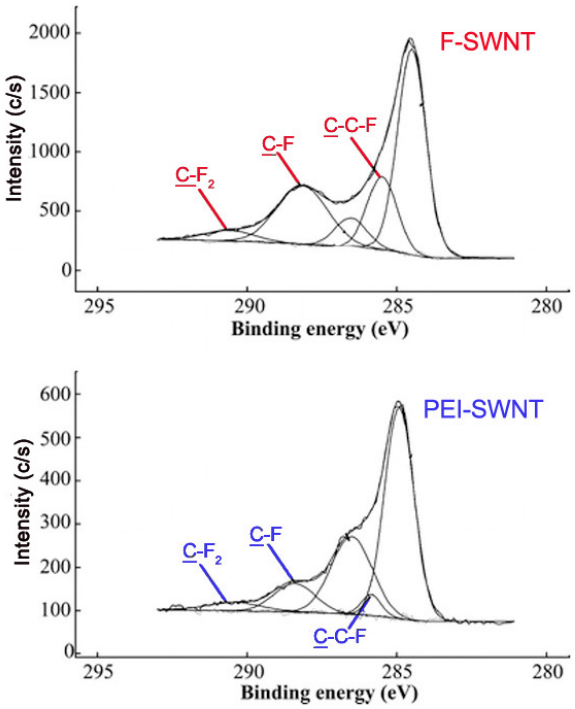

Figure 3.61: High resolution C1s XP spectra of F-SWNTs (top) and PEI-SWNTs (bottom). Adapted with permission from E. P. Dillon, C. A. Crouse, and A. R. Barron, *ACS Nano*, 2008, **2**, 156. Copyright: American Chemical Society (2008).

Table 3.4 lists various bonds and functionalities and the corresponding C1s binding energies, which may be useful in assigning peaks in a C1s spectrum, and consequently in characterizing the surface of a material.

Bond/Group	Binding Energy (eV)
C-C	**284.0-286.0**
C-C (sp^2)	284.3-284.6
C-C (sp^3)	285.0-286.0
C-N	**285.2-288.4**
C-NR_2 (amine)	285.5-286.4
O=C-NH (amide)	287.9-288.6
-C=N (nitrile)	266.3-266.8
C-O	**286.1-290.0**
O=C-OH (carboxyl)	288.0-289.4
-C-O (epoxy)	286.1-287.1
-C-OH (hydroxyl)	286.4-286.7
-C-O-C- (ether)	286.1-288.0
-C=O (aldehyde/ketone)	287.1-288.1
C-F	**287.0-293.4**
-C-F (covalent)	287.7-290.2
-C-F (ionic)	287.0-287.4
C=C-F	286.0-287.7
C-F_2	291.6-292.4
C-F_3	292.4-293.4
C-S	**285.2-287.5**
C-Cl	**287.0-287.2**

Table 3.4: Summary of selected C1s binding energies.

3.8.4.4 Conclusion

X-ray photoelectron spectroscopy is a facile and effective method for determining the elemental composition of a material's surface. As a quantitative method, it gives the relative ratios of detectable elements on the surface of the material. Additional analysis can be done to further elucidate the surface structure. Hybridization, bonding, functionalities, and reaction progress are among the characteristics that can be inferred using XPS. The application of XPS to carbon nanomaterials provides much information about the material, particularly the first few atomic layers, which are most important for the properties and uses of carbon nanomaterials.

3.8.5 Bibliography

- J. Bockris, *Modern Electrochemistry 2A*, 2nd ed., Springer (2001).
- E. P. Dillon, C. A. Crouse, and A. R. Barron, *ACS Nano*, 2008, **2**, 156.
- Y. G. Gogotsi, and I. V. Uvarova, *Nanostructured materials and coatings for biomedical and sensor applications*, Kluwer Academic Publishing (2003).

- F. Liang, J. M. Beach, P. K. Rai, W. H. Guo, R. H. Hauge, M. Pasquali, R. E. Smalley, and W. E. Billups, *Chem. Mater.*, 2006, **18**, 1520.
- P. Merel, M. Tabbal, M. Chaker, S. Moisa, and J. Margot, *Appl. Surf. Sci.*, 1998, **136**, 105.
- T. Nakajima, *Graphite fluorides and carbon-fluorine compounds*, CRC Press, Boca Raton (1991).
- I. Palhan, M. Crespin, H. Estrade-Szwarckopf, and B. Rousseau. *Chem. Phys. Lett.*, 1989, **157**, 321.
- A. Tressaud, F. Moguet, S. Flandrois, M. Chambon, C. Guimon, G. Nanse, E. Papirer, V. Gupta, and O. P. Bahl. *J. Phys. Chem. Solids*, 1996, **57**, 745.
- F. Y. Xie, W. G. Xie, J. Chen, X. Liu, D. Y. Lu, and W. H. Zhang, *J. Vac. Sci. Tech. B*, 2008, **26**, 102.
- C. M. Yang, H. Kanoh, K. Kaneko, M. Yudasaka, and S. Iijima, *J. Phys. Chem. B*, 2002, **106**, 8994.

3.9 Using XPS to Analyze Metal Nanoparticles[17]

3.9.1 Introduction

X-ray photoelectron spectroscopy (XPS) is a surface technique developed for use with thin films. More recently, however, it has been used to analyze the chemical and elemental composition of nanoparticles. The complication of nanoparticles is that they are neither flat nor larger than the diameter of the beam, creating issues when using the data obtained at face value. Samples of nanoparticles will often be large aggregates of particles. This creates problems with the analysis acquisition, as there can be a variety of cross-sections, as seen in Figure 3.62. This acquisition problem is also compounded by the fact that the surfactant may not be completely covering the particle, as the curvature of the particle creates defects and divots. Even if it is possible to create a monolayer of particles on a support, other issues are still present. The background support will be analyzed with the particle, due to their small size and the size of the beam and the depth at which it can penetrate.

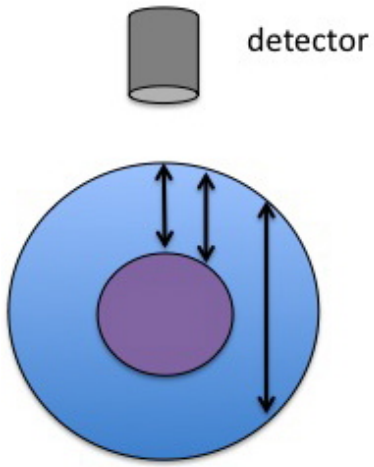

Figure 3.62: Different cross-sections of analysis possible on a nanoparticle.

[17] This content is available online at <http://cnx.org/content/m34526/1.1/>.

Many other factors can introduce changes in nanoparticles and their properties. There can be probe, environmental, proximity, and sample preparation effects. The dynamics of particles can wildly vary depending on the reactivity of the particle itself. Sputtering can also be a problem. The beam used to sputter will be roughly the same size or larger than the particles. This means that what appears in the data is not a section of particle, but an average composition of several particles.

Each of these issues needs to be taken into account and preventative measures need to be used so the data is the best representation possible.

3.9.2 Sample preparation

Sample preparation of nanoparticles is very important when using XPS. Certain particles, such as iron oxides without surfactants, will interact readily with oxygen in the air. This causes the particles to gain a layer of oxygen contamination. When the particles are then analyzed, oxygen appears where it should not and the oxidation state of the metal may be changed. As shown by these particles, which call for handling, mounting and analysis without exposure to air, knowing the reactivity of the nanoparticles in the sample is very important even before starting analysis. If the reactivity of the nanoparticle is known, such as the reactivity of oxygen and iron, then preventative steps can be taken in sample preparation in order to obtain the best analysis possible.

When preparing a sample for XPS, a powder form is often used. This preparation, however, will lead to aggregation of nanoparticles. If analysis is performed on such a sample, the data obtained will be an average of composition of each nanoparticle. If composition of a single particle is what is desired, then this average composition will not be sufficient. Fortunately, there are other methods of sample preparation. Samples can be supported on a substrate, which will allow for analysis of single particles. A pictorial representation in Figure 3.63 shows the different types of samples that can occur with nanoparticles.

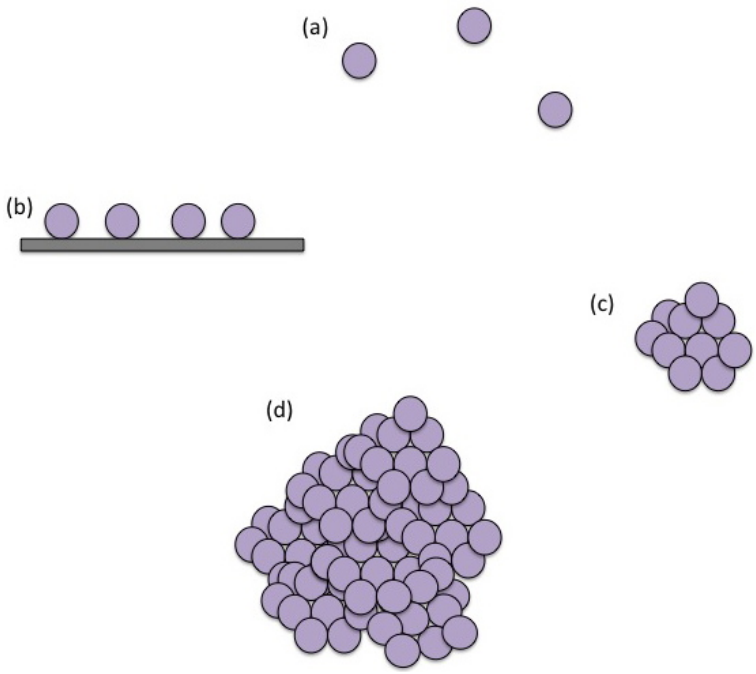

Figure 3.63: Representation of (a) a theoretical isolated nanoparticles, (b) nanoparticles suspended on a substrate, (c) an aggregate of nanoparticles, and (d) a powdered form of nanoparticles.

3.9.3 Analysis limitations

Nanoparticles are dynamic; their properties can change when exposed to new chemical environments, leading to a new set of applications. It is the dynamics of nanoparticles that makes them so useful and is one of the reasons why scientists strive to understand their properties. However, it is this dynamic ability that makes analysis difficult to do properly. Nanoparticles are easily damaged and can change properties over time or with exposure to air, light or any other environment, chemical or otherwise. Surface analysis is often difficult because of the high rate of contamination. Once the particles are inserted into XPS, even more limitations appear.

3.9.3.1 Probe effects

There are often artifacts introduced from the simple mechanism of conducting the analysis. When XPS is used to analyze the relatively large surface of thin films, there is small change in temperature as energy is transferred. The thin films, however, are large enough that this small change in energy has to significant change to its properties. A nanoparticle is much smaller. Even a small amount of energy can drastically change the shape of particles, in turn changing the properties, giving a much different set of data than expected.

The electron beam itself can affect how the particles are supported on a substrate. Theoretically, nanoparticles would be considered separate from each other and any other chemical environments, such as solvents or substrates. This, however, is not possible, as the particles must be suspended in a solution or placed on a

substrate when attempting analysis. The chemical environment around the particle will have some amount of interaction with the particle. This interaction will change characteristics of the nanoparticles, such as oxidation states or partial charges, which will then shift the peaks observed. If particles can be separated and suspended on a substrate, the supporting material will also be analyzed due to the fact that the X-ray beam is larger than the size of each individual particle. If the substrate is made of porous materials, it can adsorb gases and those will be detected along with the substrate and the particle, giving erroneous data.

3.9.3.2 Environmental effects

Nanoparticles will often react, or at least interact, with their environments. If the particles are highly reactive, there will often be induced charges in the near environment of the particle. Gold nanoparticles have a well-documented ability to undergo plasmon interactions with each other. When XPS is performed on these particles, the charges will change the kinetic energy of the electrons, shifting the apparent binding energy. When working with nanoparticles that are well known for creating charges, it is often best to use an ion gun or a coating of gold. The purpose of the ion gun or gold coating is to try to move peaks back to their appropriate energies. If the peaks do not move, then the chance of there being no induced charge is high and thus the obtained data is fairly reliable.

3.9.3.3 Proximity effects

The proximity of the particles to each other will cause interactions between the particles. If there is a charge accumulation near one particle, and that particle is in close proximity with other particles, the charge will become enhanced as it spreads, affecting the signal strength and the binding energies of the electrons. While the knowledge of charge enhancement could be useful to potential applications, it is not beneficial if knowledge of the various properties of individual particles is sought.

Less isolated (i.e., less crowded) particles will have different properties as compared to more isolated particles. A good example of this is the plasmon effect in gold nanoparticles. The closer gold nanoparticles are to each other, the more likely they will induce the plasmon effect. This can change the properties of the particles, such as oxidation states and partial charges. These changes will then shift peaks seen in XPS spectra. These proximity effects are often introduced in the sample preparation. This, of course, shows why it is important to prepare samples correctly to get desired results.

3.9.4 Conclusions

Unfortunately there is no good general procedure for all nanoparticles samples. There are too many variables within each sample to create a basic procedure. A scientist wanting to use XPS to analyze nanoparticles must first understand the drawbacks and limitations of using their sample as well as how to counteract the artifacts that will be introduced in order to properly use XPS.

One must never make the assumption that nanoparticles are flat. This assumption will only lead to a misrepresentation of the particles. Once the curvature and stacking of the particles, as well as their interactions with each other are taken into account, XPS can be run.

3.9.5 Bibliography

- D. R. Baer and M. H. Engelhard. *J. Electron Spectrosc. Rel. Phenom.*, 2009, **178-179**, 415.
- D. R. Baer, J. E. Amonette, M. H. Engelhard, D. J. Gaspar, A. S. Karakoti, S. Kuchibhatla, P. Nachimuthu, J. T. Nurmi, Y. Qiang, V. Sarathy, S. Seal, A. Sharma. P. G. Tratnyek, and C. M. Wang. *Surf. Interface Anal.*, 2008, **40**, 529.

3.10 Thermogravimetric Analysis of Single Walled Carbon Nanotubes[18]

Thermogravimetric analysis (TGA) and the associated differential thermal analysis (DTA) are widely used for the characterization of both as-synthesized and side-wall functionalized single walled carbon nanotubes (SWNTs). Under oxygen, SWNTs will pyrolyze leaving any inorganic residue behind. In contrast in an inert atmosphere since most functional groups are labile or decompose upon heating and as SWNTs are stable up to 1200 °C, any weight loss before 800 °C is used to determine the functionalization ratio of side-wall functionalized SWNTs. The following properties of SWNTs can be determined using this TGA;

1. The mass of metal catalyst impurity in as synthesized SWNTs.
2. The number of functional groups per SWNT carbon (C_{SWNT}).
3. The mass of a reactive species absorbed by a functional group on a SWNT.

Quantitative determination of these properties are used to define the purity of SWNTs, and the extent of their functionalization.

3.10.1 An overview of thermogravimetric analysis

The main function of TGA is the monitoring of the thermal stability of a material by recording the change in mass of the sample with respect to temperature. Figure 3.64 shows a simple diagram of the inside of a typical TGA.

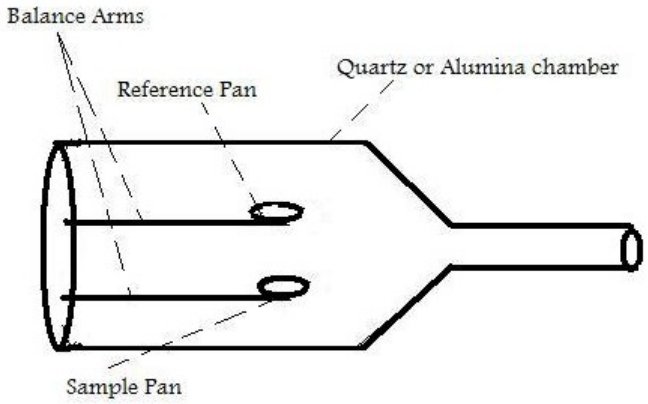

Figure 3.64: Schematic representation of a TGA apparatus.

Inside the TGA, there are two pans, a reference pan and a sample pan. The pan material can be either aluminium or platinum. The type of pan used depends on the maximum temperature of a given run. As platinum melts at 1760 °C and alumium melts at 660 °C, platinum pans are chosen when the maximum temperature exceeds 660 °C. Under each pan there is a thermocouple which reads the temperature of the pan. Before the start of each run, each pan is balanced on a balance arm. The balance arms should be calibrated to compensate for the differential thermal expansion between the arms. If the arms are not calibrated, the instrument will only record the temperature at which an event occurred and not the change

[18] This content is available online at <http://cnx.org/content/m22972/1.2/>.

in mass at a certain time. To calibrate the system, the empty pans are placed on the balance arms and the pans are weighed and zeroed.

As well as recording the change in mass, the heat flow into the sample pan (differential scanning calorimetry, DSC) can also be measured and the difference in temperature between the sample and reference pan (differential thermal analysis, DTA). DSC is quantitative and is a measure of the total energy of the system. This is used to monitor the energy released and absorbed during a chemical reaction for a changing temperature. The DTA shows if and how the sample phase changed. If the DTA is constant, this means that there was no phase change. Figure 3.65 shows a DTA with typical examples of an exotherm and an endotherm.

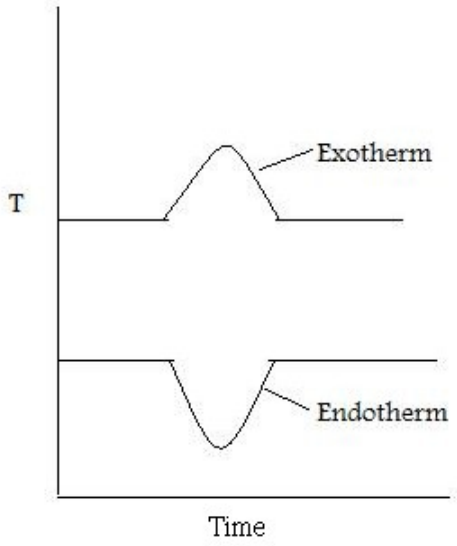

Figure 3.65: Simplified representation of the DTA for an exotherm and an endotherm.

When the sample melts, the DTA dips which signifies an endotherm. When the sample is melting it requires energy from the system. Therefore the temperature of the sample pan decreases compared with the temperature of the reference pan. When the sample has melted, the temperature of the sample pan increases as the sample is releasing energy. Finally the temperatures of the reference and sample pans equilibrate resulting in a constant DTA. When the sample evaporates, there is a peak in the DTA. This exotherm can be explained in the same way as the endotherm.

Typically the sample mass range should be between 0.1 to 10 mg and the heating rate should be 3 to 5 °C/min.

3.10.2 Determination of the mass of iron catalyst impurity in HiPCO SWNTs.

SWNTs are typically synthesized using metal catalysts. Those prepared using the HiPco method, contain residual Fe catalyst. The metal (i.e., Fe) is usually oxidized upon exposure to air to the appropriate oxide (i.e., Fe_2O_3). While it is sometimes unimportant that traces of metal oxide are present during subsequent applications it is often necessary to quantify their presence. This is particularly true if the SWNTs are to be used for cell studies since it has been shown that the catalyst residue is often responsible for observed cellular toxicity.

In order to calculate the mass of catalyst residue the SWNTs are pyrolyzed under air or O_2, and the residue is assumed to be the oxide of the metal catalyst. Water can be added to the raw SWNTs, which enhances the low-temperature catalytic oxidation of carbon. A typical TGA plot of a sample of raw HiPco SWNTs is shown in Figure 3.66.

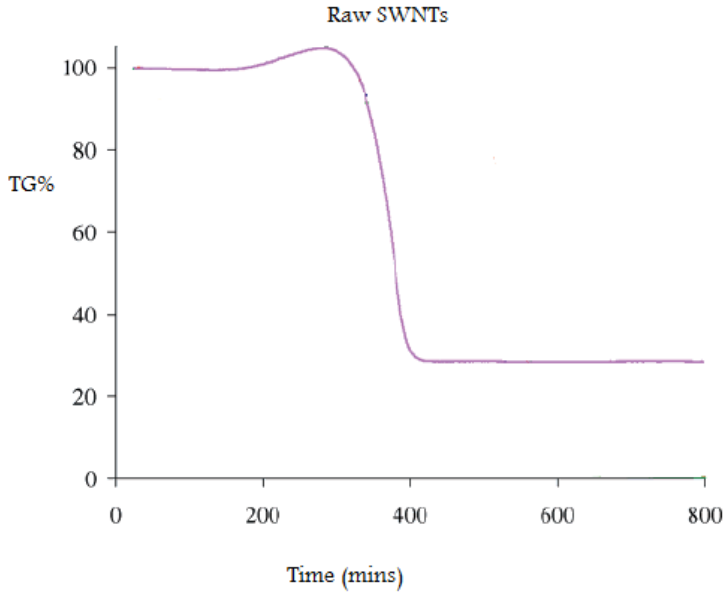

Figure 3.66: The TGA of unpurified HiPco SWNTs under air showing the residual mass associated with the iron catalyst. Adapted from I. W. Chiang, B. E. Brinson, A. Y. Huang, P. A. Willis, M. J. Bronikowski, J. L. Margrave, R. E. Smalley, and R. H. Hauge, *J. Phys. Chem. B*, 2001, **105**, 8297. Adapted from Chiang et al, 2001

The weight gain (of ca. 5%) at 300 °C is due to the formation of metal oxide from the incompletely oxidized catalyst. To determine the mass of iron catalyst impurity in the SWNT, the residual mass must be calculated. The residual mass is the mass that is left in the sample pan at the end of the experiment. From this TGA diagram, it is seen that 70% of the total mass is lost at 400 °C. This mass loss is attributed to the removal of carbon. The residual mass is 30%. Given that this is due to both oxide and oxidized metal, the original total mass of residual catalyst in raw HiPCO SWNTs is ca. 25%.

3.10.3 Determining the number of functional groups on SWNTs

The limitation of using SWNTs in any practical applications is their solubility; for example SWNTs have little to no solubility in most solvents due to aggregation of the tubes. Aggregation/roping of nanotubes occurs as a result of the high van der Waals binding energy of ca. 500 eV per μm of tube contact. The van der Waals force between the tubes is so great, that it take tremendous energy to pry them apart, making it very difficult to make combination of nanotubes with other materials such as in composite applications. The functionalization of nanotubes, i.e., the attachment of "chemical functional groups", provides the path to overcome these barriers. Functionalization can improve solubility as well as processability, and has been used to align the properties of nanotubes to those of other materials. In this regard, covalent functionalization

provides a higher degree of fine-tuning for the chemical and physical properties of SWNTs than non-covalent functionalization.

Functionalized nanotubes can be characterized by a variety of techniques, such as atomic force microscopy (AFM), transmission electron microscopy (TEM), UV-vis spectroscopy, and Raman spectroscopy, however, the quantification of the extent of functionalization is important and can be determined using TGA. Because any sample of functionalized-SWNTs will have individual tubes of different lengths (and diameters) it is impossible to determine the number of substituents per SWNT. Instead the extent of functionalization is expressed as number of substituents per SWNT carbon atom (C_{SWNT}), or more often as C_{SWNT}/substituent, since this is then represented as a number greater than 1.

Figure 3.67 shows a typical TGA for a functionalized SWNT. In this case it is polyethyleneimine (PEI) functionalized SWNTs prepared by the reaction of fluorinated SWNTs (F-SWNTs) with PEI in the presence of a base catalyst.

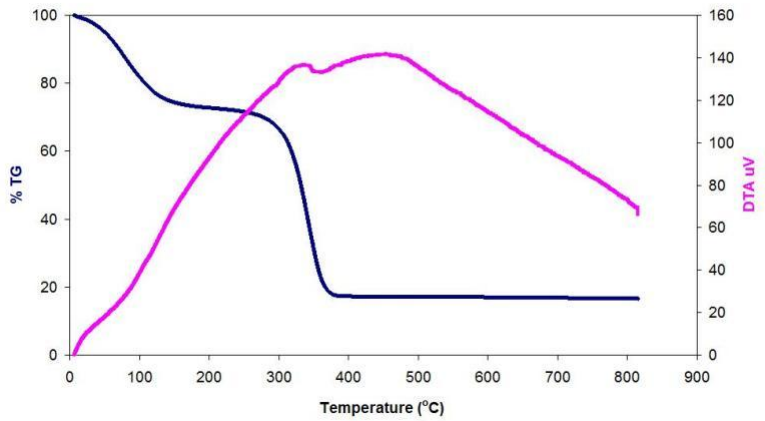

Figure 3.67: The TGA of SWNTs functionalized with polyethyleimine (PEI) under air showing the sequential loss of complexed CO_2 and decomposition of PEI.

In the present case the molecular weight of the PEI is 600 g/mol. When the sample is heated, the PEI thermally decomposes leaving behind the unfunctionalized SWNTs. The initial mass loss below 100 °C is due to residual water and ethanol used to wash the sample.

In the following example the total mass of the sample is 25 mg.

Step 1. The initial mass, M_i = 25 mg = mass of the SWNTs, residues and the PEI.

Step 2. After the initial moisture has evaporated there is 68% of the sample left. 68% of 25 mg is 17 mg. This is the mass of the PEI and the SWNTs.

Step 3. At 300 °C the PEI starts to decompose and all of the PEI has been removed from the SWNTs at 370 °C. The mass loss during this time is 53% of the total mass of the sample. 53% of 25 mg is 13.25 mg.

Step 4. The molecular weight of this PEI is 600 g/mol. Therefore there is 0.013 g / 600 g/mol = 0.022 mmole of PEI in the sample.

Step 5. 15% of the sample is the residual mass, this is the mass of the decomposed SWNTs. 15% of 25 mg is 3.75 mg. The molecular weight of carbon is 12 g/mol. So there is 0.3125 mmole of carbon in the sample.

Step 6. There is 93.4 mol% of carbon and 6.5 mol% of PEI in the sample.

3.10.4 Determination of the mass of a chemical absorbed by functionalized SWNTs

Solid-state ^{13}C NMR of PEI-SWNTs shows the presence of carboxylate substituents that can be attributed to carbamate formation as a consequence of the reversable CO_2 absorption to the primary amine substituents of the PEI. Desorption of CO_2 is accomplished by heating under argon at 75 °C.

The quantity of CO_2 absorbed per PEI-SWNT unit may be determined by initially exposing the PEI-SWNT to a CO_2 atmosphere to maximize absorption. The gas flow is switched to either Ar or N_2 and the sample heated to liberate the absorbed CO_2 without decomposing the PEI or the SWNTs. An example of the appropriate TGA plot is shown in Figure 3.68.

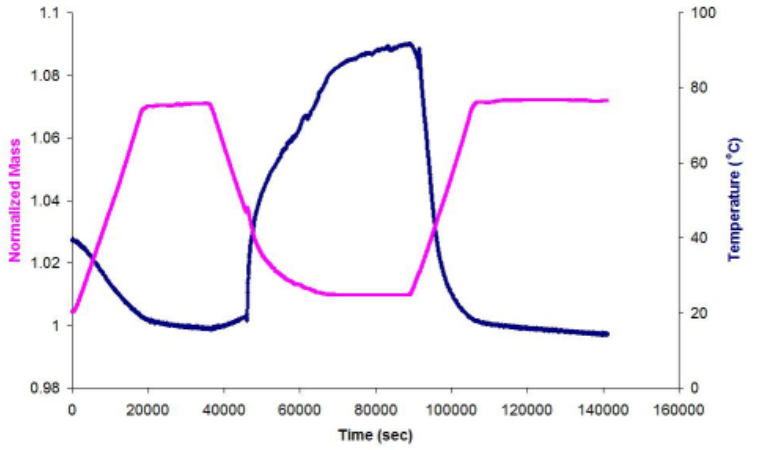

Figure 3.68: The TGA results of PEI(10000)-SWNT absorbing and desorbing CO_2. The mass has been normalized to the lowest mass recorded, which is equivalent to PEI(10000)-SWNT.

The sample was heated to 75 °C under Ar, and an initial mass loss due to moisture and/or atmospherically absorbed CO_2 is seen. In the temperature range of 25 °C to 75 °C the flow gas was switched from an inert gas to CO_2. In this region an increase in mass is seen, the increase is due to CO_2 absorption by the PEI (10000Da)-SWNT. Switching the carrier gas back to Ar resulted in the desorption of the CO_2.

The total normalized mass of CO_2 absorbed by the PEI(10000)-SWNT can be calculated as follows;

Solution Outline

Step 1. Minimum mass = mass of absorbant = $M_{absorbant}$
Step 2. Maximum mass = mass of absorbant and absorbed species = M_{total}
Step 3. Absorbed mass = $M_{absorbed}$ = M_{total} - $M_{absorbant}$
Step 4. % of absorbed species= ($M_{absorbed}/M_{absorbant}$)*100
Step 5. 1 mole of absorbed species = MW of absorbed species
Step 6. Number of moles of absorbed species = ($M_{absorbed}$/MW of absorbed species)
Step 7. The number of moles of absorbed species absorbed per gram of absorbant= ($1g/M_{total}$)*(Number of moles of absorbed species)

Solution

Step 1. $M_{absorbant}$ = Mass of PEI-SWNT = 4.829 mg

Step 2. M_{total} = Mass of PEI-SWNT and CO_2 = 5.258 mg
Step 3. $M_{absorbed}$ = M_{total} - $M_{absorbant}$ = 5.258 mg - 4.829 mg = 0.429 mg
Step 4. % of absorbed species= % of CO_2 absorbed = ($M_{absorbed}/M_{absorbant}$)*100 = (0.429/4.829)*100 = 8.8%
Step 5. 1 mole of absorbed species = MW of absorbed species = MW of CO_2 = 44 therefore 1 mole = 44g
Step 6. Number of moles of absorbed species = ($M_{absorbed}$/MW of absorbed species)= (0.429 mg / 44 g) = 9.75 μM
Step 7. The number of moles of absorbed species absorbed per gram of absorbant =(1 g/M_{total})*(Number of moles of absorbed species) = (1 g/5.258 mg)*(9.75)= 1.85 mmol of CO_2 absorbed per gram of absorbant

3.10.5 Bibliography

- I. W. Chiang, B. E. Brinson, A. Y. Huang, P. A. Willis, M. J. Bronikowski, J. L. Margrave, R. E. Smalley, and R. H. Hauge, *J. Phys. Chem. B*, 2001, **105**, 8297.
- E. P. Dillon, C. A. Crouse and A. R. Barron, *ACS Nano*, 2008, **2**, 156.

3.11 ICP-AES Analysis of Nanoparticles[19]

3.11.1 What is ICP-AES?

Inductively coupled plasma atomic emission spectroscopy (ICP-AES) is a spectral method used to determine very precisely the elemental composition of samples; it can also be used to quantify the elemental concentration with the sample. ICP-AES uses high-energy plasma from an inert gas like argon to burn analytes very rapidly. The color that is emitted from the analyte is indicative of the elements present, and the intensity of the spectral signal is indicative of the concentration of the elements that is present.

3.11.2 How does ICP-AES work?

ICP-AES works by the emission of photons from analytes that are brought to an excited state by the use of high-energy plasma. The plasma source is induced when passing argon gas through an alternating electric field that is created by an inductively couple coil. When the analyte is excited the electrons try to dissipate the induced energy moving to a ground state of lower energy, in doing this they emit the excess energy in the form of light. The wavelength of light emitted depends on the energy gap between the excited energy level and the ground state. This is specific to the element based on the number of electrons the element has and electron orbital's are filled. In this way the wavelength of light can be used to determine what elements are present by detection of the light at specific wavelengths.

As a simple example consider the situation when placing a piece of copper wire into the flame of a candle. The flame turns green due to the emission of excited electrons within the copper metal, as the electrons try to dissipate the energy incurred from the flame, they move to a more stable state emitting energy in the form of light. The energy gap between the excited state to the ground state (ΔE) dictates the color of the light or wavelength of the light.

$\Delta E = h\nu$

where h = Plank's constant, and ν is the frequency of the emitted light.

The wavelength of light is indicative of the element present. If another metal is placed in the flame such as iron a different color flame will be emitted because the electronic structure of iron is different from that of copper. This is a very simple analogy for what is happening in ICP-AES and how it is used to determine what elements are present. By detecting the wavelength of light that is emitted from the analyte one can deduce what elements are be present.

[19] This content is available online at <http://cnx.org/content/m22058/1.18/>.

Naturally if there is a lot of the material present then there will be an accumulative effect making the intensity of the signal large. However, if there were very little materials present the signal would be low. By this rationale one can create a calibration curve from analyte solutions of known concentrations, whereby the intensity of the signal changes as a function of the concentration of the material that is present. When measuring the intensity from a sample of unknown concentration the intensity from this sample can be compared to that from the calibration curve, so this can be used to determine the concentration of the analytes within the sample.

3.11.3 ICP-AES of nanoparticles to determine elemental composition

As with any sample being studied by ICP-AES nanoparticles need to be digested so that all the atoms can be vaporized in the plasma equally. If a metal containing nanoparticle were not digested using a strong acid to bring the metals atoms into solution, the form of the particle could hinder some of the material being vaporized. The analyte would not be detected even though it is present in the sample and this would give an erroneous result. Nanoparticles are often covered with a protective layer of organic ligands and this must be removed also. Further to this the solvent used for the nanoparticles may also be an organic solution and this should be removed as it too will not be miscible in the aqueous medium.

Several organic solvents have low vapor pressures so it is relatively easy to remove the solvent by heating the samples, removing the solvent by evaporation. To remove the organic ligands that are present on the nanoparticle, choric acid can be used. This is a very strong acid and can break down the organic ligands readily. To digest the particles and get the metal into solution concentrated nitric acid is often used.

A typical protocol may use 0.5 mL of concentrated nanoparticle solution and digest this with 9.5 mL of concentrated nitric acid over the period of a few days. After which 0.5 mL of the digested solution is placed in 9.5 mL of nanopure water. The reason why nanopure water is used is because DI water or regular water will have some amount of metals ions present and these will be detected by the ICP-AES measurement and will lead to figures that are not truly representative of the analyte concentration alone. This is especially pertinent when there is a very a low concentration of metal analyte to be detected, and is even more a problem when the metal to be detected is commonly found in water such as iron. Once the nanopure water and digested solution are prepared then the sample is ready for analysis.

Another point to consider when doing ICP-AES on nanoparticles to determine chemical compositions, includes the potential for wavelength overlap. The energy that is released in the form of light is unique to each element, but elements that are very similar in atomic structure will have emission wavelengths that are very similar to one another. Consider the example of iron and cobalt, these are both transition metals and sit right beside each other on the periodic table. Iron has an emission wavelength at 238.204 nm and cobalt has an emission wavelength at 238.892 nm. So if you were to try determine the amount of each element in an alloy of the two you would have to select another wavelength that would be unique to that element, and not have any wavelength overlap to other analytes in solution. For this case of iron and cobalt it would be wiser to use a wavelength for iron detection of 259.940 nm and a wavelength detection of 228.616 nm. Bearing this in mind a good rule of thumb is to try use the wavelength of the analyte that affords the best detection primarily. But if this value leads to a possible wavelength overlap of within 15 nm wavelength with another analyte in the solution then another choice should be made of the detection wavelength to prevent wavelength overlap from occurring.

Some people have also used the ICP-AES technique to determine the size of nanoparticles. The signal that is detected is determined by the amount of the material that is present in solution. If very dilute solutions of nanoparticles are being analyzed, particles are being analyzed one at a time, i.e., there will be one nanoparticle per droplet in the nebulizer. The signal intensity would then differ according to the size of the particle. In this way the ICP-AES technique could be used to determine the concentration of the particles in the solution as well as the size of the particles.

3.11.4 Calculations for ICP concentrations

In order to performe ICP-AES stock solutions must be prepared in dilute nitric acid solutions. To do this a concentrated solution should be diluted with nanopure water to prepare 7 wt% nitric acid solutions. If the concentrated solution is 69.8 wt% (check the assay amount that is written on the side of the bottle) then the amount to dilute the solution will be as such:

The density (d) of HNO_3 is 1.42 g/mL

Molecular weight of HNO_3 is 63.01

Concentrated percentage 69.8 wt% from assay. First you must determine the molarity of the concentrated solution,

Molarity = [(%)(d)/(MW)] * 10

For this assay amount the figure will be thus

M = [(69.8)(1.42) / (63.01)] * 10

$\therefore$ M = 15.73

This is the initial concentration C_I. To determine the molarity of the 7% solution will be thus:

M = [(7)(1.42) / (63.01)] * 10

$\therefore$ M = 1.58

This is the final concentration C_F. We use these figures in the following concentration to determine the amount of dilution required to dilute the concentrated nitric acid to make it a 7% solution.

$mass_I$ * $concentration_I$ = $mass_F$ * $concentration_F$

Now as we are talking about solutions the amount of mass will be measured in mL, and the concentration will be measured as a molarity, where M_I and M_F have been calculated above. In addition, the amount of dilute solution will be dependent on the user and how much is required by the user to complete the ICP analysis, for the sake of argument let's say that we need 10 mL of dilute solution, this is mL_F.

mL_I * C_I = mL_F * C_F

$\therefore$ mL_I = [mL_F * C_F]/C_I

mL_I = [10*1.58] / 15.73

$\therefore$ mL_I = 10.03 mL

This means that 10.03 mL of the concentrated nitric acid (69.8%) should be diluted up to a total of 100 mL with nanopure water.

Now that you have your stock solution with the correct percentage then you can use this solution to prepare your solutions of varying concentration. Let's take the example that the stock solution that you purchase from a supplier has a concentration of 100 ppm of analyte, which is equivalent to 1 μg/mL.

In order to make your calibration curve more accurate it is important to be aware of two issues. Firstly as with all straight-line graphs, the more points that make up the line then the better the statistics is that the line is correct. But, secondly, the more points that are used to make up the straight line mean that more room for error is introduced to the system, to avoid these errors from occurring one should be very vigilant and skilled in the use of pipetting and diluting of solutions. Especially when working with very low concentration solutions a small drop of material making the dilution above or below the exactly required amount can alter the concentration and hence affect the calibration deleteriously. The premise upon which the calculation is done is based on the same equation as earlier:

mL_I * C_I = mL_F * C_F

whereby C refers to concentration in ppm, and mL refers to mass in mL.

The choice of concentrations to make will depend on the samples and the concentration of analyte within the samples that are being analyzed. For first time users it is wise to make a calibration curve with a large range to encompass all the possible outcomes. When the user is more aware of the kind of concentrations that they are producing in their synthesis then they can narrow down the range to fit the kind of concentrations that they are anticipating.

In this example we will make concentrations ranging from 10 ppm to 0.1 ppm, with a total of five samples. In a typical ICP-AES analysis about 3 mL of solution is used, however if you have situations with substantial wavelength overlap then you may have chosen to do two separate runs and so you will need approximately 6 mL solution. In general it is wise to have at least 10 mL of solution to prepare for any eventuality that may

occur. There will also be some extra amount needed for samples that are being used for the quality control check. For this reason 10 mL should be a sufficient amount to prepare of each concentration.

We can define the unknowns in the equation as follows:

C_I = concentration of concentrated solution (ppm)

C_F = desired concentration (ppm)

M_I = initial mass of material (mL)

M_F = mass of material required for dilution (mL)

The methodology adopted works as follows. Make the high concentration solution then take from that solution and dilute further to the desired concentrations that are required.

Let's say the concentration of the stock solution from the supplier is 100 ppm of analyte. First we should dilute to a concentration of 10 ppm. To make 10 mL of 10 ppm solution we should take 1 mL of the 100 ppm solution and dilute it up to 10 mL with nanopure water, now the concentration of this solution is 10 ppm. Then we can take from the 10 ppm solution and dilute this down to get a solution with 5 ppm. To do this take 5 mL of the 10 ppm solution and dilute it to 10 mL with nanopure water, then you will have a solution of 10 mL that is 5 ppm concentration. And so you can do this successively taking aliquots from each solution working your way down at incremental steps until you have a series of solutions that have concentrations ranging from 10 ppm all the way down to 0.1 ppm or lower, as required.

3.11.5 ICP-AES at work

While ICP-AES is a useful method for quantifying the presence of a single metal in a given nanoparticle, another very important application comes from the ability to determine the ratio of metals within a sample of nanoparticles.

In the following examples we can consider the bi-metallic nanoparticles of iron with copper. In a typical synthesis 0.75 mmol of $Fe(acac)_3$ is used to prepare iron-oxide nanoparticle of the form Fe_3O_4. It is possible to replace a quantity of the Fe^{n+} ions with another metal of similar charge. In this manner bi-metallic particles were made with a precursor containing a suitable metal. In this example the additional metal precursor will be $Cu(acac)_2$.

Keep the total metal concentration in this example is 0.75 mmol. So if we want to see the effect of having 10% of the metal in the reaction as copper, then we will use 10% of 0.75 mmol, that is 0.075 mmol $Cu(acac)_2$, and the corresponding amount of iron is 0.675 mmol $Fe(acac)_3$. We can do this for successive increments of the metals until you make 100% copper oxide particles.

Subsequent Fe and Cu ICP-AES of the samples will allow the determination of Fe:Cu ratio that is present in the nanoparticle. This can be compared to the ratio of Fe and Cu that was applied as reactants. The graph Figure 3.69 shows how the percentage of Fe in the nanoparticle changes as a function of how much Fe is used as a reagent.

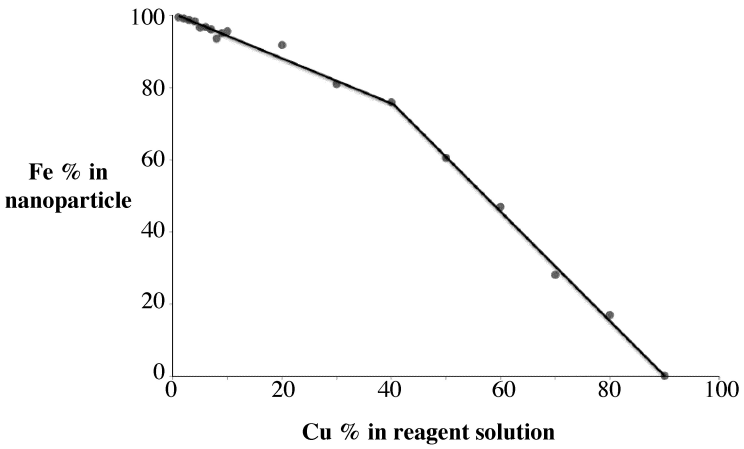

Figure 3.69: Change in iron percentage in the Fe-Cu-O nanoparticles as a function of how much iron precursor is used in the synthesis of the nanoparticles.

3.11.5.1 Determining analyte concentration

Once the nanoparticles are digested and the ICP-AES analysis has been completed you must turn the figures from the ICP-AES analysis into working numbers to determine the concentration of metals in the solution that was synthesized initially.

Let's first consider the nanoparticles that are of one metal alone. The figure given by the analysis in this case is given in units of mg/L, this is the value in ppm's. This figure was recorded for the solution that was analyzed, and this is of a dilute concentration compared to the initial synthesized solution because the particles had to be digested in acid first, then diluted further into nanopure water.

As mentioned above in the experimental 0.5 mL of the synthesized nanoparticles were first digested in 9.5 mL of concentrated nitric acid. Then when the digestion was complete 0.5 mL of this solution was dissolved in 9.5 mL of nanopure water. This was the final solution that was analyzed using ICP, and the concentration of metal in this solution will be far lower than that of the original solution. In this case the amount of analyte in the final solution being analyzed is $1/20^{th}$ that of the total amount of material in the solution that was originally synthesized.

3.11.5.2 Calculating concentration in ppm

Let us take an example that upon analysis by ICP-AES the amount of Fe detected is 6.38 mg/L. First convert the figure to mg/mL, by the following simple multiplication:

6.38 mg/L * 1/1000 L/mL = 6.38 $x10^{-3}$ mg/mL

The amount of material was diluted to a total volume of 10 mL. Therefore we should multiply this value by 10 mL to see how much mass was in the whole container.

6.38 $x10^{-3}$ mg/mL * 10 mL = 6.38 $x10^{-2}$ mg

This is the total mass of iron that was present in the solution that was analyzed using the ICP device. To convert this amount to ppm we should take into consideration the fact that 0.5 mL was initially diluted to 10 mL, to do this we should divide the total mass of iron by this amount that it was diluted to.

6.38 $x10^{-2}$ mg / 0.5 mL = 0.1276 mg/mL

This was the total amount of analyte in the 10 mL solution that was analyzed by the ICP device, to attain the value in ppm it should be mulitplied by a thousand, that is then 127.6 ppm of Fe.

3.11.5.3 Determining concentration of original solution

We now need to factor in the fact that there were several dilutions of the original solution first to digest the metals and then to dissolve them in nanopure water, in all there were two dilutions and each dilution was equivalent in mass. By diluting 0.5 mL to 10 mL , we are effectively diluting the solution by a factor of 20, and this was carried out twice.

0.1276 mg/mL * 20 = 2.552 mg/mL

This is the amount of analyte in the solution of digested particles, to covert this to ppm we should multiply it by 1/1000 mL/L, in the following way:

2.552 mg/mL * 1/1000 mL/L = 2552 mg/L

This is essentially your answer now as 2552 ppm. This is the amount of Fe in the solution of digested particles.

This was made by diluting 0.5 mL of the original solution into 9.5 mL concentrated nitric acid, which is the same as diluting by a factor of 20. To calculate how much analyte was in the original batch that was synthesized we multiply the previous figure by 20 again.

2552 ppm * 20 = 51040 ppm

This is the final amount of Fe concentration of the original batch when it was synthesized and made soluble in Hexanes.

3.11.5.4 Calculating stoichiometric ratio

Moving from calculating the concentration of individual elements now we can concentrate on the calculation of stoichiometric ratios in the bi-metallic nanoparticles.

Consider the case when we have the iron and the copper elements in the nanoparticle. The amounts determined by ICP are: iron 1.429 mg/L, and copper is 1.837 mg/L.

We must account for the molecular weights of each element by dividing the ICP obtained value, by the molecular weight for that particular element. For iron this is done simply by 1.429 mg/L / 55.85 = 0.0211. This is molar ratio of iron.

On the other hand the ICP returns a value for copper that is 1.837 mg/L / 63.55 = 0.0289.

Now to determine the percentage iron we use this simple formula:

%Fe = [(molar ratio of iron)/(sum of molar ratios)] * 100.

This gives a percentage value of 42.15% Fe.

To work out the copper percentage we calculate this amount using this equation:

% Cu = [(molar ratio of copper)/(sum of molar ratios)] * 100

This leads to an answer of 57.85% Cu.

In this way the percentage iron in the nanoparticle can be determined as function of the reagent concentration prior to the synthesis (Figure 3.69).

3.11.5.5 Determining concentration of nanoparticles in solution

The previous examples have shown how to calculate both the concentration of one analyte and the effective shared concentration of metals in the solution. These figures pertain to the concentration of elemental atoms present in solution. To use this to determine the concentration of nanoparticles we must first consider how many atoms that are being detected are in a nanoparticle. Let us consider that the Fe_3O_4 nanoparticles are of 7 nm diameter. In a 7 nm particle we expect to find 20,000 atoms. However in this analysis we have only detected Fe atoms, so we must still account for the number of oxygen atoms that form the crystal lattice also.

For every 3 Fe atoms, there are 4 O atoms. But as iron is slightly larger than oxygen, it will make up for the fact there is one less Fe atom. This is an over simplification but at this time it serves the purpose

to make the reader aware of the steps that are required to take when judging nanoparticles concentration. Let us consider that half of the nanoparticle size is attributed to iron atoms, and the other half of the size is attributed to oxygen atoms.

As there are 20,000 atoms total in a 7 nm particle, and then when considering the effect of the oxide state we will say that for every 10,000 atoms of Fe you will have a 7 nm particle. So now we must find out how many Fe atoms are present in the sample so we can divide by 10,000 to determine how many nanoparticles are present.

In the case from above, we found the solution when synthesized had a concentration 51,040 ppm Fe atoms in solution. To determine how how many atoms this equates to we will use the fact that 1 mole of material has the Avogadro number of atoms present.

51040 ppm = 51040 mg/L = 51.040 g/L.

1 mole of iron weighs 55.847 g. To determine how many moles we now have, we divide the values like this:

(51.040 g/L) / (55.847 g) = 0.9139 moles / L

The number of atoms is found by multiplying this by Avogadro's number:

(0.9139 moles/L) * (6.022 x10^{23} atoms) = 5.5 x10^{23} atoms/L

For every 10,000 atoms we have a nanoparticle of 7 nm diameter, assuming all the particles are equivalent in size we can then divide the values:

(5.5 x10^{23} atoms/L) / (10,000 atoms/np) = 5.5 x10^{19} np/L

This is the concentration of nanoparticles per liter of solution as synthesized.

3.11.5.6 Combined surface area

One very interesting thing about nanotechnology that nanoparticles can be used for is their incredible ratio between the surface areas compared with the volume. As the particles get smaller and smaller the surface area becomes more prominent. And as much of the chemistry is done on surfaces, nanoparticles are good contenders for future use where high aspect ratios are required.

In the example above we considered the particles to be of 7 nm diameters. The surface area of such a particle is 1.539 x10^{-16} m^2. So the combined surface area of all the particles is found by multiplying each particle by their individual surface areas.

(1.539 x10^{-16} m^2) * (5.5 x10^{19} np/L) = 8465 m^2/L

To put this into context, an American football field is approximately 5321 m^2. So a liter of this nanoparticle solution would have the same surface area of approximately 1.5 football fields. That is allot of area in one liter of solution when you consider how much material it would take to line the football field with thin layer of metallic iron. Remember there is only about 51 g/L of iron in this solution!

3.11.6 Bibliography

- http://www.ivstandards.com/extras/pertable/[20]
- A. Scheffer, C. Engelhard, M. Sperling, and W. Buscher, W. *Anal. Bioanal. Chem.*, 2008, **390**, 249.
- H. Nakamuru, T. Shimizu, M. Uehara, Y. Yamaguchi, and H. Maeda, *Mater. Res. Soc., Symp. Proc.*, 2007, **1056**, 11.
- S. Sun and H. Zeng, *J. Am. Chem. Soc.*, 2002, **124**, 8204.
- C. A. Crouse and A. R. Barron, *J. Mater. Chem.*, 2008, **18**, 4146.

[20] http://www.ivstandards.com/extras/pertable/

3.12 TGA/DSC-FTIR Characterization of Oxide Nanaoparticles[21]

3.12.1 Metal oxide nanoparticles

The binary compound of one or more oxygen atoms with at least one metal atom that forms a structure ≤100 nm is classified as metal oxide (MO_x) nanoparticle. MO_x nanoparticles have exceptional physical and chemical properties (especially if they are smaller than 10 nm) that are strongly related to their dimensions and to their morphology. These enhanced features are due to the increased surface to volume ratio which has a strong impact on the measured binding energies. Based on theoretical models, binding or cohesive energy is inversely related to particle size with a linear relationship (3.32).

$$E_{\mathrm{NP}} = E_{\mathrm{bulk}} \cdot \left[1 - c \cdot r^{-1}\right] \tag{3.32}$$

where E_{NP} *and* E_{bulk} is the binding energy of the nanoparticle and the bulk binding energy respectively, c is a material constant and r is the radius of the cluster. As seen from (3.32), nanoparticles have lower binding energies than bulk material, which means lower electron cloud density and therefore more mobile electrons. This is one of the features that have been identified to contribute to a series of physical and chemical properties.

3.12.1.1 Synthesis of metal oxide nanoparticles

Since today, numerous synthetic methods have been developed with the most common ones presented in Table 3.5. These methods have been successfully applied for the synthesis of a variety of materials with 0-D to 3-D complex structures. Among them, the solvothermal methods are by far the most popular ones due to their simplicity. Between the two classes of solvothermal methods, slow decomposition methods, usually called thermal decomposition methods, are preferred over the hot injection methods since they are less complicated, less dangerous and avoid the use of additional solvents.

Method	Characteristics	Advantages	Disadvantages
Solvothermal a) Slow decomposition b) Hot injection	a) Slow heating of M-precursor in the presence of ligand/surfactant precursor b) Injection of M-precursor into solution at high Temp.	a) Safe, easily carried out, variety of M-precursors to use b) Excellent control of particle distribution	a) Poor control of nucleation/ growth stages – Particle size b) Hazardous, Reproducibility depends on individual

continued on next page

[21] This content is available online at <http://cnx.org/content/m23038/1.2/>.

Template directed	Use of organic molecules or preexistent nanoparticles as templates for directing nanoparticle formation	High yield and high purity of nanoparticles	Template removal in some cases causes particle deformation or loss
Sonochemical	Ultrasound influence particle nucleation	Mild synthesis conditions	Limited applicability
Thermal evaporation	Thermal evaporation of Metal oxides	Monodisperse particle formation, excellent control in shape and structure	Extremely high temperatures, and vacuum system is required
Gas phase catalytic growth	Use of catalyst that serves as a preferential site for absorbing Metal reactants	Excellent control in shape and structure	Limited applicability

Table 3.5: Methods for synthesizing MO_x nanoparticles

A general schematic diagram of the stages involving the nanoparticles formation is shown in Figure 3.70. As seen, first step is the M-atom generation by dissociation of the metal-precursor. Next step is the M-complex formulation, which is carried out before the actual particle assembly stage. Between this step and the final particle formulation, oxidation of the activated complex occurs upon interaction with an oxidant substance. The x-axis is a function of temperature or time or both depending on the synthesis procedure.

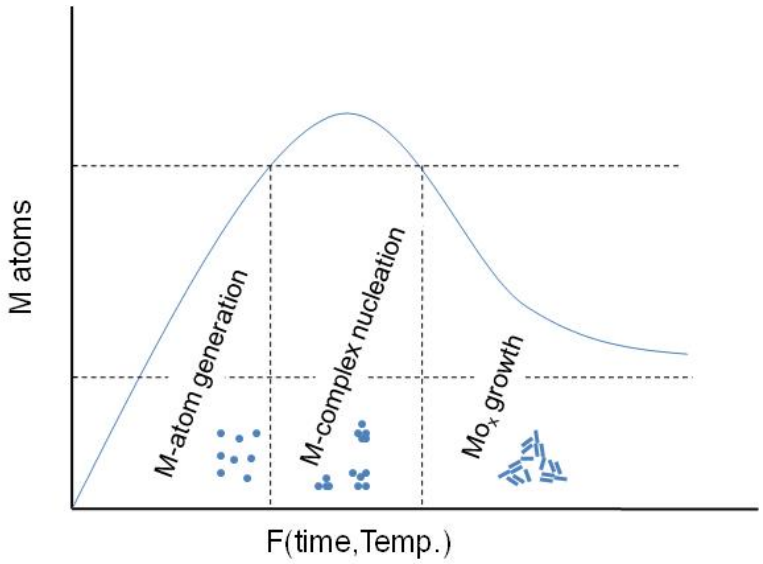

Figure 3.70: Stages of nanoparticle synthesis.

In all cases, the particles synthesized consist of MO_x nanoparticle structures stabilized by one or more types of ligand(s) as seen in Figure 3.71. The ligands are usually long-chained organic molecules that have

one more functional groups. These molecules protect the nanoparticles from attracting each other under van der Waals forces and therefore prevent them from aggregating.

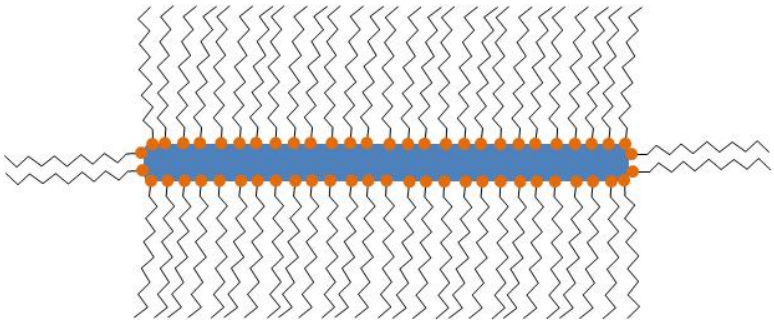

Figure 3.71: Schematic representation of a surfactant/ligand stabilized nanoparticle.

Even though often not referred to specifically, all particles synthesized are stabilized by organic (hydrophilic, hydrophobic or amphoteric) ligands. The detection and the understanding of the structure of these ligands can be of critical importance for understanding the controlling the properties of the synthesized nanoparticles.

3.12.1.1.1 Metal oxide nanoparticles synthesized via slow decomposition

In this work, we refer to MO_x nanoparticles synthesized via slow decomposition of a metal complex. In Table 3.6, a number of different MO_x nanoparticles are presented, synthesized via metal complex dissociation. Metal–MO_x and mixed MO_x nanoparticles are not discussed here.

Metal oxide	**Shape**	**Size (approx.)**
Cerium oxide	dots	5-20 nm
Iron oxide	dots, cubes	8.5-23.4 nm
Manganese oxide	Multipods	>50 nm
Zinc oxide	Hexagonal pyramid	15-25 nm
Cobalt oxide	dots	$\sim$ 10 nm
Chromium oxide	dots	12 nm
Vanadium oxide	dots	9-15 nm
Molybdenum oxide	dots	5 nm
Rhodium oxide	dots,rods	16 nm
Palladium oxide	dots	18 nm
Ruthenium oxide	dots	9-14 nm
Zirconium oxide	rods	7x30 nm
Barium oxide	dots	20 nm
Magnesium oxide	dots	4-8 nm
Calcium oxide	dots, rods	7-12 nm
Nickel oxide	dots	8-15 nm
Titanium oxide	dots and rods	2.3-30 nm
Tin oxide	dots	2.0-5.0 nm
Indium oxide	dots	$\sim$ 5 nm
Samaria	Square	$\sim$ 10 nm

Table 3.6: Examples of MO_x nanoparticles synthesized via decomposition of metal complexes.

A significant number of metal oxides synthesized using slow decomposition is reported in literature. If we use the periodic table to map the different MO_x nanoparticles (Figure 3.72), we notice that most of the alkali and transition metals generate MO_x nanoparticles, while only a few of the poor metals seem to do so, using this synthetic route. Moreover, two of the rare earth metals (Ce and Sm) have been reported to successfully give metal oxide nanoparticles via slow decomposition.

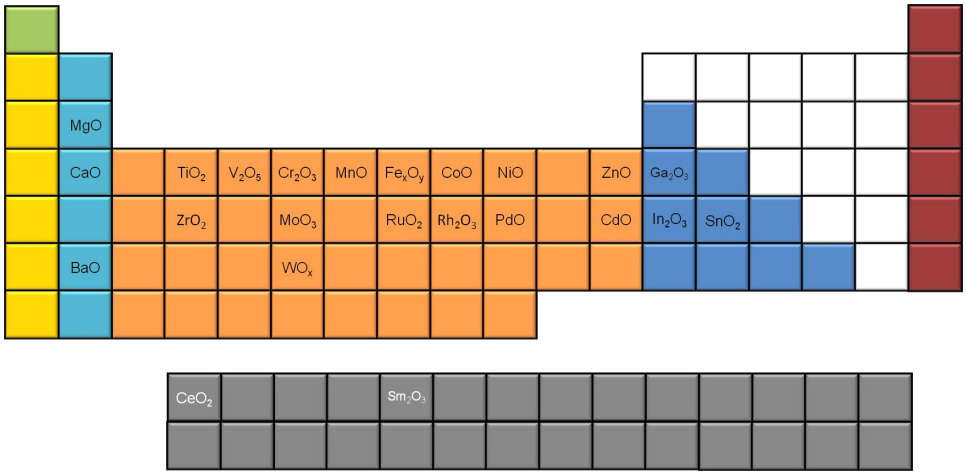

Figure 3.72: "Periodic" table of MO_x nanoparticles synthesized using the slow decomposition technique.

Among the different characterization techniques used for defining these structures, transition electron microscopy (TEM) holds the lion's share. Nevertheless, most of the modern characterization methods are more important when it comes to understanding the properties of nanoparticles. X-ray photoelectron spectroscopy (XPS), X-ray diffraction (XRD), nuclear magnetic resonance (NMR), IR spectroscopy, Raman spectroscopy, and thermogravimetric analysis (TGA) methods are systematically used for characterization.

3.12.1.2 Synthesis and characterization of WO_{3-x} nanorods

The synthesis of WO_{3-x} nanorods is based on the method published by Lee et al. A slurry mixture of $Me_3NO \bullet 2H_2O$, oleylamine and $W(CO)_6$ was heated up to 250 °C at a rate of 3 °C/min (Figure 3.73). The mixture was aged at this temperature for 3 hours before cooling down to room temperature.

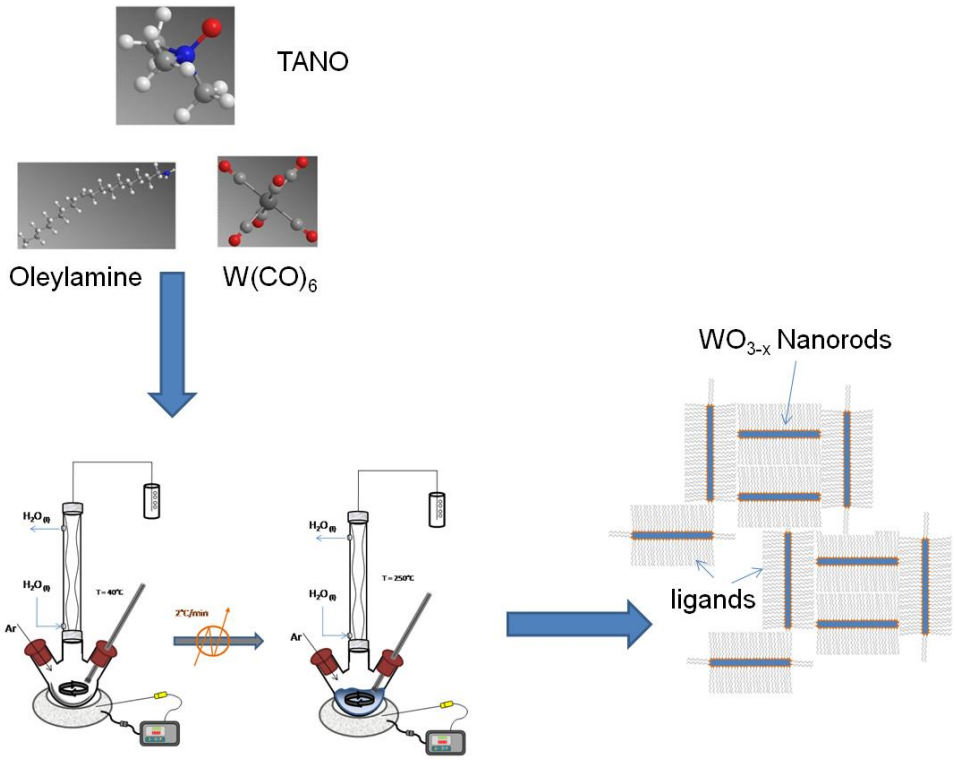

Figure 3.73: Experimental setup for synthesis of WO_{3-x} nanorods.

Multiple color variations were observed between 100 - 250 °C with the final product having a dark blue color. Tungsten oxide nanorods ($W_{18}O_{49}$ identified by XRD) with a diameter of 7±2 nm and 50±2 nm long were acquired after centrifugation of the product solution. A TEM image of the $W_{18}O_{49}$ nanorods is shown in Figure 3.74.

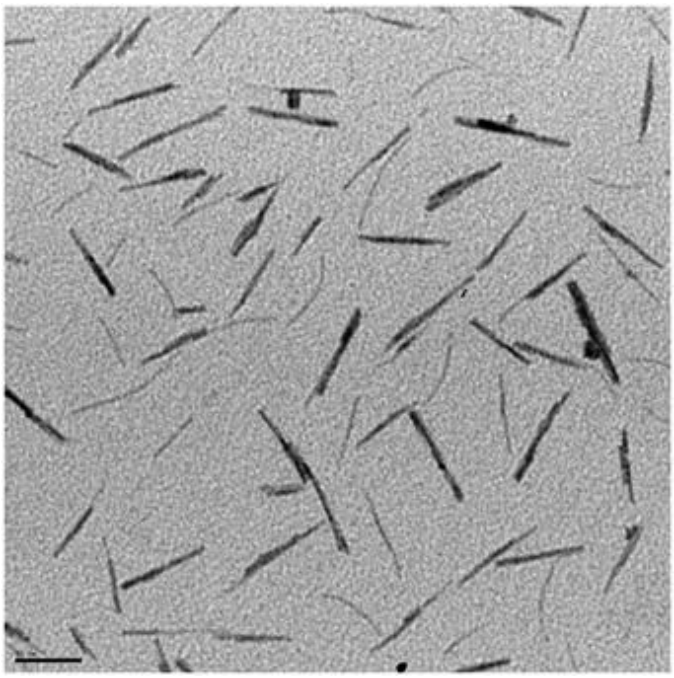

Figure 3.74: TEM image of WO_{3-x} nanorods.

3.12.2 Thermogravimetric analysis (TGA)/differential scanning calorimetry (DSC)

Thermogravimetric analysis (TGA) is a technique widely used for determining the organic and inorganic content of various materials. Its basic rule of function is the high precision measurement of weight gain/loss with increasing temperature under inert or reactive atmospheres. Each weight change corresponds to physical (crystallization, phase transformation) or chemical (oxidation, reduction, reaction) processes that take place by increasing the temperature. The sample is placed into platinum or alumina pan and along with an empty or standard pan are placed onto two high precision balances inside a high temperature oven. A method for pretreating the samples is selected and the procedure is initiated. Differential scanning calorimetry (DSC) is a technique usually accompanying TGA and is used for calculating enthalpy energy changes or heat capacity changes associated with phase transitions and/or ligand-binding energy cleavage.

In Figure 3.75 the TGA/DSC plot acquired for the ligand decomposition of WO_{3-x} nanorods is presented. The sample was heated at constant rate under N_2 atmosphere up to 195 °C for removing moisture and then up to 700 °C for removing the oleylamine ligands. It is important to use an inert gas for performing such a study to avoid any premature oxidation and/or capping agent combustion. 26.5% of the weight loss is due to oleylamine evaporations which means about 0.004 moles per gram of sample. After isothermal heating at 700 °C for 25 min the flow was switched to air for oxidizing the ligand-free WO_{3-x} to WO_3. From the DSC curve we noticed the following changes of the weight corrected heat flow:

1. From 0 – 10 min assigned to water evaporation.
2. From 65 – 75 min assigned to OA evaporation.

3. From 155 – 164 min assigned to WO_{3-x} oxidation.
4. From 168 – 175 min is also due to further oxidation of W^{5+} atoms.

The heat flow increase during the WO_{3-x} to WO_3 oxidation is proportional to the crystal phase defects (or W atoms of oxidation state +5) and can be used for performing qualitative studies between different WO_x nanoparticles.

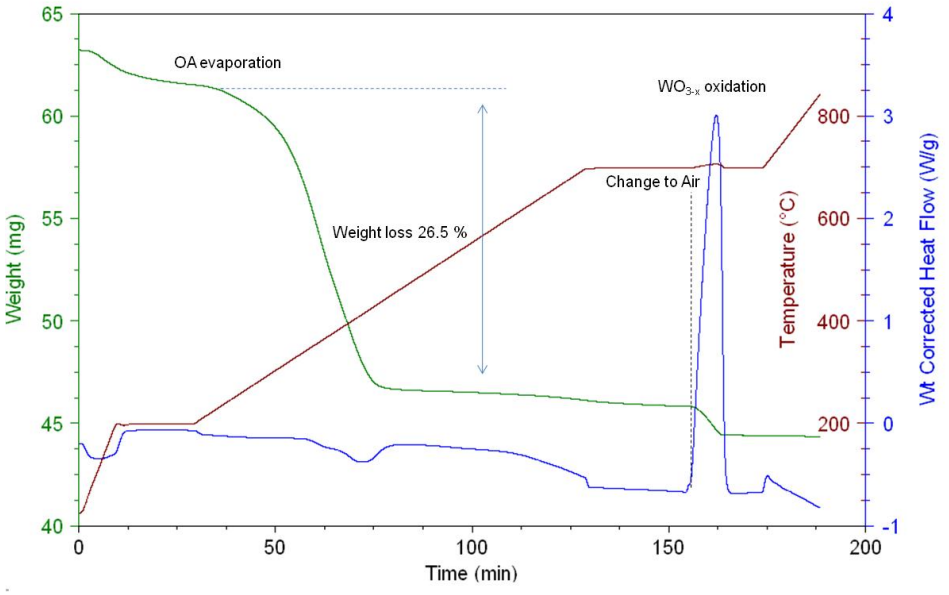

Figure 3.75: TGA/DSC plot for WO_{3-x} nanorods.

The detailed information about the procedure used to acquire the TGA/DSC plot shown in Figure 3.75 is as follows.

Step 1. Select gas (N_2 with flow rate 50 mL/min.)
Step 2. Ramp 20 °C/min to 200 °C.
Step 3. Isothermal for 20 min.
Step 4. Ramp 5 °C/min to 700 °C.
Step 5. Isothermal for 25 min.
Step 6. Select gas (air).
Step 7. Isothermal for 20 min.
Step 8. Ramp 10 °C/min to 850 °C.
Step 9. Cool down

3.12.3 Fourier transform infrared spectroscopy

Fourier transform infrared spectroscopy (FTIR) is the most popular spectroscopic method used for characterizing organic and inorganic compounds. The basic modification of an FTIR from a regular IR instrument is a device called interferometer, which generates a signal that allows very fast IR spectrum acquisition. For

doing so, the generatated interferogram has to be "expanded" using a Fourier transformation to generate a complete IR frequency spectrum. In the case of performing FTIR transmission studies the intensity of the transmitted signal is measured and the IR fingerprint is generated (3.33).

$$T = \frac{I}{I_b} = e^{c\varepsilon l} \tag{3.33}$$

Where I is the intensity of the samples, I_b is the intensity of the background, c is the concentration of the compound, ε is the molar extinction coefficient and l is the distance that light travels through the material. A transformation of transmission to absorption spectra is usually performed and the actual concentration of the component can be calculated by applying the Beer-Lambert law (3.34).

$$A = -\ln(T) = c\varepsilon l \tag{3.34}$$

A qualitative IR-band map is presented in Figure 3.76. The absorption bands between 4000 to 1600 cm^{-1} represent the group frequency region and are used to identify the stretching vibrations of different bonds. At lower frequencies (from 1600 to 400 cm^{-1}) vibrations due to intermolecular bond bending occurs upon IR excitation and therefore are usually not taken into account.

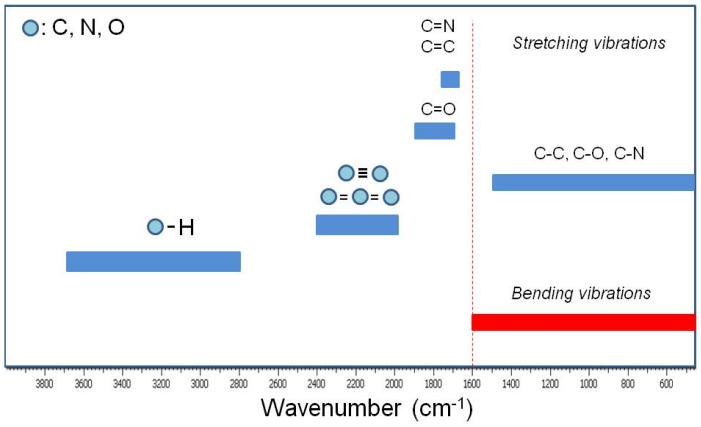

Figure 3.76: Selected FTIR stretching and bending modes associated with the typical ligands used for nanoparticle stabilization.

3.12.4 TGA/DSC–FTIR characterization

TGA/DSC is a powerful tool for identifying the different compounds evolved during the controlled pyrolysis and therefore provide qualitative and quantitative information about the volatile components of the sample. In metal oxide nanoparticle synthesis TGA/DSC-FTIR studies can provide qualitative and quantitative information about the volatile compounds of the nanoparticles.

TGA–FTIR results presented below were acquired using a Q600 Simultaneous TGA/DSC (SDT) instrument online with a Nicolet 5700 FTIR spectrometer. This system has a digital mass flow control and two gas inlets giving the capability to switch reacting gas during each run. It allows simultaneous weight change and differential heat flow measurements up to 1500 °C, while at the same time the outflow line is connected to the FTIR for performing gas phase compound identification. Grand-Schmidt thermographs were usually constructed to present the species evolution with time in 3 dimensions.

Selected IR spectra are presented in Figure 3.77. Four regions with intense peaks are observed. Between 4000 – 3550 cm^{-1} due to O-H bond stretching assigned to H_2O that is always present and due to due to N-H group stretching that is assigned to the amine group of oleylamine. Between 2400 – 2250 cm^{-1} due to O=C=O stretching, between 1900 – 1400 cm^{-1} which is mainly to C=O stretching and between 800 – 400 cm^{-1} cannot be resolved as explained previously.

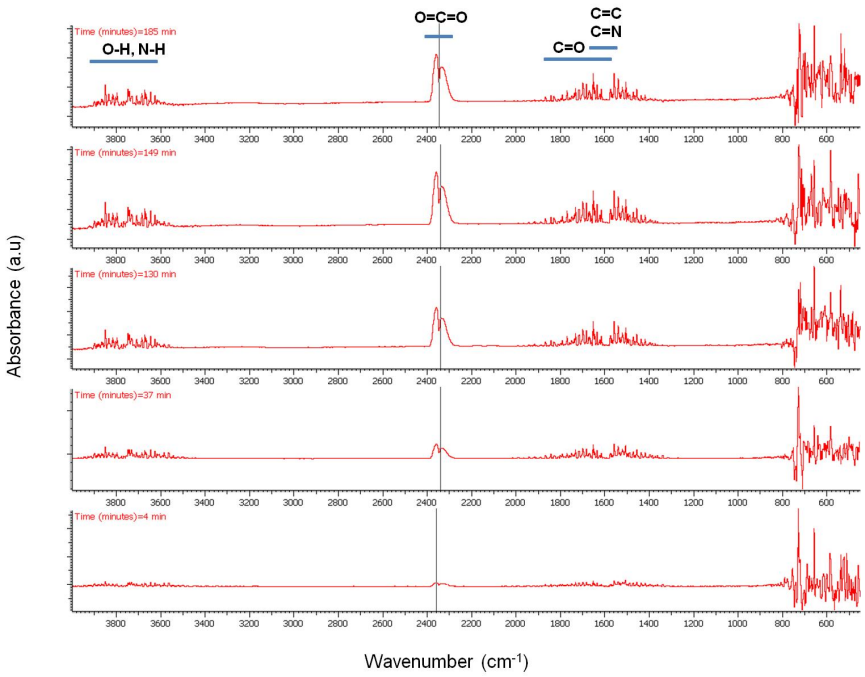

Figure 3.77: FTIR spectra of products from WO_{3-x} pyrolysis.

The peak intensity evolution with time can be more easily observed in Figure 3.78 and Figure 3.79. As seen, CO_2 evolution increases significantly with time especially after switching our flow from N_2 to air. H_2O seems to be present in the outflow stream up to 700 °C while the majority of the N-H amine peaks seem to disappear at about 75 min. C=N compounds are not expected to be present in the stream which leaves bands between 1900 – 1400 cm^{-1} assigned to C=C and C=O stretching vibrations. Unsaturated olefins resulting from the cracking of the oleylamine molecule are possible at elevated temperatures as well as the presence of CO especially under N_2 atmosphere.

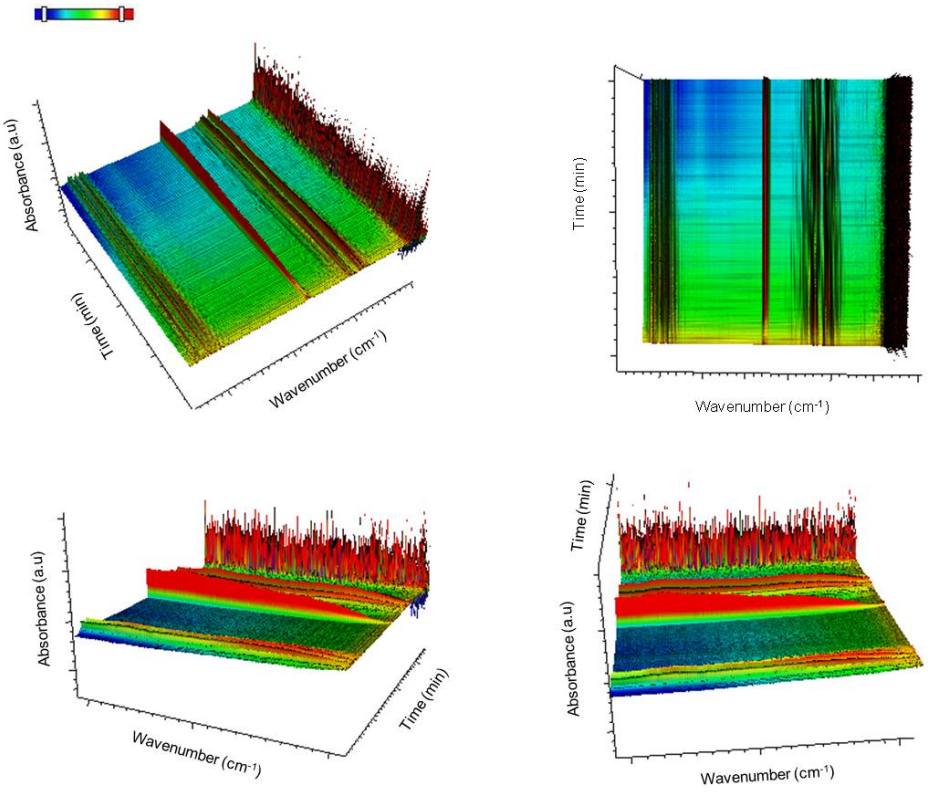

Figure 3.78: 3D representation of FTIR Spectra of the volatile compounds of WO_{3-x}.

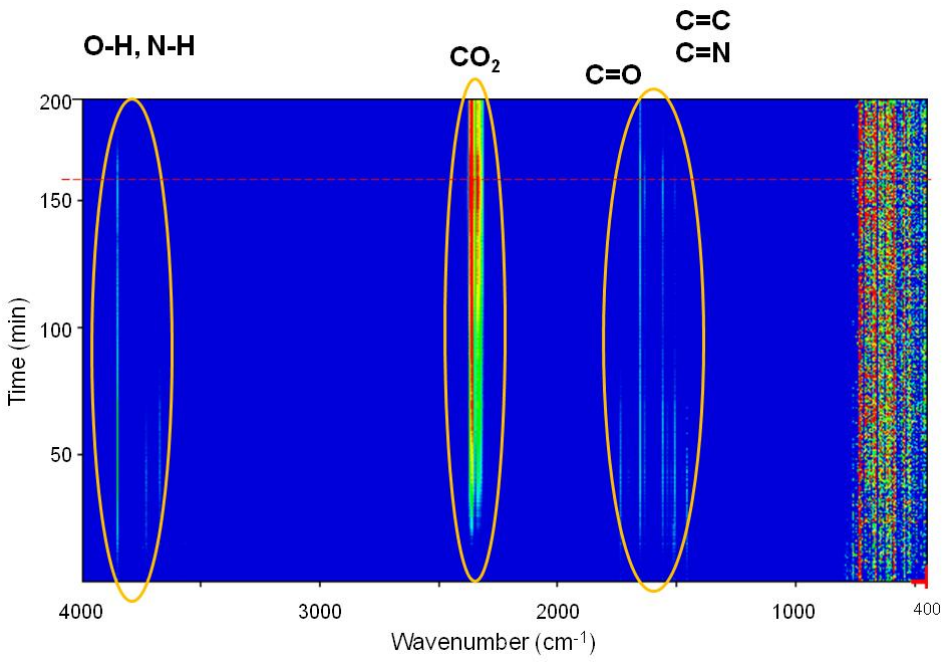

Figure 3.79: Intensity profile of FTIR spectra of the volatile compounds formed from the pyrolysis of WO_{3-x}.

From the above compound identification we can summarize and propose the following applications for TGA-FTIR. First, more complex ligands, containing aromatic rings and maybe other functional groups may provide more insight in the ligand to MO_x interaction. Second, the presence of CO and CO_2 even under N_2 flow means that complete O_2 removal from the TGA and the FTIR cannot be achieved under these conditions. Even though the system was equilibrated for more than an hour, traces of O_2 are existent which create errors in our calculations.

3.12.5 Bibliography

- R. D. Parra and H. H. Farrell, *J. Phys. Chem. C*, 2009, **113**, 4786.
- S. C. Vanithakumari and K. K. Nanda, *J. Phys. Chem. B*, 2006, **110**, 6985.
- M. Wautelet and D. Duvivier, *Eur. J. Phys.*, 2007, **28**, 953.
- X. Wang and Y. Li, *J. Am. Chem. Soc.*, 2002, **124**, 2880.
- F. K. R. N. Greta and R. Patzke, *Angew. Chem., Int. Ed.*, 2002, **41**, 2446.
- Z. W. Pan, Z. R. Dai, and Z. L. Wang, *Science*, 2001, **291**, 1947.
- H. Gu and M. D. Soucek, *Chem. Mater.*, 2007, **19**, 1103.
- L. M. Bronstein, X. Huang, J. Retrum, A. Schmucker, M. Pink, B. D. Stein, and B. Dragnea, *Chem. Mater.*, 2007, **19**, 3624.
- D. Zitoun, N. Pinna, N. Frolet, and C. Belin, *J. Am. Chem. Soc.*, 2005, **127**, 15034.
- S. -H. Choi, E. -G. Kim, J. Park, K. An, N. Lee, S. C. Kim, and T. Hyeon, *J. Phys. Chem., B*, 2005, **109**, 14792.
- M. Epifani, J. Arbiol, R. Diaz, M. J. Peralvarez, P. Siciliano, and J. R. Morante, *Chem. Mater.*, 2005, **17**, 6468.

- T. Yu, J. Joo, Y. I. Park, and T. Hyeon, *J. Am. Chem. Soc.*, 2006, **128**, 1786.
- K. Lee, W. S. Seo, and J. T. Park, *J. Am. Chem. Soc.*, 2003, **125**, 3408.
- C. A. Emeis, *J. Catalysis*, 1993, **141**, 347.
- P. R. Griffiths, J. A. De Haseth, *Fourier Transform Infrared Spectrometry*. Wiley-Interscience, New York (2007)

3.13 Theory of A Superconducting Quantum Interference Device (SQUID)[22]

3.13.1 Introduction

One of the most sensitive forms of magnetometry is SQUID magnetometry. This uses technique uses a combination of superconducting materials and Josephson junctions to measure magnetic fields with resolutions up to $\sim 10^{-14}$ kG or greater. In the proceeding pages we will describe how a SQUID actually works.

3.13.2 Electron-pair waves

In superconductors the resistanceless current is carried by pairs of electrons, known as Cooper Pairs. A Cooper Pair is a pair of electrons. Each electron has a quantized wavelength. With a Cooper pair each electrons wave couples with its opposite number over a large distances. This phenomenon is a result of the very low temperatures at which many materials will superconduct.

What exactly is superconductance? When a material is at very low temperatures, its crystal lattice behaves differently than when it higher temperatures. Usually at higher temperatures a material will have large vibrations called in the crystal lattice. These vibrations scatter electrons as they pass through this lattice (Figure 3.80), and this is the basis for bad conductance.

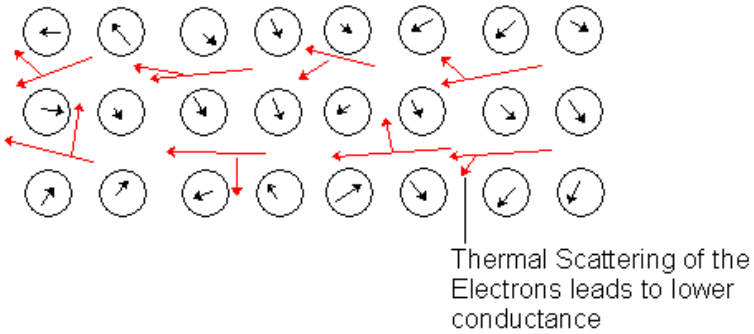

Figure 3.80: Schematic representation of the scattering of electrons as they pass through a vibrating lattice.

[22] This content is available online at <http://cnx.org/content/m22750/1.3/>.

With a superconductor the material is designed to have very small vibrations, these vibrations are lessened even more by cooling the material to extremely low temperatures. With no vibrations there is no scattering of the electrons and this allows the material to superconduct.

The origin of a Cooper pair is that as the electron passes through a crystal lattice at superconducting temperatures it negative charge pulls on the positive charge of the nuclei in the lattice through coulombic interactions producing a ripple. An electron traveling in the opposite direction is attracted by this ripple. This is the origin of the coupling in a Cooper pair (Figure 3.81).

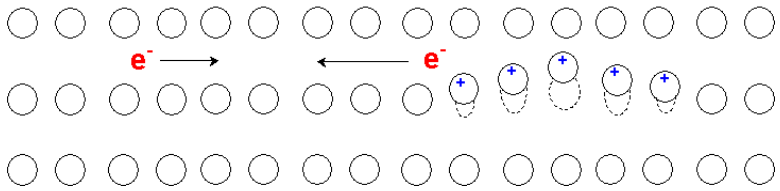

Figure 3.81: Schematic representation of the Cooper pair coupling model.

A passing electron attracts the lattice, causing a slight ripple toward its path. Another electron passing in the opposite direction is attracted to that displacement (Figure 3.82).

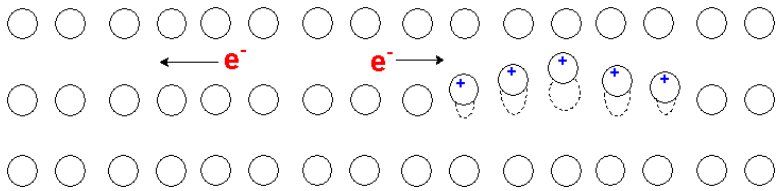

Figure 3.82: Schematic representation of Cooper pair coupling

Due to the coupling and the fact that for each pair there is two spin states (Figure 3.83).

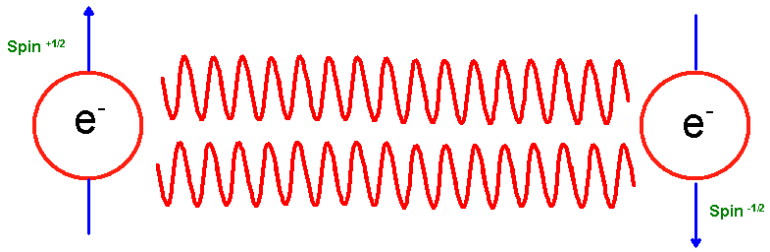

Figure 3.83: Schematic representation of the condensation of the wavelengths of a Cooper pairs

Each pair can be treated as a single particle with a whole spin, not half a spin such as is usually the case with electrons. This is important, as an electron which is classed in a group of matter called Fermions are governed by the Fermi exclusion principle which states that anything with a spin of one half cannot occupy the same space as something with the same spin of one half. This turns the electron means that a Cooper pair is in fact a Boson the opposite of a Fermion and this allows the Coopers pairs to condensate into one wave packet. Each Coopers pair has a mass and charge twice that of a single electron, whose velocity is that of the center of mass of the pair. This coupling can only happen in extremely cold conditions as thermal vibrations become greater than the force that an electron can exert on a lattice. And thus scattering occurs.

Each pair can be represented by a wavefunction of the form

$$\Phi_p = \Phi e^{i(p.r)/\hbar}$$

where P is the net momentum of the pair whose center of mass is at r. However, all the Cooper pairs in a superconductor can be described by a single wavefunction yet again due to the fact that the electrons are in a Coopers pair state and are thus Bosons in the absence of a current because all the pairs have the same phase - they are said to be "phase coherent"

$$\Psi_p = \Psi e^{i(p.r)/\hbar}$$

This electron-pair wave retains its phase coherence over long distances, and essentially produces a standing wave over the device circuit. In a SQUID there are two paths which form a circle and are made with the same standing wave (Figure 3.84). The wave is split in two sent off along different paths, and then recombined to record an interference pattern by adding the difference between the two.

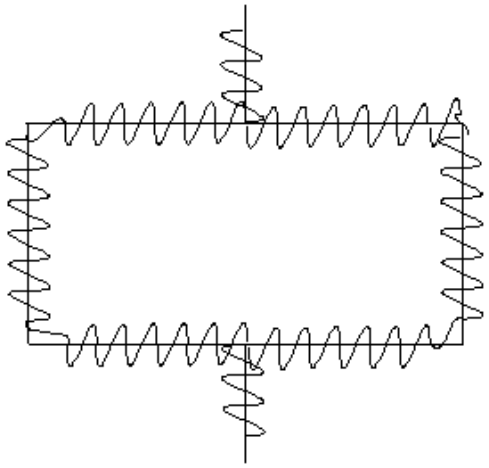

Figure 3.84: Schematic representation of a standing wave across a SQUID circuit.

This allows measurement at any phase differences between the two components, which if there is no interference will be exactly the same, but if there is a difference in their path lengths or in some interaction that the waves encounters such as a magnetic field it will correspond in a phase difference at the end of each path length.

A good example to use is of two water waves emanating from the same point. They will stay in phase if they travel the same distance, but will fall out of phase if one of them has to deviate around an obstruction such as a rock. Measuring the phase difference between the two waves then provides information about the obstruction.

3.13.3 Phase and coherence

Another implication of this long range coherence is the ability to calculate phase and amplitude at any point on the wave's path from the knowledge of its phase and amplitude at any single point, combined with its wavelength and frequency. The wavefunction of the electron-pair wave in the above eqn. can be rewritten in the form of a one-dimensional wave as

$$\Psi_p = \Psi sin 2\pi\left(\frac{x}{\lambda} - vt\right)$$

If we take the wave frequency, V, as being related to the kinetic energy of the Cooper pair with a wavelength, λ, being related to the momentum of the pair by the relation $\lambda = h/p$ then it is possible to evaluate the phase difference between two points in a current carrying superconductor.

If a resistanceless current flows between points X and Y on a superconductor there will be a phase difference between these points that is constant in time.

3.13.4 Effect of a magnetic field

The parameters of a standing wave are dependent on a current passing through the circuit; they are also strongly affected by an applied magnetic field. In the presence of a magnetic field the momentum, p, of a particle with charge q in the presence of a magnetic field becomes $mV + qA$ where A is the magnetic vector potential. For electron-pairs in an applied field their moment P is now equal to $2mV+2eA$.

In an applied magnetic field the phase difference between points X and Y is now a combination of that due to the supercurrent and that due to the applied field.

3.13.5 The fluxoid

One effect of the long range phase coherence is the quantization of magnetic flux in a superconducting ring. This can either be a ring, or a superconductor surrounding a non-superconducting region. Such an arrangement can be seen in Figure 3.85 where region N has a flux density B within it due to supercurrents flowing around it in the superconducting region S.

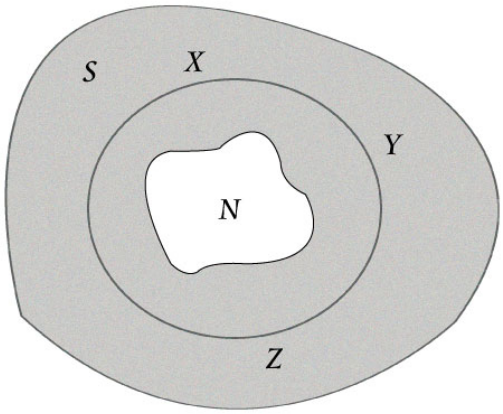

Figure 3.85: Superconductor enclosing a non-superconducting region. Adaped from J. Bland Thesis M. Phys (Hons)., 'A Mossbauer spectroscopy and magnetometry study of magnetic multilayers and oxides.' Oliver Lodge Labs, Dept. Physics, University of Liverpool.

In the closed path XYZ encircling the non-superconducting region there will be a phase difference of the electron-pair wave between any two points, such as X and Y, on the curve due to the field and the circulating current.

If the superelectrons are represented by a single wave then at any point on XYZX it can only have one value of phase and amplitude. Due to the long range coherence the phase is single valued also called quantized meaning around the circumference of the ring $\Delta\phi$ must equal 2πn where n is any integer. Due to the wave only having a single value the fluxoid can only exist in quantized units. This quantum is termed the fluxon, ϕ_0, given by

$$\Phi_0 = \frac{h}{2e} = 2.07x10^{-15}Wb$$

3.13.6 Josephson tunneling

If two superconducting regions are kept totally isolated from each other the phases of the electron-pairs in the two regions will be unrelated. If the two regions are brought together then as they come close electron-pairs will be able to tunnel across the gap and the two electron-pair waves will become coupled. As the separation

decreases, the strength of the coupling increases. The tunneling of the electron-pairs across the gap carries with it a superconducting current as predicted by B.D. Josephson and is called "Josephson tunneling" with the junction between the two superconductors called a "Josephson junction" (Figure 3.86).

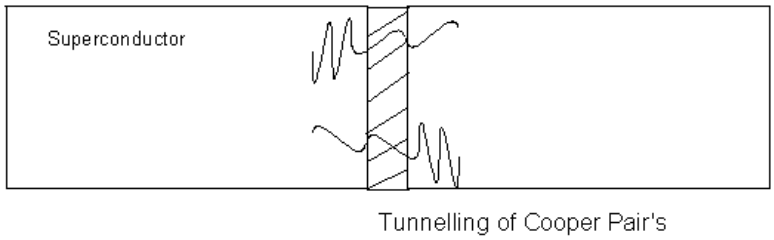

Figure 3.86: Schematic representation of the tunneling of Cooper pairs across a Josephson junction.

The Josephson tunneling junction is a special case of a more general type of weak link between two superconductors. Other forms include constrictions and point contacts but the general form is of a region between two superconductors which has a much lower critical current and through which a magnetic field can penetrate.

3.13.7 Superconducting quantum interference device (SQUID)

A superconducting quantum interference device (SQUID) uses the properties of electron-pair wave coherence and Josephson Junctions to detect very small magnetic fields. The central element of a SQUID is a ring of superconducting material with one or more weak links called Josephesons Junctions. An example is shown in the below. With weak-links at points W and X whose critical current, i_c, is much less than the critical current of the main ring. This produces a very low current density making the momentum of the electron-pairs small. The wavelength of the electron-pairs is thus very long leading to little difference in phase between any parts of the ring.

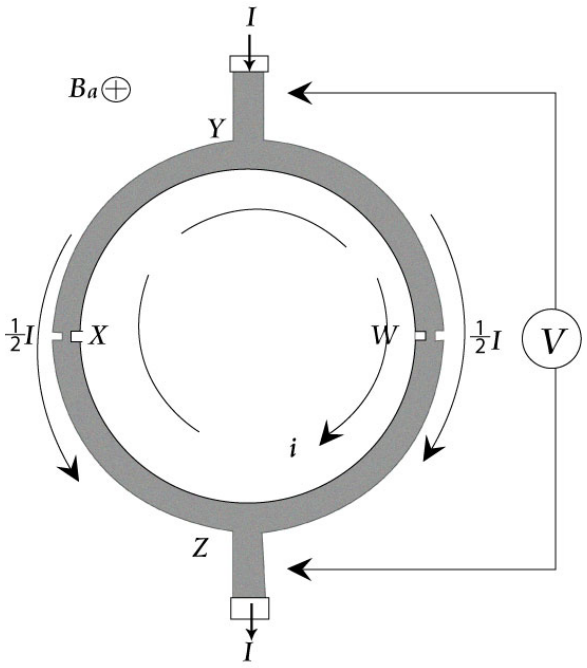

Figure 3.87: Superconducting quantum interference device (SQUID) as a simple magnetometer. Adaped from J. Bland Thesis M. Phys (Hons)., 'A Mossbauer spectroscopy and magnetometry study of magnetic multilayers and oxides.' Oliver Lodge Labs, Dept. Physics, University of Liverpool.

If a magnetic field, Ba , is applied perpendicular to the plane of the ring (Figure 3.88), a phase difference is produced in the electron-pair wave along the path XYW and WZX. One of the features of a superconducting loop is that the magnetic flux, Φ, passing through it which is the product of the magnetic field and the area of the loop and is quantized in units of $\Phi_0 = h/$ (2e), where h is Planck's constant, $2e$ is the charge of the Cooper pair of electrons, and Φ_0 has a value of 2×10^{-15} tesla m^2. If there are no obstacles in the loop, then the superconducting current will compensate for the presence of an arbitrary magnetic field so that the total flux through the loop (due to the external field plus the field generated by the current) is a multiple of Φ_0.

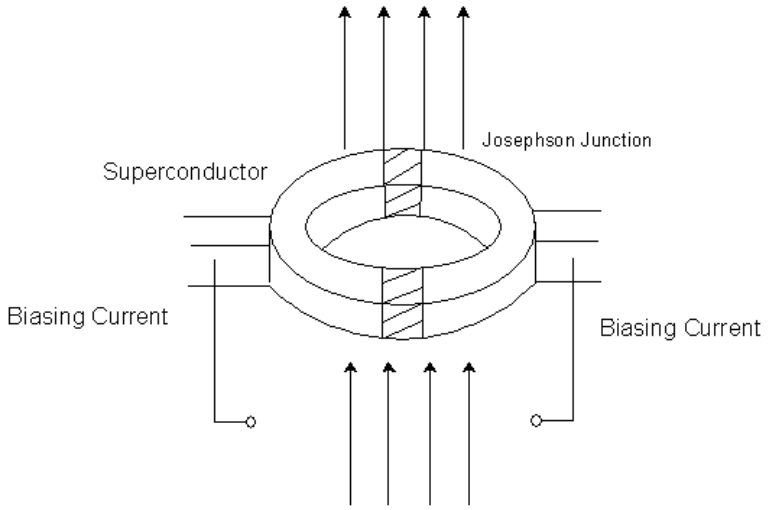

Figure 3.88: Schematic representation of a SQUID placed in a magnetic field.

Josephson predicted that a superconducting current can be sustained in the loop, even if its path is interrupted by an insulating barrier or a normal metal. The SQUID has two such barriers or 'Josephson junctions'. Both junctions introduce the same phase difference when the magnetic flux through the loop is 0, Φ_0, $2\Phi_0$ and so on, which results in constructive interference, and they introduce opposite phase difference when the flux is $\Phi_0/2$, $3\Phi_0/2$ and so on, which leads to destructive interference. This interference causes the critical current density, which is the maximum current that the device can carry without dissipation, to vary. The critical current is so sensitive to the magnetic flux through the superconducting loop that even tiny magnetic moments can be measured. The critical current is usually obtained by measuring the voltage drop across the junction as a function of the total current through the device. Commercial SQUIDs transform the modulation in the critical current to a voltage modulation, which is much easier to measure.

An applied magnetic field produces a phase change around a ring, which in this case is equal

$$\Delta\phi(B) = 2\pi\frac{\Phi_a}{\Phi_0}$$

where Φ_a is the flux produced in the ring by the applied magnetic field. The magnitude of the critical measuring current is dependent upon the critical current of the weak-links and the limit of the phase change around the ring being an integral multiple of 2π. For the whole ring to be superconducting the following condition must be met

$$\alpha + \beta + 2\pi\frac{\Phi_a}{\Phi_o} = n.2\pi$$

where α and β are the phase changes produced by currents across the weak-links and $2\pi\Phi_a/\Phi_o$ is the phase change due to the applied magnetic field.

When the measuring current is applied α and β are no longer equal, although their sum must remain constant. The phase changes can be written as

$$\alpha = \pi\left[n - \frac{\Phi_a}{\Phi_o}\right] - \delta$$

$$\beta = \pi\left[n - \frac{\Phi_a}{\Phi_o}\right] + \delta$$

where δ is related to the measuring current I. Using the relation between current and phase from the above Eqn. and rearranging to eliminate i we obtain an expression for I,

$$I_c = 2i_c \left| cos\pi \frac{\Phi_a}{\Phi_o} . sin\delta \right|$$

As sinδ cannot be greater than unity we can obtain the critical measuring current, I_c from the above

$$I_c = 2i_c \left| cos\pi \frac{\Phi_a}{\Phi_o} \right|$$

which gives a periodic dependence on the magnitude of the magnetic field, with a maximum when this field is an integer number of fluxons and a minimum at half integer values as shown in the below figure.

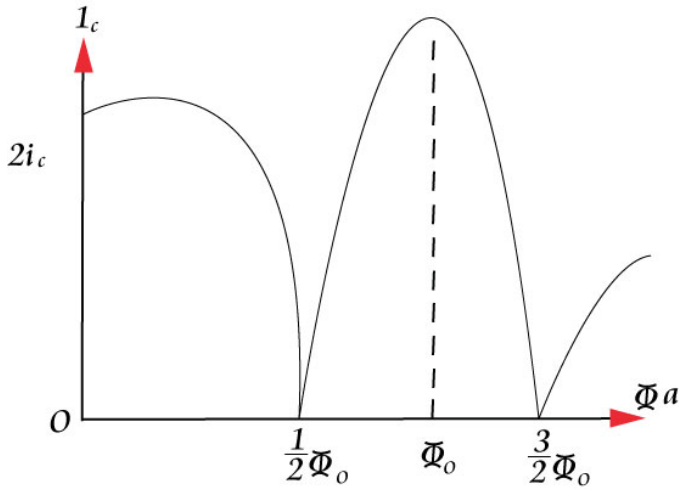

Figure 3.89: Critical measuring current, I_c, as a function of applied magnetic field. Adaped from J. Bland Thesis M. Phys (Hons)., 'A Mossbauer spectroscopy and magnetometry study of magnetic multilayers and oxides.' Oliver Lodge Labs, Dept. Physics, University of Liverpool.

3.13.8 Bibliography

- J. Bland, Thesis M. Phys (Hons)., 'A Mossbauer spectroscopy and magnetometry study of magnetic multilayers and oxides.' Oliver Lodge Labs, Dept. Physics, University of Liverpool.

- J. P. Cleuziou, W. Wernsdorfer, V. Bouchiat,T. Ondarçuhu, and M. Monthioux, *Nature Nanotech.*, 2006, **1**, 53.
- W. G. Jenksy, S. S. H. Sadeghiz, and J. P. Wikswo Jr., *J. Phys. D: Appl. Phys.*, 1997, **30**, 293.
- R. L. Fagaly, *Review of Scientific Instruments*, 2006, **77**, 101101.
- Quantum Design, Operating manual for the MPMS, 1999.

3.14 Practical Guide to Using a Superconducting Quantum Interference Device[23]

SQUIDs offer the ability to measure at sensitivities unachievable by other magnetic sensing methodologies. However, their sensitivity requires proper attention to cryogenics and environmental noise. SQUIDs should only be used when no other sensor is adequate for the task. There are many exotic uses for SQUID however we are just concerned with the laboratory applications of SQUID.

In most physical and chemical laboratories a device called a MPMS (Figure 3.90) is used to measure the magnetic moment of a sample by reading the output of the SQUID detector. In a MPMS the sample moves upward through the electronic pick up coils called gradiometers. One upward movement is one whole scan. Multiple scans are used and added together to improve measurement resolution. After collecting the raw voltages, there is computation of the magnetic moments of the sample.

The MPMS measures the moment of a sample by moving it through a liquid Helium cooled, superconducting sensing coil. Many different measurements can be carried out using an MPMS however we will discuss just a few.

Figure 3.90: A MPMS work station.

[23]This content is available online at <http://cnx.org/content/m22968/1.2/>.

3.14.1 Using an magnetic property measurement dystem (MPMS)

3.14.1.1 DC magnetization

DC magnetization is the magnetic per unit volume (M) of a sample. If the sample doesn't have a permanent magnetic moment, a field is applied to induce one. The sample is then stepped through a superconducting detection array and the SQUID's output voltage is processed and the sample moment computed. Systems can be configured to measure hysteresis loops, relaxation times, magnetic field, and temperature dependence of the magnetic moment.

A DC field can be used to magnetize samples. Typically, the field is fixed and the sample is moved into the detection coil's region of sensitivity. The change in detected magnetization is directly proportional to the magnetic moment of the sample. Commonly referred to as SQUID magnetometers, these systems are properly called SQUID susceptometers (Figure 3.91). They have a homogeneous superconducting magnet to create a very uniform field over the entire sample measuring region and the superconducting pickup loops. The magnet induces a moment allowing a measurement of magnetic susceptibility. The superconducting detection loop array is rigidly mounted in the center of the magnet. This array is configured as a gradient coil to reject external noise sources. The detection coil geometry determines what mathematical algorithm is used to calculate the net magnetization.

An important feature of SQUIDs is that the induced current is independent of the *rate* of flux change. This provides uniform response at all frequencies i.e., true dc response and allows the sample to be moved slowly without degrading performance. As the sample passes through a coil, it changes the flux in that coil by an amount proportional to the magnetic moment M of the sample. The peak-to-peak signal from a complete cycle is thus proportional to twice M. The SQUID sensor shielded inside a niobium can is located where the fringe fields generated by the magnet are less than 10 mT. The detection coil circuitry is typically constructed using NbTi (Figure 3.92). This allows measurements in applied fields of 9 T while maintaining sensitivities of $10{-}8$ emu. Thermal insulation not shown is placed between the detection coils and the sample tube to allow the sample temperature to be varied.

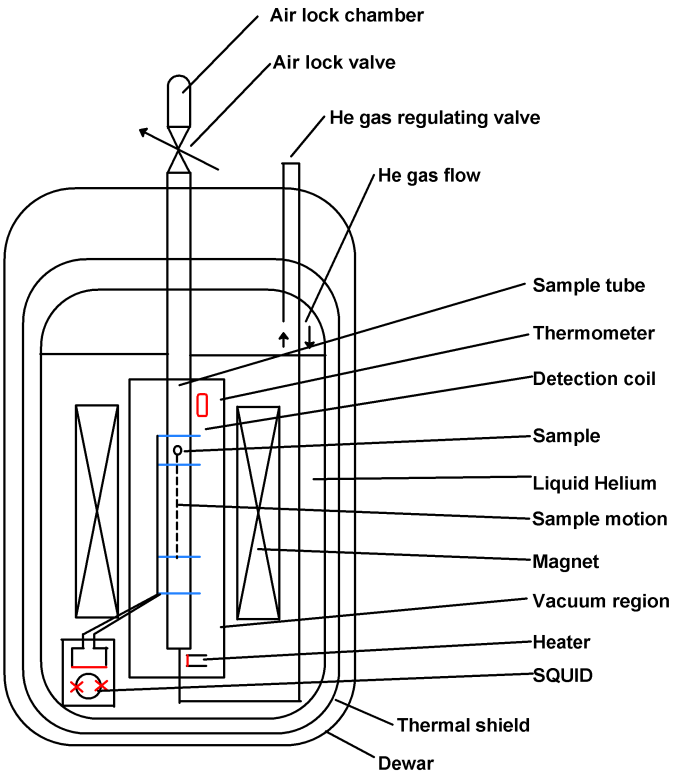

Figure 3.91: Schematic diagram of a MPMSR. Adapted from L. Fagaly, *Review of Scientific Instruments*, 2006, **77**, 101101.

The use of a variable temperature insert can allow measurements to be made over a wide range 1.8–400 K. Typically, the sample temperature is controlled by helium gas flowing slowly past the sample. The temperature of this gas is regulated using a heater located below the sample measuring region and a thermometer located above the sample region. This arrangement ensures that the entire region has reached thermal equilibrium prior to data acquisition. The helium gas is obtained from normal evaporation in the Dewar, and its flow rate is controlled by a precision regulating valve.

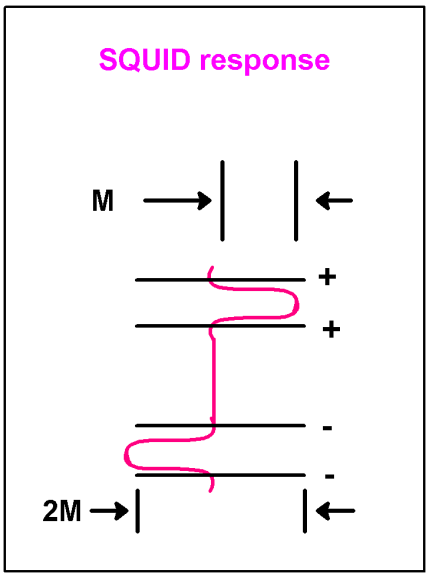

Figure 3.92: Signal output of an MPMS. Adapted from L. Fagaly, *Review of Scientific Instruments*, 2006, **77**, 101101.

3.14.2 Procedures when using an MPMS

3.14.2.1 Calibration

The magnetic moment calibration for the SQUID is determined by measuring a palladium standard over a range of magnetic fields and then by adjusting to obtain the correct moment for the standard. The palladium standard samples are effectively point sources with an accuracy of approximately 0.1%.

3.14.2.2 Sample mounting considerations

The type, size and geometry of a sample is usually sufficient to determine the method you use to attach it to the sample. However mostly for MPMS measurements a plastic straw is used. This is due to the straw having minimal magnetic susceptibility.

However there are a few important considerations for the sample holder design when mounting a sample for measurement in a magnetometer. The sample holder can be a major contributor to the background signal. Its contribution can be minimized by choosing materials with low magnetic susceptibility and by keeping the mass to a minimum such as a plastic straw mentioned above.

The materials used to hold a sample must perform well over the temperature range to be used. In a MPMS, the geometric arrangement of the background and sample is critical when their magnetic susceptibilities will be of similar magnitude. Thus, the sample holder should optimize the sample's positioning in the magnetometer. A sample should be mounted rigidly in order to avoid excess sample motion during measurement. A sample holder should also allow easy access for mounting the sample, and its background contribution should be easy to measure. This advisory introduces some mounting methods and discusses some of the more important considerations when mounting samples for the MPMS magnetometer. Keep in mind that these are only recommendations, not guaranteed procedures. The researcher is responsible for assuring that the methods and materials used will meet experimental requirements.

3.14.2.2.1 Sample Mounts

3.14.2.2.1.1 Platform mounting

For many types of samples, mounting to a platform is the most convenient method. The platform's mass and susceptibility should be as small as possible in order to minimize its background contribution and signal distortion.

3.14.2.2.1.2 Plastic disc

A plastic disc about 2 mm thick with an outside diameter equivalent to the pliable plastic tube's diameter (a clear drinking straw is suitable) is inserted and twisted into place. The platform should be fairly rigid. Mount samples onto this platform with glue. Place a second disc, with a diameter slightly less than the inside diameter of the tube and with the same mass, on top of the sample to help provide the desired symmetry. Pour powdered samples onto the platform and place a second disc on top. The powders will be able to align with the field. Make sure the sample tube is capped and ventilated.

3.14.2.2.1.3 Crossed threads

Make one of the lowest mass sample platforms by threading a cross of white cotton thread (colored dyes can be magnetic). Using a needle made of a nonmagneticmetal, or at least carefully cleaned, thread some white cotton sewingthread through the tube walls and tie a secure knot so that the thread platform isrigid. Glue a sample to this platform or use the platform as asupport for a sample in a container. Use an additional thread cross on top to holdthe container in place.

3.14.2.2.1.4 Gelatin capsule

Gelatin capsules can be very useful for containing and mounting samples. Many aspects of using gelatin capsules have been mentioned in the section, Containing the Sample. It is best if the sample is mounted near the capsule's center, or if it completely fills the capsule. Use extra capsule parts to produce mirror symmetry. The thread cross is an excellent way of holding a capsule in place.

3.14.2.2.1.5 Thread mounting

Another method of sample mounting is attaching the sample to a thread that runs through the sample tube. The thread can be attached to the sample holder at the ends of the sample tube with tape, for example. This method can be very useful with flat samples, such as those on substrates, particularly when the field is in the plane of the film. Be sure to close the sample tube with caps.

- Mounting with a disc platform.
- Mounting on crossed threads.
- Long thread mounting.

3.14.2.2.2 Steps for inserting the sample

1. Cut off a small section of a clear plastic drinking straw. The section must be small enough to fit inside the straw.
2. Weigh and measure the sample.
3. Use plastic tweezers to place the sample inside the small straw segment. It is important to use plastic tweezers not metallic ones as these will contaminate the sample.
4. Place the small straw segment inside the larger one. It should be approximately in the middle of the large drinking straw.
5. Attach the straw to the sample rod which is used to insert the sample into the SQUID machine.
6. Insert the sample rod with the attached straw into the vertical insertion hole on top of the SQUID.

3.14.2.3 Centre the sample

The sample must be centered in the SQUID pickup coils to ensure that all coils sense the magnetic moment of the sample. If the sample is not centered, the coils read only part of the magnetic moment.

During a centering measurement the MPMS scans the entire length of the samples vertical travel path, and the MPMS reads the maximum number of data points. During centering there are a number of terms which need to be understood.

1. A scan length is the length of a scan of a particular sample which should usually try and be the maximum of the sample.
2. A sample is centered when it is in the middle of a scan length. The data points are individual voltage readings plotting response curves in centering scan data files.
3. Autotracking is the adjustment of a sample position to keep a sample centered in SQUID coils. Autotracking compensates for thermal expansion and contraction in a sample rod.

As soon as a centering measurement is initiated, the sample transport moves upward, carrying the sample through the pickup coils. While the sample moves through the coils, the MPMS measures the SQUID's response to the magnetic moment of the sample and saves all the data from the centering measurement.

After a centering plot is performed the plot is examined to determine whether the sample is centered in the SQUID pickup coils. The sample is centered when the part of the large, middle curve is within 5cm of the half-way point of the scan length.

The shape of the plot is a function of the geometry of the coils. The coils are wound in a way which strongly rejects interference from nearby magnetic sources and lets the MPMS function without a superconducting shield around the pickup coils.

3.14.2.4 Geometric considerations

To minimize background noise and stray field effects, the MPMS magnetometer pick-up coil takes the form of a second-order gradiometer. An important feature of this gradiometer is that moving a long, homogeneous sample through it produces no signal as long as the sample extends well beyond the ends of the coil during measurement.

As a sample holder is moved through the gradiometer pickup coil, changes in thickness, mass, density, or magnetic susceptibility produce a signal. Ideally, only the sample to be measured produces this change. A homogeneous sample that extends well beyond the pick-up coils does not produce a signal, yet a small sample does produce a signal. There must be a crossover between these two limits. The sample length (along the field direction) should not exceed 10 mm. In order to obtain the most accurate measurements, it is important to keep the sample susceptibility constant over its length; otherwise distortions in the SQUID signal (deviations from a dipole signal) can result. It is also important to keep the sample close to the magnetometer centerline to get the most accurate measurements. When the sample holder background contribution is similar in magnitude to the sample signal, the relative positions of the sample and the materials producing the background are important. If there is a spatial offset between the two along the magnet axis, the signal produced by the combined sample and background can be highly distorted and will not be characteristic of the dipole moment being measured.

Even if the signal looks good at one temperature, a problem can occur if either of the contributions are temperature dependent.

Careful sample positioning and a sample holder with a center, or plane, of symmetry at the sample (i.e. materials distributed symmetrically about the sample, or along the principal axis for a symmetry plane) helps eliminate problems associated with spatial offsets.

3.14.2.5 Containing the Sample

Keep the sample space of the MPMS magnetometer clean and free of contamination with foreign materials. Avoid accidental sample loss into the sample space by properly containing the sample in an appropriate

sample holder. In all cases it is important to close the sample holder tube with caps in order to contain a sample that might become unmounted. This helps avoid sample loss and subsequent damage during the otherwise unnecessary recovery procedure. Position caps well out of the sample-measuring region and introduce proper venting.

3.14.2.6 Sample preparation workspace

Work area cleanliness and avoiding sample contamination are very important concerns. There are many possible sources of contamination in a laboratory. Use diamond tools when cutting hard materials. Avoid carbide tools because of potential contamination by the cobalt binder found in many carbide materials. The best tools for preparing samples and sample holders are made of plastic, titanium, brass, and beryllium copper (which also has a small amount of cobalt). Tools labeled non-magnetic can actually be made of steel and often be made "magnetic" from exposure to magnetic fields. However, the main concern from these "non-magnetic" tools is contamination by the iron and other ferrous metals in the tool. It is important to have a clean white-papered workspace and a set of tools dedicated to mounting your own samples. In many cases, the materials and tools used can be washed in dilute acid to remove ferrous metal impurities. Follow any acid washes with careful rinsing with deionized water.

Powdered samples pose a special contamination threat, and special precautions must be taken to contain them. If the sample is highly magnetic, it is often advantageous to embed it in a low susceptibility epoxy matrix like Duco cement. This is usually done by mixing a small amount of diluted glue with the powder in a suitable container such as a gelatin capsule. Potting the sample in this way can keep the sample from shifting or aligning with the magnetic field. In the case of weaker magnetic samples, measure the mass of the glue after drying and making a background measurement. If the powdered sample is not potted, seal it into a container, and watch it carefully as it is cycled in the airlock chamber.

3.14.2.7 Pressure equalization

The sample space of the MPMS has a helium atmosphere maintained at low pressure of a few torr. An airlock chamber is provided to avoid contamination of the sample space with air when introducing samples into the sample space. By pushing the purge button, the airlock is cycled between vacuum and helium gas three times, then pumped down to its working pressure. During the cycling, it is possible for samples to be displaced in their holders, sealed capsules to explode, and sample holders to be deformed. Many of these problems can be avoided if the sample holder is properly ventilated. This requires placing holes in the sample holder, out of the measuring region that will allow any closed spaces to be opened to the interlock chamber.

3.14.2.8 Air-sensitive samples and liquid samples

When working with highly air-sensitive samples or liquid samples it is best to first seal the sample into a glass tube. NMR and EPR tubes make good sample holders since they are usually made of a high-quality, low-susceptibility glass or fused silica. When the sample has a high susceptibility, the tube with the sample can be placed onto a platform like those described earlier. When dealing with a low susceptibility sample, it is useful to rest the bottom of the sample tube on a length of the same type of glass tubing. By producing near mirror symmetry, this method gives a nearly constant background with position and provides an easy method for background measurement (i.e., measure the empty tube first, then measure with a sample). Be sure that the tube ends are well out of the measuring region.

When going to low temperatures, check to make sure that the sample tube will not break due to differential thermal expansion. Samples that will go above room temperature should be sealed with a reduced pressure in the tube and be checked by taking the sample to the maximum experimental temperature prior to loading it into the magnetometer. These checks are especially important when the sample may be corrosive, reactive, or valuable.

3.14.2.9 Oxygen contamination

This application note describes potential sources for oxygen contamination in the sample chamber and discusses its possible effects. Molecular oxygen, which undergoes an antiferromagnetic transition at about 43 K, is strongly paramagnetic above this temperature. The MPMS system can easily detect the presence of a small amount of condensed oxygen on the sample, which when in the sample chamber can interfere significantly with sensitive magnetic measurements. Oxygen contamination in the sample chamber is usually the result of leaks in the system due to faulty seals, improper operation of the airlock valve, outgassing from the sample, or cold samples being loaded.

3.14.3 Bibliography

- J. Bland, Thesis M. Phys (Hons)., 'A Mossbauer spectroscopy and magnetometry study of magnetic multilayers and oxides.' Oliver Lodge Labs, Dept. Physics, University of Liverpool.
- Quantum Design, Operating manual for the MPMS, 1999.
- R. L. Fagaly, *Review of Scientific Instruments*, 2006, **77**, 101101.

Chapter 4

Fundamentals for Nanotechnology

4.1 Magnetics[1]

4.1.1 Magnetic moments

The magnetic moment of a material is the incomplete cancellation of the atomic magnetic moments in that material. Electron spin and orbital motion both have magnetic moments associated with them (Figure 4.1), but in most atoms the electronic moments are oriented usually randomly so that overall in the material they cancel each other out (Figure 4.2), this is called diamagnetism.

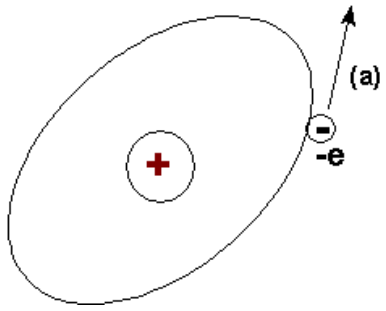

Figure 4.1: Orbital magnetic moment.

[1] This content is available online at <http://cnx.org/content/m22749/1.4/>.

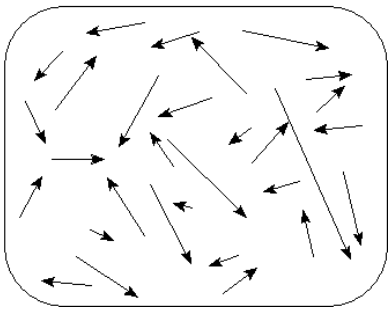

Figure 4.2: Magnetic moments in a diamagnetic sample.

If the cancellation of the moments is incomplete then the atom has a net magnetic moment. There are many subclasses of magnetic ordering such as para-, superpara-, ferro-, antiferro- or ferrimagnetisim which can be displayed in a material and which usually depends, upon the strength and type of magnetic interactions and external parameters such as temperature and crystal structure atomic content and the magnetic environment which a material is placed in.

$$\mu_B = \frac{eh}{4\pi m} = 9.72x10^{-24} J/T$$

The magnetic moments of atoms, molecules or formula units are often quoted in terms of the Bohr magneton, which is equal to the magnetic moment due to electron spin

4.1.2 Magnetization

The magnetisim of a material, the extent that which a material is magnetic, is not a static quantity, but varies compared to the environment that a material is placed in. It is similar to the temperature of a material. For example if a material is placed in an oven it will heat up to a temperature similar to that of the ovens. However the speed of heating of that material, and also that of cooling are determined by the atomic structure of the material. The magnetization of a material is similar. When a material is placed in a magnetic field it maybe become magnetized to an extent and retain that magnetization after it is removed from the field. The extent of magnetization, and type of magnetization and the length of time that a material remains magnetized, depends again on the atomic makeup of the material.

Measuring a materials magnetisim can be done on a micro or macro scale. Magnetisim is measured over two parameters direction and strength. Thus magnetization has a vector quantity. The simplest form of a magnetometer is a compass. It measures the direction of a magnetic field. However more sophisticated instruments have been developed which give a greater insight into a materials magnetisim.

So what exactly are you reading when you observe the output from a magnetometer?

The magnetisim of a sample is called the magnetic moment of that sample and will be called that from now on. The single value of magnetic moment for the sample, is a combination of the magnetic moments on the atoms within the sample (Figure 4.3), it is also the type and level of magnetic ordering and the physical dimensions of the sample itself.

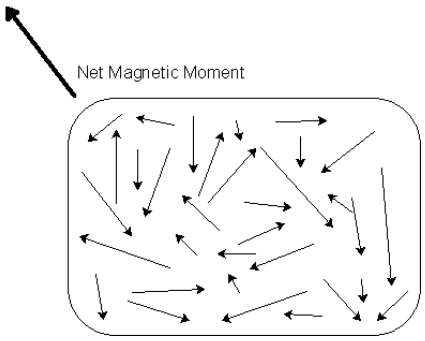

Figure 4.3: Schematic representations of the net magnetic moment in a diamagnetic sample.

The "intensity of magnetization", M, is a measure of the magnetization of a body. It is defined as the magnetic moment per unit volume or

$M = m/V$

with units of Am (emucm^3 in cgs notation).

A material contains many atoms and their arrangement affects the magnetization of that material. In Figure 4.4 (a) a magnetic moment m is contained in unit volume. This has a magnetization of m Am. Figure 4.4 (b) shows two such units, with the moments aligned parallel. The vector sum of moments is $2m$ in this case, but as the both the moment and volume are doubled M remains the same. In Figure 4.4 (c) the moments are aligned antiparallel. The vector sum of moments is now 0 and hence the magnetization is 0 Am.

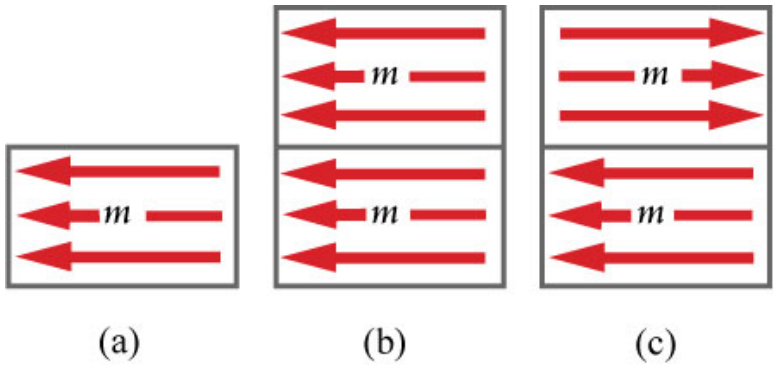

Figure 4.4: Effect of moment alignment on magnetization: (a) Single magnetic moment, (b) two identical moments aligned parallel and (c) antiparallel to each other. Adapted from J. Bland Thesis M. Phys (Hons)., 'A Mossbauer spectroscopy and magnetometry study of magnetic multilayers and oxides.' Oliver Lodge Labs, Dept. Physics, University of Liverpool

Scenarios (b) and (c) are a simple representation of ferro- and antiferromagnetic ordering. Hence we would expect a large magnetization in a ferromagnetic material such as pure iron and a small magnetization

in an antiferromagnet such as γ-Fe_2O_3

4.1.3 Magnetic Response

When a material is passed through a magnetic field it is affected in two ways:

1. Through its susceptibility.
2. Through its permeability.

4.1.3.1 Magnetic susceptibility

The concept of magnetic moment is the starting point when discussing the behavior of magnetic materials within a field. If you place a bar magnet in a field it will experience a torque or *moment* tending to align its axis in the direction of the field. A compass needle behaves in the same way. This torque increases with the strength of the poles and their distance apart. So the value of magnetic moment tells you, in effect, 'how big a magnet' you have.

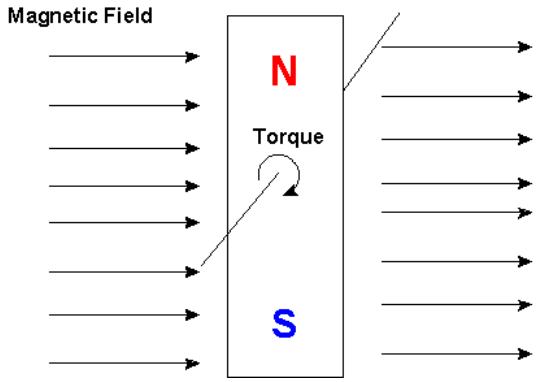

Figure 4.5: Schematic representation of the torque or moment that a magnet experiences when it is placed in a magnetic field. The magnetic will try to align with the magnetic field.

If you place a material in a weak magnetic field, the magnetic field may not overcome the binding energies that keep the material in a non magnetic state. This is because it is energetically more favorable for the material to stay exactly the same. However, if the strength of the magnetic moment is increased, the torque acting on the smaller moments in the material, it may become energetically more preferable for the material to become magnetic. The reasons that the material becomes magnetic depends on factors such as crystal structure the temperature of the material and the strength of the field that it is in. However a simple explanation of this is that as the magnetic moment strength increases it becomes more favorable for the small fields to align themselves along the path of the magnetic field, instead of being opposed to the system. For this to occur the material must rearrange its magnetic makeup at the atomic level to lower the energy of the system and restore a balance.

It is important to remember that when we consider the magnetic susceptibility and take into account how a material changes on the atomic level when it is placed in a magnetic field with a certain moment. The moment that we are measuring with our magnetometer is the total moment of that sample.

$$\chi = \frac{M}{H}$$

where χ = susceptibility, M = variation of magnetization, and H = applied field.

4.1.3.2 Magnetic permeability

Magnetic permeability is the ability of a material to conduct an electric field. In the same way that materials conduct or resist electricity, materials also conduct or resist a magnetic flux or the flow of magnetic lines of force (Figure 4.6).

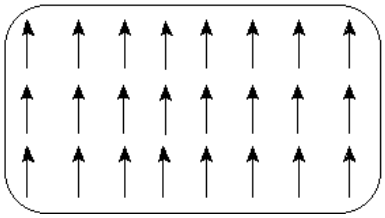

Figure 4.6: Magnetic ordering in a ferromagnetic material.

Ferromagnetic materials are usually highly permeable to magnetic fields. Just as electrical conductivity is defined as the ratio of the current density to the electric field strength, so the magnetic permeability, μ, of a particular material is defined as the ratio of flux density to magnetic field strength. However unlike in electrical conductivity magnetic permeability is nonlinear.

μ = B/H

Permeability, where μ is written without a subscript, is known as absolute permeability. Instead a variant is used called relative permeability.

$\mu = \mu_o$ x μ_r

Absolute permeability is a variation upon 'straight' or absolute permeability, μ, but is more useful as it makes clearer how the presence of a particular material affects the relationship between flux density and field strength. The term 'relative' arises because this permeability is defined in relation to the permeability of a vacuum, μ_0.

$\mu_r = \mu/\mu_o$

For example, if you use a material for which $\mu_r = 3$ then you know that the flux density will be three times as great as it would be if we just applied the same field strength to a vacuum.

4.1.3.2.1 Initial permeability

Initial permeability describes the relative permeability of a material at low values of B (below 0.1 T). The maximum value for μ in a material is frequently a factor of between 2 and 5 or more above its initial value.

Low flux has the advantage that every ferrite can be measured at that density without risk of saturation. This consistency means that comparison between different ferrites is easy. Also, if you measure the inductance with a normal component bridge then you are doing so with respect to the initial permeability.

4.1.3.2.2 Permeability of a vacuum in the SI

The permeability of a vacuum has a finite value - about 1.257×10^{-6} H m^{-1} - and is denoted by the symbol μ_0. Note that this value is constant with field strength and temperature. Contrast this with the situation in ferromagnetic materials where μ is strongly dependent upon both. Also, for practical purposes, most non-ferromagnetic substances (such as wood, plastic, glass, bone, copper aluminum, air and water) have permeability almost equal to μ_0; that is, their relative permeability is 1.0.

The permeability, μ, the variation of magnetic induction,

$$B = \mu_o(H + M)$$

with applied field,

μ = B/H

4.1.4 Background contributions

A single measurement of a sample's magnetization is relatively easy to obtain, especially with modern technology. Often it is simply a case of loading the sample into the magnetometer in the correct manner and performing a single measurement. This value is, however, the sum total of the sample, any substrate or backing and the sample mount. A sample substrate can produce a substantial contribution to the sample total.

For substrates that are diamagnetic, under zero applied field, this means it has no effect on the measurement of magnetization. Under applied fields its contribution is linear and temperature independent. The diamagnetic contribution can be calculated from knowledge of the volume and properties of the substrate and subtracted as a constant linear term to produce the signal from the sample alone. The diamagnetic background can also be seen clearly at high fields where the sample has reached saturation: the sample saturates but the linear background from the substrate continues to increase with field. The gradient of this background can be recorded and subtracted from the readings if the substrate properties are not known accurately.

4.1.5 Hysteresis

When a material exhibits hysteresis, it means that the material responds to a force and has a history of that force contained within it. Consider if you press on something until it depresses. When you release that pressure, if the material remains depressed and doesn't spring back then it is said to exhibit some type of hysteresis. It remembers a history of what happened to it, and may exhibit that history in some way. Consider a piece of iron that is brought into a magnetic field, it retains some magnetization, even after the external magnetic field is removed. Once magnetized, the iron will stay magnetized indefinitely. To demagnetize the iron, it is necessary to apply a magnetic field in the opposite direction. This is the basis of memory in a hard disk drive.

The response of a material to an applied field and its magnetic hysteresis is an essential tool of magnetometry. Paramagnetic and diamagnetic materials can easily be recognized, soft and hard ferromagnetic materials give different types of hysteresis curves and from these curves values such as saturation magnetization, remnant magnetization and coercivity are readily observed. More detailed curves can give indications of the type of magnetic interactions within the sample.

4.1.6 Diamagnetism and paramagnetizm

The intensity of magnetization depends upon both the magnetic moments in the sample and the way that they are oriented with respect to each other, known as the magnetic ordering.

Diamagnetic materials, which have no atomic magnetic moments, have no magnetization in zero field. When a field is applied a small, negative moment is induced on the diamagnetic atoms proportional to the applied field strength. As the field is reduced the induced moment is reduced.

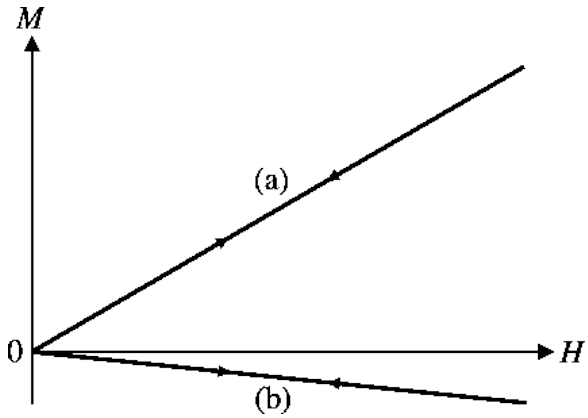

Figure 4.7: Typical effect on the magnetization, M, of an applied magnetic field, H, on (a) a paramagnetic system and (b) a diamagnetic system. Adapted from J. Bland Thesis M. Phys (Hons)., 'A Mossbauer spectroscopy and magnetometry study of magnetic multilayers and oxides.' Oliver Lodge Labs, Dept. Physics, University of Liverpool

In a paramagnet the atoms have a net magnetic moment but are oriented randomly throughout the sample due to thermal agitation, giving zero magnetization. As a field is applied the moments tend towards alignment along the field, giving a net magnetization which increases with applied field as the moments become more ordered. As the field is reduced the moments become disordered again by their thermal agitation. The figure shows the linear response M v H where μH $\ll$ kT.

4.1.7 Ferromagnetism

The hysteresis curves for a ferromagnetic material are more complex than those for diamagnets or paramagnets. Below diagram shows the main features of such a curve for a simple ferromagnet.

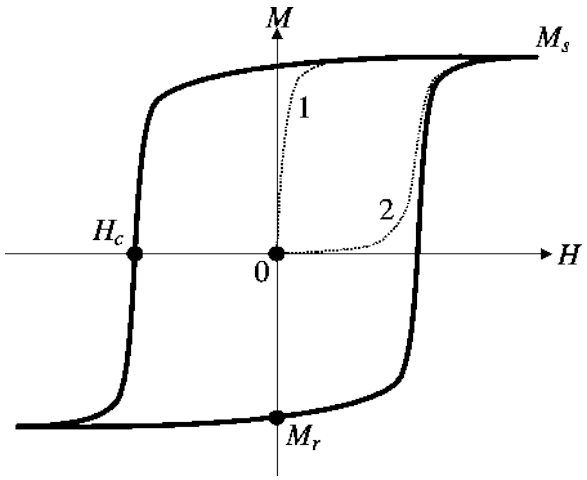

Figure 4.8: Schematic of a magnetization hysteresis loop in a ferromagnetic material showing the saturation magnetization, M_s, coercive field, H_c, and remnant magnetization, M_r. Virgin curves are shown dashed for nucleation (1) and pinning (2) type magnets. Adapted from J. Bland Thesis M. Phys (Hons)., 'A Mossbauer spectroscopy and magnetometry study of magnetic multilayers and oxides.' Oliver Lodge Labs, Dept. Physics, University of Liverpool

In the virgin material (point 0) there is no magnetization. The process of magnetization, leading from point 0 to saturation at $M = M_s$, is outlined below. Although the material is ordered ferromagnetically it consists of a number of ordered domains arranged randomly giving no net magnetization. This is shown in below (a) with two domains whose individual saturation moments, M_s, lie antiparallel to each other.

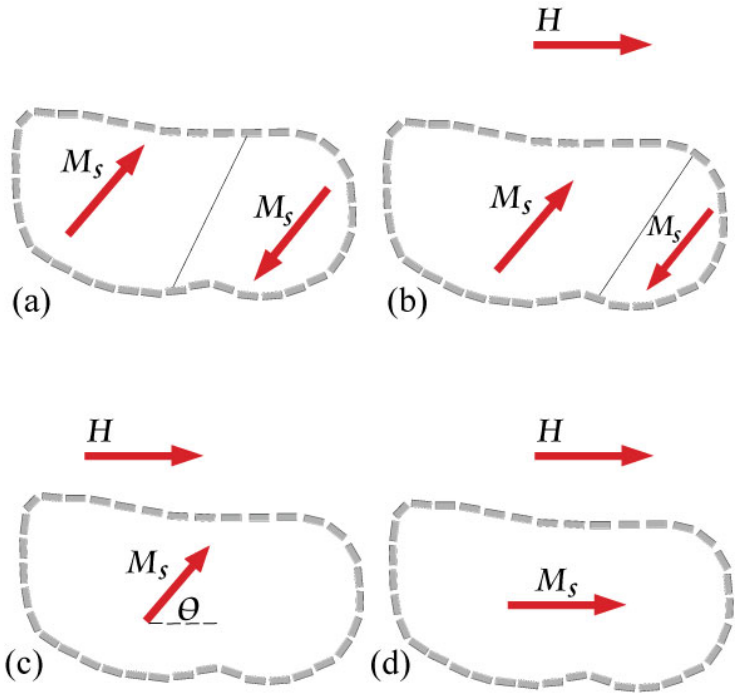

Figure 4.9: The process of magnetization in a demagnetized ferromagnet. Adaped from J. Bland Thesis M. Phys (Hons)., 'A Mossbauer spectroscopy and magnetometry study of magnetic multilayers and oxides.' Oliver Lodge Labs, Dept. Physics, University of Liverpool

As the magnetic field, H, is applied, (b), those domains which are more energetically favorable increase in size at the expense of those whose moment lies more antiparallel to H. There is now a net magnetization; M. Eventually a field is reached where all of the material is a single domain with a moment aligned parallel, or close to parallel, with H. The magnetization is now $M = M_s \mathrm{Cos}\Theta$ where Θ is the angle between M_s along the easy magnetic axis and H. Finally M_s is rotated parallel to H and the ferromagnet is saturated with a magnetization $M = M_s$.

The process of domain wall motion affects the shape of the virgin curve. There are two qualitatively different modes of behavior known as nucleation and pinning, shown in Figure 4.8 as curves 1 and 2, respectively.

In a nucleation-type magnet saturation is reached quickly at a field much lower than the coercive field. This shows that the domain walls are easily moved and are not pinned significantly. Once the domain structure has been removed the formation of reversed domains becomes difficult, giving high coercivity. In a pinning-type magnet fields close to the coercive field are necessary to reach saturation magnetization. Here the domain walls are substantially pinned and this mechanism also gives high coercivity.

4.1.8 Remnance

As the applied field is reduced to 0 after the sample has reached saturation the sample can still possess a remnant magnetization, M_r. The magnitude of this remnant magnetization is a product of the saturation magnetization, the number and orientation of easy axes and the type of anisotropy symmetry. If the axis

of anisotropy or magnetic easy axis is perfectly aligned with the field then $M_r = M_s$, and if perpendicular $M_r = 0$.

At saturation the angular distribution of domain magnetizations is closely aligned to H. As the field is removed they turn to the nearest easy magnetic axis. In a cubic crystal with a positive anisotropy constant, $K1$, the easy directions are <100>. At remnance the domain magnetizations will lie along one of the three <100> directions. The maximum deviation from H occurs when H is along the <111> axis, giving a cone of distribution of 55° around the axis. Averaging the saturation magnetization over this angle gives a remnant magnetization of 0.832 Ms.

4.1.9 Coercivity

The coercive field, H_c, is the field at which the remnant magnetization is reduced to zero. This can vary from a few Am for soft magnets to 10^7Am for hard magnets. It is the point of magnetization reversal in the sample, where the barrier between the two states of magnetization is reduced to zero by the applied field allowing the system to make a Barkhausen jump to a lower energy. It is a general indicator of the energy gradients in the sample which oppose large changes of magnetization.

The reversal of magnetization can come about as a rotation of the magnetization in a large volume or through the movement of domain walls under the pressure of the applied field. In general materials with few or no domains have a high coercivity whilst those with many domains have a low coercivity. However, domain wall pinning by physical defects such as vacancies, dislocations and grain boundaries can increase the coercivity.

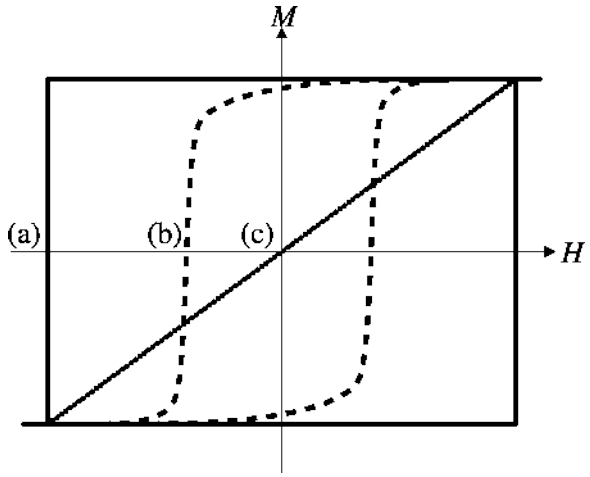

Figure 4.10: Shape of hysteresis loop as a function of Θ_H, the angle between anisotropy axis and applied field H, for: (a) Θ_H, = 0 °, (b) 45 ° and (c) 90 °. Adaped from J. Bland Thesis M. Phys (Hons)., 'A Mossbauer spectroscopy and magnetometry study of magnetic multilayers and oxides.' Oliver Lodge Labs, Dept. Physics, University of Liverpool

The loop illustrated in Figure 4.10 is indicative of a simple bi-stable system. There are two energy minima: one with magnetization in the positive direction, and another in the negative direction. The depth of these minima is influenced by the material and its geometry and is a further parameter in the strength of the coercive field. Another is the angle, Θ_H, between the anisotropy axis and the applied field. The above fig

shows how the shape of the hysteresis loop and the magnitude of H_c varies with Θ_H. This effect shows the importance of how samples with strong anisotropy are mounted in a magnetometer when comparing loops.

4.1.10 Temperature dependence

A hysteresis curve gives information about a magnetic system by varying the applied field but important information can also be gleaned by varying the temperature. As well as indicating transition temperatures, all of the main groups of magnetic ordering have characteristic temperature/magnetization curves. These are summarized in Figure 4.11 and Figure 4.12. At all temperatures a diamagnet displays only any magnetization induced by the applied field and a small, negative susceptibility.

The curve shown for a paramagnet (Figure 4.11) is for one obeying the Curie law,

$$\chi = \frac{C}{T}$$

and so intercepts the axis at $T = 0$. This is a subset of the Curie-Weiss law,

$$\chi = \frac{C}{T-\theta}$$

where θ is a specific temperature for a particular substance (equal to 0 for paramagnets).

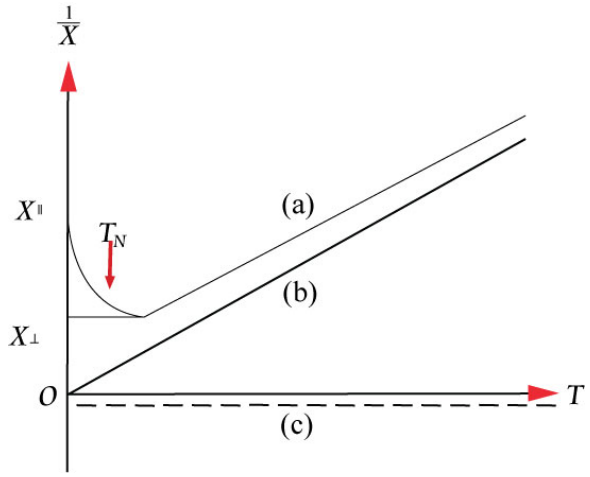

Figure 4.11: Variation of reciprocal susceptibility with temperature for: (a) antiferromagnetic, (b) paramagnetic and (c) diamagnetic ordering. Adaped from J. Bland Thesis M. Phys (Hons)., 'A Mossbauer spectroscopy and magnetometry study of magnetic multilayers and oxides.' Oliver Lodge Labs, Dept. Physics, University of Liverpool

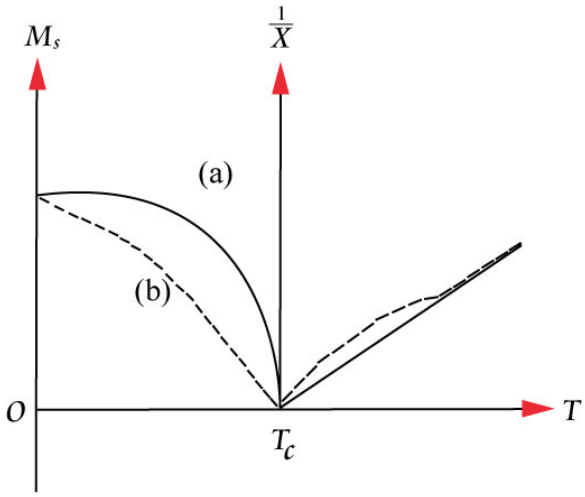

Figure 4.12: Variation of saturation magnetization below, and reciprocal susceptibility above T_c for: (a) ferromagnetic and (b) ferrimagnetic ordering. Adaped from J. Bland Thesis M. Phys (Hons)., 'A Mossbauer spectroscopy and magnetometry study of magnetic multilayers and oxides.' Oliver Lodge Labs, Dept. Physics, University of Liverpool

Above T_N and T_C both antiferromagnets and ferromagnets behave as paramagnets with $1/\chi$ linearly proportional to temperature. They can be distinguished by their intercept on the temperature axis, $T = \Theta$. Ferromagnetics have a large, positive Θ, indicative of their strong interactions. For paramagnetics $\Theta = 0$ and antiferromagnetics have a negative Θ.

The net magnetic moment per atom can be calculated from the gradient of the straight line graph of $1/\chi$ versus temperature for a paramagnetic ion, rearranging Curie's law to give

$$\mu = \sqrt{\frac{3Ak}{N_x}}$$

where A is the atomic mass, k is Boltzmann's constant, N is the number of atoms per unit volume and x is the gradient.

Ferromagnets below T_C display spontaneous magnetization. Their susceptibility above T_C in the paramagnetic region is given by the Curie-Weiss law

where g is the gyromagnetic constant. In the ferromagnetic phase with T greater than T_C the magnetization M (T) can be simplified to a power law, for example the magnetization as a function of temperature can be given by

$$M(T) \approx (T_c - T)^{\beta}$$

where the term β is typically in the region of 0.33 for magnetic ordering in three dimensions.

The susceptibility of an antiferromagnet increases to a maximum at T_N as temperature is reduced, then decreases again below T_N. In the presence of crystal anisotropy in the system this change in susceptibility depends on the orientation of the spin axes: χ (parallel)decreases with temperature whilst χ (perpendicular) is constant. These can be expressed as

$$\chi \perp = \frac{C}{2\theta}$$

where C is the Curie constant and Θ is the total change in angle of the two sublattice magnetizations away from the spin axis, and

$$\chi \parallel = \frac{2n_g\mu_H^2 B'(J,a_0')}{2kT + n_g\mu_H^2\gamma\rho B'(J,a_0')}$$

where n_g is the number of magnetic atoms per gramme, B' is the derivative of the Brillouin function with respect to its argument a', evaluated at a'_0, μ_H is the magnetic moment per atom and γ is the molecular field coefficient.

4.1.11 Bibliography

- U. Gradmann, Handbook of Magnetic Materials, vol. 7.
- B. D. Cullity, *Introduction to Magnetic Materials*, Addison-Wesley, Massachusettes (1972).
- G. Bertotti, *Hysteresis in Magnetism*, Academic Press, San Diego (1998).
- S. Chikazumi, S. H. Charap, *Physics of Magnetisim*, Krieger Publishing Company (1978).
- J. Bland, Thesis M. Phys (Hons)., 'A Mossbauer spectroscopy and magnetometry study of magnetic multilayers and oxides.' Oliver Lodge Labs, Dept. Physics, University of Liverpool.

4.2 Brownian Motion[2]

NOTE: "This module was developed as part of a Rice University Class called "Nanotechnology: Content and Context[3] " initially funded by the National Science Foundation under Grant No. EEC-0407237. It was conceived, researched, written and edited by students in the Fall 2005 version of the class, and reviewed by participating professors."

[2]This content is available online at <http://cnx.org/content/m14354/1.3/>.
[3]http://frazer.rice.edu/nanotech

Figure 4.13: Clarkia pulcgella

This plant was Clarkia pulchella, of which the grains of pollen, taken from antherae full grown, but before bursting, were filled with particles or granules of unusually large size, varying from nearly 1/4000th to 1/5000th of an inch in length, and of a figure between cylindrical and oblong, perhaps slightly flattened, and having rounded and equal extremities. While examining the form of these particles immersed in water, I observed many of them very evidently in motion; their motion consisting not only of a change of place in the fluid, manifested by alterations in their relative positions, but also not unfrequently of a change of form in the particle itself; a contraction or curvature taking place repeatedly about the middle of one side, accompanied by a corresponding swelling or convexity on the opposite side of the particle. In a few instances the particle was seen to turn on its longer axis. These motions were such as to satisfy me, after frequently repeated observation, that they arose neither from currents in the fluid, nor from its gradual evaporation, but belonged to the particle itself.- **-Robert Brown, 1828**

4.2.1 Introduction

The physical phenomena described in the excerpt above by Robert Brown, the nineteenth-century British botanist and surgeon, have come collectively to be known in his honor by the term Brownian motion.

Brownian motion, a simple stochastic process, can be modeled to mathematically characterize the random movements of minute particles upon immersion in fluids. As Brown once noted in his observations under a microscope, particulate matter such as, for example, pollen granules, appear to be in a constant state of agitation and also seem to demonstrate a vivid, oscillatory motion when suspended in a solution such as water.

We now know that Brownian motion takes place as a result of thermal energy and that it is governed by the kinetic-molecular theory of heat, the properties of which have been found to be applicable to all diffusion phenomena.

But how are the random movement of flower gametes and a British plant enthusiast who has been dead for a hundred and fifty years relevant to the study and to the practice of nanotechnology? This is the main question that this module aims to address. In order to arrive at an adequate answer, we must first examine

the concept of Brownian motion from a number of different perspectives, among them the historical, physical, mathematical, and biological.

4.2.2 Objectives

By the end of this module, the student should be able to address the following critical questions.

- Robert Brown is generally credited to have discovered Brownian motion, but a number of individuals were involved in the actual development of a theory to explain the phenomenon. Who were these individuals, and how are their contributions to the theory of Brownian motion important to the history of science?

- Mathematically, what is Brownian motion? Can it be described by means of a mathematical model? Can the mathematical theory of Brownian motion be applied in a context broader than that of simply the movement of particles in fluid?

- What is kinetic-molecular theory, and how is it related to Brownian motion? Physically, what does Brownian motion tell us about atoms?

- How is Brownian motion involved in cellular activity, and what are the biological implications of Brownian motion theory?

- What is the significance of Brownian motion in nanotechnology? What are the challenges posed by Brownian motion, and can properties of Brownian motion be harnessed in a way such as to advance research in nanotechnology?

4.2.3 A Brief History of Brownian Motion

Figure 4.14: Robert Brown (1773 - 1858)

The phenomenon that is known today as Brownian motion was actually first recorded by the Dutch physiologist and botanist Jan Ingenhousz. Ingenhousz is most famous for his discovery that light is essential to

plant respiration, but he also noted the irregular movement exhibited by motes of carbon dust in ethanol in 1784.

Adolphe Brongniart made similar observations in 1827, but the discovery of Brownian motion is generally accredited to Scottish-born botanist Robert Brown, even though the manuscript regarding his aforementioned experiment with primrose pollen was not published until nearly thirty years after Ingenhousz' death.

At first, he attributed the movement of pollen granules in water to the fact that the pollen was "alive." However, he soon observed the same results when he repeated his experiment with tiny shards of window glass and again with crystals of quartz. Thus, he was forced to conclude that these properties were independent of vitality. Puzzled, Brown was in the end never able to adequately explain the nature of his findings.

The first person to put forward an actual theory behind Brownian motion was Louis Bachelier, a French mathematician who proposed a model for Brownian motion as part of his PhD thesis in 1900.

Five years later in 1905, Albert Einstein completed his doctoral thesis on osmotic pressure, in which he discussed a statistical theory of liquid behavior based on the existence of molecules. He later applied his liquid kinetic-molecular theory of heat to explain the same phenomenon observed by Brown in his paper Investigations on the Theory of the Brownian Movement. In particular, Einstein suggested that the random movements of particles suspended in liquid could be explained as being a result of the random thermal agitation of the molecules that compose the surrounding liquid.

The subsequent observations of Theodor Svedberg and Felix Ehrenhaft on Brownian motion in colloids and on particles of silver in air, respectively, helped to support Einstein's theory, but much of the experimental work to actually test Einstein's predictions was carried out by French physicist Jean Perrin, who eventually won the Nobel Prize in physics in 1926. Perrin's published results of his empirical verification of Einstein's model of Brownian motion are widely credited for finally settling the century-long dispute about John Dalton's theory for the existence of atoms.

4.2.4 Brownian Motion and Kinetic Theory

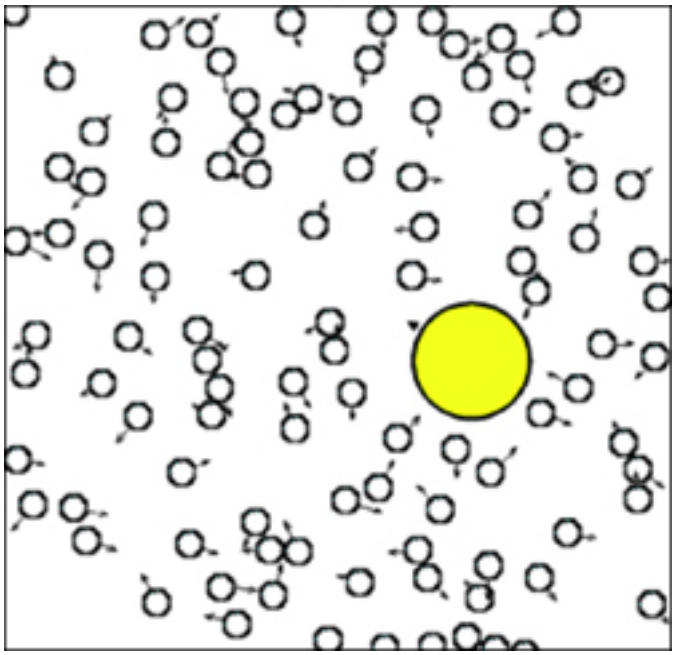

Figure 4.15: A grain of pollen colliding with water molecules moving randomly in all directions as a result of heat energy.

The kinetic theory of matter states that all matter is made up of atoms and molecules, that these atoms and molecules are in constant motion, and that collisions between these atoms and molecules are completely elastic.

The kinetic-molecular theory of heat involves the idea that heat as an entity is manifested simply in the form of these moving atoms and molecules. This theory is comprised of the following five postulates.

1. Heat is a form of energy.
2. Molecules carry two types of energy: potential and kinetic.
3. Potential energy results from the electric force between molecules.
4. Kinetic energy results from the motion of molecules.
5. Energy converts continuously between potential energy and kinetic energy.

Einstein used the postulates of both theories to develop a model in order to provide an explanation of the properties of Brownian motion.

Brownian motion is characterized by the constant and erratic movement of minute particles in a liquid or a gas. The molecules that make up the fluid in which the particles are suspended, as a result of the inherently random nature of their motions, collide with the larger suspended particles at random, making them move, in turn, also randomly. Because of kinetics, molecules of water, given any length of time, would move at random so that a small particle such as Brown's pollen would be subject to a random number of collisions of random strength and from random directions.

Described by Einstein as the "white noise" of random molecular movements due to heat, Brownian motion arises from the agitation of individual molecules by thermal energy. The collective impact of these molecules against the suspended particle yields enough momentum to create movement of the particle in spite of its sometimes exponentially larger size.

According to kinetic theory, the temperature at which there is no movement of individual atoms or molecules is absolute zero (-273 K). As long as a body retains the ability to transfer further heat to another body – that is, at any temperature above absolute zero – Brownian motion is not only possible but also inevitable.

4.2.5 Brownian Motion as a Mathematical Model

The Brownian motion curve is considered to be the simplest of all random motion curves. In Brownian motion, a particle at time t and position p will make a random displacement r from its previous point with regard to time and position. The resulting distribution of r is expected to be Gaussian (normal with a mean of zero and a standard deviation of one) and to be independent in both its x and y coordinates.

Thus, in summary a Brownian motion curve can be defined to be a set of random variables in a probability space that is characterized by the following three properties.

For all time $h > 0$, the displacements $X(t+h) - X(t)$ have Gaussian distribution.

The displacements $X(t+h) - X(t)$, $0 < t1 < t2 < \ldots$ tn, are independent of previous distributions.

The mean displacement is zero.

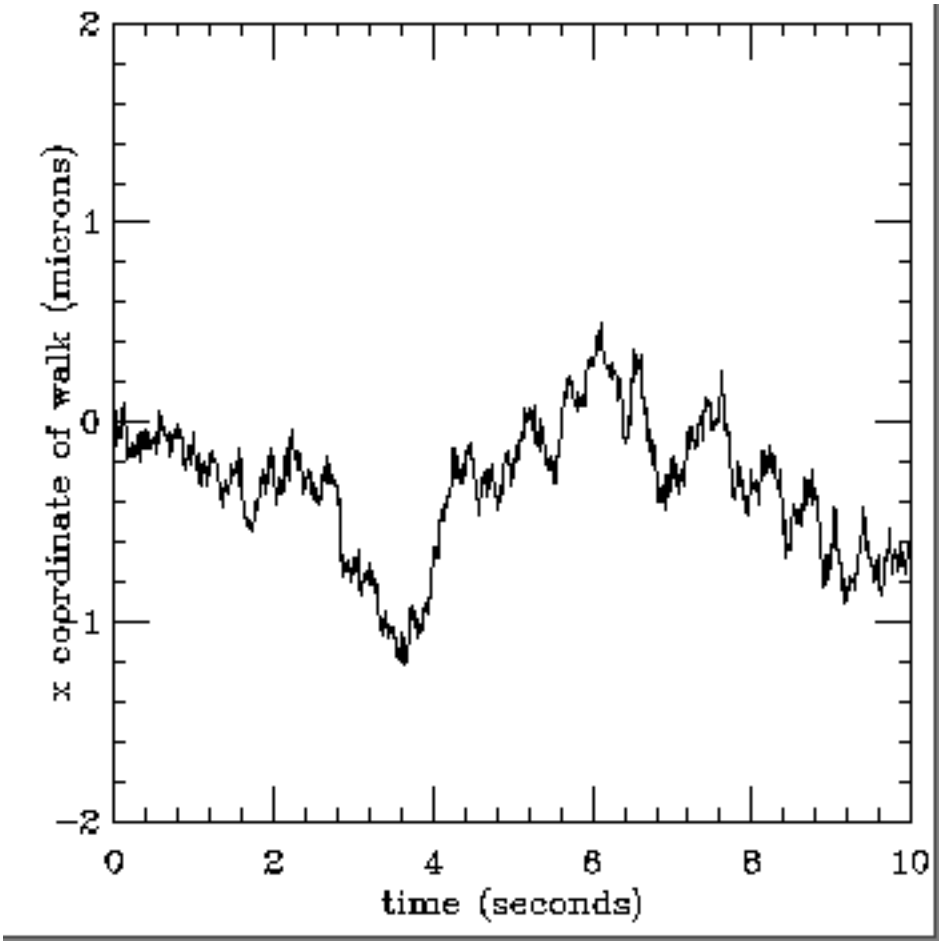

Figure 4.16: A Brownian motion curve – time vs.x-coordinate of walk.

From a resulting curve, it is evident that Brownian motion fulfills the conditions of the Markov property and can therefore be regarded as Markovian. In the field of theoretical probability, a stochastic process is Markovian if the conditional distribution of future states of the process is conditionally independent of that of its past states. In other words, given X(t), the values of X before time t are irrelevant in predicting the future behavior of X.

Moreover, the trajectory of X is continuous, and it is also recurrent, returning periodically to its origin at 0. Because of these properties, the mathematical model for Brownian motion can serve as a sophisticated random number generator. Therefore, Brownian motion as a mathematical model is not exclusive to the context of random movement of small particles suspended in fluid; it can be used to describe a number of phenomena such as fluctuations in the stock market and the evolution of physical traits as preserved in fossil records.

When the simulated Brownian trajectory of a particle is plotted onto an x-y plane, the resulting curve can be said to be self-similar, a term that is often used to describe fractals. The idea of self-similarity means that for every segment of a given curve, there is either a smaller segment or a larger segment of the same curve that is similar to it. Likewise, a fractal is defined to be a geometric pattern that is repeated at indefinitely smaller scales to produce irregular shapes and surfaces that are impossible to derive by means of classical geometry.

Figure 5. The simulated trajectory of a particle in Brownian motion beginning at the origin (0,0) on an x-y plane after 1 second, 3 seconds, and 10 seconds. Because of the fractal nature of Brownian motion curves, the properties of Brownian motion can be applied to a wide variety of fields through the process of fractal analysis. Many methods for generating fractal shapes have been suggested in computer graphics, but some of the most successful have been expansions of the random displacement method, which generates a pattern derived from properties of the fractional Brownian motion model. Algorithms and distribution functions that are based upon the Brownian motion model have been used to develop applications in medical imaging and in robotics as well as to make predictions in market analysis, in manufacturing, and in decision making at large.

4.2.6 Rectified Brownian Motion

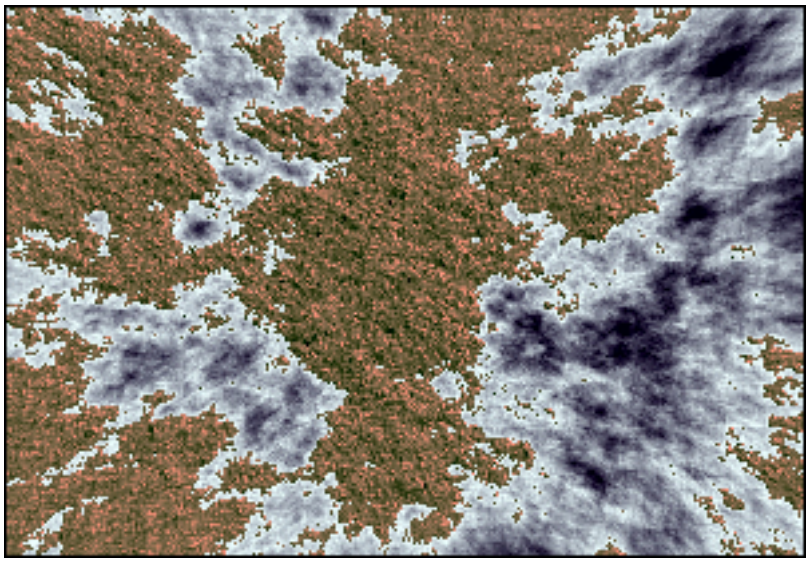

Figure 4.17: A random Brownian "walk" method fractal.

In recent years, biomedical research has shown that Brownian motion may play a critical role in the transport of enzymes and chemicals both into and out of cells in the human body.

Within the cells of the body, intracellular microtubule-based movement is directed by the proteins kinesin and dynein. The long-accepted explanation for this transport action is that the kinesins, fueled by energy provided by ATP, use their two appendage-like globular heads to "walk" deliberately along the lengths of the microtubule paths to which they are attached. Kinesin, as a motor protein, has conventionally been understood to allow for the movement of objects within cells by harnessing the energy released from either the breaking of chemical bonds or the energy released across a membrane in an electrochemical gradient. The kinesin proteins thus were believed to function as cellular "tow trucks" that pull chemicals or enzymes along these microtubule pathways.

New research, however, posits that what appeared to be a deliberate towing action along the microtubules is actually a result of random motion controlled by ATP-directed chemical switching commands. It is now argued that kinesins utilize rectified Brownian motion (converting this random motion into a purposeful unidirectional one).

We begin with a kinesin protein with both of its globular heads chemically bound to a microtubule path. According to the traditional power stroke model for motor proteins, the energy from ATP hydrolysis provides the impetus to trigger a chemo-mechanical energy conversion, but according to the rectified Brownian motion model, the energy released by ATP hydrolysis causes an irreversible conformational switch in the ATP binding protein, which in turn results in the release of one of the motor protein heads from its microtubule track. Microtubules are composed of fibrous proteins and include sites approximately 8 nm apart where kinesin heads can bind chemically. This new model suggests that the unbound kinesin head, which is usually 5-7 nm in diameter, is moved about randomly because of Brownian motion in the cellular fluid until it by chance encounters a new site to which it can bind. Because of the structural limits in the kinesin and because of the spacing of the binding sites on the microtubules, the moving head can only reach one possible binding site – that which is located 8 nm beyond the bound head that is still attached to the microtubule. Thus, rectified Brownian motion can only result in moving the kinesin and its cargo 8 nm in one direction along the length of the microtubule. Once the floating head binds to the new site, the process begins again with the original two heads in interchanged positions. The mechanism by which random Brownian motion results in movement in only one pre-determined direction is commonly referred to a Brownian ratchet.

Ordinarily, Brownian motion is not considered to be purposeful or directional on account of its sheer randomness. Randomness is generally inefficient, and though in this case only one binding site is possible, the kinesin head can be likened to encounter that binding site by "trial and error." For this reason, Brownian motion is normally thought of as a fairly slow process; however, on the nanometer scale, Brownian motion appears to be carried out at a very rapid rate. In spite of its randomness, Brownian motion at the nanometer scale allows for rapid exploration of all possible outcomes.

4.2.7 Brownian Motion and Nanotechnology

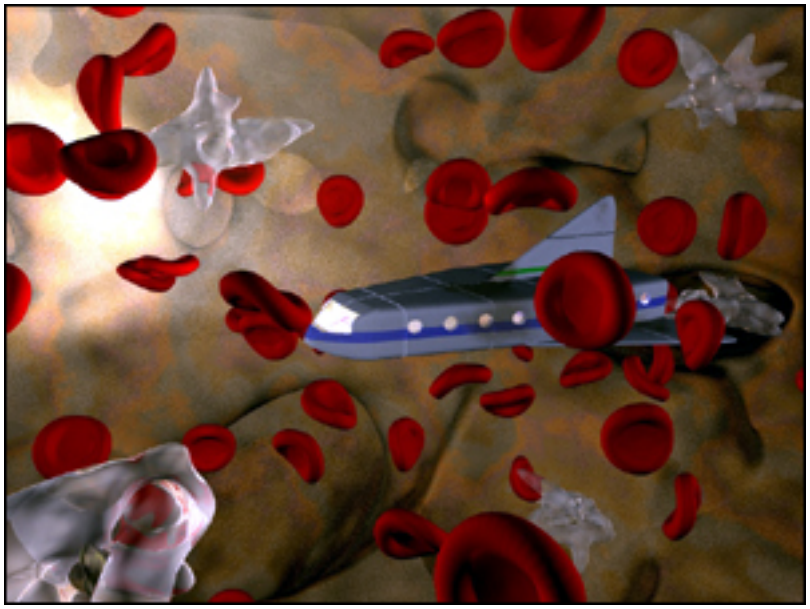

Figure 4.18: An artist's rendition of a tourist submarine, shrunk to cellular size, in Asimov's Fantastic Voyage.

If one were to assume that Brownian motion does not exercise a significant effect on his or her day-to-day existence, he or she, for all practical purposes, would be correct. After all, Brownian motion is much too weak and much too slow to have major (if any) consequences in the macro world. Unlike the fundamental forces of, for instance, gravity or electromagnetism, the properties of Brownian motion govern the interactions of particles on a minute level and are therefore virtually undetectable to humans without the aid of a microscope. How, then, can Brownian motion be of such importance?

As things turn out, Brownian motion is one of the main controlling factors in the realm of nanotechnology. When one hears about the concept of nanotechnology, tiny robots resembling scaled down R2D2-style miniatures of the larger ones most likely come to mind. Unfortunately, creating nano-scale machines will not be this easy. The nano-ships that are shrunk down to carry passengers through the human bloodstream in Asimov's Fantastic Voyage, for example, would due to Brownian motion be tumultuously bumped around and flexed by the molecules in the liquid component of blood. If, miraculously, the forces of Brownian motion did not break the Van der Waals bonds maintaining the structure of the vessel to begin with, they would certainly make for a bumpy voyage, at the least.

Eric Drexler's vision of rigid nano-factories creating nano-scale machines atom by atom seems amazing. While it may eventually be possible, these rigid, scaled-down versions of macro factories are currently up against two problems: surface forces, which cause the individual parts to bind up and stick together, and Brownian motion, which causes the machines to be jostled randomly and uncontrollably like the nano-ships of science fiction.

As a consequence, it would seem that a basic scaling down of the machines and robots of the macro world will not suffice in the nano world. Does this spell the end for nanotechnology? Of course not. Nature has already proven that this realm can be conquered. Many organisms rely on some of the properties of the nano world to perform necessary tasks, as many scientists now believe that motor proteins such as kinesins in cells rely on rectified Brownian motion for propulsion by means of a Brownian ratchet. The Brownian

ratchet model proves that there are ways of using Brownian motion to our advantage.

Brownian motion is not only be used for productive motion; it can also be harnessed to aid biomolecular self-assembly, also referred to as Brownian assembly. The fundamental advantage of Brownian assembly is that motion is provided in essence for free. No motors or external conveyance are required to move parts because they are moved spontaneously by thermal agitation. Ribosomes are an example of a self-assembling entity in the natural biological world. Another example of Brownian assembly occurs when two single strands of DNA self-assemble into their characteristic double helix. Provided simply that the required molecular building blocks such as nucleic acids, proteins, and phospholipids are present in a given environment, Brownian assembly will eventually take care of the rest. All of the components fit together like a lock and key, so with Brownian motion, each piece will randomly but predictably match up with another until self-assembly is complete.

Brownian assembly is already being used to create nano-particles, such as buckyballs. Most scientists view this type of assembly to be the most promising for future nano-scale creations.

Bibliography

[1] *Rice University Shared Equipment Authority.* http://sea.rice.edu/, 17 October 2005.

[2] Annual Conference of the Electron Microscope Group of the Institute of Physics: EMAG 1997, http://www2.eng.cam.ac.uk/~bcb/cwo1.htm. *Charles Oatley: Pioneer of the Scanning Electron Microscopy*, 16 Oct 2005.

[3] Davis Baird and Ashley Shew. *Probing the History of Scanning Tunneling Microscopy.* http://cms.ifs.tudarmstadt.de/fileadmin/phil/nano/baird-shew.pdf, 17 Oct 2005.

[4] Peter Bedrossian. *Scanning Tunneling Microscopy: Opening a New Era of Materials Engineering.* Lawrence Livermore National Laboratory, http://www.llnl.gov/str/Scan.html, 17 Oct 2005.

[5] Lisa Benatar and Rebeca Howland. *A Practical Guide to Scanning Probe Microscopy.* ThermoMicroscopes, http://web.mit.edu/cortiz/www/AFMGallery/PracticalGuide.pdf, 1993-2000. 18 Oct 2005.

[6] Material Science and Engineering Department at Iowa State University, http://mse.iastate.edu/microscopy/home.html. *Welcome to the World of Scanning Electron Microscopy*, 16 Oct 2005.

Index of Keywords and Terms

Keywords are listed by the section with that keyword (page numbers are in parentheses). Keywords do not necessarily appear in the text of the page. They are merely associated with that section. *Ex.* apples, § 1.1 (1) **Terms** are referenced by the page they appear on. *Ex.* apples, 1

Attributions

Collection: *Nanotechnology for the Oil and Gas Industry*
Edited by: Andrew R. Barron
URL: http://cnx.org/content/col10700/1.11/
License: http://creativecommons.org/licenses/by/3.0/

Module: "Preface to Nanotechnology for the Oil and Gas Industry"
By: Andrew R. Barron
URL: http://cnx.org/content/m25743/1.2/
Page: 1
Copyright: Andrew R. Barron
License: http://creativecommons.org/licenses/by/3.0/

Module: "The Early History of Nanotechnology"
By: Andrew R. Barron
URL: http://cnx.org/content/m35280/1.1/
Pages: 3-13
Copyright: Andrew R. Barron
License: http://creativecommons.org/licenses/by/3.0/
Based on: The Early History of Nanotechnology
By: Devon Fanfair, Salil Desai, Christopher Kelty
URL: http://cnx.org/content/m14504/1.1/

Module: "Buckyballs: Their history and discovery"
By: Martha Farnsworth, Maclovio Fernandez, Luca Sabbatini
URL: http://cnx.org/content/m14355/1.1/
Pages: 13-23
Copyright: Martha Farnsworth, Maclovio Fernandez, Luca Sabbatini, John S. Hutchinson
License: http://creativecommons.org/licenses/by/2.0/

Module: "Introduction to Nanoparticle Synthesis"
By: Andrew R. Barron
URL: http://cnx.org/content/m22372/1.2/
Page: 25
Copyright: Andrew R. Barron
License: http://creativecommons.org/licenses/by/3.0/

Module: "Carbon Nanomaterials"
By: Andrew R. Barron
URL: http://cnx.org/content/m22580/1.4/
Pages: 25-36
Copyright: Andrew R. Barron
License: http://creativecommons.org/licenses/by/3.0/

Module: "Graphene"
By: Christopher E. Hamilton, Andrew R. Barron
URL: http://cnx.org/content/m29187/1.3/
Pages: 36-40
Copyright: Christopher E. Hamilton, Andrew R. Barron
License: http://creativecommons.org/licenses/by/3.0/

Module: "Oxide Nanoparticles"
By: Andrew R. Barron
URL: http://cnx.org/content/m22969/1.2/
Pages: 41-45
Copyright: Andrew R. Barron
License: http://creativecommons.org/licenses/by/3.0/

Module: "Synthesis of Magnetite Nanoparticles"
By: Ezekial Fisher, Andrew R. Barron
URL: http://cnx.org/content/m22167/1.6/
Pages: 45-46
Copyright: Ezekial Fisher, Andrew R. Barron
License: http://creativecommons.org/licenses/by/3.0/

Module: "Kitchen Synthesis of Nanorust"
By: Mary McHale
URL: http://cnx.org/content/m20813/1.3/
Pages: 46-51
Copyright: Mary McHale
License: http://creativecommons.org/licenses/by/3.0/

Module: "Semiconductor Nanoparticles"
By: Andrew R. Barron
URL: http://cnx.org/content/m22374/1.4/
Pages: 51-52
Copyright: Andrew R. Barron
License: http://creativecommons.org/licenses/by/3.0/

Module: "Silver Nanoparticles: A Case Study in Cutting Edge Research"
By: Alvin Orbaek, Mary McHale, Andrew R. Barron
URL: http://cnx.org/content/m19597/1.11/
Pages: 52-64
Copyright: Alvin Orbaek, Mary McHale, Andrew R. Barron
License: http://creativecommons.org/licenses/by/3.0/

Module: "The Application of VSI (Vertical Scanning Interferometry) to the Study of Crystal Surface Processes"
By: Inna Kurganskaya, Andreas Luttge, Andrew R. Barron
URL: http://cnx.org/content/m22326/1.4/
Pages: 65-76
Copyright: Inna Kurganskaya, Andrew R. Barron
License: http://creativecommons.org/licenses/by/3.0/

Module: "Beyond Optical Microscopy"
By: Melissa Dominguez, Sean McCudden, McKenzie Smith, Kevin Kelly
URL: http://cnx.org/content/m14353/1.2/
Pages: 76-87
Copyright: Melissa Dominguez, Sean McCudden, McKenzie Smith, Kevin Kelly
License: http://creativecommons.org/licenses/by/2.0/

Module: "TEM Imaging of Carbon Nanomaterials"
By: Zhengzong Sun, Andrew R. Barron
URL: http://cnx.org/content/m22963/1.5/
Pages: 87-93
Copyright: Zhengzong Sun, Andrew R. Barron
License: http://creativecommons.org/licenses/by/2.0/

Module: "Characterization of Covalently Functionalized Single-Walled Carbon Nanotubes"
By: Liling Zeng, Andrew R. Barron
URL: http://cnx.org/content/m22299/1.4/
Pages: 94-97
Copyright: Liling Zeng, Andrew R. Barron
License: http://creativecommons.org/licenses/by/3.0/

Module: "Characterization of Single-Walled Carbon Nanotubes by Raman Spectroscopy"
By: Richa Sethi, Andrew R. Barron
URL: http://cnx.org/content/m22925/1.2/
Pages: 98-112
Copyright: Richa Sethi, Andrew R. Barron
License: http://creativecommons.org/licenses/by/3.0/

Module: "Mossbauer Analysis of Iron Oxide Nanoparticles"
By: Ezekial Fisher, Andrew R. Barron
URL: http://cnx.org/content/m22619/1.3/
Pages: 112-114
Copyright: Ezekial Fisher, Andrew R. Barron
License: http://creativecommons.org/licenses/by/3.0/

Module: "Measuring the Specific Surface Area of Nanoparticle Suspensions using NMR"
By: Varun Shenoy Gangoli, Andrew R. Barron
URL: http://cnx.org/content/m34663/1.1/
Pages: 114-124
Copyright: Varun Shenoy Gangoli
License: http://creativecommons.org/licenses/by/3.0/

Module: "XPS of Carbon Nanomaterials"
By: Ariana Bratt, Andrew R. Barron
URL: http://cnx.org/content/m34549/1.2/
Pages: 125-140
Copyright: Ariana Bratt, Andrew R. Barron
License: http://creativecommons.org/licenses/by/3.0/

Module: "Using XPS to Analyze Metal Nanoparticles"
By: Lauren Harrison, Andrew R. Barron
URL: http://cnx.org/content/m34526/1.1/
Pages: 140-143
Copyright: Lauren Harrison, Andrew R. Barron
License: http://creativecommons.org/licenses/by/3.0/

Module: "Thermogravimetric Analysis of Single Walled Carbon Nanotubes"
By: Caoimhe de Fréin, Andrew R. Barron
URL: http://cnx.org/content/m22972/1.2/
Pages: 144-149
Copyright: Caoimhe de Fréin, Andrew R. Barron
License: http://creativecommons.org/licenses/by/3.0/

Module: "ICP-AES Analysis of Nanoparticles"
By: Alvin Orbaek, Andrew R. Barron
URL: http://cnx.org/content/m22058/1.18/
Pages: 149-155
Copyright: Alvin Orbaek, Andrew R. Barron
License: http://creativecommons.org/licenses/by/3.0/

Module: "TGA/DSC-FTIR Characterization of Oxide Nanaoparticles"
By: Nikolaos Soultanidis, Andrew R. Barron
URL: http://cnx.org/content/m23038/1.2/
Pages: 156-168
Copyright: Nikolaos Soultanidis, Andrew R. Barron
License: http://creativecommons.org/licenses/by/3.0/

Module: "Theory of A Superconducting Quantum Interference Device (SQUID)"
By: Samuel Maguire-Boyle, Andrew R. Barron
URL: http://cnx.org/content/m22750/1.3/
Pages: 168-177
Copyright: Samuel Maguire-Boyle, Andrew R. Barron
License: http://creativecommons.org/licenses/by/3.0/

Module: "Practical Guide to Using a Superconducting Quantum Interference Device"
By: Samuel Maguire-Boyle, Andrew R. Barron
URL: http://cnx.org/content/m22968/1.2/
Pages: 177-184
Copyright: Samuel Maguire-Boyle, Andrew R. Barron
License: http://creativecommons.org/licenses/by/3.0/

Module: "Magnetics"
By: Samuel Maguire-Boyle, Andrew R. Barron
URL: http://cnx.org/content/m22749/1.4/
Pages: 185-197
Copyright: Samuel Maguire-Boyle, Andrew R. Barron
License: http://creativecommons.org/licenses/by/3.0/

Module: "Brownian Motion"
By: Jason Holden, Kevin Kelly
URL: http://cnx.org/content/m14354/1.3/
Pages: 197-206
Copyright: Jason Holden, Kevin Kelly
License: http://creativecommons.org/licenses/by/2.0/

Nanotechnology for the Oil and Gas Industry
Provides an overview of nanotechnology for researchers and business leaders in the oil and gas industry

About Connexions
Since 1999, Connexions has been pioneering a global system where anyone can create course materials and make them fully accessible and easily reusable free of charge. We are a Web-based authoring, teaching and learning environment open to anyone interested in education, including students, teachers, professors and lifelong learners. We connect ideas and facilitate educational communities.

Connexions's modular, interactive courses are in use worldwide by universities, community colleges, K-12 schools, distance learners, and lifelong learners. Connexions materials are in many languages, including English, Spanish, Chinese, Japanese, Italian, Vietnamese, French, Portuguese, and Thai. Connexions is part of an exciting new information distribution system that allows for **Print on Demand Books**. Connexions has partnered with innovative on-demand publisher QOOP to accelerate the delivery of printed course materials and textbooks into classrooms worldwide at lower prices than traditional academic publishers.